W boson measurement in the muonic decay channel at forward rapidity with ALICE

Jianhui Zhu

UNIVERSITE BRETAGNE LOIRE

IMT Atlantique
Bretagne-Pays de la Loire
École Mines-Télécom

Thèse de Doctorat

Jianhui ZHU

Mémoire présenté en vue de l'obtention du
grade de Docteur de IMT ATLANTIQUE
sous le sceau de l'Université Bretagne Loire

École doctorale : 3MPL

Discipline : Constituants élémentaires et physique théorique
Spécialité : Physique des Ions Lourds
Unité de recherche : Subatech, Nantes, France

Soutenue le 01 avril 2017
Thèse N° : 2017IMTA0014

Mesure de la production du boson W dans le canal muonique à rapidité à l'avant avec ALICE

W boson measurement in the muonic decay channel at forward rapidity with ALICE

JURY

Rapporteurs :	**Nicole BASTID**, Professeur, LPC, Université Clermont Auvergne, France
	Yugang MA, Professeur, Shanghai Institute of Applied Physics, CAS, Chine
Examinateurs :	**Zhongbao YIN,** Professeur, Central China Normal University, Chine
	Xiaoming ZHANG, Chargé de Recherche, Central China Normal University, Chine
Co-encadrant :	**Daicui ZHOU**, Professeur, Central China Normal University, Chine
Directeur de Thèse :	**Ginés MARTINEZ-GARCIA**, Directeur de Recherche CNRS, Subatech, Ecole des Mines-Telecom, France
Co-directeur de Thèse :	**Diego STOCCO**, Chargé de Recherche, Subatech, Ecole des Mines-Telecom, France

Mesure de la production du boson W dans le canal muonique à rapidité à l'avant avec ALICE

Résumé

Selon le modèle standard, la matière est constituée de particules fondamentales : les quarks, les leptons et les bosons médiateurs d'interaction. Les quarks sont les particules soumises à l'interaction forte, qui est véhiculée par les gluons, et peuvent avoir six saveurs différentes. Les leptons et les quarks sont soumis à l'interaction électrofaible, véhiculée par les bosons $W^{\pm}$, Z° et les photons. Le modèle standard explique de nombreux résultats et prédit l'existence d'une particule, le boson de Higgs, qui est responsable de la masse des autres particules. Dans le modèle standard, l'interaction forte entre les quarks et les gluons (partons) est décrite par la théorie de la ChromoDynamique Quantique (QCD). La constante de couplage de l'interaction forte change avec l'énergie/distance entre particules. Elle est notamment grande à petites impulsions/grandes distances et petite à grandes impulsions/petites distances. Par conséquent, les partons sont confinés dans les hadrons (confinement), mais ils se comportent comme des particules quasi-libres à petites distances et hautes énergies d'interaction (liberté asymptotique). Les calculs de QCD sur réseau (lattice-QCD) prédisent que, dans des conditions extrêmes de densité d'énergie ($\gtrsim 1$ GeV/fm^3) et/ou densité numérique des baryons ($\gtrsim 1$ fm^{-3}), les partons ne sont plus confinés à l'intérieur des hadrons (déconfinement), et un nouvel état de la matière est formé, constitué par quarks et gluons : le Plasma de Quarks et de Gluons (QGP). Ce nouvel état de la matière était le plus abondant lors de premières microsecondes après le Big Bang et pourrait exister aujourd'hui au cœur des étoiles à neutrons où la densité du nombre baryonique est très élevée. L'étude du QGP donne donc des informations importantes sur l'interaction forte, les propriétés de la matière à très haute température et l'évolution de l'univers lors de ses premiers instants.

Les conditions pour la formation du QGP peuvent être reproduites en laboratoire à travers la collision d'ions lourds ultra-relativistes. Deux faisceaux d'ions lourds, accélérés à une vitesse très proche de la vitesse de la lumière, s'entrechoquent créant dans la zone de la collision des densités d'énergie extrêmement élevées qui peuvent mener à la formation du QGP. Le QGP créé va subir d'une violente expansion relativiste dans le vide qui entoure la zone de la collision. Lors de cette expansion, la densité d'énergie du milieu diminue et en quelques dizaines de fm/c le milieu se confine en produisant une matière hadronique (gaz de hadrons). Bien qu'il soit impossible d'observer les QGP directement, certaines observables bien précises ont la particularité d'être très sensibles

à la formation du QGP, notamment les jet de haute énergie, les quarks lourds, les quarkonia et la production de photons et de dileptons. En revanche la production de boson électrofaibles ne devrait pas être affectée par la présence du QGP et représente une référence unique qui n'a jamais été mesurée dans les collisions entre ions lourds avant la construction du grand collisionneur de hadrons au CERN.

En général, le taux de production de particules ou leurs distributions cinématiques peuvent être modifiés par la présence du QGP par rapport aux observations faites dans les collisions proton-proton. Toutefois, certaines modifications par rapport à la production en collisions proton-proton ne sont pas dues à la présence d'un milieu deconfiné, mais à des effets liés à l'utilisation des ions lourds, telle que la modification de la fonction de distribution partonique (PDF) dans les noyaux (comme le shadowing, la saturation de gluons, etc).

À cause de sa grande masse, le boson W est produit lors des collisions partoniques dures dans la phase initiale de la collision des noyaux, avant la formation du QGP. Ses produits de désintégration leptoniques ne sont pas affectés par la présence du milieu deconfiné, car ils ne sont pas sensibles à l'interaction forte. Il s'agit donc d'un canal idéal pour la compréhension des effets nucléaires non liées au QGP. En particulier, la mesure des bosons vecteurs dans un large intervalle en rapidité permet d'étudier les PDF nucléaires (nPDF) dans une région de haute virtualité $Q^2 \sim (100\ \text{GeV})^2$ et de fraction d'impulsion du parton dans le nucléon (x-Bjorken) qui est actuellement peu contrainte par les données. En outre, l'étude de l'asymétrie de charge des bosons $W^{\pm}$, qui sont produits principalement lors des processus $u\bar{d} \to W^+$ et $d\bar{u} \to W^-$ à hautes énergies, permet de tester la dépendance des modification des PDFs par rapport à la saveur des quarks. En collision proton-proton, le taux de production du boson W est bien connu, et sa mesure peut être donc utilisée comme chandelle standard pour l'estimation de la luminosité. Comme pour les collisions Pb–Pb, la fonction de distribution partonique en collisions proton-plomb est affectée par les effets nucléaires tels que le shadowing et la saturation de gluons. Par conséquent, l'étude de boson W est très importante pour comprendre la distribution partonique dans le noyau.

Le Grand Collisionneur de Hadrons (LHC) de l'Organisation Européenne pour la Recherche Nucléaire (CERN) qui se trouve à Genève en Suisse fonctionne depuis 2009 et il a produit des collisions en proton-proton à des énergies du centre de masse de $\sqrt{s} = 7$, 8 et 13 TeV, des collisions proton-plomb à des énergies par nucléon de $\sqrt{s_{\text{NN}}} = 5.02$ et 8.16 TeV ainsi que des collisions plomb-plomb à 2.76 et 5.02 TeV. Le LHC a marqué un nouveau chapitre dans le domaine de la physique des hautes énergies. L'énergie du centre de masse atteinte au LHC est jusqu'à 25 fois plus grande que celle atteinte par le Relativistic Heavy Ion Collider (RHIC) au Laboratoire Na-

tional de Brookaven aux Etats Unis, ce qui permet d'étudier le QGP dans un nouveau régime d'énergie.

ALICE (A Large Ion Collider Experiment) est la seule parmi les 4 expériences installées au LHC à être spécifiquement conçue pour la physique des ions lourds. Elle est constituée d'un tonneau central complété par un spectromètre à muon vers l'avant ainsi que des détecteurs pour les mesures à grandes rapidités. Le spectromètre à muon couvre la région de pseudo-rapidité $-4.0 < \eta < -2.5$. En collision proton-proton, le référentiel du centre de masse coïncide avec celui du laboratoire et on mesure donc des muons avec une rapidité entre $-4.0 < y_{\rm cms} < -2.5$. En collision proton-plomb, par contre, la différence d'impulsion entre le proton et l'ion mène à une déviation de la rapidité du système de centre de masse. En renversent la direction de circulation des deux faisceaux, il est donc possible de mesurer des muons avec $2.03 < y_{\rm cms} < 3.53$ (protons voyageant vers le spectromètre) et $-4.46 < y_{\rm cms} < -2.96$ (protons s'éloignant du spectromètre). On note aussi que la région de rapidité couverte par le spectromètre à muon d'ALICE est complémentaire de celle des expériences ATLAS et CMS. Le spectromètre à muons se compose d'un aimant dipolaire avec un champ magnétique intégré de 3 T.m de cinq stations de trajectographie composées de chambres proportionnelles multifils à lecture bi-cathodique et de deux stations de déclenchement composées de chambres à plaques résistives et de plusieurs éléments d'absorption. Les stations de trajectographie sont placées en aval d'un absorbeur frontal conique en carbone, béton et acier, d'une longueur épaisseur de 4.1 m (correspondant à 10 longueurs d'interaction nucléaire) qui filtre les hadrons, électrons et photons produits au point d'interaction. Les stations de déclenchement sont placées après une paroi de fer d'une épaisseur de 1.2 m (7.2 longueurs d'interaction) qui absorbe les hadrons secondaires s'échappant de l'absorbeur et des muons de faible impulsion, provenant principalement de la désintégration des hadrons légers. Enfin, un blindage de faisceau conique recouvrant le tube faisceau protège le spectromètre des particules produites lors de l'interaction des particules de grande rapidité avec le tube lui-même.

La centralité de la collision est mesurée à partir de l'énergie déposée dans calorimètre à zéro dégrée pour neutrons (ZN) en direction de l'ion de plomb qui se fragmente. Le nombre moyen de collisions nucléon-nucléon binaires $< N_{\rm coll} >$ est obtenu à partir de la "méthode hybride", qui se repose sur l'hypothèse que la multiplicité mesurée des particules chargées à mi-rapidité est proportionnelle au nombre moyen de nucléons qui participent à la collision $< N_{\rm part} >$. Les valeurs de $< N_{\rm part} >$ pour une classe de centralité ZN donnée sont calculées en mettant à l'échelle le nombre moyen de participants dans des collisions MB $< N_{\rm part}^{\rm MB} >$, estimé avec un Glauber Monte Carlo, par le rapport de la multiplicité moyenne des particules chargées mesurées à mi-

rapidité pour la même classe de centralité ZN et celle de MB. Ces valeurs sont désignées par $< N_{\mathrm{part}}^{\mathrm{mult}} >$ pour indiquer l'hypothèse utilisée pour la mise à l'échelle. Le nombre correspondant de collisions binaires est alors obtenu comme: $< N_{\mathrm{coll}}^{\mathrm{mult}} >=< N_{\mathrm{part}}^{\mathrm{mult}} > -1$. Les incertitudes systématiques sont estimées en utilisant différentes hypothèses.

Cette thèse a pour objectif, la mesure de la production du boson W vers l'avant dans le canal muonique en collisions proton-plomb à 5.02 TeV et proton-proton à 8 TeV avec l'expérience ALICE au LHC. Pour les collisions proton-plomb, la production de bosons W a été également étudiée en fonction de la centralité de la collision. Il s'agit de la première mesure du boson W à grandes rapidités en collisions proton-plomb. Dans ce travail, nous avons tout d'abord étudié les caractéristiques cinématiques des muons issus de la désintégration du boson W par des simulations, afin d'en extraire sa contribution à la distribution d'impulsion transverse (p_{T}). On observe que la contribution est maximale pour $p_{\mathrm{T}} \sim 40$ GeV/c. A plus basse impulsion transverse la source principale de muons est la désintégration des hadrons contenant un quark charmé ou beau. A haute impulsion transverse la contribution principale du bruit de fond est constituée par des muons issus de la désintégration de Z°/γ^{*}. La distribution cinématique des différentes contributions est décrite par des "templates" obtenues avec des simulations MC qui utilisent des calculs de QCD comme générateur. La contribution du signal est obtenue en ajustant les données avec ces templates. Le nombre de muons ainsi estimé est corrigé par l'acceptance et l'efficacité du détecteur et normalisé pour obtenir la section efficace. L'asymétrie de charge, définie comme le rapport entre la différence de production des muons positifs et négatifs sur la production totale, est mesurée également. Les mesures sont comparées avec des calculs de QCD perturbative au Next-to-Leading Order (NLO) et Next-to-Next-to-Leading Order (NNLO). Les résultats en collisions proton-proton sont en bon accord avec la théorie (Figure 1). Dans le cas des collisions

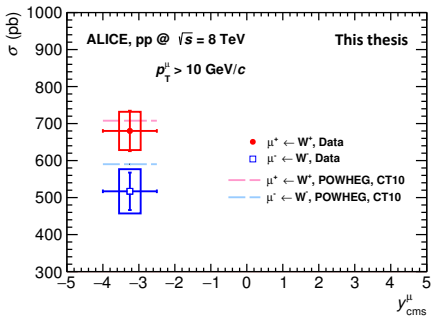

Figure 1: Section efficace de muon avec un $p_{\mathrm{T}}^{\mu} > 10$ GeV/c provenants de la décroissance du bosons $\mathrm{W}^{\pm}$ dans les collisions pp à 8 TeV. La mesure a été comparée à la prédiction obtenue avec le logiciel POWHEG en utilisant les fonction de distribution de partons CT10.

proton-plomb, on compare avec des calculs qui incluent qui incluent ou non les modifications nucléaires des PDFs. Les mesures expérimentales sont compatibles avec les deux cas dans les incertitudes actuelles (Figure 2). En collision proton-plomb, on mesure aussi la section efficace de la production de muons issus de la désintégration des bosons W divisée par le nombre moyen de collision nucléon-nucléon, en fonction de la centralité de l'événement, déterminée avec différents estimateurs. Comme la production du boson W est proportionnelle aux collisions nucléon-nucléon, son taux de production par collision nucléon-nucléon devrait être constant en fonction de la centralité si les estimateurs ne sont pas biaisés. La mesure montre que la dépendance est plate pour tous les estimateurs dans les incertitudes expérimentales qui sont entre 8 et 16% (Figure 3).

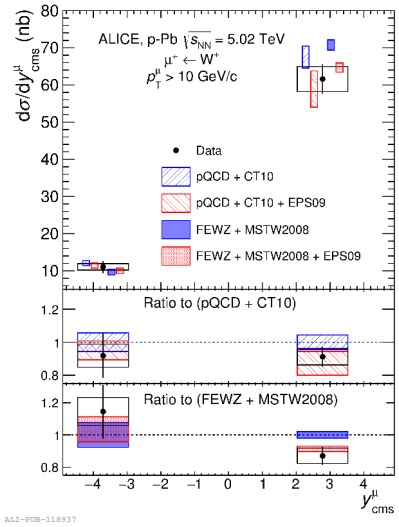

Figure 2: Section efficace différentielle en rapidité des muon positifs de $p_T^\mu > 10$ GeV/c provenant de la décroissance du boson W^+. Les mesures sont comparées aux modèles théoriques incluant ou pas les effets de shadowing des fonctions des distribution des partons selon la paramétrisation EPS09.

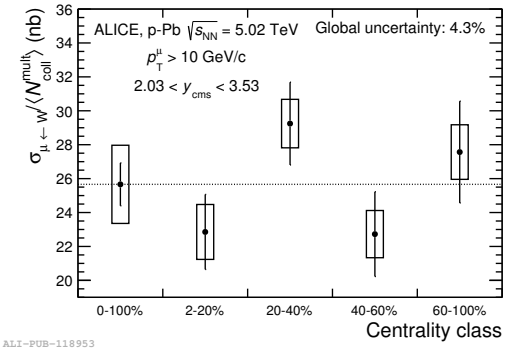

Figure 3: Section efficaces des muons de $p_T^\mu > 10$ GeV/c provenant de la décroissance du boson W normalisé par les nombre de collisions binaires, en fonction de la centralité de la collision proton-plomb. La centralité a été estimée par un les calorimètre à zéro degrés ZN.

Ce mémoire est divisé en 7 chapitres. Après une introduction des connaissances générales de physique des hautes énergies, le chapitre 1 introduit principalement le modèle standard et le diagramme de phase de la matière nucléaire et le chapitre 2 se focalise sur la théorie électrofaible, la motivation de physique de la présente thèse. Le chapitre 3 présente les principes de conception des détecteurs d'ALICE et l'utilisation des différents sous-détecteurs et le chapitre 4 montre l'acquisition et le traitement des données. Le chapitre 5 décrit la méthode d'extraction des signaux du boson W dans les données en collisions proton-plomb et dans le chapitre 6 la même méthode est utilisée pour l'analyse en collisions proton-proton. Le chapitre 7 est un résumé des résultat obtenus et les perspectives de ces études.

En conclusion, cette thèse présente la première mesure des bosons W avec le détecteur ALICE. Dans les collisions proton-proton, les calculs théoriques reproduisent correctement les mesures qui ont des incertitudes entre 8 et 16%. Dans les collisions proton-plomb, les calculs théoriques des collisions nucléon-nucléon renormalisés par le nombre de collisions binaires reproduisent également les données. Toutefois, les calculs tenant compte du shadowing des gluons dans le noyau de plomb semblent être un meilleur accord avec les mesures, notamment à rapidité positive où les effets du shadowing devraient être plus importants. L'étude de la production de boson W en fonction de la centralité de la collision p–Pb a permis de vérifier la loi d'échelle avec le nombre de collisions nucléon-nucléon avec une précision de 15%. Certains résultats de ce travail de thèse ont été publiés dans la revue Journal of High Energy Physics, volume 1702, page 77 par la collaboration ALICE avec le titre "W and Z boson production in p–Pb collisions at 5.02 TeV".

Mots-clés : Collisions d'ions lourds; Collisions d'hadrons; Plasma de Quarks et de Gluons (QGP); Grand Collisionneur de Hadron (LHC); A Large Ion Collider Experiment (ALICE); Organisation Européenne pour la Recherche Nucléaire (CERN); Boson électrofaible; Muon; Fonction de distribution des partons; Collisions proton - plomb; Collisions proton - proton

W boson measurement in the muonic decay channel at forward rapidity with ALICE

Abstract

With the beginning of the Large Hadron Collider (LHC) at CERN in 2009, a new era in Quark-Gluon Plasma (QGP) physics has started by studying heavy-ion collisions at high energies in the centre of mass frame (25 times larger than those in the RHIC collider at BNL). The LHC represents today an ideal tool to study the properties of QGP in the laboratory. ALICE (A Large Ion Collider Experiment) is the only experiment of LHC specifically designed to measure those properties. A wide variety of observables can be studied by means of the 18 sub-detectors of the ALICE apparatus, which are grouped in two main elements: the central barrel and the muon spectrometer. With the muon spectrometer, we can detect high transverse momentum muons and dimuons in order to measure open heavy flavours, quarkonia and electroweak bosons production.

The high collision energies available at the LHC allow for an abundant production of hard probes, such as quarkonia, high-p_{T} jets and vector bosons (W, Z), which are produced in initial hard parton scattering processes. The latter decay before the formation of the QGP, which is a deconfined phase of Quantum ChromoDynamics (QCD) matter produced in high-energy heavy-ion collisions. Furthermore, their leptonic decay products do not interact strongly with the QGP. The electroweak bosons provide a way for benchmarking in-medium modifications to coloured probes. In Pb–Pb and p–Pb collisions, precise measurements of W-boson production can constrain the nuclear Parton Distribution Functions (nPDFs), which could be modified with respect to the nucleon due to shadowing or gluon saturation. In addition, they can be used to test the scaling of hard particle production with the number of binary nucleon–nucleon collisions. Especially in p–Pb collisions, the measurement of W yields at forward and backward rapidity allows us to probe the modification of nPDFs at small and large Bjorken-x, respectively. Such measurements can be benchmarked in pp collisions, where W-boson production is theoretically known with good precision. Also, the charge asymmetry of leptons from W-boson decays is a sensitive probe of up and down quark densities in a nucleon inside a nucleus.

ALICE has already completed data taking of large data samples of pp collisions at $\sqrt{s} = 7$, 8 and 13 TeV, p–Pb collisions at $\sqrt{s_{\mathrm{NN}}} = 5.02$ TeV and Pb–Pb collisions at $\sqrt{s_{\mathrm{NN}}} = 2.76$ and 5.02 TeV. The data samples collected in Run 1 (i.e. in year 2009-2013) allowed us to study the production of

heavy flavours and W-boson through their muonic decay channel in pp and p–Pb collisions. The production of W-boson in pp collisions at 8 TeV and p–Pb collisions at 5.02 TeV are measured with the ALICE muon spectrometer via the inclusive p_{T}-differential muon yield. In pp collisions the rapidity covered by muon spectrometer is $-4 < y_{\mathrm{cms}} < -2.5$ and in p–Pb collisions it separates into forward rapidity (p-going direction, $2.03 < y_{\mathrm{cms}} < 3.53$) and backward rapidity (Pb-going direction, $-4.46 < y_{\mathrm{cms}} < -2.96$) via changing beam direction. These rapidity regions are complementary to the one of ATLAS (A Toroidal LHC ApparatuS, $|\eta_{\mathrm{lab}}| < 2.5$) and CMS (Compact Muon Solenoid, $|\eta_{\mathrm{lab}}| < 2.4$) experiments.

This thesis consists of four parts. Part I is the introduction of high-energy physics and contains two chapters. Chapter 1 is a general knowledge of QCD and QGP, and Chapter 2 concentrates on the electroweak theory and the motivation of investigating of W-boson in heavy-ion collisions. Part II presents the ALICE experiment, which involves hardware, software, the online data taking and the offline data selection. Chapter 3 shows the design of the structure including central barrel and forward muon spectrometer and Chapter 4 gives an account of data. Part III is the core content, which reveals the detail of W-boson measurement in p–Pb (Chapter 5) and pp (Chapter 6) collisions. Finally, the conclusions are drawn in part IV (Chapter 7).

Keywords: Heavy ion collisions; HIC; Hadronic collisions; Quark Gluon Plasma; QGP; LHC; ALICE; CERN; Electroweak boson; Muon; Parton distribution functions; PDF; Nuclear parton distribution functions; nPDF; p–Pb collisions; pp collisions; 5 TeV; 8 TeV

Acknowledgments

I would like to express my gratitude to all those who helped me during the writing of this thesis. My deepest gratitude goes first and foremost to all my supervisors, Daicui Zhou at CCNU in Wuhan (China), Gines Martinez and Diego Stocco at SUBATECH in Nantes (France), for their constant encouragement and guidance during my PhD career. Especially thank Diego for his experience, useful discussions and excellent ability in data analysis.

I am indebted to Philippe Pillot for discussions on the resolution of muon tracks, which is the challenge of this thesis. Also thank Francesco Bossu and Kgotlaesele Johnson Senosi for their collaboration and cross-check step by step in the analysis. I'm also grateful to Zaida Conesa Del Valle and Francesco Prino for their suggestions and comments during the research. I appreciate Yugang Ma and Nicole Bastid for carefully reading this manuscript and providing useful comments and suggestions.

High tribute shall be paid to Nicole Bastid and Philippe Crochet for their discussions in muon analysis and help in life when i was in Clermont-Ferrand from August to December, 2011.

My cordial and sincere thanks go to the whole member of ALICE group at Nantes, Laurent Aphecetche, Guillaume Batigne, Marie Germain, Alexandre Shabetai, Astrid Morreale, Javier Martin, Lucile Ronflette, Benjamin Audurier and etc for their warm help during my stay in Nantes.

I am also very grateful to all member of ALICE group at Wuhan, Zhongbao Yin, Xiaoming Zhang, Yaxian Mao, Hua Pei, Dong Wang, Fan Zhang, Xiangrong Zhu, Mengliang Wang, Ruina Dang, Shuang Li, Jiebin Luo, Liang Zheng, Hui Li, Wenzhao Luo, Xinye Peng, Xiaowen Ren, Yonghong Zhang, Zuman Zhang, Haitao Zhang, Hongsheng Zhu and etc for discussions in analysis and help in my daily life.

Special thanks should go to China Scholarship Council (CSC) and France China Particle Physics Laboratory (FCPPL) to provide me the funding support for stay in Nantes.

Last but not the least, big thanks go to my family who has shared with me my worries, frustrations, and hopefully my ultimate happiness in eventually finishing this thesis.

Contents

Part I

Introduction

Science is a wonderful thing if one does not have to earn a living at it. One should earn one's living by work of which one is sure one is capable. Only when we do not have to be accountable to anyone can we find joy in scientific endeavor.

Albert Einstein

1

Particle physics in heavy-ion collisions

During my doctoral career, the top three questions I have been asked are: what is a "particle"? why do you study it? how to use it in our daily life? I was perturbed each time when I chatted with my friends on my major. It is difficult to use simple words to explain what we researched to them since they do not have background in this field. Particles can not be seen with our own eyes and belong to the microscopic world, which means a special way is needed to investigate their physical properties. Many scientists began to think about how to describe particles via physical formula and how to design experimental devices to measure them. Thus, a lot of physical models were proposed in theory and some huge machines were built in experiment. So far, the most successful and a well-tested theory in particle physics is the Standard Model (SM). Let us start by describing what is the SM.

1.1 Standard model

All matter is made of elementary particles which arise in two basic types called quarks and leptons, shown in the left panel of Figure 1.1. Each of them consists of six particles, which are organized in "generations". The lightest and most stable particles build up the first generation (quarks: up and down, leptons: electron and electron neutrino), while the heavier and less stable particles belong to the second generation (quarks: charm and strange, leptons: muon and muon

neutrino) and third generation (quarks: top and bottom, leptons: tau and tau neutrino). All stable matter in the universe is made of particles that belong to the first generation; any heavier particles quickly decay to the most stable level. Quarks and leptons have their antiparticles with the same mass and opposite charge named anti-quarks and anti-leptons, respectively.

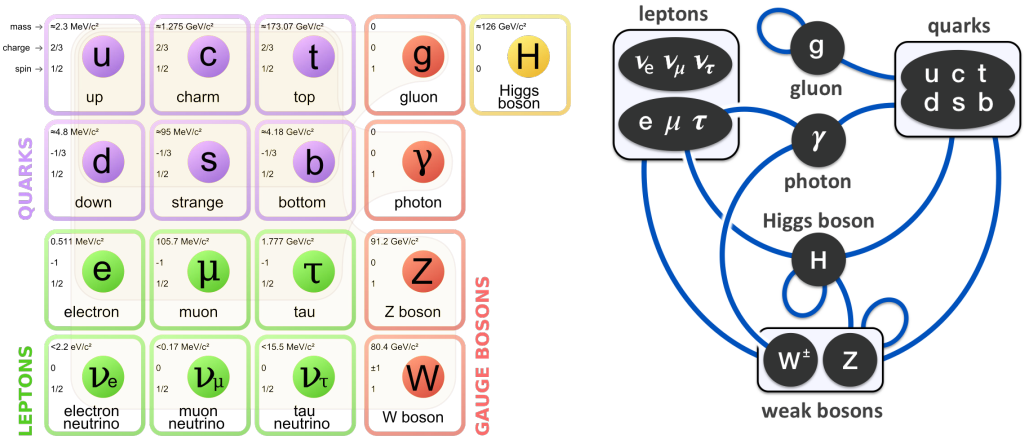

Figure 1.1: The SM of elementary particles (left) and summary of interactions between particles described by the SM (right).

In the broadest sense, a particle is a quantity of matter. In physics, a particle is a small object to which can be ascribed several physical properties such as charge or mass. We have already learned in the earlier schools that matter is made of atoms and atoms are made of smaller constituents: protons, neutrons and electrons. Protons and neutrons are made of quarks, while electrons are not. As far as we know, quarks and electrons are fundamental particles, not made of anything smaller. You can not have half an electron or one-third of a quark. And all particles of a given type are precisely identical to each other: they have little license plates that distinguish them. Any two electrons with the same energy will produce the same result in a detector, and that's what makes them fundamental: they do not come in a variety pack.

The SM of particle physics (formulated in the 1970s) describes the world in terms of particles (fermions, with fractional spin) and forces (which are mediated by bosons, with integer spin). Fermions obey a statistical rule described by Enrico Fermi (1901–1954) from Italy, Paul Dirac (1902–1984) from England, and Wolfgang Pauli (1900–1958) from Austria called the exclusion principle. Simply stated, fermions can not occupy the same quantum state at the same time (two fermions can not be described by the same quantum numbers). All quarks and leptons, as well as any composite particle made of an odd number of these, are fermions. Bosons, in contrast, have no problem occupying the same quantum state at the same time (more formally, two or more

bosons may be described by the same quantum numbers). The statistical rules that bosons obey were first described by Satyendra Bose (1894–1974) from India and Albert Einstein (1879–1955) from Germany. As the particles that make up light and other forms of electromagnetic radiation, photons are the bosons we have the most direct experience with. All of these are described by Quantum Field Theory.

There are four fundamental forces in the nature: the strong force, the weak force, the electromagnetic force and the gravitational force. They work at different ranges and have different strengths. Gravity is the weakest force and has an infinite range (as well as the electromagnetic force). It is accurately described by the general theory of relativity proposed by Albert Einstein in 1915 [1]. Gravity is not included in the SM, which is actually a fundamental problem that has to be solved. However for the practical purposes of particle interactions, the effect of gravity is so weak to be negligible. The other three fundamental forces described by exchange of force-carrier particles, which belong to the family of bosons, are shown in the right panel of Figure 1.1. The strong force is carried by the gluon, the weak force is carried by the W and Z bosons and the electromagnetic force is carried by the photon. These force-carrier particles are called "gauge bosons". The electromagnetic interaction and the weak interaction in SM are described as two different aspects of a single electroweak interaction. This theory was developed around 1968 by Sheldon Glashow, Abdus Salam and Steven Weinberg, and they were awarded the 1979 Nobel prize in physics for their contributions to the theory of the unified weak and electromagnetic interaction between elementary particles, including, inter alia, the prediction of the weak neutral current.

The Higgs boson was the last missing piece of the SM puzzle. It is a different kind of force carrier from the other elementary forces, and it gives mass to quarks as well as the W and Z bosons. Whether it also gives mass to neutrinos remains to be clarified. Its existence has been confirmed by two experiments (ATLAS and CMS) on the Large Hadron Collider at CERN (European Organization for Nuclear Research *) on 4 July 2012. This experimental discovery of Higgs boson [2, 3] led that the Nobel prize in physics was awarded jointly to Professors Francois Englert and Peter Higgs for the prediction of this fundamental particle on 8 October 2013 .

*The abbreviation "CERN" is denominated according to its old name in French, Conseil Europeen pour la Recherche Nucleaire

1.1.1 Quantum ChromoDynamics

Quantum ChromoDynamics (QCD) is a type of quantum field theory [4] called a non-abelian gauge theory with symmetry group SU(3) that describes the strong interactions between quarks and gluons. In QCD, the analogous of the electric charge is a property called "color". There are three kinds of color charges, which are called red, green and blue, using the same terminology for colors perceived by humans. They are just quantum parameters and completely unrelated to familiar phenomenon of color in daily life. The quarks carry only one color, while the gluons are a combination of color and anti-color. The fact that the gluon carries a color charge is a fundamental difference compared to photons, since it allows for self-interaction. There are eight different gluon types which form a SU(3) octet [5] :

$$R\bar{G}, R\bar{B}, G\bar{R}, G\bar{B}, B\bar{R}, B\bar{G}, \frac{1}{\sqrt{2}}(R\bar{R} - G\bar{G}), \frac{1}{\sqrt{6}}(R\bar{R} + G\bar{G} - 2B\bar{B})$$

The combination of color and anti-color for gluons and how a gluon changes the color of quarks are shown in Figure 1.2. The symmetric singlet state $\frac{1}{\sqrt{3}}(R\bar{R} + G\bar{G} + B\bar{B})$ does not exist because it can not mediate color. All observed particles do not carry a net color charge and they are white or colorless.

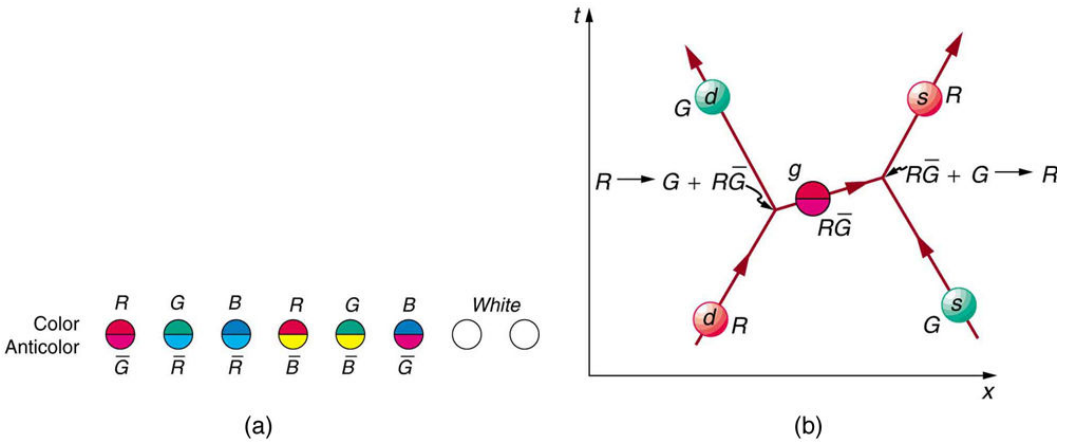

Figure 1.2: The combination of color and anti-color for gluons (a), and how a gluon changes the color of quarks (b).

The peculiarities of QCD are:

- coupling constant larger than unity
- confinement phenomena

- gluons carry colour and the asymptotic freedom
- spontaneous breaking to the chiral symmetry in the limit of zero-mass quark

1.1.2 Lagrangian of QCD

The QCD Lagrangian is given by [6]

$$\mathcal{L} = \sum_q \bar{\psi}_{q,a}(i\gamma^\mu \partial_\mu \delta_{ab} - g_s \gamma^\mu t^C_{ab} \mathcal{A}^C_\mu - m_q \delta_{ab})\psi_{q,b} - \frac{1}{4} F^A_{\mu\nu} F^{A\mu\nu} \tag{1.1}$$

The γ^μ are the Dirac γ-matrices; the $\psi_{q,a}$ are quark-field spinors for a quark of flavor q and mass m_q, with a color-index a that runs from $a = 1$ to $N_c = 3$, i.e. quarks have three "colors"; $\mathcal{A}^C$ are gluon fields with C running from 1 to $N_c^2 - 1 = 8$, i.e. there are eight kinds of gluons and they transform under the adjoint representation of the SU(3) color group; the t^C_{ab} are eight 3×3 matrices and are the generators of the SU(3) group; the quantity g_s (or $\alpha_s = \frac{g_s^2}{4\pi}$) is the QCD coupling constant. The coupling g_s (or α_s) and the quark masses m_q are the fundamental parameters of QCD. Finally, the field tensor $F^A_{\mu\nu}$ is given by

$$F^A_{\mu\nu} = \partial_\mu \mathcal{A}^A_\nu - \partial_\nu \mathcal{A}^A_\mu - g_s f_{ABC} \mathcal{A}^B_\mu \mathcal{A}^C_\nu \tag{1.2}$$

where the structure constants of the SU(3) group f_{ABC} are

$$[t^A, t^B] = i f_{ABC} t^C \tag{1.3}$$

Three useful color-algebra relations include:

$$\begin{aligned} t^A_{ab} t^A_{bc} &= C_F \delta_{ac} \qquad (C_F \equiv (N_c^2 - 1)/(2N_c) = 4/3) \\ f_{ACD} f_{BCD} &= C_A \delta_{AB} \qquad (C_A \equiv N_c = 3) \\ t^A_{ab} t^B_{ab} &= T_R \delta_{AB} \qquad (T_R = 1/2) \end{aligned} \tag{1.4}$$

C_F and C_A are the color-factors ("Casimir") associated with gluon emission from a quark and a gluon respectively. T_R is the color-factor for a gluon to split to a $q\bar{q}$ pair.

The last term in Eq. 1.2 makes a fundamental dynamical difference between QCD and Quantum EletroDynamics (QED), which leads to self-interactions between the gluons and asymptotic

freedom.

1.1.2.1 Confinement and asymptotic freedom

In physics, a coupling constant or gauge coupling parameter is a number that determines the strength of the force in an interaction. In QCD, the strong interaction is governed by a strong coupling constant α_s defined as:

$$\alpha_s(Q^2) = \frac{4\pi}{(11 - \frac{2}{3}n_f)\ln(\frac{Q^2}{\Lambda^2_{\mathrm{QCD}}})} \tag{1.5}$$

where Q^2 is the momentum transferred in the interaction, n_f is the number of light flavors with $m_q \ll Q$ and Λ_{QCD} is the non-perturbative QCD scale. The intensity of the strong interaction decreases at short distances and increases when quarks move apart as observed in Figure 1.3.

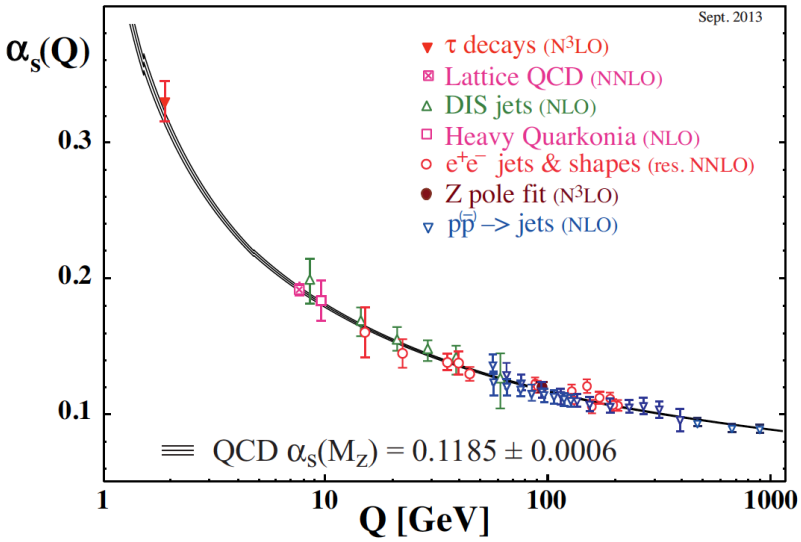

Figure 1.3: Summary of measurements of α_s as a function of the energy scale Q. The respective degree of QCD perturbative theory used in the extraction of α_s is indicated in brackets (NLO: next-to-leading order; NNLO: next-to-next-to leading order; res. NNLO: NNLO matched with resummed next-to-leading logs; N^{3}LO: next-to-NNLO) [6].

Therefore, the behavior of this running coupling constant provides two peculiarities of QCD. For small values of Q^2, i.e. at large distances or small energies, α_s becomes large. On the contrary, at small distance or large transferred momentum, α_s becomes weak, quarks and gluons behave as free particles, which is known as asymptotic freedom [7, 8]. This was first proposed by David J. Gross, Frank Wilczek and H. David Politzer in 1973 who shared the Nobel Prize in physics in 2004.

In the region where the transferred momentum is large (the distance of interaction is small), physical observations can be calculated by truncated series like leading order (LO), next-to-leading order (NLO) and so on. The perturbative QCD (pQCD) was proven to describe the high energy interaction with high accuracy. On the other hand, at small transverse momenta p_T (large distances) the strong coupling has large values and quarks are confined in neutral color states, the mesons and the baryons. This is well described by Lattice QCD calculations, which uses a non-perturbative approach in solving the QCD equation in a lattice of space and time.

1.1.2.2 Chiral symmetry breaking and restoration

A chiral phenomenon is one that is not identical to its mirror image. In particle physics, the spin is used to define a handedness. The helicity of a particle is right-handed if the direction of its spin is the same as the direction of its motion. While it is left-handed if the directions of spin and motion are opposite (Figure 1.4). Mathematically, the helicity of left-handed is negative, for right-handed it is positive. A symmetry transformation between the left-handed and right-handed is called parity. Invariance under parity by a Dirac fermion is called chiral symmetry.

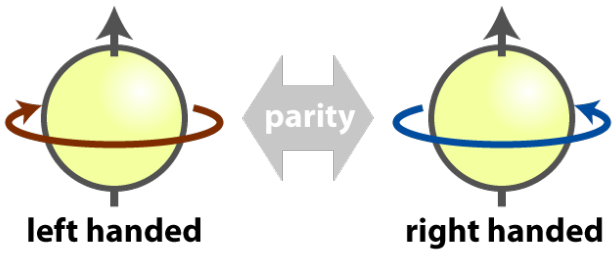

Figure 1.4: Illustration of the helicity of a spin 1/2 particle as being left or right-handed.

Considering QCD with two massless quarks u and d, Eq. 1.1 can be written:

$$\mathcal{L} = \sum_{q=u,d} \bar{\psi}_{q,a}(i\gamma^\mu \partial_\mu \delta_{ab} - g_s \gamma^\mu t^C_{ab} \mathcal{A}^C_\mu)\psi_{q,b} - \frac{1}{4} F^A_{\mu\nu} F^{A\mu\nu} \tag{1.6}$$

It is invariant under the chiral transformation:

$$\psi \rightarrow e^{i\theta\gamma^5}\psi \tag{1.7}$$

where θ is the generator of SU(2) group. Note that gluon fields are not affected by chiral transformations, so gluon degrees of freedom can be neglected for the present discussion. In terms of

left-handed and right-handed spinors, the chiral transformation becomes $SU(2)_L \times SU(2)_R$. If additional quark flavors are taken into account, the dimensionality of the chiral group increases, i.e., when three quarks *u*, *d* and *s* are considered the chiral group is $SU(3)_L \times SU(3)_R$. This symmetry of the Lagrangian is called flavor chiral symmetry.

As a matter of fact, it turns out that when we consider the non-zero values of the quark masses $m_u \simeq 2.3$ MeV and $m_d \simeq 4.8$ MeV, chiral symmetry is explicitly broken. The origin of the symmetry breaking may be described as an analog to magnetization, the fermion condensate (vacuum condensate of bilinear expressions involving the quarks in the QCD vacuum). The chiral condensation is defined as:

$$< \bar{\psi}\psi > = < \bar{\psi}_L \psi_R + \bar{\psi}_R \psi_L > \tag{1.8}$$

where $\psi_{L/R}$ are spinors of left- and right-handed particles. In the vacuum, $< \bar{\psi}\psi > \neq 0$, the quark mass is non-zero and the chiral symmetry is spontaneously broken. But at high energy one expects a restoration of the chiral symmetry, which is predicted for light quarks (*u*, *d* and *s*) not for heavier quarks (*c*, *b* and *t*), $< \bar{\psi}\psi > = 0$. In this case the quarks recover their almost-null mass of the QCD Lagrangian instead of their constituent mass, of the order of ~ 300 MeV [9]. According to the chiral symmetry breaking the QCD explains the existence of the eight Goldstone bosons (π°, π^+, π^-, K°, K^+, K^-, $\bar{K}^\circ$, η_8) with small mass values.

The principal and obvious consequence of this symmetry breaking is the generation of 99% of the mass of nucleons, and hence the bulk of all visible matter, out of very light quarks. For example, for the proton, of mass $m_p = 938$ MeV, the valence quarks, with $m_u \simeq 2.3$ MeV, $m_d \simeq 4.8$ MeV, only contribute by about 9 MeV to its mass, the bulk of it arising out of QCD chiral symmetry breaking, instead. Yoichiro Nambu was awarded the 2008 Nobel prize in physics for his understanding of this phenomenon.

Due to the restoration of the chiral symmetry, a phase transition of hadronic matter would be expected.

1.1.3 QCD phase diagram

As discussed above, quarks and gluons can not be observed directly at low energy, as they are confined inside colorless bound states (hadrons). However, QCD indicates that at high energy and/or baryonic density the strongly interacting matter undergoes a phase transition to a state where quarks and gluons are not confined into hadrons: the quark-gluon plasma (QGP). In the

phase diagram of QCD, the transition between the hadronic and QGP phases is not well known either theoretically or experimentally. A commonly conjectured form of the phase diagram in terms of the temperature T as a function of the baryonic-chemical potential μ_B is depicted in Figure 1.5.

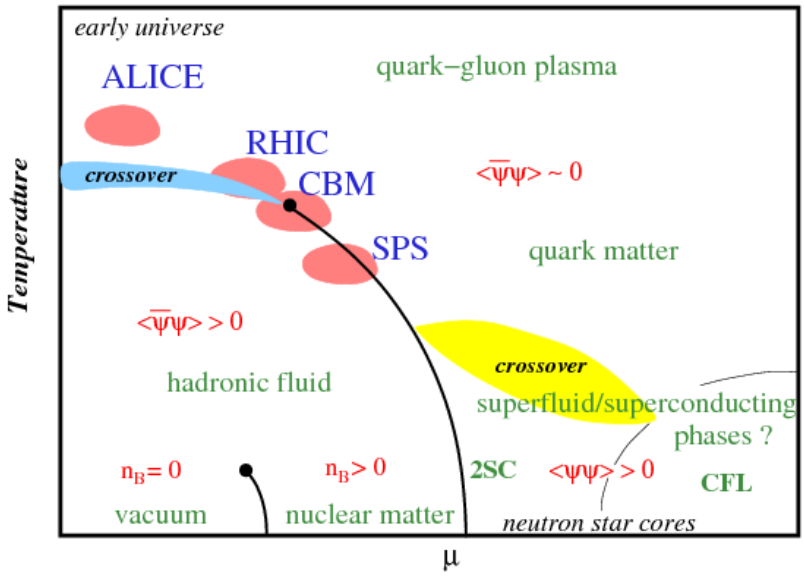

Figure 1.5: Schematic phase diagram of QCD matter in the plane of temperature T and baryonic-chemical potential μ_B [10].

To perform calculations in the regime of high temperature and large coupling strength and to research a phase transition from normal hadronic matter to deconfined QCD matter, the lattice QCD theory was created. It has been performed for two-flavor (u, d) and three-flavor (u, d, s) quarks to establish the equation of state of nuclear matter. Figure 1.6 shows the energy density scaled by the temperature to the fourth power ε/T^4 as a function of temperature divided by the critical temperature T/T_c. It indicates a phase transition from hadronic matter to the QGP at a critical temperature of $T_c \approx 170$ MeV $\approx 10^{12}$ K at $\mu_B = 0$ and at an energy density $\varepsilon_c \approx 1$ GeV/fm^3. Such temperatures were present in the early phase of the evolution of the universe, at about 1 μs after the Big Bang. On the other hand, density exceeding the above critical value is also conjectured to be present in the interior of compact, dense stellar objects, such as the neutron stars at $T \sim 0$.

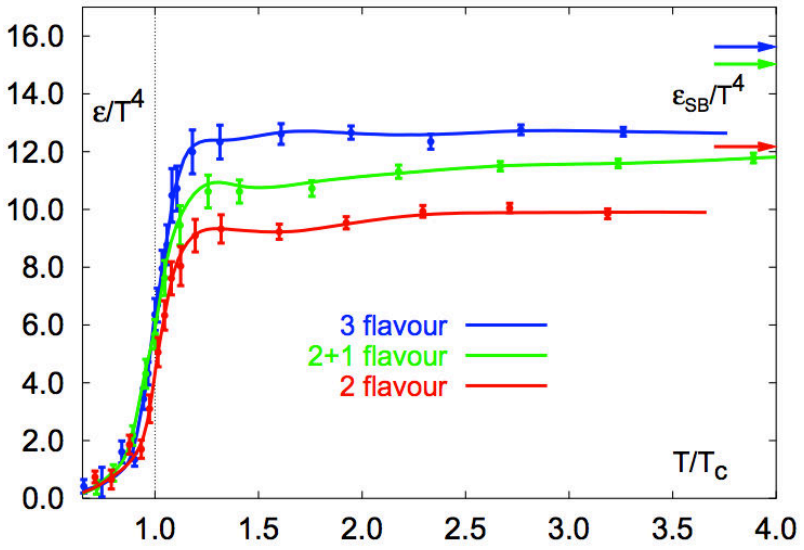

Figure 1.6: The evolution of the scaled energy density as a function of T/T_c from Lattice QCD calculation [11].

1.2 Heavy-ion collisions

The QGP can be produced in laboratory through ultra-relativistic heavy-ion collisions. The Relativistic Heavy Ion Collider (RHIC) and the Large Hadron Collider (LHC) operate at high energies, where the initial excess of quarks over antiquarks is negligible compared to the total number of created particles and the crossing time for heavy-ion collisions is much smaller than the formation time for the plasma, resulting in a low net baryon density. On the other hand, various experiments at lower energies aim to study the system at large net densities, for example RHIC II or the future Facility for Antiproton and Ion Research (FAIR) in Darmstadt (Germany). One of the most important objectives in the latter experiments is to identify a possible critical endpoint on the phase diagram, beyond which the transition becomes of first order. Developing our theoretical understanding of the QCD phase diagram can prove highly beneficial for designing these next generation experiments.

According to the "Big Bang" theoretical model, in few microseconds after the big bang, the universe was filled with a hot, dense soup made of all kinds of particles moving at near light speed. This mixture was dominated by quarks and gluons. In those first moments of extreme temperature, however, quarks and gluons were bound only weakly, free to move on their own in QGP. Historically, T. D. Lee in collaboration with G. C. Wick first speculated about an abnormal nuclear state, where nucleon mass is zero or near zero in an extended volume and non-zero outside the volume [12]. They also suggested that an effective way to search for these new objects

is through high-energy heavy-ion collisions. To recreate conditions similar to those of the very early universe, powerful accelerators make head-on collisions between massive ions, such as gold or lead nuclei. In these heavy-ion collisions the hundreds of protons and neutrons inside such nuclei smash into one another at energies of a few 10^{12} electron volts each. The QGP is formed in these collisions.

1.2.1 The Big Bang

The Big Bang theory is the prevailing cosmological model for the universe from the earliest known periods through its subsequent large-scale evolution [13, 14]. According to the prospect of hot Big Bang Model [15], the universe expanded from a very high density and high temperature state that occurred about 13.7 billion years ago, which happened at $t \sim 10^{-11}$ s after the big bang, and then the temperature went down during the expansion. After one Planck time of expansion, a phase transition caused a cosmic inflation, during which the Universe grew exponentially. As the inflationary period ends, the Universe consists of a QGP, which is the main focus of the heavy-ion physics. When the expansion continued until the temperature dropped to 10^{12} K, quarks began to combine into protons, neutrons and other baryons. As time progressed, some of the protons and neutrons formed deuterium, helium, and lithium nuclei. Later, electrons combined with protons and these low-mass nuclei to form neutral atoms. Due to gravity, clouds of atoms contracted into stars, where hydrogen and helium fused into more massive chemical elements. Exploding stars (supernovae) form the most massive elements and disperse them into space. Our earth was formed from supernova debris. Figure 1.7 shows the time evolution of the universe from the big bang to the present time.

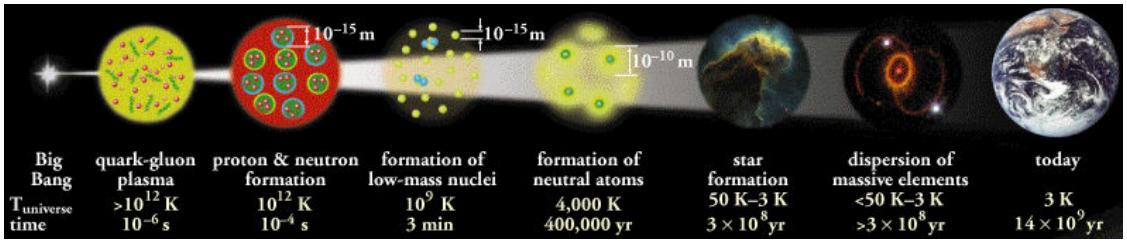

Figure 1.7: The evolution of the universe.

The purpose of the research on the high-energy physics is not only to understand the properties of particles and the interaction between them but also to investigate how the universe began and expanded. How can we recreate the conditions that were present at the early universe? For-

tunately, physicists have found the answer by designing and building powerful accelerators to perform ultra-relativistic heavy-ion collisions.

1.2.2 Evolution of heavy-ion collisions

As presented in Figure 1.8, the evolution of an ultra-relativistic heavy-ion collision can be summarized as follows:

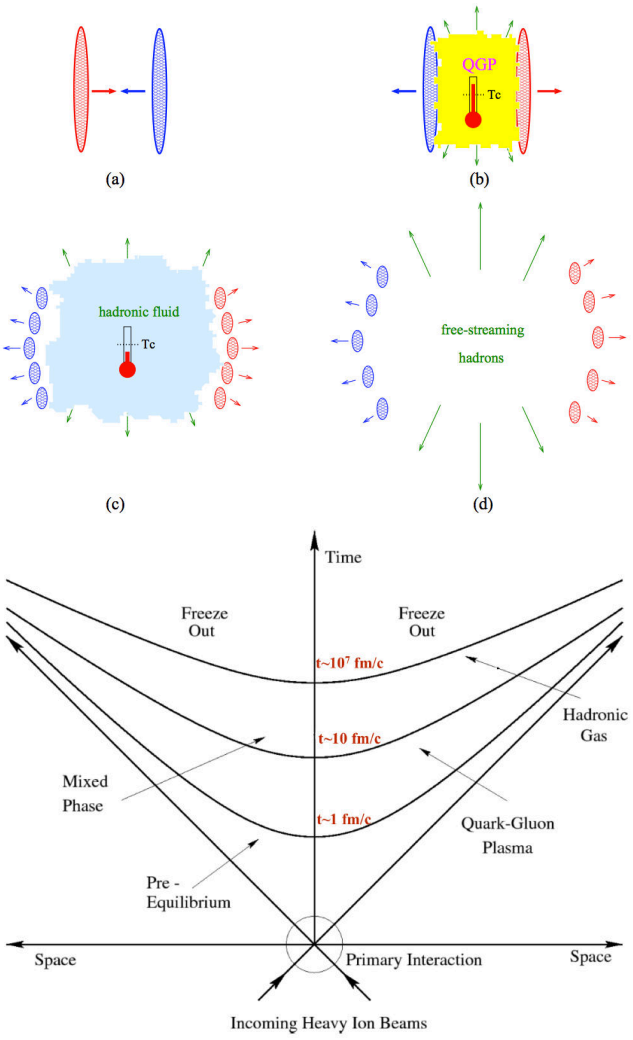

Figure 1.8: Top four figures: schematic view of the various stages of a heavy-ion collision. The thermometers indicate when thermal equilibrium might be attained. (a) the two nuclei before the collision, (b) the formation of a QGP if a high enough energy density is achieved, (c) the later hadronization, (d) free-streaming of the hadrons towards the detectors. [9] Bottom figure: sketch of the evolution of heavy-ion collisions in space and time. [16].

- Initial stage: the two colliding nuclei accelerated close to the speed of light are squeezed

in the direction of the incoming heavy-ion beams due to Lorentz contraction and are assumed as pancake in the laboratory frame.

- Pre-equilibrium: a lot of inelastic nucleon-nucleon collisions occur in the overlap region of the colliding nuclei and a large amount of energy is deposited near the collision point. Hard processes happen first and shortly after that soft processes take place. Partons are produced within this high-energy density environment via hard processes ($\tau \sim 0$). The pre-equilibrium state lasts for a typical time scale $\tau \sim 1\,\mathrm{fm}/c$. By partons interaction, both high and low p_T objects are created during this process. The multiple scattering among constituent quarks and gluons and between particles created during the collisions lead to a rapid increase in the entropy in the system which could eventually lead to equilibrium. These initial processes among partons can be divided into two parts [17]: hard processes which have large momentum transfer Q ($Q \gg \Lambda_{QCD}$), short timescale and a production cross section that is proportional to the number of binary collisions ($\sigma_{hard} \propto N_{coll}$); soft processes which have small Q, long timescale and a production cross section proportional to the number of participants ($\sigma_{soft} \propto N_{part}$). The majority of particles comes from soft processes.

- QGP formation and thermalization: a rapid increase in the entropy could lead to thermalization and the temperature rises rapidly. If the attained energy density exceeds a critical energy density, the QGP might be formed.

- Hadronization and Freeze-out: after QGP formation, the system tends to expand and cools down towards a hadronic phase. During this procedure, a "mixed phase" is expected to exist between the QGP phase and hadronic phase. When the energy density is too low to allow inelastic collisions to create particles, the chemical freeze-out is attained. The system continues to increase its extent and gets colder; at some point the elastic collisions are no longer possible and the system reaches the kinetic freeze-out. At this moment the fireball disintegrates and hadrons escape.

1.2.3 Heavy-ion facilities

Experimental attempts to create the QGP in the laboratory and measure its properties have been carried out for more than 40 years, by studying collisions of heavy nuclei and analyzing the

fragments and produced particles emerging from such collisions. During that period, center of mass energy per pair of colliding nucleons ($\sqrt{s_{\mathrm{NN}}}$) have risen steadily as follows:

- 1975-1985: $\sqrt{s_{\mathrm{NN}}} \sim 2$ GeV at the Bevalac at Lawrence Berkeley National Laboratory (LBNL) [18, 19, 20, 21]
- 1987-1995: $\sqrt{s_{\mathrm{NN}}} \sim 5$ GeV at the Alternating Gradient Synchrotron (AGS) at Brookhaven National Laboratory (BNL) [21]
- 2000-now: $\sqrt{s_{\mathrm{NN}}} \leq 200$ GeV at the Relativistic Heavy Ion Collider (RHIC) at BNL. Four experiments, PHENIX, STAR, BRAHMS and PHOBOS, are operated at this facility. [21]
- 1987-now: $\sqrt{s_{\mathrm{NN}}} \leq 450$ GeV at the Super Proton Synchrotron (SPS) accelerator at CERN [21]
- 2009-now: $\sqrt{s_{\mathrm{NN}}} \leq 5.02$ TeV at the Large Hadron Collider (LHC) at CERN

One of the earliest experiments of heavy-ion collisions dates back to Bevalac at LBNL. The heavy-ion collisions with higher energies were carried out in the AGS at BNL for Au nuclei at $\sqrt{s_{\mathrm{NN}}} = 5$ GeV and the SPS at CERN for Pb nuclei at $\sqrt{s_{\mathrm{NN}}} = 17$ GeV. Those accelerators were fixed-target experiments and the energies were not sufficient to fully produce the QGP. The construction of the RHIC collider at BNL allowed to significantly increase the collision energy, delivering pp, d-Au, Cu-Cu, Cu-Au and Au-Au collisions up to $\sqrt{s_{\mathrm{NN}}} = 200$ GeV. The results of the experiments at RHIC show that a hot and dense matter is created, thus providing a strong indication of the creation of the first human-made QGP. With the beginning of the heavy-ion program at the LHC at CERN, heavy-ion physics has entered a new energy regime. LHC has delivered Pb-Pb collisions at $\sqrt{s_{\mathrm{NN}}} = 2.76$ TeV (in 2011) and $\sqrt{s_{\mathrm{NN}}} = 5.02$ TeV (in 2016). It is believed that the properties of the hot medium does not fundamentally change from RHIC to LHC [22, 23], though several intriguing anomalies are reported in particle production [24, 25]. The analyses of azimuthal anisotropy show that the medium still behaves as a fluid with small viscosity, which is important information since it has been naively expected that the QGP becomes slightly more weakly-coupled with increasing energy due to the QCD asymptotic freedom.

Some of the mentioned heavy-ion facilities together with the typical parameters related to particle production in nucleus-nucleus collisions and global features of the produced systems are summarized in Table 1.1.

Parameters	SPS	RHIC	LHC
Beam type	Pb-Pb	Au-Au	Pb-Pb
$\sqrt{s_{NN}}$ (GeV)	17	200	2760
$dN_{ch}/dy\|_{y=0}$	500	850	1600
τ°_{QGP} (fm/c)	$\sim$ 1	$\sim$ 0.2	$\sim$ 0.1
T_{QGP}/T_c	1.1	1.9	3-4.2
ε (at 1 fm/c) (GeV/fm^3)	$\sim$ 3	$\sim$ 5	15
τ_{QGP} (fm/c)	$\leq$ 2	2-4	$\geq$ 10
τ_f (fm/c)	$\sim$ 4	$\sim$ 7	$\sim$ 10
V_f (fm^3)	$\sim 10^3$	$2-3\times10^3$	$\sim 5\times10^3$
μ_B (MeV)	250	20	$\sim$ 0
Process	soft $\rightarrow$ semi-hard $\rightarrow$ hard		

Table 1.1: Global features of the medium created at SPS, RHIC and LHC energies [26, 27]. From top to bottom, the following quantities are presented: center of mass energy per nucleon pair ($\sqrt{s_{NN}}$), the charged-particle density at mid-rapidity ($dN_{\rm ch}/dy|_{y=0}$), the equilibration time of the QGP ($\tau^{\circ}_{\rm QGP}$), the ratio of the QGP temperature to the critical temperature ($T_{\rm QGP}/T_c$), the energy density (ε), the lifetime of the QGP ($\tau_{\rm QGP}$), the lifetime of the system at freeze-out (τ_f), the volume of the system at freeze-out (V_f), the baryonic chemical potential (μ_B).

1.2.4 Characteristic of collisions and experimental observables

As discussed in Section 1.2.2, the two nuclei collide nearly at the speed of light and are squeezed in the direction of beam axis in the laboratory frame. At RHIC energy, $\sqrt{s_{NN}} = 200$ GeV, Lorentz dilation factor is $\gamma \sim 100$ for a projectile nuclei, which means the nucleus of diameter $\sim$ 14 fm is reduced to $\sim$ 0.1 fm. At the LHC energy $\sqrt{s_{NN}} = 5.02$ TeV, $\gamma \sim 2500$ and the nucleus is squeezed to $\sim$ 0.005 fm. The hot medium would be produced in the overlapping area between the two passing nuclei. The collision axis is conventionally chosen as z-axis, and often referred to as the longitudinal direction as opposed to the transverse plane, which is perpendicular to the collision axis. In non-central collisions, the resulting geometry of a hot medium is elliptic in the transverse direction. The schematic pictures of the collision geometry of symmetric nuclei are shown in Figure 1.9.

1.2.4.1 Coordinate system

It is more convenient to introduce the relativistic $\tau - \eta_s$ coordinate system to describe the heavy-ion system, where

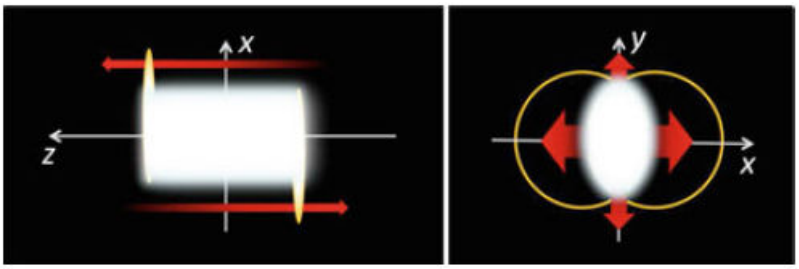

Figure 1.9: Schematic pictures of the geometry of non-central heavy-ion collisions with the longitudinal relativistic expansion (left) and the transverse expansion (right).

$$\begin{aligned} \tau &= \sqrt{t^2 - z^2} \\ \eta_s &= \frac{1}{2}\ln\frac{t+z}{t-z} \end{aligned} \tag{1.9}$$

are the proper time and the space-time rapidity. The space-time rapidity is a dimensionless variable that can be interpreted as a hyperbolic angle. They satisfy the relations $t = \tau\cosh\eta_s$ and $z = \tau\sinh\eta_s$. $\eta_s = 0$ corresponds to the t axis and $\eta = \pm\infty$ corresponds to the light cone. Similarly, one defines the transverse mass m_T and the rapidity y in momentum space as

$$\begin{aligned} m_T &= \sqrt{E^2 - p_z^2} \\ y &= \frac{1}{2}\ln\frac{E+p_z}{E-p_z} \end{aligned} \tag{1.10}$$

In heavy-ion collisions, the transverse momentum $p_T = \sqrt{m_T^2 - m^2}$ and the pseudo-rapidity $\eta = \frac{1}{2}\ln(\frac{|p|+p_z}{|p|-p_z})$ are useful variables because they are independent of mass. At relativistic energies, they are quite close to the transverse mass and the rapidity, respectively, and become identical in the relativistic massless limit.

The polar coordinate system is often employed in analyses of the transverse dynamics. The angle in the configuration space is denoted as φ and in the momentum space as φ_p. They are related to the variables in Cartesian coordinates as $(x, y) = (r\cos\varphi, r\sin\varphi)$ and $(p_x, p_y) = (p_T\cos\varphi_p, p_T\sin\varphi_p)$.

1.2.4.2 Centrality

A collision can be very different if the heavy ions collide head on or just graze each other. In particular, the multiplicity of the produced particles increases from peripheral to central colli-

sions. In order to describe the dynamics of the nucleus-nucleus collision process, the collisions are classified into different centrality classes, which are related with the impact parameter. The geometrical overlap region is parameterized by the impact parameter "b", defined as the distance between the central points of the colliding nuclei. The degree of centrality "C" of a given subset of collisions can be indicated as a function of the corresponding cut-off of the impact parameter "b_c":

$$C = \frac{\int_0^{b_c} 2\pi b db}{\sigma_{\text{inel}}} \tag{1.11}$$

where σ_{inel} is the total inelastic cross section of a nucleus-nucleus collision. It represents the probability that a collision occurs at $b < b_c$. The centrality percentile can be quantified by the pure geometry of the impact parameter via optical Glauber model [28]. Figure 1.10 presents the schematic view of a collision with the optical Glauber model.

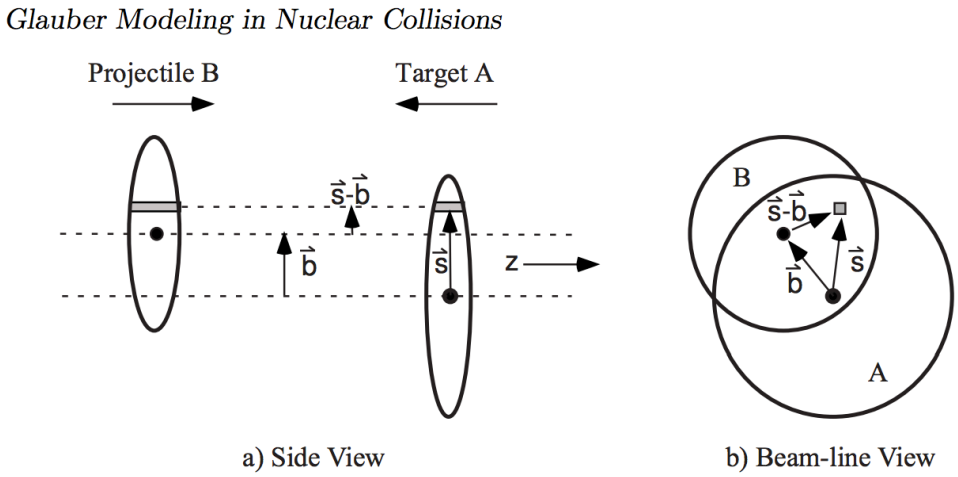

Figure 1.10: Schematic representation of the Optical Glauber Model geometry, with transverse (a) and longitudinal (b) views. [28].

Since the impact parameter is not directly measurable, experimentally one usually uses observables like the number of produced charged particles as shown in Figure 1.11 or the number of participants [†] to classify centralities. Usually the central collisions refer to collisions with $0 < C < 0.1$ and the peripheral collisions correspond to collisions with $0.9 < C < 1$. The nuclei involved in the primary collisions are called "participants" and their total number indicated as N_{part}, and others are called "spectators". The total number of binary nucleon-nucleon

[†]The number of spectators ($N_{\text{spec}} = N - N_{\text{part}}$) can be measured by Zero Degree Calorimeters (see Section 3.3).

collisions is indicated as N_{coll}.

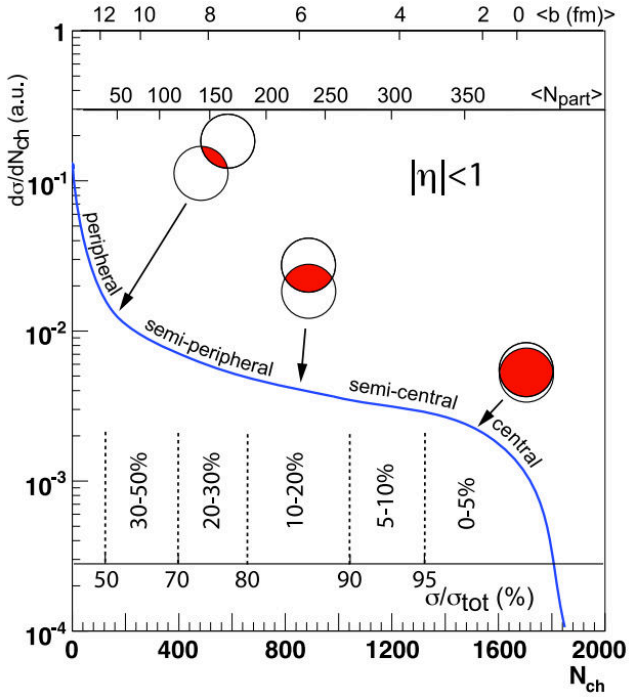

Figure 1.11: A cartoon example of the correlation of the final-state observable N_{ch} with Glauber calculated quantities (b, N_{part}). The plotted distribution and various values are illustrative and not actual measurements. [28].

The spectators will go through the collision region keeping their initial velocity as shown in Bjorken's model [29] of Figure 1.12.

The average number of nucleon-nucleon collisions $< N_{\text{coll}} >$ at an impact parameter b is given by $< N_{\text{coll}}(b) >=< T_{\text{AA}} > (b)\sigma_{\text{NN}}$, where σ_{NN} is the total proton-proton inelastic cross section and T_{AA} is the nuclear thickness function, defined as:

$$T_{\text{AB}}(b) = \int T_{\text{A}}(s)T_{\text{B}}(s-b)d^2s \tag{1.12}$$

where

$$T_{\text{A}}(s) = \int \varrho_{\text{A}}(s,z)dz \tag{1.13}$$

The nucleon distribution inside the nucleus is assumed to follow a Woods-Saxon density profile:

$$\varrho_{\text{A}}(s) = \frac{\varrho_{\text{o}}}{1+\exp(\frac{s-s_{\text{o}}}{a})} \tag{1.14}$$

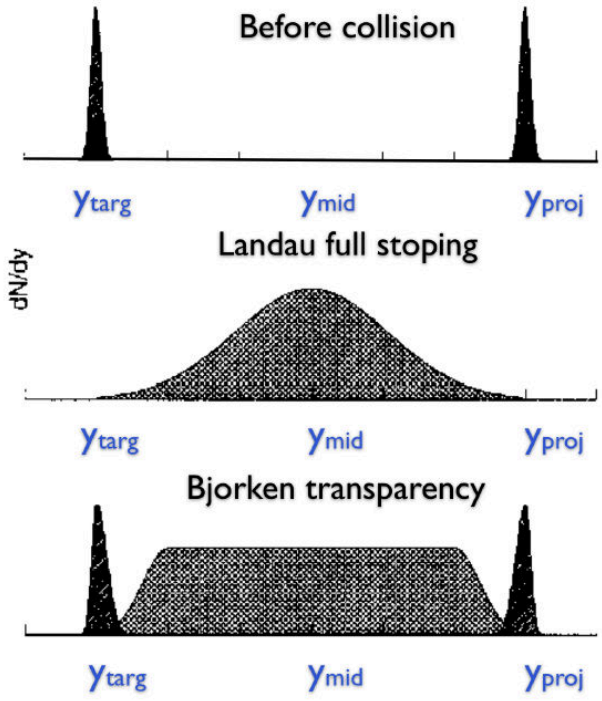

Figure 1.12: The rapidity distribution of particles in heavy-ion collisions. Top: before collisions. Middle: after collisions with Landau's full stopping model. Bottom: after collisions with Bjorken's model.

where s is the distance from a given point of the nucleus to the center of the nucleus. The parameters a and s_0 are obtained empirically from electron scattering experiments. The Glauber model [28] provides a quantitative description of the geometrical configuration of the nuclei when they collide and basically describe the nucleus-nucleus interaction in terms of the elementary nucleon-nucleon cross sections. For each centrality, the geometric parameters of nucleus-nucleus collisions (N_{part}, N_{coll}, $T_{\text{AA}}(b)$, b) are estimated with this model.

1.2.4.3 Experimental observables

Theoretically the rough process of the evolution has been assumed and a series of models, functions and formula have been created to calculate and explain physical phenomenons in heavy-ion collisions. While experimentally the only things we can see are digital signals of detector response caused by various types of particles like protons, neutrons, pions, kaons, electrons, muons, photons. Through technical analysis these different particles can be identified. Deservedly they become the probes that let us to infer the properties and phases of the matter formed in the collisions and can be classified as global, initial and final state observables [30].

- Global observables: the global observables provide general information about the colli-

sions such as the centrality, the reaction plane, the volume, the expansion velocity and the initial energy density. These quantities can be inferred from the measurement of the charged particle multiplicity, the transverse energy and the hadrons kinematics (among others). The collision centrality can be obtained from measurements of particle multiplicity and of the energy carried by spectator nucleons. Moreover, studies of the transverse energy as a function of centrality carry information about the energy density, duration and opacity of the fireball.

- Initial-state observables: the probes which are not affected by the QGP formation are considered as initial-state observables. This means that they have the same behavior in the presence of cold nuclear matter (p-A collisions) and the QGP (A-B collisions). Electroweak bosons include high-p_T γ, $W^{\pm}$ and Z° are considered as initial-state probes as they do not interact strongly. The particularities and interest of weak bosons will be further discussed in Chapter 2. For what concerns photon production, different processes must be distinguished. On one hand, there are direct photons, which can be separated as prompt photons coming from the initial hard collisions and thermal photons emitted in the secondary collisions either in the QGP phase or the hadronic phase. On the other hand, there are decay photons, mainly from π and η decays, more than direct photons quantitatively.

- Final-state observables: The final-state observables provide information about the QGP and hadronic phase, which are obtained from the hadron yields and kinematic properties. There are many probes related to this kind of observables like the transverse momentum distribution and the relative yield of the hadron species, the high-p_T particle correlations, the flow and so on.

It is worth mentioning that hard probes are defined as high-energy probes produced in the hard partonic scattering in the initial stage of the collision [31]. The production of hard probes involves a large transfer of energy-momentum at a scale $Q \gg \Lambda_{QCD}$. Such hard probes include the production of Drell-Yan dileptons, massive gauge bosons, heavy quarks, prompt photons, high-p_T partons observed as jets and high-p_T hadrons.

1.2.4.3.1 Charged-particle spectra

The hadron yield is an indispensable observable to study heavy-ion collisions since hadrons constitute the bulk of the produced medium. Due to the strong interaction in the medium, the

p_T spectra of charged particles as shown in the top panel of Figure 1.13 is considered to contain the information at the latest stage of the collisions. The p_T dependence is similar for the pp reference and for peripheral Pb-Pb collisions, exhibiting a power law behavior at $p_T > 3$ GeV/c, which is characteristic of perturbative parton scattering and vacuum fragmentation [32]. On the contrary, the spectral shape in central collisions clearly deviates from the scaled pp reference and is closer to an exponential in the p_T range below 5 GeV/c.

The distribution of rapidity dN/dy or the distribution of pseudo-rapidity $dN/d\eta$, is a basic observable to quantify particle production in the system (bottom panel of Figure 1.13 [33]). The charged-particle multiplicities at mid-rapidity are $dN_{ch}/d\eta \sim 650$ at $\sqrt{s_{NN}} = 200$ GeV at RHIC and $dN_{ch}/d\eta \sim 1600$ at LHC in the most central colliisons [34, 35, 36, 37, 38]. From peripheral to central collisions we observe an increase of two orders of magnitude in the number of produced charged particles. No strong evolution of the overall shape of the charged-particle pseudo-rapidity density distributions as a function of collision centrality is observed. The total charged-particle multiplicity is found to scale approximately with the number of participating nucleons. This would suggest that hard contributions to the total charged-particle multiplicity are small.

1.2.4.3.2 Jets

A jet is the collimated set of hadrons resulting from the fragmentation of a parton. In general, the collision of high-energy particles can produce jets of elementary particles that emerge from these collisions. If the partons traverse on their path to a dense colored medium, they can lose energy. The result of the energy loss can be detected as modifications of jet yields and jet properties. This phenomenon is commonly referred to as the jet quenching. The jet quenching was first proposed by Bjorken [39] as an experimental tool to investigate properties of the dense medium.

Figure 1.14 shows the two-particle azimuthal distribution $D(\Delta\varphi)$, defined as:

$$D(\Delta\varphi) = \frac{1}{N_{\text{trigger}}} \frac{1}{\varepsilon} \frac{dN}{d(\Delta\varphi)} \tag{1.15}$$

measured by STAR experiment for trigger particles with $4 < p_T^{\text{trig}} < 6$ GeV/c and associated particles with $2 < p_T < p_T^{\text{trig}}$ for pp, p-Au and Au-Au collisions. N_{trigger} is the number of trigger particles, ε is the tracking efficiency of the associated particles. The azimuthal distributions in pp

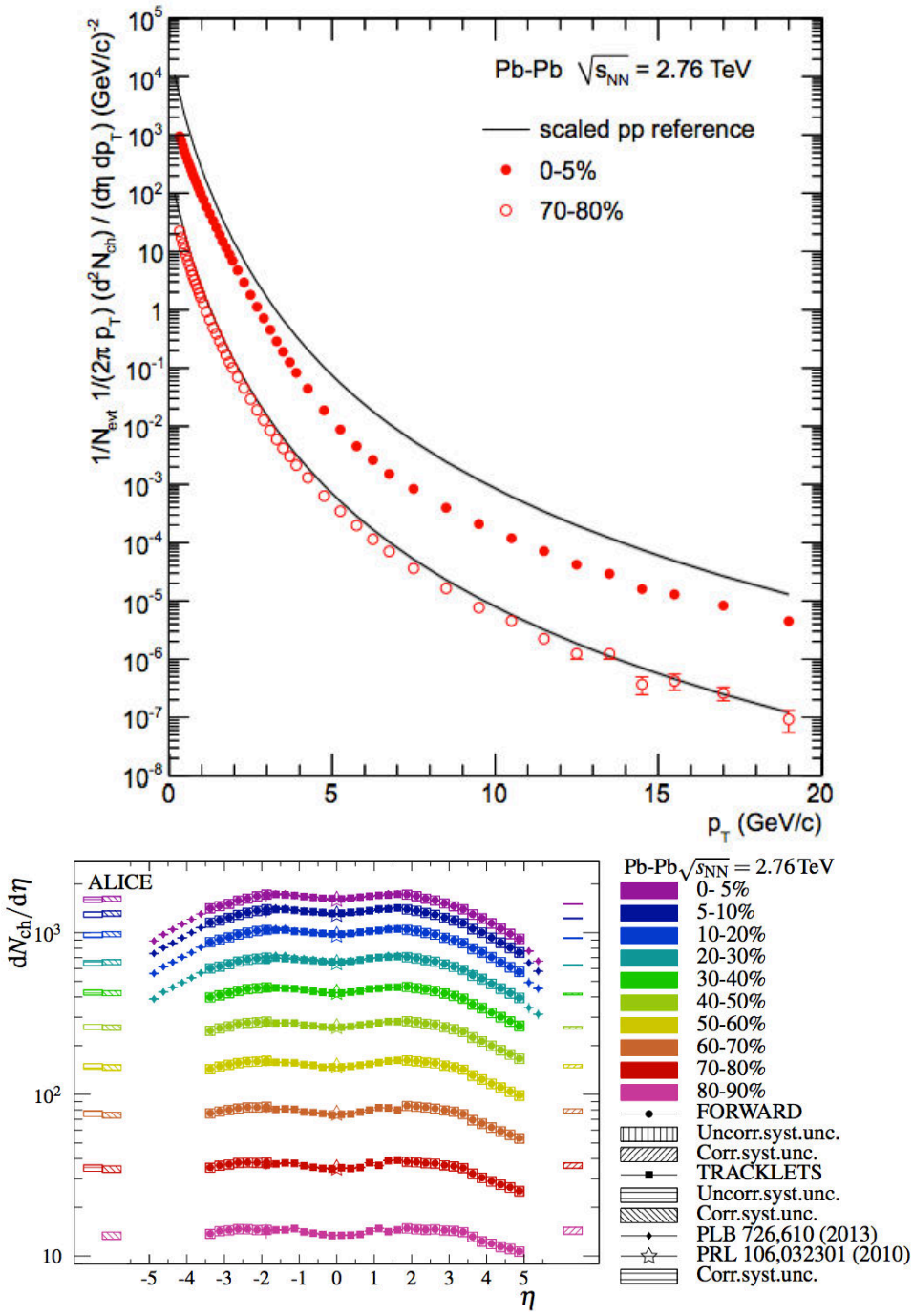

Figure 1.13: (Top) The p_T spectra of the charged particles for central and peripheral collisions in the same collisions at $\sqrt{s_{NN}} = 2.76$ TeV by ALICE Collaboration. [32] (Bottom) The pseudo-rapidity distributions of the charged particles for different centralities in Pb-Pb collisions at $\sqrt{s_{NN}} = 2.76$ TeV by ALICE Collaboration. [33].

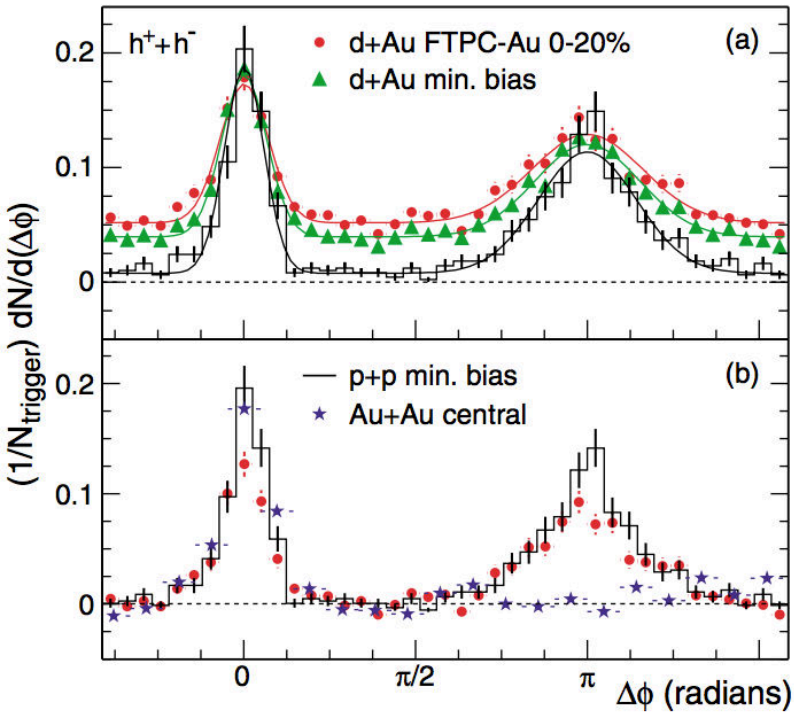

Figure 1.14: (a) Efficiency corrected two-particle azimuthal correlation distributions for minimum bias and central d-Au collisions, and for pp collisions. (b) Comparison of two-particle correlations for central Au-Au collisions to those seen in pp and central d-Au collisions. [40].

and d-Au collisions include a near-side ($\Delta\varphi \sim 0$) peak and a back-to-back away-side ($\Delta\varphi \sim \pi$) peak [40], while the away-side peak disappears in central Au-Au collisions [41]. This is consistent with the fact that the near-side jet is produced near the surface and the away-side jet is completely absorbed when traversing the medium (Figure 1.15). It might be an evidence to indicate that the QGP is produced in high-energy heavy-ion collisions.

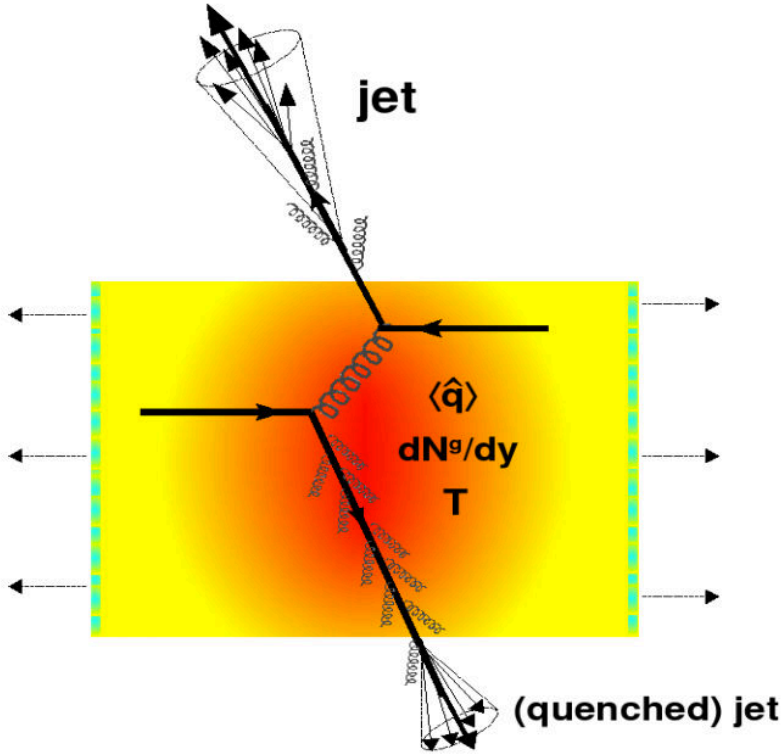

Figure 1.15: Jet quenching in a head-on nucleus-nucleus collision. Two quarks suffer a hard scattering: one goes out directly to the vacuum, radiates a few gluons and hadrons, the other goes through the dense plasma created (characterised by transport coefficient $\hat{q}$, gluon density dN^g/dy and temperature T), suffers energy loss and finally fragments outside into a (quenched) jet. [42].

1.2.4.3.3 Nuclear modification factor

In order to study the suppression and to disentangle hot (QGP) and cold nuclear matter effects, the nuclear modification factors (R_{pPb}, R_{AA}) are defined as:

$$R_{\mathrm{pPb}} = \frac{d^2N_{\mathrm{pPb}}/dydp_{\mathrm{T}}}{< T_{\mathrm{pPb}} > d^2\sigma_{\mathrm{pp}}^{\mathrm{INEL}}/dydp_{\mathrm{T}}}$$
$$R_{\mathrm{AA}} = \frac{d^2N_{\mathrm{AA}}/dydp_{\mathrm{T}}}{< T_{\mathrm{AA}} > d^2\sigma_{\mathrm{pp}}^{\mathrm{INEL}}/dydp_{\mathrm{T}}} \quad (1.16)$$

where AA denotes a nucleus-nucleus collision and pp is the proton-proton reference. N_{pPb} (N_{AA}) and $\sigma_{\mathrm{pp}}^{\mathrm{INEL}}$ represent the yield of particles in p-Pb (Pb-Pb) and the inelastic cross section in pp collisions, respectively. In p-Pb (similar as Pb-Pb), the nuclear overlap function is defined as $< T_{\mathrm{pPb}} >=< N_{\mathrm{coll}} > /\sigma_{\mathrm{INEL}}^{\mathrm{NN}}$ and is determined from the Glauber model. $< N_{\mathrm{coll}} >$ is the average number of binary nucleon-nucleon collisions. In absence of nuclear effects, one expects that the nucleus-nucleus behaves like an incoherent superposition of nucleon-nucleon collisions. Thus, the R_{pPb} (R_{AA}) is expected to be equal to unity for hard processes. This is not the case when the QGP is formed. Also, even if there is no medium formed, the R_{pPb} (R_{AA}) is not equal to unity due to the cold nuclear matter effects, such as the shadowing and antishadowing effect [43], the multiple parton scattering called Cronin effect [44], energy loss in cold nuclear matter.

The nuclear modification factor R_{AA} in Pb-Pb collisions at $\sqrt{s_{\mathrm{NN}}} = 2.76$ TeV is shown for two centrality intervals in the top left panel of Figure 1.16. There is a significant suppression of charged hadron yields for the most central (0-5%) collisions. The nuclear modification factor displays a minimum at around $p_{\mathrm{T}} = 6 \sim 7$ GeV/c and a significant rise for $p_{\mathrm{T}} > 7$ GeV/c, indicating a reduction of the relative energy loss. For peripheral collisions (70-80%), a smaller suppression and a weak p_{T} dependence is observed.

In the bottom left panel of Figure 1.16, the nuclear modification factor R_{pPb} in p-Pb collisions at $\sqrt{s_{\mathrm{NN}}} = 5.02$ TeV is shown for charged particles, in comparison with R_{AA} for most central (0-5%) collisions measured by ALICE and CMS. Moreover, comparisons are also shown for particles which are not sensitive to QCD dynamics (direct photon, $\mathrm{W}^{\pm}$, Z^{0}) measured by CMS. For $p_{\mathrm{T}} \gtrsim 2$ GeV/c, the R_{pPb} is consistent with unity showing that the large suppression observed for R_{AA} at high p_{T} is related to the jet quenching in QGP and not to initial-state effects.

A comparison of the p-Pb data to model calculations is important for the understanding of the cold nuclear matter effects. In the right panel of Figure 1.16, the R_{pPb} for $|\eta_{\mathrm{cms}}| < 0.3$ is compared to theoretical predictions. Some predictions based on the Color Glass Condensate (CGC) model [45, 46] are consistent with the measurement within uncertainties. Leading order (LO) pQCD calculations incorporating cold nuclear matter effects underestimate the data at high

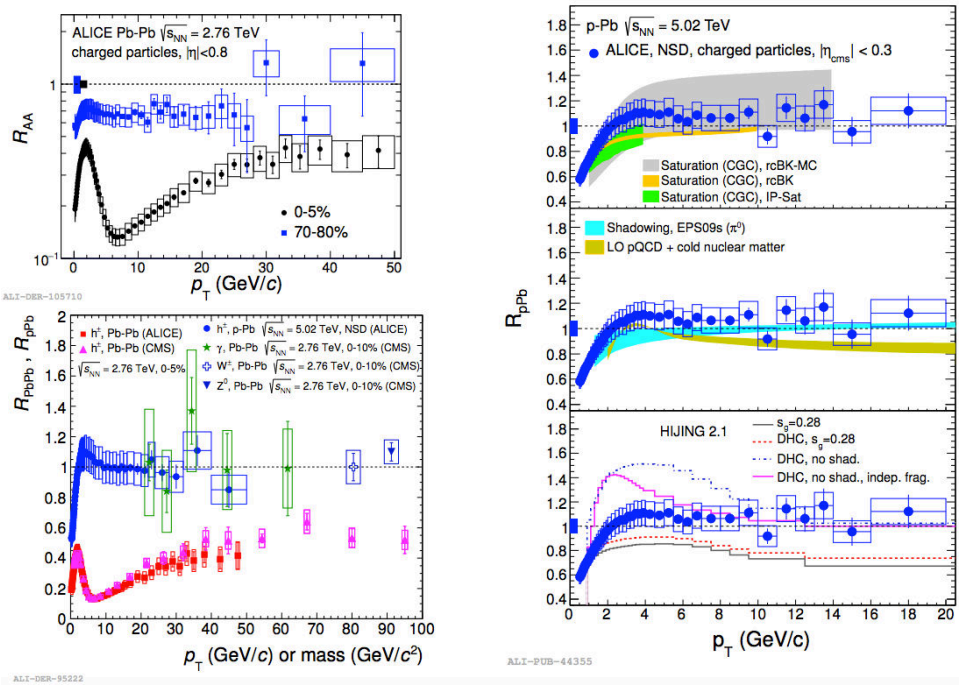

Figure 1.16: R_{AA} and R_{pPb} of charged particles. (Top left) R_{AA} is shown in central (0-5%) and peripheral (70-80%) Pb-Pb collisions. (Bottom left) Comparisons of R_{AA} and R_{pPb} measured by ALICE and CMS. (Right) R_{pPb} from ALICE for $|\eta_{cms}| < 0.3$ (symbols) are compared to model calculations (bands or lines).

p_T, while the shadowing calculations based on NLO with EPS09s PDFs and DSS fragmentation functions [47] describe the data well for $p_T > 6$ GeV/c. The HIJING model [48] 2.1 (with shadowing) describes the trend observed in the data.

1.2.4.3.4 Anisotropic flow

Anisotropic flow is a phenomenological term used to describes the collective evolution of the system, observed as an overall pattern which correlates the momenta of the final-state particles [49]. In non-central collisions the interaction region is almond shaped. If the medium is formed, pressure gradients arise that transform the anisotropy in space in an anisotropy in the momentum. The anisotropy can be studied with the Fourier series expansion of the azimuthal distribution of particles in momentum space [50, 51]. The spectrum of particles is expressed as

$$\frac{dN}{d\varphi p_T dp_T dy} = \frac{1}{2\pi}\frac{dN}{p_T dp_T dy}[1 + 2\sum_n v_n(p_T, y)\cos(n\varphi - n\Psi)] \tag{1.17}$$

where $v_n(p_T, y)$ are the Fourier coefficients and Ψ is the reaction plane, which contains the impact parameter and the beam direction as shown in Figure 1.17. This leads to

$$v_n(p_T, y) = \int d\varphi cos(n\varphi - n\Psi) \frac{dN}{d\varphi p_T dp_T dy} / \int d\varphi \frac{dN}{d\varphi p_T dp_T dy} \tag{1.18}$$

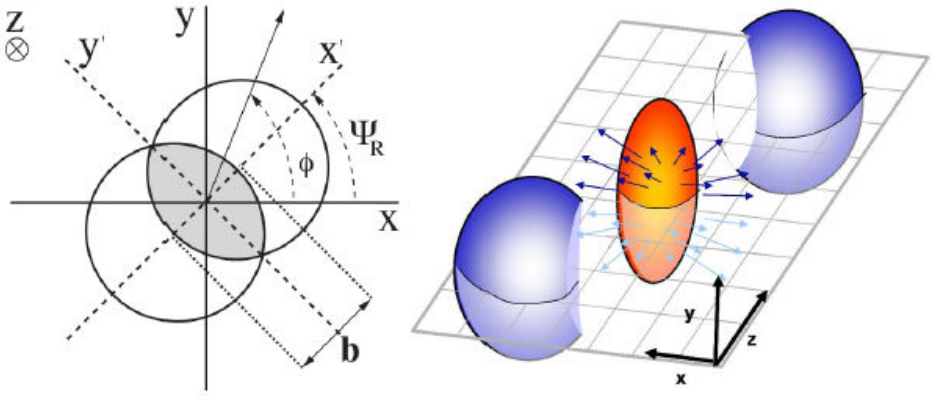

Figure 1.17: Geometry of the collision in a two-dimension plane (left panel) and a three-dimension plane (right panel).

where φ denotes the azimuthal angle in the transverse plane, Ψ is the azimuthal angle of the reaction plane. The first and second coefficient of the expansion, v_1 and v_2 are called directed and elliptic flow, respectively. The study of flow provides a sensitive tool to characterize the strongly interacting system created in the heavy-ion collisions.

1.2.4.3.5 Electroweak probes

Precise measurements of final states containing multiple electroweak bosons (W, Z or γ) provide a powerful probe of the gauge structure of the SM, and are therefore a promising way to search for new physics beyond the SM. W and Z bosons are produced in initial hard parton scattering processes and decay before the formation of the QGP. Furthermore, their leptonic decay products do not interact strongly with the QGP. The electroweak bosons introduce a way for benchmarking in-medium modifications to coloured probes. In Pb–Pb and p–Pb collisions, precise measurements of W- and Z-boson production can constrain the nuclear Parton Distribution Functions (nPDFs), which could be modified with respect to the nucleon due to shadowing or gluon saturation, and they can be used to test the scaling of hard particle production with the number of binary nucleon–nucleon collisions. In particular in p–Pb collisions, the measurement of W yields at forward and backward rapidity allows us to probe the modification of nPDFs at small and large Bjorken-x, respectively. Such measurements can be benchmarked in pp collisions, where W- and Z-boson production is theoretically known with good precision. Also, the charge

asymmetry of leptons from W-boson decays is a sensitive probe of up and down quark densities in a nucleon inside a nucleus.

The details for the production of W and Z bosons will be discussed in Chapter 2.

So many people today — and even professional scientists — seem to me like someone who has seen thousands of trees but has never seen a forest. A knowledge of the historic and philosophical background gives that kind of independence from prejudices of his generation from which most scientists are suffering. This independence created by philosophical insight is — in my opinion — the mark of distinction between a mere artisan or specialist and a real seeker after truth.

Albert Einstein

2

Weak bosons in heavy-ion collisions

The W and Z bosons are together known as the weak or more generally as the intermediate vector bosons. These elementary particles mediate the weak interaction and the respective symbols are W^+, W^- and Z°. The W bosons are named via the first letter of the weak force. They have either a positive or a negative elementary electric charge, and W^+ is the anti-particle of W^-. The Z boson is named by the physicist Steven Weinberg [52]. It is electrically neutral and is its own antiparticle. The three particles are very short-lived with a half-life of about 3×10^{-25} s. They have masses almost 100 times larger than the proton mass. Their large masses limit the range of the weak nuclear force, whose influence is confined to a distance of only about 10^{-17} meter [*].

In heavy-ion collisions, how are they produced and how do they decay? We already know that weak bosons do not interact strongly, but how are their productions affected by the nuclear effects? Here and all through this thesis work we will discuss on those issues.

2.1 Discovery of weak bosons

The existence of weak bosons and their properties were predicted in the late 1960s by the physicists Sheldon Lee Glashow, Steven Weinberg and Abdus Salam. Their theoretical efforts, now called the electroweak theory, explain that the electromagnetic force and the weak force, long

[*] As established by quantum mechanics, the range of any given force tends to be inversely proportional to the mass of the particle transmitting it.

considered as separate entities, are actually manifestations of the same basic interaction. Just like the electromagnetic force is transmitted by means of carrier particles knows as photon, the weak force is exchanged via these three types of intermediate vector bosons. Their electroweak theory postulated not only the W bosons necessary to explain beta decay, but also a new Z boson that had never been observed. They shared the 1979 Nobel Prize in physics for this theory.

In low-energy processes such as radioactive beta decay shown in Figure 2.1, the heavy W particles can be exchanged only because the uncertainty principle in quantum mechanics allows fluctuations in mass-energy over sufficiently short timescales. Such W particles can never be observed directly. However, detectable W bosons can be produced in particle-accelerator experiments involving collisions between subatomic particles, provided that the collision energy is high enough. The first such machine was the Super Proton Synchrotron (SPS), where unambiguous signals of W bosons and Z bosons were seen respectively in January and May 1983 during two experiments UA1 (led by Carlos Rubbia) [53] and UA2 (led by Pierre Darriulat) [54]. The two teams observed numerous definite instances of weak bosons in proton-antiproton collision experiments that were carried out in a 540 GeV colliding-beam storage ring. It is worth mentioning that Simon van der Meer is the architect of the "beam cooling" which permitted to make intense antiproton beams feasible and allowed the discovery of the W and Z. The CERN physicist Carlo Rubbia and engineer Simon van der Meer were awarded the 1984 Nobel Prize for Physics in recognition of their roles in the discovery of the W and Z particles.

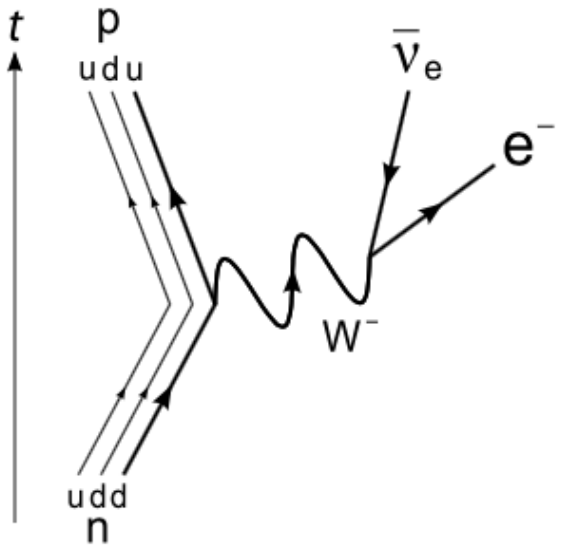

Figure 2.1: The Feynman diagram for beta decay of a neutron into a proton, electron, and electron antineutrino via an intermediate heavy W boson.

2.2 Formation and decay

Since their discovery, the W and Z bosons have been extensively studied at the CERN LEP e^+e^- collider [55], the Fermilab Tevatron $p\bar{p}$ collider [56, 57] and in pp [58, 59, 60, 61, 62, 63, 64, 65], p–Pb [66, 67, 68, 69] and Pb–Pb [58, 70] collisions at the LHC. The currently most precise value of their physical properties and decay modes of W^+ are shown in Figure 2.2 [6]. The dominant decay channel is hadronic with a branching ratio $67.41 \pm 0.27\%$ while the branching ratio of muonic decay channel is $10.63 \pm 0.15\%$.

W $J = 1$

Charge $= \pm 1\ e$
Mass $m = 80.385 \pm 0.015$ GeV
$m_Z - m_W = 10.4 \pm 1.6$ GeV
$m_{W^+} - m_{W^-} = -0.2 \pm 0.6$ GeV
Full width $\Gamma = 2.085 \pm 0.042$ GeV
$\langle N_{\pi^\pm} \rangle = 15.70 \pm 0.35$
$\langle N_{K^\pm} \rangle = 2.20 \pm 0.19$
$\langle N_p \rangle = 0.92 \pm 0.14$
$\langle N_{\text{charged}} \rangle = 19.39 \pm 0.08$

W^- modes are charge conjugates of the modes below.

W^+ DECAY MODES		Fraction (Γ_i/Γ)	Confidence level	p (MeV/c)
$\ell^+\nu$	[b]	$(10.86 \pm 0.09)\ \%$		–
$e^+\nu$		$(10.71 \pm 0.16)\ \%$		40192
$\mu^+\nu$		$(10.63 \pm 0.15)\ \%$		40192
$\tau^+\nu$		$(11.38 \pm 0.21)\ \%$		40173
hadrons		$(67.41 \pm 0.27)\ \%$		–
$\pi^+\gamma$		$< 7 \times 10^{-5}$	95%	40192
$D_s^+\gamma$		$< 1.3 \times 10^{-3}$	95%	40168
cX		$(33.3 \pm 2.6)\ \%$		–
$c\bar{s}$		$(31\ ^{+13}_{-11})\ \%$		–
invisible	[c]	$(1.4 \pm 2.9)\ \%$		–

Figure 2.2: The physical properties and decay modes of W^+ [6]. [b] l indicates each type of lepton (e, μ and τ), not sum over them. [c] Invisible mode represents the width for the decay of the W boson into a charged particle with momentum below detectability, $p < 200$ MeV/c.

Weak bosons are formed early due to their large mass: $t_f \sim 1/\mathcal{M} \sim 10^{-3}$ fm/c. Their decay

time is inversely proportional to their widths

$$\begin{aligned} t_d(W^{\pm} \to X) &\simeq \frac{1}{2.085\,\text{GeV}} = 0.09\,\text{fm}/c \\ t_d(Z^{\circ} \to X) &\simeq \frac{1}{2.495\,\text{GeV}} = 0.08\,\text{fm}/c \end{aligned} \tag{2.1}$$

Therefore weak bosons are produced and decay before QGP is formed. As a result their decay products might be sensitive to QGP. However, their leptonic decay channels should not be affected by the QGP, since leptons do not decay strongly. Here and all through this thesis work we will focus on the muonic decay channel.

2.2.1 Generation of weak boson

The structure of a proton-proton collision at the LHC as built up by event generators can be described by a few main steps: hard process, parton shower, hadronization, underlying event [†] [71, 72, 73, 74] and unstable particle decays [75].

Deep inelastic scattering experiments, which involve bombardment of protons by electrons, disclosed the proton composition and triggered the development of the parton model [76]. According to this model, protons consist of three valence quarks: two u quarks and one d quark. These quarks spontaneously produce gluons, which can split into additional quark-antiquark pairs, known as "see quarks". The fraction of the total proton momentum carried by each constituent is usually labeled "x", and varies from 0 to 1. Parton distribution functions (PDFs, see Section 2.2.2 for details) are probability distributions of x for different kinds of partons.

According to the factorization assumed by Drell and Yan [77], a hard scattering collision between proton A and B can be viewed as an interaction between two free partons a and b with respective momentum fractions x_a and x_b weighted by the probability of carrying these momentum fractions (PDFs). The parton-parton interaction can be calculated in the condition of perturbative quantum chromodynamics (pQCD). However, the PDFs are not calculable and have to be determined experimentally. The illustration of the factorization theorem in a hard-scattering process is shown in Figure 2.3.

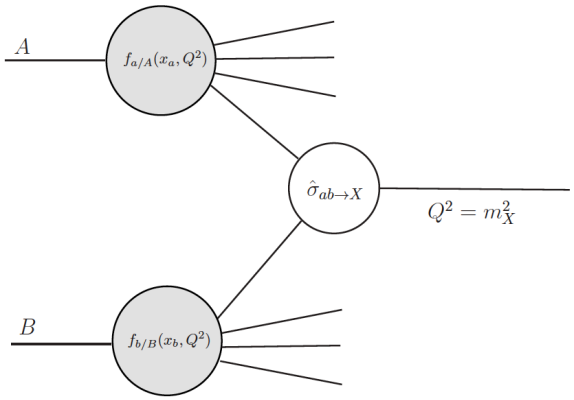

Figure 2.3: Illustration of the factorization theorem in a hard-scattering process. $\hat{\sigma}$ is the hard scattering cross section, while f is represent PDFs for each incoming proton. [78].

The hadronic W boson production is a hard process and can be generically described by the

[†] The underlying event (UE) is all what is seen in a hadron collider event which is not coming from the primary hard scattering (high energy, high momentum impact) process. It was first defined in 2002 and contents of UE include initial and final state radiation, beam-beam remnants, multiple parton interactions, pile-up, noise.

Eq. 2.2:

$$\sigma_{AB\to W} = \sum_{\text{partons}} \int dx_a dx_b f_{a/A}(x_a, \mu_F^2) f_{b/B}(x_b, \mu_F^2) \cdot \\ [\hat{\sigma}_{LO}(x_a x_b s) + \alpha_s(\mu_R^2)\hat{\sigma}_{NLO}(x_a x_b s) + (\alpha_s(\mu_R^2))^2 \hat{\sigma}_{NNLO}(x_a x_b s) + \ldots] \tag{2.2}$$

The partonic cross section $\hat{\sigma}$ is written as a power series of the strong interaction coupling constant α_s. The cross section of each order depends on the energy scale $Q^2 \equiv x_a x_b s$, where $\sqrt{s}$ is the center-of-mass energy of hadron collisions. α_s depends on a non-physical parameter μ_R - the renormalization scale of the QCD running coupling. The PDFs $f_{a/A}(x_a, \mu_F^2)$ and $f_{b/B}(x_b, \mu_F^2)$ depend on another non-physical parameter μ_F - the factorization scale. This is the energy scale that separates the perturbative from the non-perturbative parts of the calculation, the latter being absorbed into the definition of the PDF.

In principle, the cross section is independent of the renormalization and factorization scales if the expansion is carried to all order of α_s. However, considering the practical situation, the calculation is stopped at NLO or Next-to-Next-to-Leading Order (NNLO) and some dependence of the cross section on these non-physical parameters is retained. The conventional treatment is to choose μ_R and μ_F to be the same order as the typical momentum transfer in the hard-scattering process. In particular, in the case of the W boson production, μ_R and μ_F are both set to the mass of the produced W boson.

As weak bosons have large mass, they are produced in initial hard partonic scattering processes, where the center-of-mass energy is maximum. The lowest order process for W/Z production is the quark (f) and anti-quark ($\bar{f}$) annihilation process (Figure 2.4):

$$f_i + \bar{f}_j \to W, \qquad f_i + \bar{f}_i \to Z \tag{2.3}$$

Higher order processes include gluon and photon initial and final state radiation. The second order processes are:

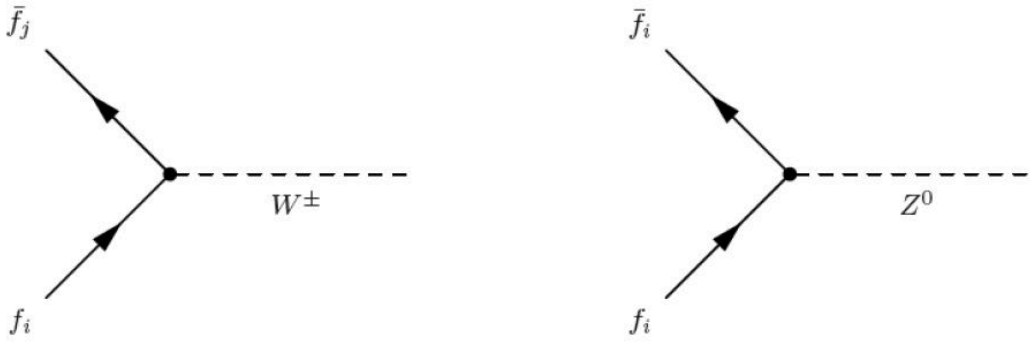

Figure 2.4: Lowest order Feynman diagram for W/Z production.

$$\begin{aligned} f_i + g &\to \mathrm{W} + f_k, & f_i + g &\to \mathrm{Z} + f_i, \\ f_i + \bar{f}_j &\to \mathrm{W} + g, & f_i + \bar{f}_i &\to \mathrm{Z} + g, \\ f_i + \gamma &\to \mathrm{W} + f_k, & f_i + \gamma &\to \mathrm{Z} + f_i, \\ f_i + \bar{f}_j &\to \mathrm{W} + \gamma, & f_i + \bar{f}_i &\to \mathrm{Z} + \gamma \end{aligned} \tag{2.4}$$

The corresponding Feynman diagrams for W production are shown in Figure 2.5.

The cross section $\hat{\sigma}$ of the lowest order process can be calculated with quantum field theory techniques [6]:

$$\hat{\sigma}(q\bar{q}' \to \mathrm{W}) = 2\pi |V_{qq'}|^2 \frac{G_F}{\sqrt{2}} \mathcal{M}_{\mathrm{W}}^2 \cdot \delta(Q^2 - \mathcal{M}_{\mathrm{W}}^2) \tag{2.5}$$

where $|V_{qq'}|$ is the relevant element from the Cabibbo-Kobayashi-Maskawa (CKM) quark mixing matrix [79], G_F is the Fermi coupling constant, $\mathcal{M}_{\mathrm{W}}$ is the mass of the W boson and δ is the Dirac delta function. Beyond the leading order, the relation becomes more complicated and the restraint on $Q^2 = \mathcal{M}_{\mathrm{W}}^2$ is released.

Figure 2.6 shows that the dominant contribution to W production comes from u-d scattering and the dominant channel for Z production is through $u\bar{u}$ and $d\bar{d}$ annihilation. The quarks are valence quarks and the anti-quarks come from the sea. The s-c scattering contribution to the total W production cross section is around 17% for W^+ and 23% for W^- [80] and the remaining processes only contribute to about 1% to 3%.

The cross section for W and Z production taking into account the LO, NLO, NNLO contributions are presented in Figure 2.7. It has been estimated that NLO corrections achieve to

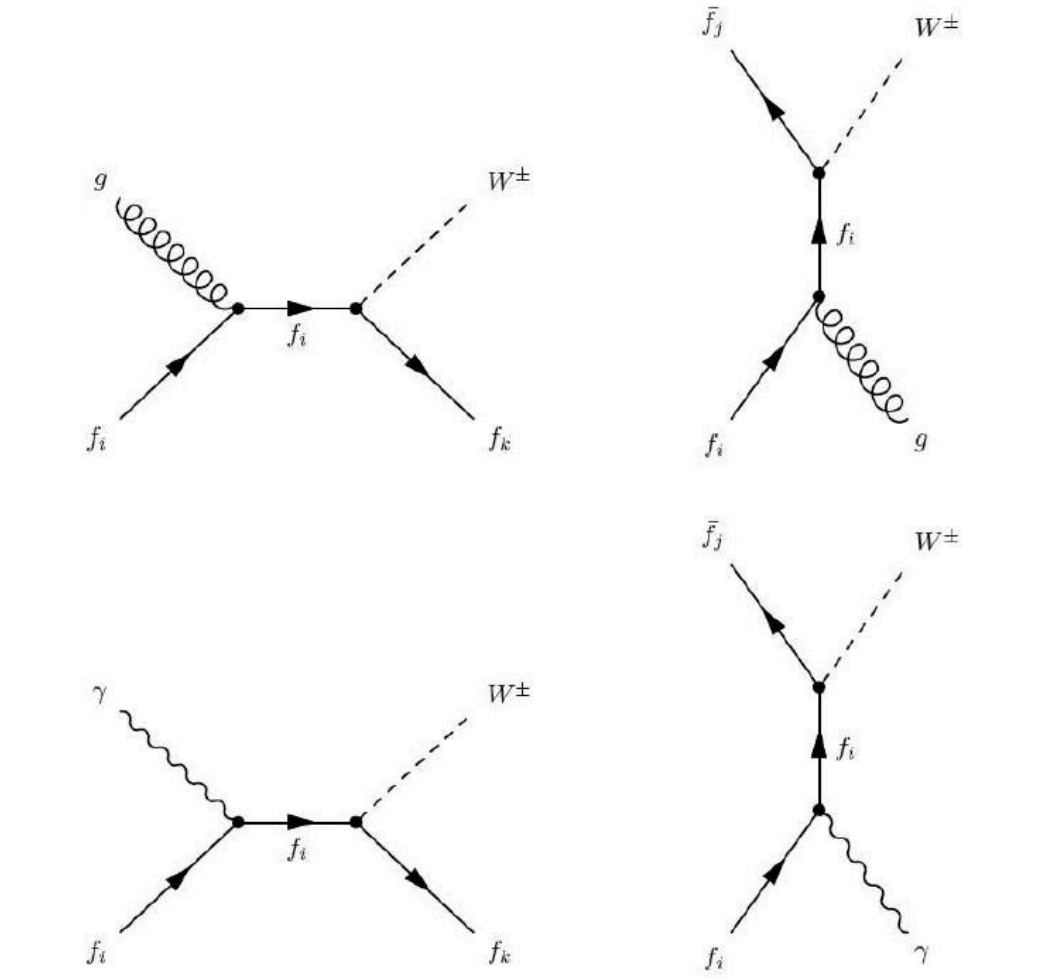

Figure 2.5: Second order Feynman diagram for W production.

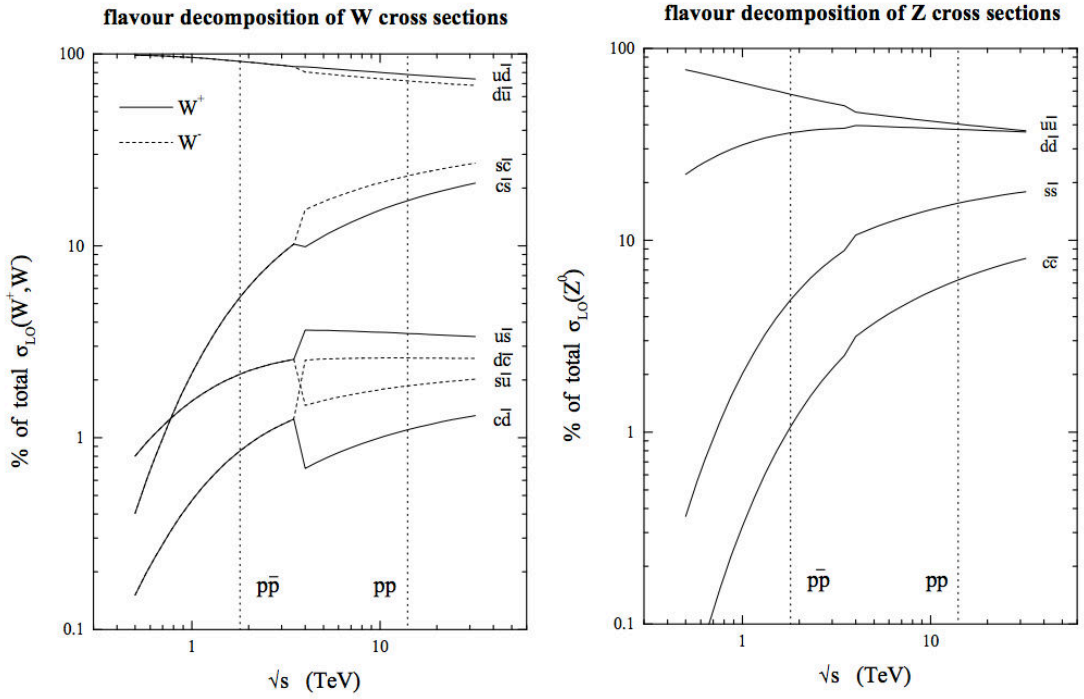

Figure 2.6: Contributions of several quark-antiquark processes to $W^{\pm}$ and Z° production cross sections at LO. [80].

13% of the complete NLO cross section [81]. On the other hand, NNLO corrections are small and are dominated by the uncertainty of the PDFs, which has been estimated to be about 2-8% [82]. The uncertainty on theoretical yields of NNLO predictions is below 1% [82]. Therefore the production of electroweak bosons at the LHC can help in constraining the PDFs.

2.2.1.1 Monte-Carlo generators

In order to fully understand an event at hadron collider, several additional effects, with respect to the physics of hard collisions mentioned above, should be considered during collisions as shown in Figure 2.8. Particles are able to radiate additional particles after leaving the hard scattering vertex, which must be taken into account via Monte-Carlo programs. This process is referred to cascades of radiation produced from QCD processes and interactions and is called parton showering. Besides, particles carrying color can not exist in free form and recombine into colorless duplets or triplets. This process is the formation of hadrons out of quarks and gluons and is called hadronization. All of these processes are involved in Monte-Carlo generators.

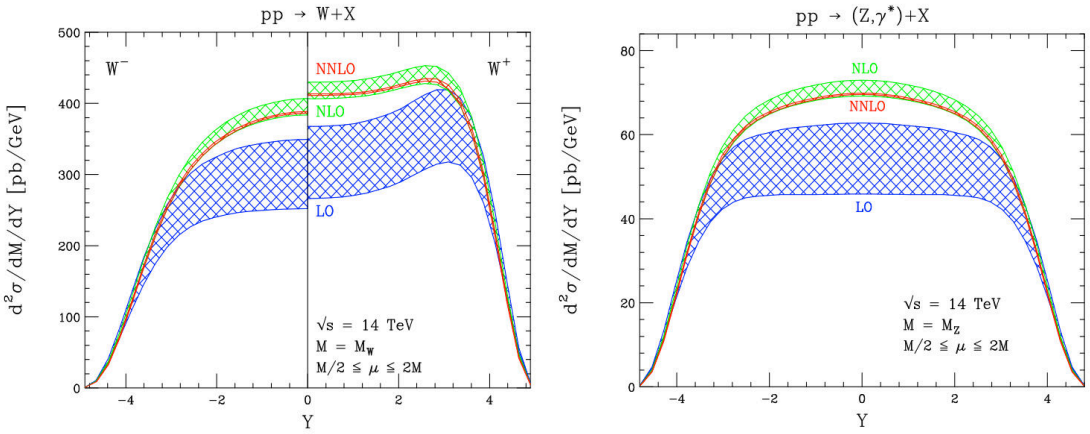

Figure 2.7: Cross section of W (left) and Z boson production in pp collisions at $\sqrt{s} = 14$ TeV, estimated at LO, NLO and NNLO with the MRST PDF set. Since the distributions are symmetric in Y, only half of the rapidity range is shown for W^+ and W^-. The bands indicate the common variation of the renormalization and factorization scales in the range $M/2 \leqslant \mu \leqslant 2M$. [82].

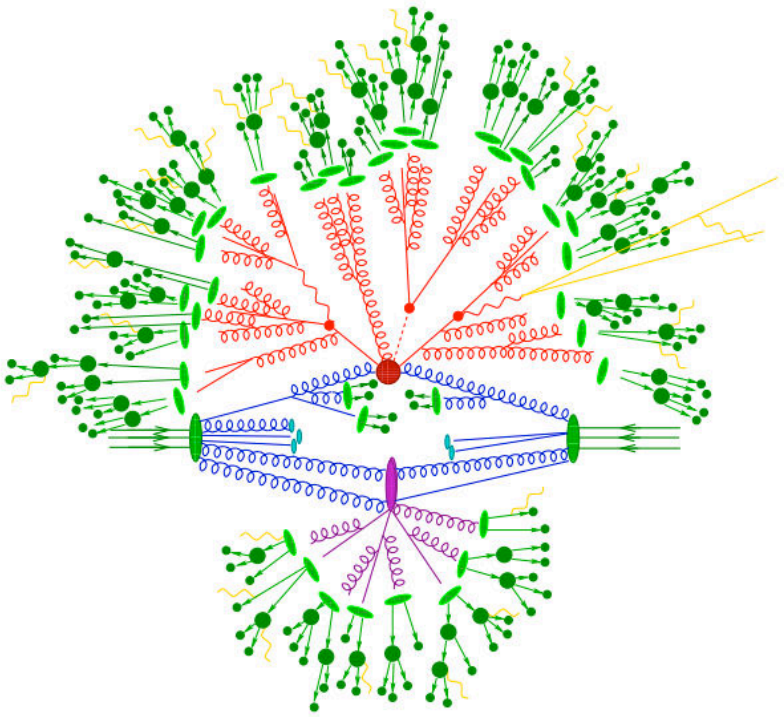

Figure 2.8: Sketch of a hadron-hadron collision as simulated by a Monte-Carlo event generator. The red blob in the center represents the hard collision, surrounded by a tree-like structure representing Bremsstrahlung as simulated by parton showers. The purple blob indicates a secondary hard scattering event. Parton-to-hadron transitions are represented by light green blobs, dark green blobs indicate hadron decays, while yellow lines signal soft photon radiation. [83].

Various MC event generator programs use different approximations for the different steps in calculations which might slightly change the final result. Some of commonly used event generators are listed below:

- PYTHIA [84] is a general purpose event generator, which is commonly used in high energy physics due to its easy handling and relatively large predictive power. It can simulate lepton-lepton, lepton-hadron and hadron-hadron interactions with a broad field of theoretical models. The hard scattering process is however calculated in leading order approximation and the higher order corrections are approximated with a parton shower approach, which has limited accuracy for predicting events with higher jet multiplicity. PYTHIA is interfaced with Photos [85] for QED bremsstrahlung simulation.

- POWHEG (Positive Weight Hardest Emission Generator) [86, 87] is a prescription for interfacing NLO QCD calculations with parton shower generator. POWHEG produces events with positive (constant) weight and furthermore does not depend on the subsequent shower Monte Carlo program. It can be easily interfaced to any modern shower generators such as PYTHIA and HERWIG.

- FEWZ (Fully Exclusive W and Z production) [88, 89, 90] computes the production cross section of W and Z bosons in hadron collisions through the NNLO in perturbative QCD. Leptonic decays of W and Z bosons with full spin correlations as well as finite width effects and gamma-Z interference are included.

2.2.2 Parton distribution functions

Parton distribution functions quantify the probability distributions of the momentum fraction x at a squared energy scale Q^2 for partons within a hadron. They can not be calculated perturbatively but rather are determined through global fits to various experimental data [78]. The weak boson production in pp collisions mostly depends on PDFs in proton. Theoretical predictions of hadronic W and Z production cross sections were calculated to LO pQCD in PYTHIA and NLO and NNLO pQCD using the programs FEWZ [88, 89, 90] and DYNNLO [91, 92, 93]. These are the only available programs that allow the computation of NNLO cross section when applying kinematic cuts. The following PDF families were used in this thesis:

- CTEQ6 [94]
- CT10 [95]
- MSTW2008 [96]

Two major groups, CTEQ [97] and MRST [98], provide semi-regular updates to the parton distributions when new data and/or theoretical developments become available. In addition, there are also PDFs available from Alekhin [99] and from the two HERA experiments [100, 101, 102, 103]. Since experiments may operate at different energy transfer points, the PDFs are extrapolated to a common energy scale Q^2 in fits to experimental data, which is implemented via the so-called DGLAP evolution equations [104, 105, 106]. Assuming $u(x)$ and $d(x)$ as PDFs for up and down quarks, $\bar{u}(x)$ and $\bar{d}(x)$ for the corresponding anti-quarks, the valence quarks in a proton are indicated as $u_v = u - \bar{u}$ and $d_v = d - \bar{d}$, which means the following constraints in the proton PDFs [107] :

$$\int_0^1 [u(x) - \bar{u}(x)]dx = 2 \qquad \int_0^1 [d(x) - \bar{d}(x)]dx = 1 \tag{2.6}$$

$$\textit{and} \qquad \int_0^1 [q(x) - \bar{q}(x)]dx = 0 \qquad \textit{for} \quad q = s, c, b, t \tag{2.7}$$

Figure 2.9 presents an example of proton PDFs from the CT10 NNLO analysis of QCD at four different Q^2 scales [108]. From the curves, one can easily obtain that (1) valence quarks tend to carry a much higher fraction of proton momentum and (2) gluon and sea quarks increase dramatically at higher energy scales. PDFs uncertainties regularly play an important role in searches

for new physics and precision measurements at collider experiments, so a lot of work has been done to develop PDFs [109, 110, 111, 96, 112, 113, 114].

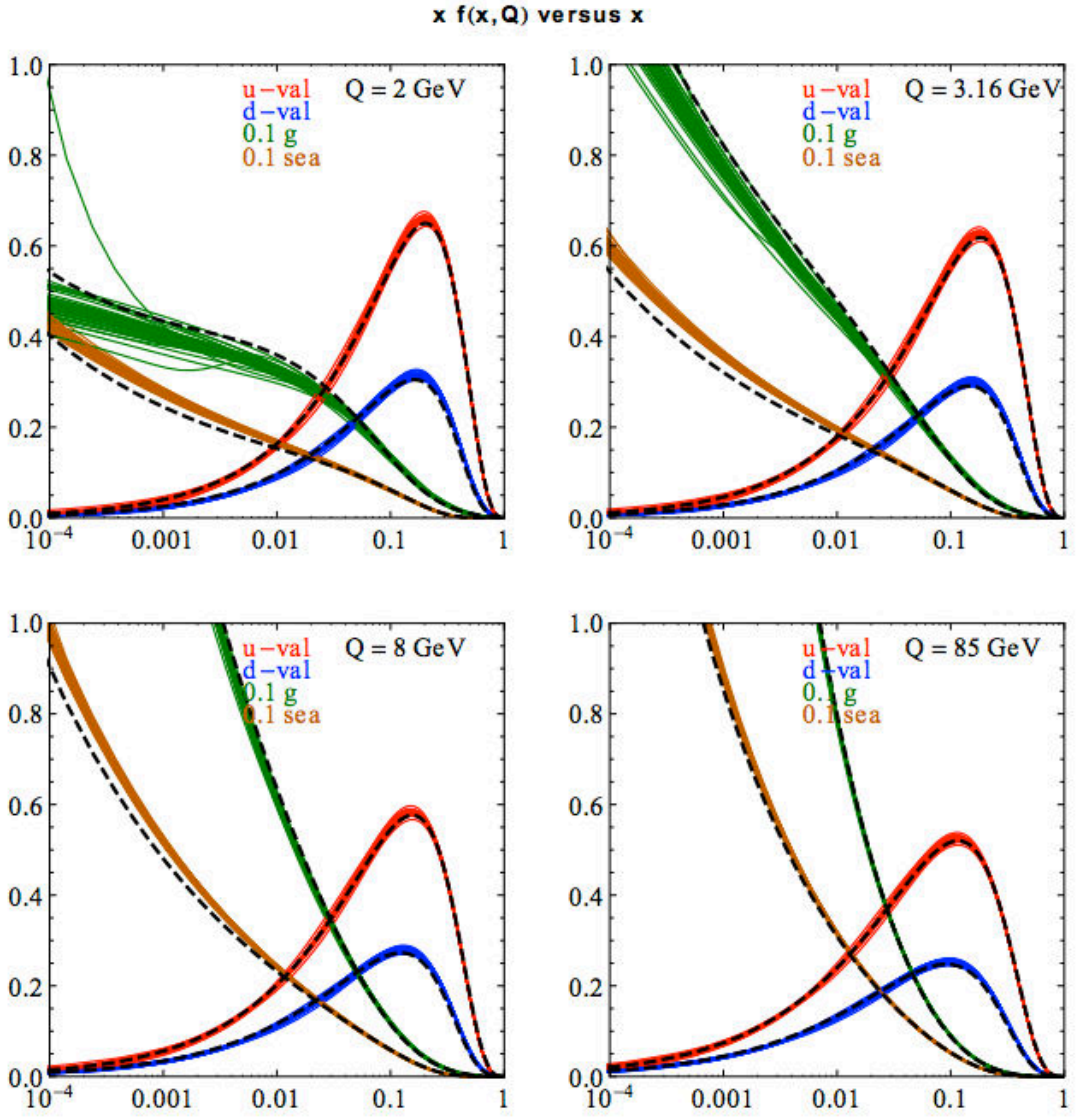

Figure 2.9: CT10NNLO parton distribution functions at Q=2, Q=3.16, Q=8, Q=85 GeV. [108].

The rapidity of W boson is related to parton momentum fractions x_a and x_b by the following relation at LO:

$$y_W \equiv \frac{1}{2} \cdot \ln\left(\frac{E + p_z}{E - p_z}\right) = \frac{1}{2} \cdot ln\left(\frac{x_a}{x_b}\right) \tag{2.8}$$

Considering $Q^2 = m_W^2$ and $Q^2 = x_a x_b s$, one can obtain a relation between the rapidity of W boson and PDF momentum fractions of quark-antiquark pair that annihilate to produce the W

boson:

$$x_a = \frac{m_W}{\sqrt{s}} e^{y_W}, \qquad x_b = \frac{m_W}{\sqrt{s}} e^{-y_W} \tag{2.9}$$

where m_W is the W mass and $\sqrt{s}$ is the center-of-mass energy. This relation implies that W bosons produced at mid-rapidity mainly come from sea quark interactions, while W bosons produced at large rapidity mainly come from the interaction of a valence quark. Therefore, at large-rapidity we can easily obtain the relation $\frac{N_{W^+}}{N_{W^-}} \approx \frac{N_{u-\text{quark}}}{N_{d-\text{quark}}}$. Since the valence quark composition of the proton is "uud", one expects that two times more W^+ than W^- ($N_{W^+} \approx 2N_{W^-}$) will be produced at large rapidity in proton-proton collisions. On the other hand, for the case of heavy-ion collisions, one has Z protons (uud) and N neutrons (udd), which means that $(2Z+N)$ u valence quarks and $(Z+2N)$ d valence quarks are involved. Therefore at large rapidity one expects:

$$\frac{N_{W^+}}{N_{W^-}} = \frac{2Z+N}{Z+2N} \qquad N_{W^-} = 1.15 N_{W^+} \qquad \text{(for Pb-Pb collisions)} \tag{2.10}$$

The kinematic coverage in the (x, Q^2) plane for W production at the LHC in the central (ATLAS and CMS) and forward (LHCb) regions is summarized in Figure 2.10. The coverage of ALICE for W production is inside the LHCb bounds. The region of large-x, small-Q^2 is dominated by the fixed target experiments. A large region of phase space is covered by deep inelastic scattering experiments such as HERA. The larger Q^2 region is explored by the experiments at collider.

2.2.2.1 Weak boson production in heavy-ion collisions: nPDFs

In heavy-ion collisions one should consider both the fact that there are neutrons and the nuclear effects, which is different from pp collisions. For instance, PDFs in nuclei are not equal to the superposition of PDFs of their nucleons. For each parton flavour i, one can define the nuclear parton distribution functions (nPDFs) as:

$$f_i^A(x, Q^2) \equiv R_i^A(x, Q^2) f_i^p(x, Q^2) \tag{2.11}$$

where A is the mass number of the nucleus and $R_i^A(x, Q^2)$ denotes the nuclear modifications with respect to the free proton PDF f_i^p. The PDFs of the bound [‡] neutrons are obtained through

[‡] In quantum physics, a bound state is a special quantum state of a particle subject to a potential such that the

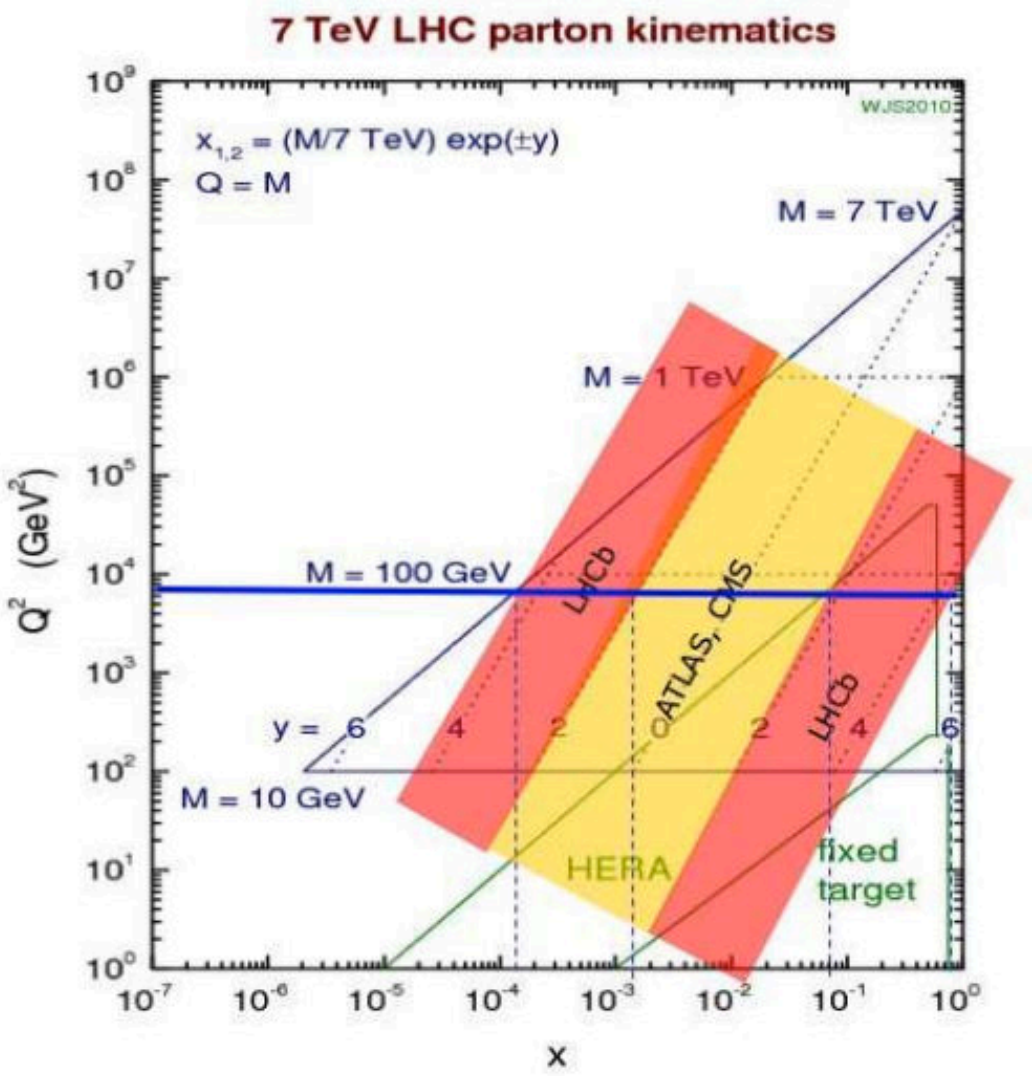

Figure 2.10: The kinematic coverage in the (x, Q^2) plane for W production at the LHC in the central (ATLAS and CMS) and forward (LHCb) regions [115, 116]. The coverage of ALICE for W production ($2.5 < y < 4.0$) is inside the LHCb bounds.

isospin symmetry ($u^{n/A} = d^{p/A}$ etc.), which is exact for isoscalar nuclei and assumed to hold also for the non-isoscalar nuclei [117].

In this thesis, the EPS09 [118, 119] NLO parameterisation of the nuclear modification of the PDFs was used. In EPS09, only three different corrections at the initial scale Q_0^2 are considered: R_V^A for valence quarks, R_S^A for all sea quarks, and R_G^A for gluons. These are parametrized by piecewise functions

$$R_i^A(x) = \begin{cases} a_0 + (a_1 + a_2 x)[\exp(-x) - \exp(-x_a)], & x \leq x_a \\ b_0 + b_1 x + b_2 x^2 + b_3 x^3, & x_a \leq x \leq x_e \\ c_0 + (c_1 - c_2 x)(1-x)^{-\beta}, & x_e \leq x \leq 1 \end{cases} \tag{2.12}$$

where the parameters a_i, b_i, c_i, β, x_a and x_e are A-dependent. Combining the three pieces together to give a continuous function with vanishing first derivatives at matching points x_a and x_e, eradicates 6 out of the 13 parameters. The remaining ones are expressed in terms of the following 6 parameters with obvious explanations:

- y_0 : Height to which shadowing levels as $x \to 0$
- x_a, y_a : Position and height of the antishadowing maximum
- x_e, y_e : Position and height of the EMC minimum
- β : Slope factor in the Fermi-motion part

the remaining parameter c_0 is fixed to $c_0 = 2y_e$. The roles of these parameters are illustrated in Figure 2.11 which also roughly indicates which x-regions are meant by the commonly used terms: shadowing [43], antishadowing [43], EMC effect [120] and Fermi motion [§] [121].

Few other groups, which have so far presented results from a global analysis of nPDFs, are listed below:

- EKS98 [122, 123] was the first global analysis performed for the nPDFs. This LO analysis demonstrated that the measured cross sections for deep inelastic lepton-nucleus scattering (DIS) and for the Drell-Yan (DY) dilepton production in proton-nucleus collisions and in particular the log Q^2-slopes of F_2^{Sn}/F_2^C can all be reproduced and the momentum and

particle has a tendency to remain localised in one or more regions of space.

[§]The Fermi motion is the quantum motion of nucleons bound inside a nucleus

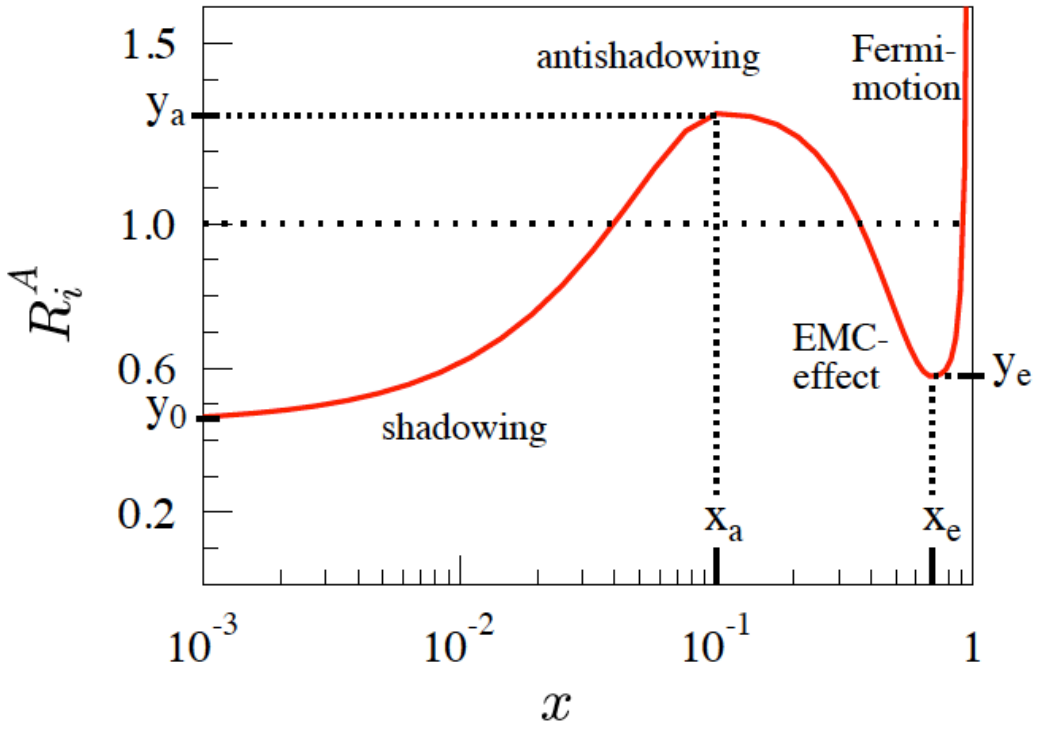

Figure 2.11: An illustration of the fit function $R_i^A(x)$ and the role of the parameters x_a, x_e, y_0, y_a and y_e in EPS09 parameterisation. [118].

baryon number sum rules required simultaneously within the DGLAP framework [117]. The original data fitting in EKS98 was done by eye only.

- HKM [124] and HKN [125] were the first nPDF global analysis with χ^2 minimization automated and also uncertainties estimated. The nuclear DY data were not included in HKM but were added in HKN. These analyses were still at the LO level.

- nDS [126] was the first NLO global analysis for the nPDFs

The weak boson production in heavy-ion collisions is sensitive to the nPDF in nuclei in the region of large Q^2 and large x.

2.2.3 W muonic decay channel

As we saw in Section 2.2, the W boson mainly decays hadronically. However, this decay mode suffer from a large background due to jets. The leptonic decay mode provides a much cleaner signature experimentally. Especially events with a high energy muon are relatively rare, the

muonic decay channel provides a clean signature. Figure 2.12 presents the muonic decay channel studied in this thesis:

$$W^+ \rightarrow \mu^+ \nu_\mu \qquad W^- \rightarrow \mu^- \bar{\nu}_\mu$$

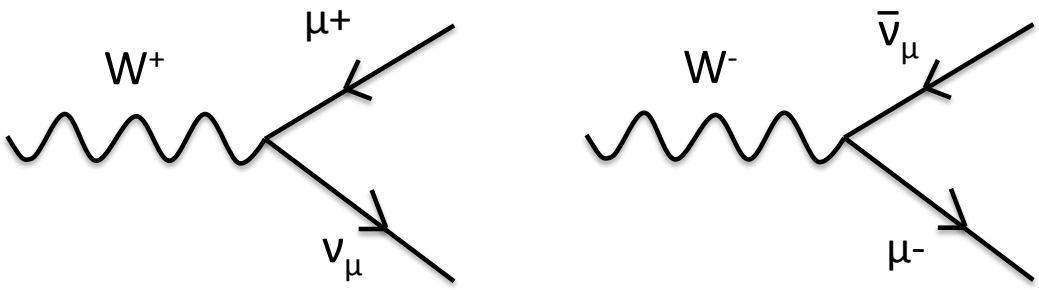

Figure 2.12: W boson decays into a muon and a neutrino.

The reconstruction of the W boson via leptonic decay channel is complicated by the fact that one can not directly measure the neutrino. The vector - axial vector (V-A) nature of the W decay conserves the correlation between W boson rapidity y_W and muon pseudorapidity η_μ [127]. The V-A structure implies that the decay of the charged lepton is not isotropic. In particular, the parton-level cross section in the rest frame of the W can be expressed in terms of the angle between the W and the decay lepton as:

$$\frac{d\sigma}{d\cos\theta^*} \propto (1 \pm \cos\theta^*)^2 \tag{2.13}$$

The sign depends on the product of the W and the decay lepton helicities. The preferred angular decay orientations for W^- and W^+ are shown in Figure 2.13. The weak interaction only couples left-handed fermions and right-handed anti-fermions. According to the angular momentum conservation, the outgoing fermion or anti-fermion (l or $\bar{l}$) follows the direction of the incoming fermion or anti-fermion (q or $\bar{q}$). The cross section is maximal when the outgoing lepton or anti-lepton goes in the direction of the incoming quark or anti-quark. As a result, W^- produced at large-rapidity will preferably emit μ^- in their momentum direction and W^+ will preferably emit μ^+ in the opposite direction.

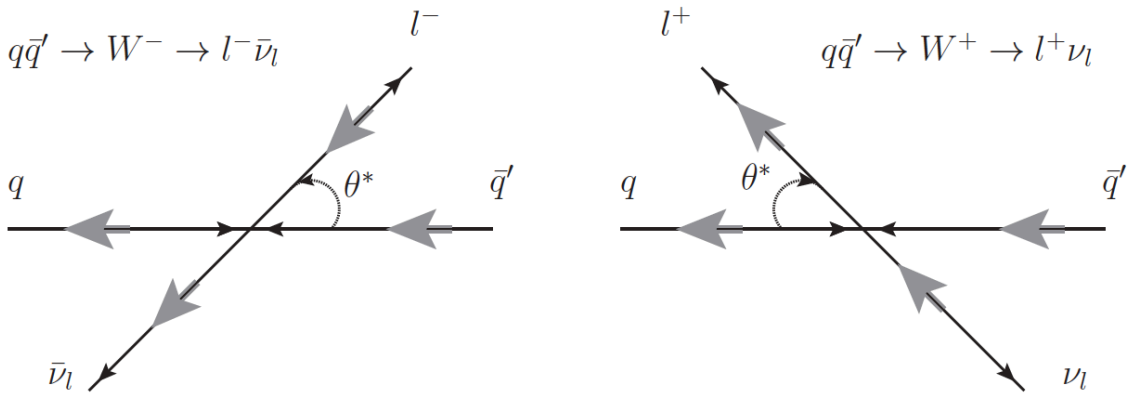

Figure 2.13: W production and leptonic decay diagram showing the favored opening angle between the quark q and the lepton l in the rest frame of the W. The small black arrows correspond to the direction of motion while the large gray arrows indicate the spin. The W spin always points in the direction of the incoming anti-quark. [127].

Part II

ALICE Experiment

Imagination is more important than knowledge. For knowledge is limited, whereas imagination embraces the entire world, stimulating progress, giving birth to evolution.

Albert Einstein

3 The ALICE experiment

3.1 The Large Hadron Collider

The Large Hadron Collider (LHC) is a two-ring-superconducting accelerator and collider installed in the existing 26.7 km tunnel that was constructed between 1984 and 1989 for the Large Electron Positron Collider (LEP) machine at the CERN [128]. It is located at a depth ranging from 50 to 175 meters beneath the France–Switzerland border near Geneva, Switzerland and is by far the word's largest and most powerful particle accelerator and collider. The LHC produces head-on collisions between two beams of particles, either protons or heavy ions (up to Pb^{82+}), which are produced and pre-accelerated in a chain of accelerators (see Figure 3.1) and then injected into the LHC, where they are further accelerated to energies up to 7 TeV for protons and 2.76 TeV for Pb per nucleon. The LHC nominal running conditions are summarized in Table 3.1. This new energy record will allow us to test the predictions of different theories of particle physics, and in particular to study the property of the fundamental particle Higgs boson predicted by the SM, the large family of new particles predicted by supersymmetric theoretical models, the nature of dark matter and the new state of matter (QGP).

The two particle beams cycling with opposite directions in the LHC ring collide in four different locations, where the collision products are detected by six experiments:

- ALICE (A Large Ion Collider Experiment) [131], a specialized heavy-ion experiment de-

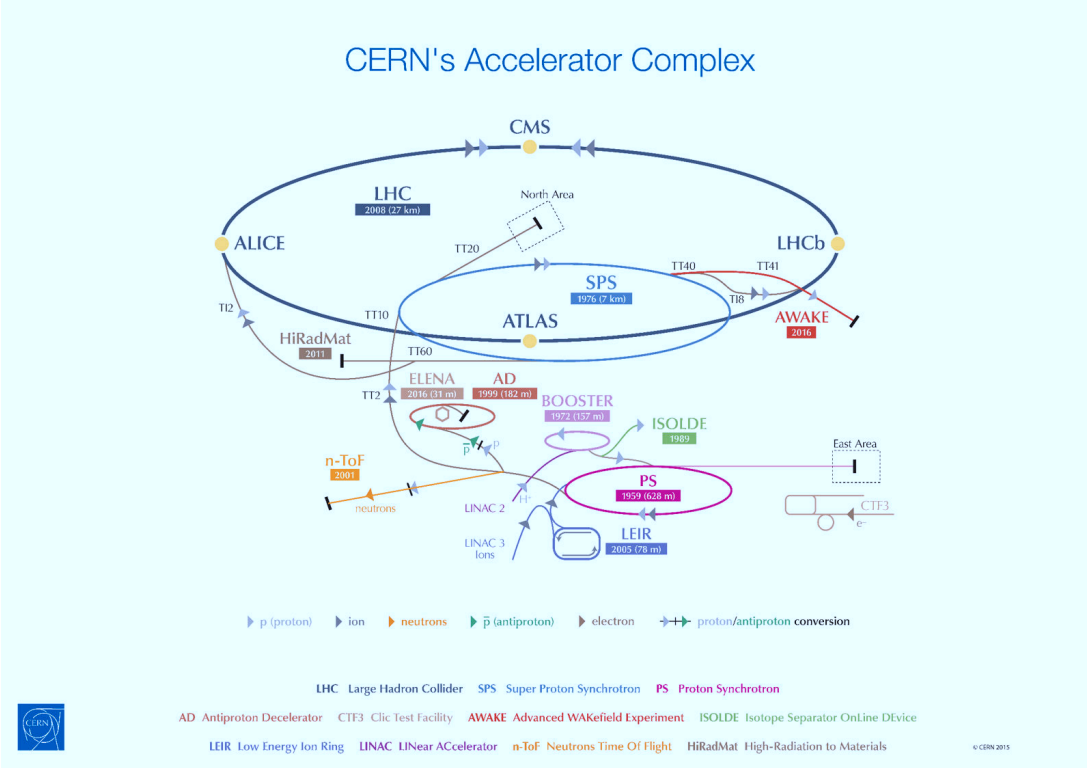

Figure 3.1: The CERN accelerator complex [129].

Collision beams	$\sqrt{s_{\mathrm{NN}}}$ (TeV)	L ($\mathrm{cm}^{-2}\mathrm{s}^{-1}$)	Running time per year (s)	σ_{geom} (b)
pp	14.0	10^{34}	10^{7}	0.07
Pb–Pb	5.5	10^{27}	10^{6}	7.7
p–Pb	8.8	10^{29}	10^{6}	1.9

Table 3.1: The LHC nominal run conditions for different collision system, center-of-mass energy, integrated luminosity, running time and the geometrical cross sections [30, 130].

signed to study the physics of strongly interacting matter and the quark-gluon plasma in nucleus-nucleus collisions at the LHC.

- ATLAS (A Toroidal LHC ApparatuS) [132], a general-purpose experiment, looking for new particles such as the Higgs boson and the physics beyond the SM.

- CMS (Compact Muon Solenoid) [133], with similar purposes as ATLAS.

- LHCb (Large Hadron Collider beauty) [134], is dedicated to precision measurements of CP violation and rare decays of B hadrons.

- LHCf (Large Hadron Collider forward) [135], sharing the interaction point with ATLAS,

is dedicated to the measurement of neutral particles emitted in the very forward region of LHC collisions to provide data for calibrating the hadron interaction models that are used in the study of Extremely High-Energy Cosmic-Rays.

- TOTEM (TOTal and Elastic Measurement) [136], sharing the interaction point with CMS, measures the total pp cross section with the luminosity independent method and study elastic and diffractive scatterings at the LHC.

The ALICE collaboration consists of approximately 1800 members from 174 institutes in 42 countries [137] and has published 155 papers since 2010 [138]. The performance of the ALICE detectors and analysis methods for various physics observables are described in Physics Performance Reports [139, 140, 141] and the technical details of each detectors are presented in Technical Design Reports [142]. In the following sections, I will provide a brief introduction of the ALICE detectors, focusing on the main performances for physics.

3.2 ALICE setup

The ALICE apparatus (Figure 3.2) has overall dimensions of $16 \times 16 \times 26$ m^3 and a total weight of $\sim 10^4$ t [139]. It is designed to cope with the highest particle multiplicities expected in central Pb-Pb collisions at the LHC (dN_{ch}/dy up to 8000) and is able to track and identify particles in a large range of transverse momentum (p_{T}), from very low ($\sim$100 MeV/c) up to fairly high ($\sim$100 GeV/c) p_{T}. However the measurement showed a much smaller multiplicity of charged particles. The ALICE official reference frame is a right-handed orthogonal Cartesian system with the z-axis parallel to the beam line and pointing in the direction opposite to the MUON Spectrometer, the x-axis aligned to the local horizon and pointing to the accelerator center and the y-axis perpendicular to the other two and pointing upward.

The ALICE detector consists of three parts:

- Global Detectors: the Zero Degree Calorimeter (ZDC), the Photon Multiplicity Detector (PMD), the Forward Multiplicity Detector (FMD), T0 and V0 detectors, which are located at small angles in the forward and backward rapidity regions. They are used for global event characterization (such as multiplicity measurement, centrality determination and event plane reconstruction in heavy-ion collisions) and event triggering.

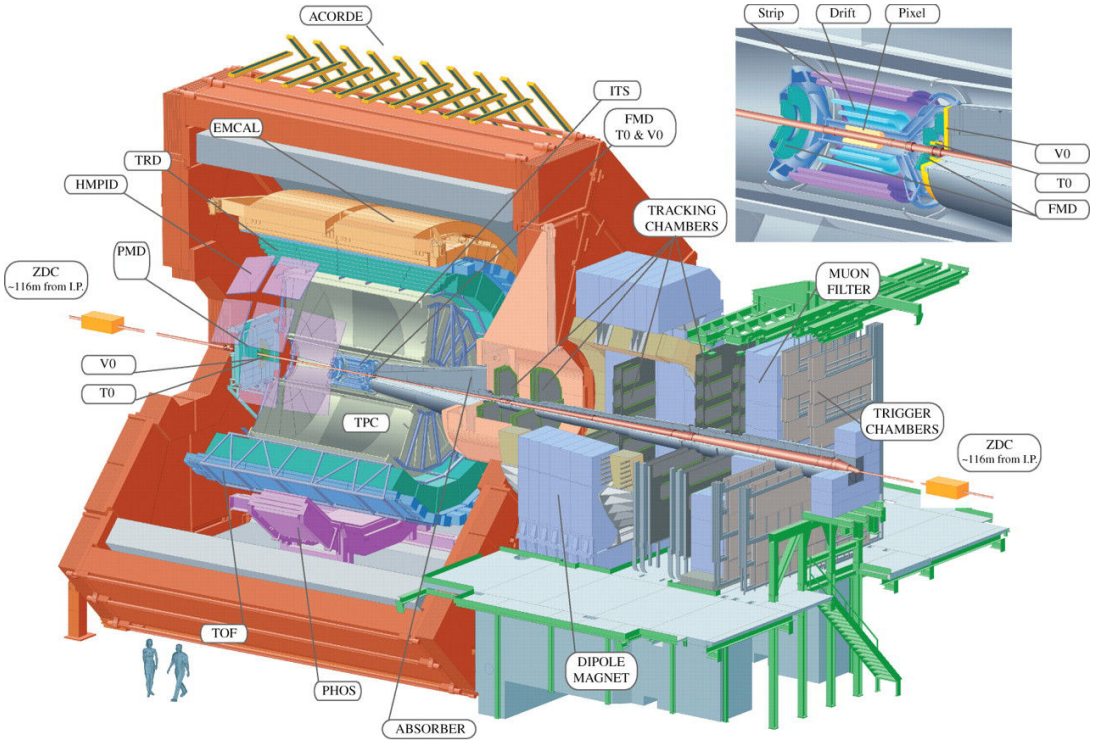

Figure 3.2: Schematic layout of the ALICE experiment at the CERN LHC. The central-barrel detectors (ITS, TPC, TRD, TOF, PHOS, EMCal, and HMPID) are embedded in a solenoid with magnetic field B = 0.5 T and address particle production at midrapidity. The cosmic-ray trigger detector ACORDE is positioned on top of the magnet. Forward detectors (PMD, FMD, V0, T0, and ZDC) are used for triggering, event characterization and multiplicity studies. The MUON spectrometer covers the pseudo-rapidity range $-4.0 < \eta < -2.5$. [139].

- Central Barrel Detectors: the central detector system covers the pseudo-rapidity range $|\eta| < 0.9$ and is embedded in the L3 solenoid magnet, which provides a solenoid magnetic field of up to B = 0.5 T. It consists, from inside to outside, of the Inner Tracking System (ITS) made of six cylindrical layers, two Silicon Pixel Detectors (SPD), two Silicon Drift Detectors (SDD) and two Silicon Strip Detectors (SSD), the cylindrical Time-Projection Chamber (TPC), the Transition Radiation Detector (TRD), the Time-Of-Flight (TOF), the High Momentum Particle Identification Detector (HMPID) and two electromagnetic calorimeters: the PHOton Spectrometer (PHOS) and the ElectroMagnetic CALorimeter (EMCal *). All of the central barrel detectors cover the full azimuth except HMPID, PHOS and EMCal. They allow for primary vertex reconstruction, tracking charged particles and Particle Identification (PID) for charged hadrons, photons and electrons.

- Forward muon spectrometer: the forward muon arm covers the pseudo-rapidity range $-4 < \eta < -2.5$. It is mainly designed for the measurement of quarkonia down to $p_T = 0$ via their $\mu^+\mu^-$ decay channel, and of heavy-flavours in the semi-muonic decay channel. In addition, the production of weakly interacting probes ($W^{\pm}$ and Z^0 bosons) and low mass resonances (ϱ, ω, φ) is also studied. The analysis presented in this thesis is based on the data collected with this muon spectrometer. A detailed description of the detector layout and features will be proved in Section 3.5.

The experiment is completed by an array of scintillators for triggering on cosmic rays (ALICE COsmic Ray DEtector, ACORDE) on the top of the L3 magnet. Table 3.2 summarizes the acceptances, positions and dimensions of the various detection elements.

A short summary of pseudo-rapidity coverage and the particle identification capabilities of the ALICE detectors is presented in Figure 3.3.

*The extension of EMCal by adding calorimeter modules on the opposite side (Di-Jet Calorimeter, DCal) are other important ingredients and it is installed in the second year of Run 2. The details are described in [143].

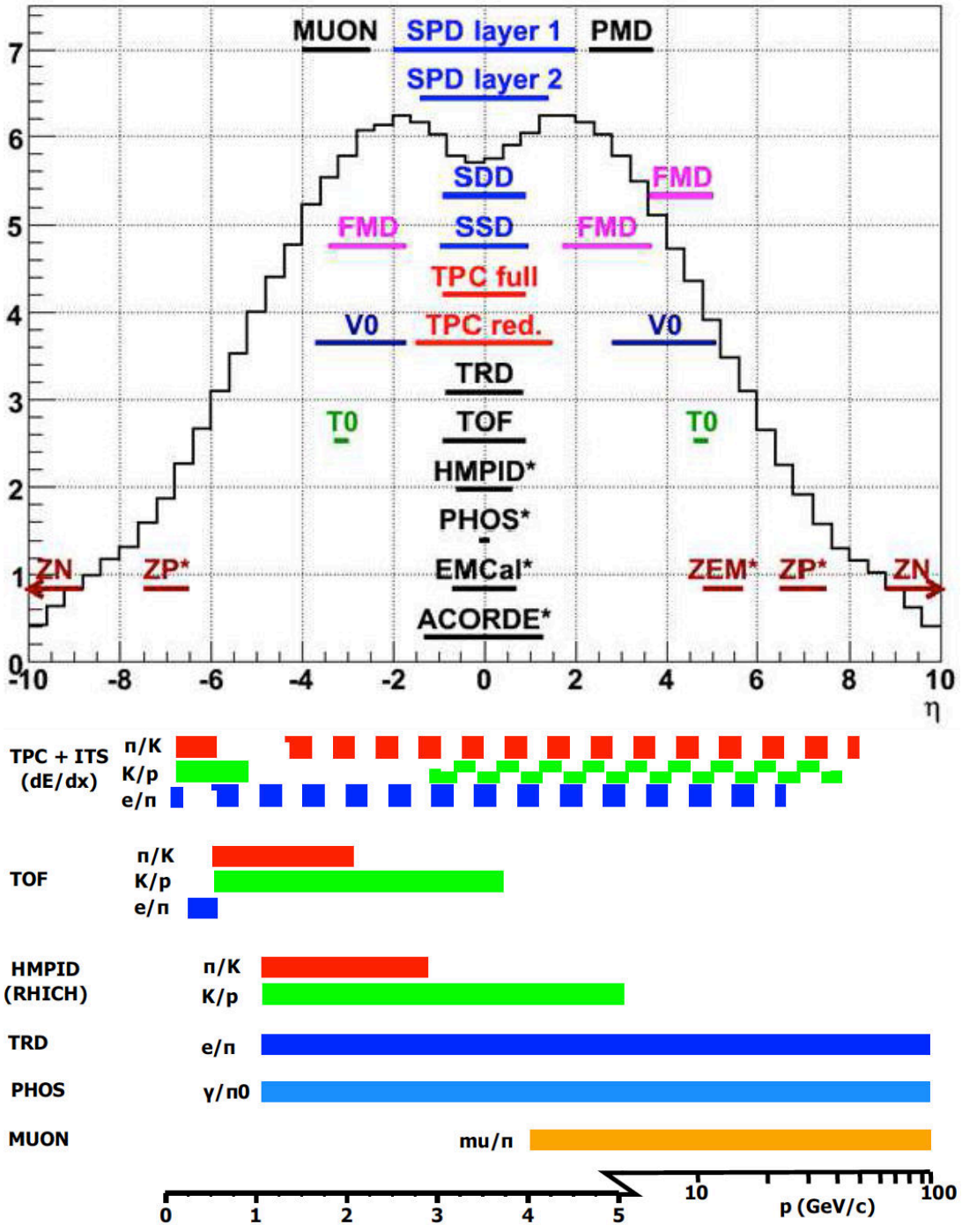

Figure 3.3: Pseudo-rapidity coverage of the ALICE detectors (top panel) and the particle identification capabilities of the detectors (bottom panel). [144].

Detector	Acceptance (η,ϕ)	Position (m)	Dimension (m^2)
ZDC: ZN	$\lvert\eta\rvert > 8.8$	± 113	2×0.0049
ZDC: ZP	$6.5 < \lvert\eta\rvert < 7.5$ $-10^\circ < \phi < 10^\circ$	± 113	2×0.027
ZDC: ZEM	$4.8 < \lvert\eta\rvert < 5.7$ $-16^\circ < \phi < 16^\circ$ and $-164^\circ < \phi < 169^\circ$	7.3	2×0.0049
PMD	$2.3 < \eta < 3.7$	3.64	2.59
FMD Disk 1	$3.62 < \eta < 5.03$	inner: 3.2	0.266
FMD Disk 2	$1.7 < \eta < 3.68$	inner: 0.834 outer: 0.752	
FMD Disk 3	$-3.4 < \eta < -1.7$	inner: -0.628 outer: -0.752	
ToA	$4.61 < \eta < 4.92$	3.75	0.0038
ToC	$-3.28 < \eta < -2.97$	-0.727	0.0038
VoA	$2.8 < \eta < 5.1$	3.4	0.548
VoC	$-3.7 < \eta < -1.7$	-0.897	0.315
ITS layer 1, 2 (SPD)	$\lvert\eta\rvert < 2, \lvert\eta\rvert < 1.4$	0.039, 0.076	0.21
ITS layer 3, 4 (SDD)	$\lvert\eta\rvert < 0.9, \lvert\eta\rvert < 0.9$	0.150, 0.239	1.31
ITS layer 5, 6 (SSD)	$\lvert\eta\rvert < 0.97, \lvert\eta\rvert < 0.97$	0.380, 0.430	5.0
TPC	$\lvert\eta\rvert < 0.9$ (r = 2.8 m) $\lvert\eta\rvert < 1.5$ (r = 1.4 m)	0.848, 2.466	readout 32.5 m^2 Vol. 90 m^3
TRD	$\lvert\eta\rvert < 0.84$	2.90, 3.68	716
TOF	$\lvert\eta\rvert < 0.9$	3.87	141
HMPID	$\lvert\eta\rvert < 0.6$ $1.2^\circ < \phi < 58.8^\circ$	5.0	11
PHOS	$\lvert\eta\rvert < 0.12$ $220^\circ < \phi < 320^\circ$	4.6	8.6
EMCAL	$\lvert\eta\rvert < 0.7$ $80^\circ < \phi < 187^\circ$	4.36	44
ACORDE	$\lvert\eta\rvert < 1.3$ $-60^\circ < \phi < 60^\circ$	48.5	43
Muon Tracking station 1	$-4.0 < \eta < -2.5$	-5.36	4.7
Muon Tracking station 2		-6.86	7.9
Muon Tracking station 3		-9.83	14.4
Muon Tracking station 4		-12.92	26.5
Muon Tracking station 5		-14.22	41.8
Muon Trigger station 1		-16.12	64.6
Muon Trigger station 2		-17.12	73.1

Table 3.2: Names, acceptances, positions and dimensions of the ALICE detector subsystems [139, 131].

3.3 Global detectors

The ZDC, PMD, FMD, To and Vo located at small angles are used for global event characterization like centrality, multiplicity and trigger decisions in the collisions. Further details are presented below.

3.3.0.1 ZDC: Zero Degree Calorimeter [145]

The Zero Degree Calorimeters detect the energy of the spectator nucleons in order to determine the overlap region of the two colliding nuclei. It is composed of four calorimeters, two to detect protons (ZP) and two to detect neutrons (ZN). They are located 113 meters away from the interaction point on both sides, along the beam line. That is why we call them Zero Degree Calorimeters. The system is completed by two electromagnetic calorimeters (ZEM, that estimates the participating nucleons), both placed at about 7 m from the interacting point (in the opposite side of the muon spectrometer), which allow to resolve ambiguities in the determination of the centrality.

3.3.0.2 PMD: Photon Multiplicity Detector [146]

The PMD is a pre-shower detector placed at about 360 cm from the interaction point (in the side opposite to the muon spectrometer), which allows to measure the multiplicity and spatial ($\eta - \phi$) distribution of photons on an event-by-event basis, in the forward region ($2.3 < \eta < 3.7$), and provides the estimation of the transverse electromagnetic energy and of the reaction plane on an event-by-event basis. It is composed of two identical planes of detectors, made of gas proportional counters with honeycomb structure and wire readout, with a $3X_0$ thick lead converter in between them: the front detector plane is used for vetoing charged particles while the detector plane behind the converter is the pre-shower plane and registers hits from both photons and charged hadrons. This allows to disentangle the photon signal.

3.3.0.3 FMD: Forward Multiplicity Detector [147]

The FMD consists of five rings of silicon strip detectors with 51200 silicon strip channels. It provides information of the charged particle multiplicity in the pseudo-rapidity range $-3.4 < \eta < -1.7$ (muon spectrometer side) and $1.7 < \eta < 5.1$ (PMD side) and allows to determine the multiplicity, correlations, collective flow and the reaction plane event-by-event. Together, the

ITS and the FMD provide an early charged particle multiplicity measurement for $-3.4 < \eta < 5.1$ in all colliding systems.

3.3.0.4 T0 [147]

The T0 is made of two arrays of Cherenkov counters (T0A and T0C), with a time resolution better than 50 ps, asymmetrically placed at 72.7 cm (muon spectrometer side, T0C) and 375 cm (PMD side, T0A) from the interaction vertex, with a pseudo-rapidity coverage of $-3.28 < \eta < -2.97$ (T0C) and $4.61 < \eta < 4.92$ (T0A), respectively. It is designed to provide a T0 signal for the TOF detector, to measure the vertex position with a precision of ± 1.5 cm.

3.3.0.5 V0 [147]

The V0 consists of two arrays of scintillator material, located at 90 cm (muon spectrometer side, V0C) and 340 cm (PMD side, V0A) from the interaction point, with a pseudo-rapidity coverage of $-3.8 < \eta < -1.7$ (V0C) and $2.8 < \eta < 5.1$ (V0A). The measurement of the time-of-flight difference between the detectors allows to identify and reject the beam-gas events. The coincidence of a signal between the V0A and V0C is used as a minimum bias trigger. Moreover, the V0 is used to determine the centrality of the event in Pb–Pb collisions via a Glauber model fit of the signal amplitude.

3.4 Central barrel detectors

The detector system at central rapidity, called central barrel, is able to identify hadrons, electrons and photons from very low transverse momenta around 100 MeV/c to large momenta of 100 GeV/c. It consists of the ITS featuring six layers of high-resolution silicon detectors, the TPC as the main tracking system of the experiment, the TRD which provides electron identification and the TOF for particle identification. These detectors have full azimuthal and central rapidity ($|\eta| < 0.9$) coverage. The design also includes two small-area detectors: an array of ring-imaging Cherenkov detectors for identification of high-momentum particles (HMPID) and an electromagnetic calorimeter made of high density crystals (PHOS, EMCal and DCal). The central barrel is covered by a magnetic field of a maximum 0.5 T. Further details of each detector in central barrel are presented below.

3.4.0.1 ITS: Inner Tracking System [148]

The ITS provides tracking and vertex reconstruction near the interaction point. It is made of six cylindrical layers of silicon detector covering $|\eta| < 0.9$. The innermost two layers are Silicon Pixel Detectors (SPD), the two intermediate layers are Silicon Drift Detectors (SDD) and the two external layers are Silicon Strip Detectors (SSD). The ITS can localize the primary vertex with a resolution better than 100 μm in the transverse plane, reconstruct secondary vertexes and improve the TPC measurements, extending the momentum coverage down to 100 MeV/c.

3.4.0.2 TPC: Time Projection Chamber [149]

The TPC is the main tracking detector of the central barrel. It is in charge of tracking and provides particle identification via dE/dx. It allows to reconstruct charged-particle p_T from 100 MeV/c (with 1% resolution) up to 100 GeV/c (with 5% resolution if ITS is included as well). The detection of low momentum particles is achievable with a low magnetic field ($\leq$ 0.5 T). The TPC has an inner radius of about 85 cm and an outer one of about 250 cm with a total length of about 500 cm. However this leads to a 88 μs drift time, which limits the luminosity that the ALICE experiment can afford.

The study of soft hadronic observables requires a resolution of 1% for momenta between 100 MeV/c and 1 GeV/c, while the detection of hard probes needs a 10% resolution for tracks with p_T = 100 GeV/c. The resolution on the relative momentum between two particles, necessarily for the measurement of two-particle correlations, has to be better than 5 MeV/c. Finally, the TPC can provide particle identification by the measurement of dE/dx.

3.4.0.3 TRD: Transition Radiation Detector [150, 151]

The TRD covers the pseudo-rapidity range $|\eta| < 0.9$ and is located between the TPC and the TOF detectors. It consists of 18 sectors of 6 layers each with a 5 fold segmentation along the beam direction, for a total of $18 \times 5 \times 6 = 540$ detector modules. Each module consists of a radiator of 4.8 cm thickness and a multi-wire proportional chamber (MWPC) with cathode pad readout. The TRD provides electron identification for momenta larger than 1 GeV/c, where the pion rejection capability through energy loss measurement in the TPC is no longer sufficient. Together with the ITS and the TPC, they allow to measure the production of light and heavy vector meson resonances, and of open charm and beauty according to the determination of the impact parameter. A similar technique can be used to separate the directly produced J/Ψ mesons from

those arising from B-hadron decays. The TRD increases the ALICE pion rejection capabilities by a factor of 100 for electron momenta above 3 GeV/c.

3.4.0.4 TOF: Time Of Flight [152, 153]

The TOF is a large area array covering $|\eta| < 0.9$ and provides particle identification in the intermediate momentum range, from 0.2 to 2.5 GeV/c. Coupled with the ITS and the TPC, it allows for event-by-event identification of pions, kaons and protons. Its large coverage demands the use of a gaseous detector. Multi-gap Resistive Plate Chambers were chosen, providing an intrinsic time resolution of better than 40 ps and an efficiency close to 100%. The detector is segmented in 18 sectors in the azimuthal angle ϕ and 5 segments in z. The identification of the hadrons relies in their different time of flight vs momentum behavior. The ITS-TPC reconstructed tracks are projected into the TOF, and for the matched particles the travel length (l) is calculated from the track momentum (p). The time of flight (t) allows to evaluate the particle mass as: $m = p\sqrt{t^2/(l^2-1)}$. The resulting mass separation as a function of the momentum for pions, kaons and protons is shown in Figure 3.4.

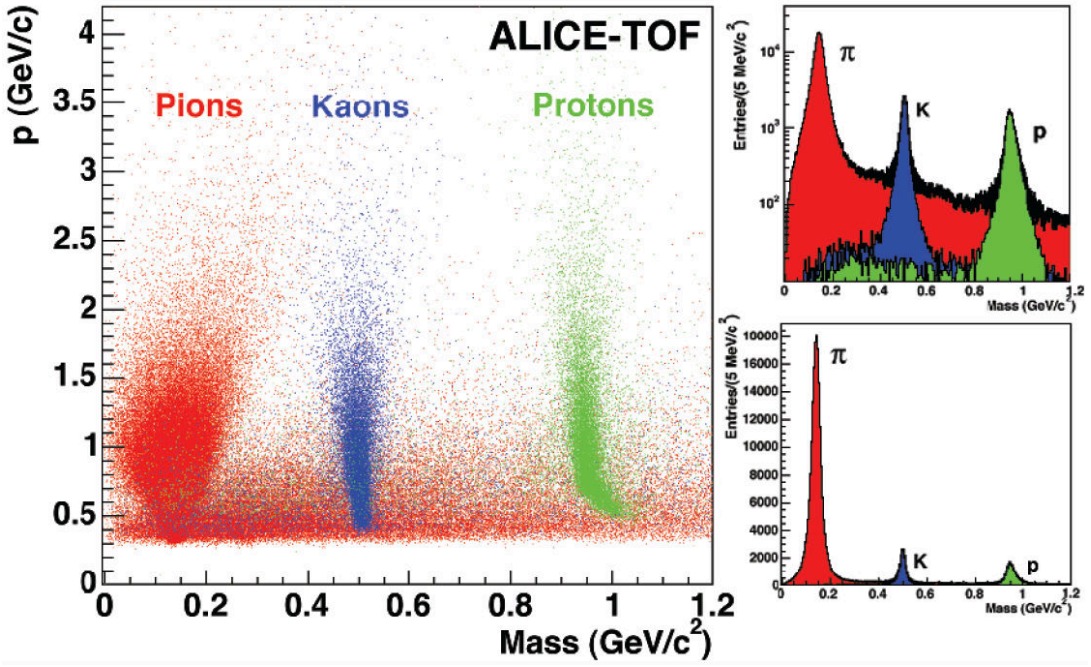

Figure 3.4: Mass separation as a function of momentum with the TOF detector, for 200 HIJING central PbPb events and with a simulated overall TOF time resolution of 80 ps. The right plots present the corresponding mass distributions for 0.5 < P < 4.2 GeV/c on a logarithmic (upper plot) and linear (lower plot) scale. The distributions from pions, kaons and protons are respectively indicated by the labelled histograms, while the black histogram represents the inclusive distribution from all particle species. [140].

3.4.0.5 HMPID: High Momentum Particle Identification Detector [154]

The HMPID, located at a radius of 5 m, is one of the outer detectors of ALICE. Its azimuthal and pseudo-rapidity coverage are of $\Delta\phi = 57.61^{\circ}$ and $|\eta| < 0.6$, respectively. It is made of 7 modules of 1.5×1.5 m^2 of proximity focusing Ring Imaging Cherenkov (RICH) counters. The detector allows for track-by-track discrimination of π/K up to 3 GeV/c and of K/p up to 5 GeV/c.

3.4.0.6 PHOS: PHOton Spectrometer [155]

The PHOS is located at the bottom of the central barrel at 460 cm from the interaction point. It covers a pseudo-rapidity and azimuthal angle range of $|\eta| < 0.12$ and $\Delta\phi = 100^{\circ}$, respectively. It is composed by a charge particle veto (CPV) and an electromagnetic calorimeter (EMC). The CPV consists of multi-wire proportional chambers (MWPC) with cathode pad readout. The EMC is made of lead-tungsten crystals, readout by Avalanche Photo-Diodes (APD). The electromagnetic showers emitted by a photon or another electrically neutral particle provide a signal in the EMC, but not in the CPV, and can therefore be separated by charged-particle showers. The time of flight measurement with nanosecond precision enables discrimination between photons and neutral baryons, which is particularly useful for neutron discrimination. Neutral mesons can be measured as well through the two-photons decay channel.

3.4.0.7 EMCal: ElectroMagnetic Calorimeter [156]

The EMCal covers the $|\eta| < 0.7$ region and $80^{\circ} < \varphi < 187^{\circ}$ ($260^{\circ} < \varphi < 327^{\circ}$ for Di-jet Calorimeter) in azimuthal angle. The EMCal is a Pb-scintillator sampling calorimeter which is much larger than PHOS, but with lower granularity and resolution. In conjunction with the TPC and other barrel detectors it measures jet production rates and fragmentation functions.

3.5 Forward muon spectrometer

The ALICE forward muon spectrometer is designed to detect muons with a polar angle of $171^{\circ} < \vartheta < 178^{\circ}$ with respect to the beam axis, corresponding to a pseudo-rapidity coverage of $-4.0 < \eta < -2.5$. This allows the study of open heavy flavours (D and B mesons), quarkonium (charmonium and bottomonium) and low-mass vector mesons (ϱ, ω, φ) production by their muonic decay channels in a wide transverse momentum range in a region complementary to the one explored by the ALICE central barrel and other LHC experiments, like ATLAS and CMS.

The layout of the muon spectrometer is shown in Figure 3.5. It consists of a passive front absorber to reduce the contamination of hadrons from the interaction vertex. Muon tracks are then reconstructed by tracking chambers consisting of five stations of multi-wire proportional chambers with cathode pad readout. The third station is placed inside a dipole magnet providing an integrated magnetic field of 3 Tm. Muon identification is ensured by matching the reconstructed tracks with the signal provided by the trigger system, which consists of four layers of Resistive Place Chambers placed behind an iron absorber. The spectrometer is shielded throughout its length by a dense absorber tube, with a diameter of about 60 cm, which surrounds the beam pipe. The main characteristics of the detector are summarized in Table 3.3.

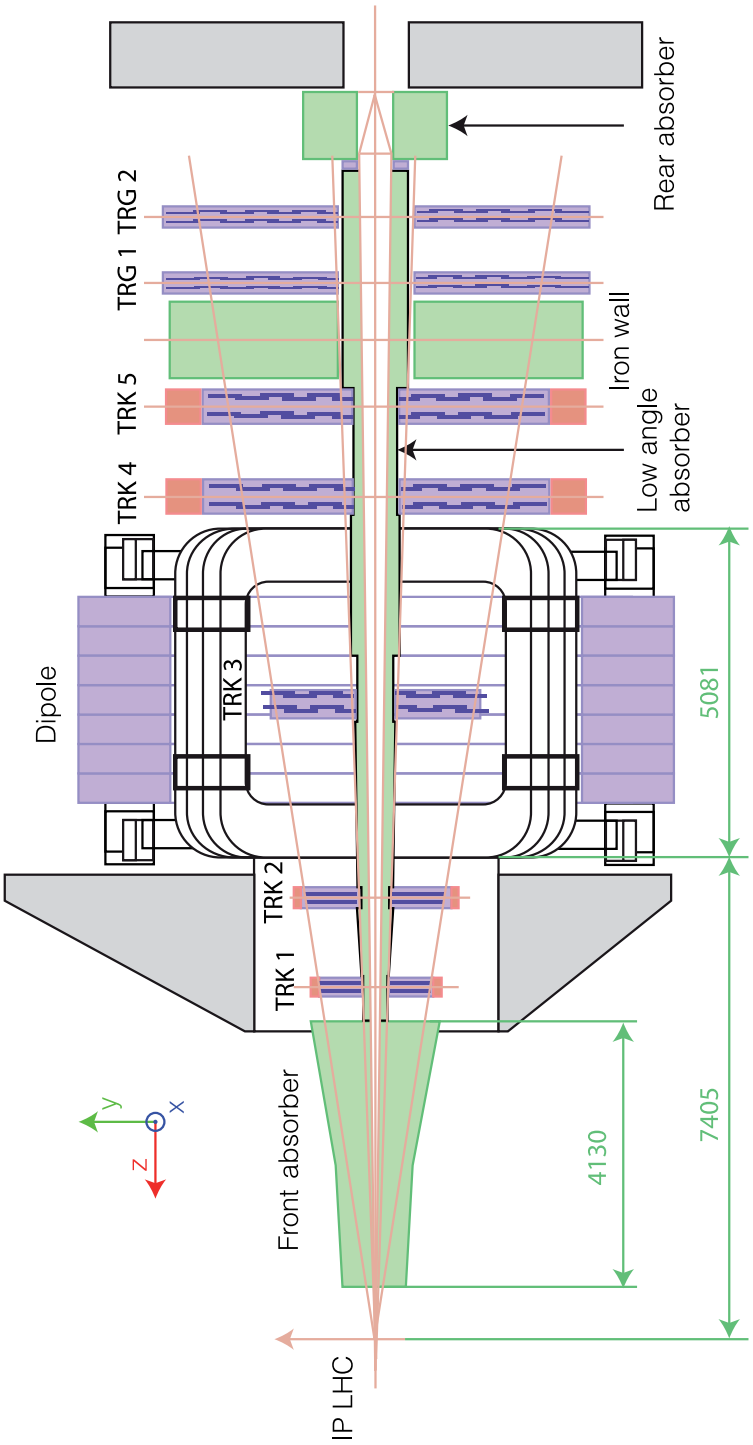

Figure 3.5: The longitudinal section of muon spectrometer. [157].

Muon Detection	
Polar, azimuthal angle coverage	$171^{o} \leq \vartheta \leq 178^{o}$
Minimum muon momentum	4 GeV/c
Pseudo-rapidity coverage	$-4.0 < \eta < -2.5$
Front Absorber	
Longitudinal position (from IP)	-5030 mm $\leq z \leq$ -900 mm
Total thickness (materials)	($\sim 10\lambda_{int}$, $\sim 60X_{o}$) ((carbon-concrete-steel)
Dipole Magnet	
Nominal magnetic field, field integral	0.67 T, 3 Tm
Free gap between poles	2.972-3.956 m
Overall magnet length	4.97 m
Longitudinal position (from IP)	-z = 9.94 m (centre of the dipole coils)
Tracking Chambers	
No. of stations, no. of planes per station	5, 2
Longitudinal position of stations	-z = 5357, 6860, 9830, 12920, 14221 mm
Anode-cathode gap (equal to wire pitch)	2.1 mm for st. 1; 2.5 mm for st. 2-5
Gas mixture	80%Ar/20%CO_2
Pad size st. 1 (bending plane)	4.2×6.3, 4.2×12.6, 4.2×25.2 mm^2
Pad size st. 2 (bending plane)	5×7.5, 5×15, 5×30 mm^2
Pad size st. 3, 4 and 5 (bending plane)	5×25, 5×50, 5×100 mm^2
Max. hit dens. st. 1-5 (central Pb-Pb $\times$ 2)	5.0, 2.1, 0.7, 0.5, $0.6 \cdot 10^{-2}$ hits/cm^2
Spatial resolution (bending plane)	$\simeq 70\ \mu$m
Trigger Chambers	
No. of stations, no. of planes per station	2, 2
Longitudinal position of stations	-z = 16120, 17120 mm
Total no. of RPCs, total active surface	72, $\sim$140 m^2
Gas gap	single, 2 mm
Electrode material and resistivity	Bakelite^{TM}, ϱ=2-8 $\times 10^9$ Ω cm
Gas mixture	Ar/$C_2H_2F_4$/i-buthane/SF_6 (50.5/41.3/7.2/1)
Pitch of readout strips (bending plane)	10.6, 21.2, 42.5 mm (for trigger st. 1)
Max. strip occupancy bend. (non bend.) plane	3% (10%) in central Pb-Pb
Maximum hit rate on RPCs	3 (40) Hz/cm^2 in Pb-Pb (Ar-Ar)
Trigger Electronics	
Total no. of FEE channels	2.1×10^4
No. of local trigger cards	234 + 8

Table 3.3: Summary of the main characteristics of the muon spectrometer. [131].

3.5.1 The absorbers

The main goal of the absorbers in the muon spectrometer is to protect it from the high background produced in the central Pb-Pb collisions. Four absorbers are used for this purpose: the front absorber, the beam shield, the iron wall and the rear absorber.

3.5.1.1 Front absorber

The geometry of the front absorber is shown in Figure 3.6. The front absorber is 4 m long, corresponding to about 10 interaction length (λ_{int}) and weights 37 tons. The absorber is located at 90 cm from the interaction point inside the L3 magnet. The absorber is mainly made of carbon, concrete, steel and consists of a central cone within the acceptance of the spectrometer, an outer shield to protect the central detectors of ALICE and an inner shield at polar angles smaller than 2° to absorb particles emanating from the beam-pipe. It has two main functions:

- a significant reduction of the forward flux of charged particles and of background of muons from pions and kaons decay by limiting the free path of primary pions and kaons via minimizing the distance between the absorber and the interaction point and by using materials with low nuclear interaction length. The external part of the absorber is made of lead and tungsten to protect the detectors from the particle flux emanated by particles crossing the absorber.

- limitation of the multiple scattering which could affect the mass resolution of the spectrometer by using materials with high radiation length in the absorber layer close to the interaction point and with high atomic number at the rear end. The central part, near the interaction point, is made of graphite (a low Z material) to reduce muon multiple scattering effects. The rear region is made of concrete + steel in $2.5 < \eta < 3.6$ and concrete + tunsten in $3.6 < \eta < 4.0$ to absorb the secondary particles generated in the absorber, low energy neutrons and protons. The lead layer wrapping the whole absorber is designed to avoid the particles back-scattering into the TPC.

3.5.1.2 Beam shield

The low angle absorber (Figure 3.7) is designed to minimize the high background produced by the interactions with the beam pipe of particles (mainly pions and kaons) emitted at small angles ($\theta < 2°$). This shield, made of tungsten and lead is covered by a stainless steel layer. [158]

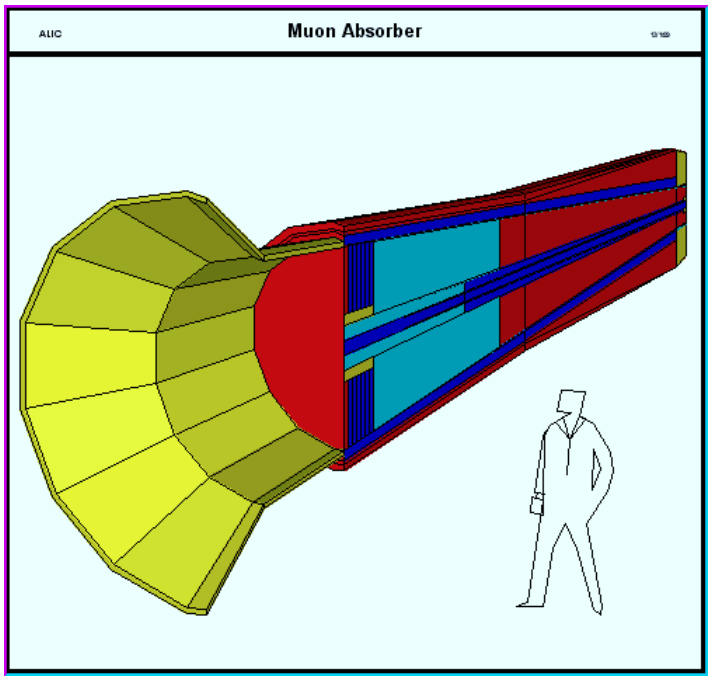

Figure 3.6: The geometry of the front absorber.

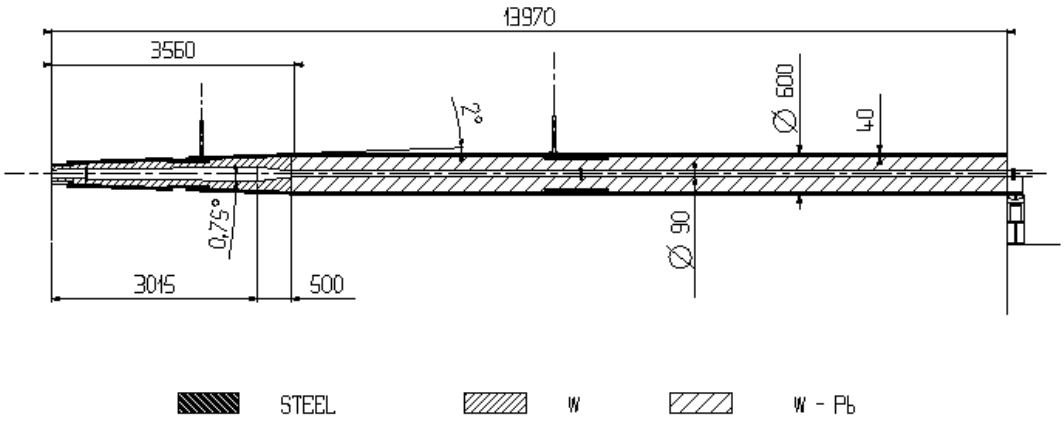

Figure 3.7: The design of the beam shield. [159].

3.5.1.3 Iron wall

The iron wall is installed between the last tracking station and the first trigger chamber. It stops hadrons and secondary particles that punch through the absorber. Since the wall is located downstream the tracking stations, it does not affect the mass resolution of the detector. The front absorber and the iron wall introduce a cut on the momentum of about 4 GeV/c for the muons.

3.5.1.4 Rear absorber

The trigger chamber must be protected from the background generated by the accelerator (beam-gas residual interaction). This background is proportional to the luminosity of the beam and, therefore, is very high during the pp collisions data taking period. The rear absorber has recently been extended to fully cover the tunnel aperture.

3.5.2 The dipole magnet

The dipole magnet (Figure 3.8) is located at 7 m from the interaction point and has 5 m of length and 900 tons of weight. It consists of resistive coils in a horseshoe shape and has an angular acceptance of $171^{\circ} < \theta < 178^{\circ}$. The warm dipole magnet generates a maximum central field of 0.67 T and an integral field of 3 Tm. The direction of the magnetic field generated by the dipole magnet lies in the horizontal plane, perpendicular to the beam pipe line, defining a bending plane (yz plane) and a non bending plane (xz plane). The polarity of the magnet can be reverted within a short time.

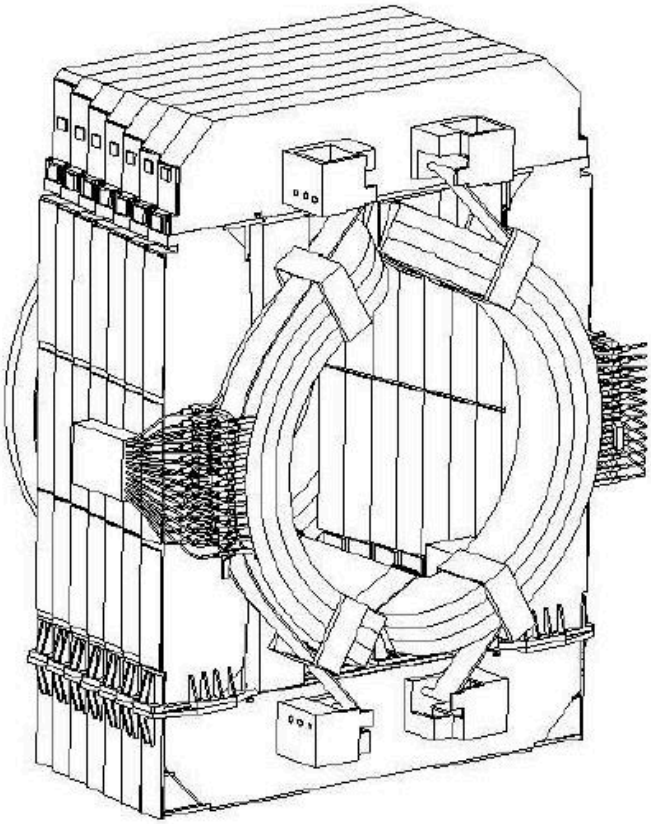

Figure 3.8: The layout of the dipole magnet.

3.5.3 The tracking chambers

The tracking system of the muon spectrometer covers a total area of about 100 m² and is composed of five stations, each consisting of two planes of Cathode Pad Chambers (CPC, Figure 3.9). Each chamber is read out by two cathode planes in two orthogonal projections (x-y) to provide two-dimensional hit information. The two stations before and after the dipole magnet measure the corresponding track angles and the station located inside the magnet adds sagitta information. The reconstruction algorithm requires hits in at least 1 chamber out of 2 in the first three stations and of at least 3 chambers out of 4 in stations 4 and 5. This means that, in principle it can lose up to 4 detection planes without losing efficiency. The chambers are arranged in a projective geometry from 2.5 to 20 m² and are slightly larger than the acceptance of the spectrometer to account for bending in the magnetic field. The main constraints to the performance of the tracking system are the following:

- a spatial resolution better than 100 μm in order to disentangle the Υ mass with a mass resolution of 100 MeV, and to operate in a maximum hit density of about 5×10^{-2} cm^{-2}, the rate expected in central Pb-Pb collisions;
- a resolution along the non-bending plane (parallel to the magnetic field) better than about 2 mm to allow an efficient track finding.

These requirements are fulfilled by employing Multi-Wire Proportional Chambers (MWPC) with cathode pad readout. Each chamber in all five tracking stations consists of a central anode plane with wires equally spaced parallel to the y axis and sandwiched between two cathode planes. The wires have a high voltage of ~1600 V, while the cathode planes are grounded. It allows to generate an electric field with its maximum value at the wire surface, decreasing as 1/r near the wires. The segmentation of the cathode pads was designed to keep the occupancy at a 5% level: the size of the pads increases with the radius since the hit density decreases with the distance from the beam pipe. In total there are 1.1×10^{6} channels.

The chamber thickness is limited to $0.03X_{0}$ in order to minimize multiple scattering of the muons in the chamber by using composite material, such as carbon fibres. The individual chambers were designed based on standard MWPC technology taking into account the particular constraints on the different tracking stations. The first two tracking stations are based on a quadrant structure with the readout electronics distributed on their surface, while the others have a slat architecture. A layout of the cathode plane for a quadrant of the Station 1 is shown in Figure 3.10

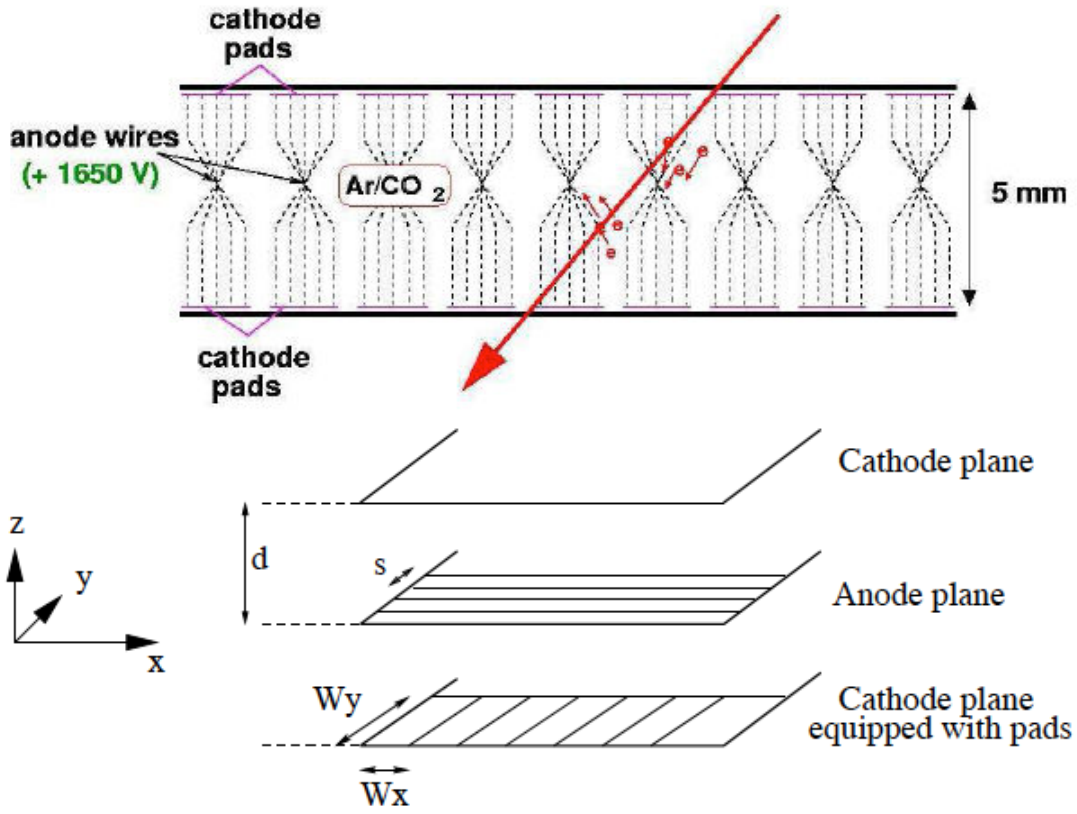

Figure 3.9: Cathode Pad Chamber layout [30, 160]. The cathode chamber of Stations 2 is narrower, 4 mm instead of 5 mm. In addition both cathodes are segmented and equipped of electronic to get x and y position of the track. In the case of Station 1 the segmentation is the same in both cathodes.

(a). Figure 3.10 (b) shows a photography of the Station 1. Figures 3.10 (c) and (d) show the same for the stations with a slat architecture. Within a tracker chamber the quadrants (or slats) overlap to avoid dead zones, i.e. zones without active detection area.

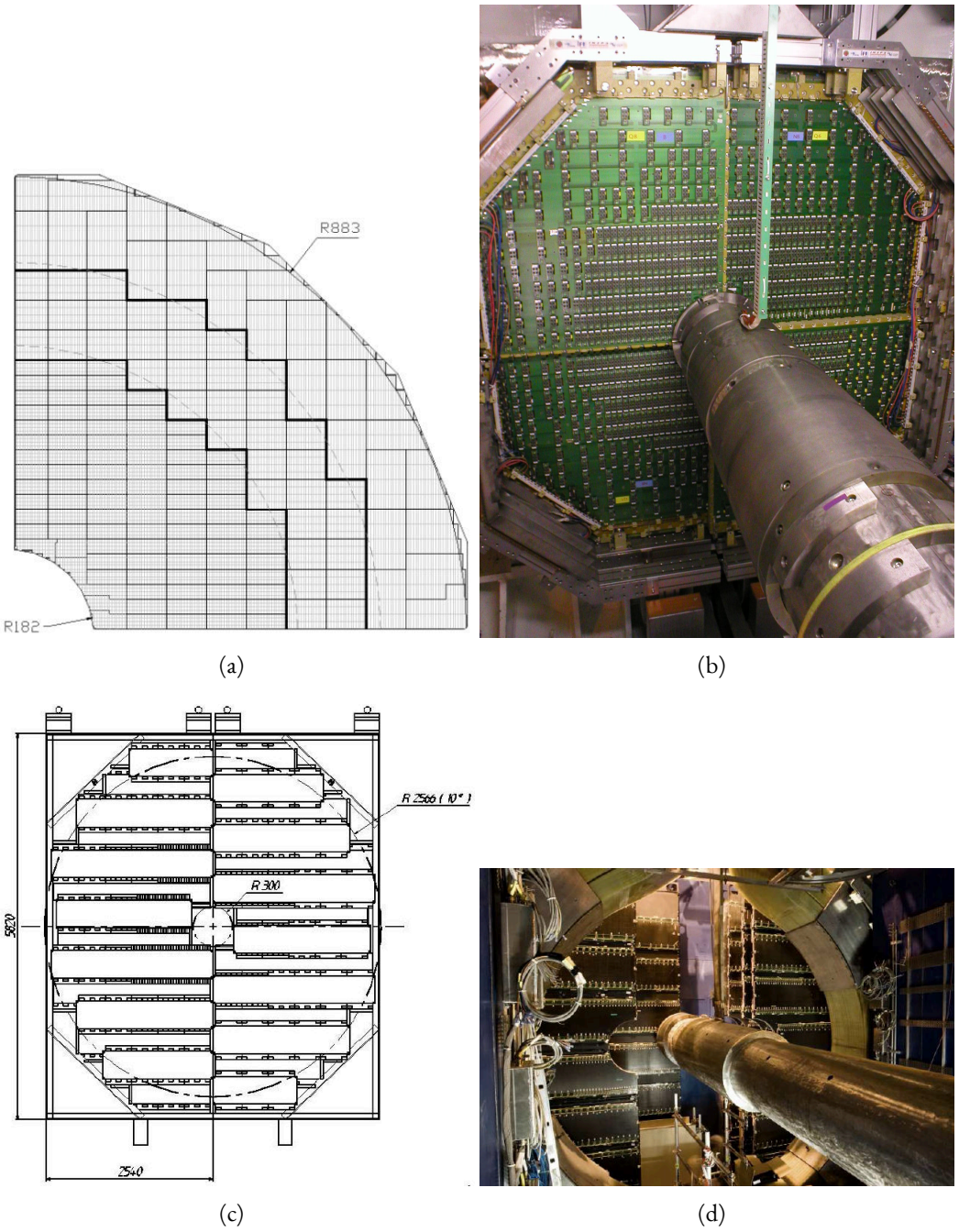

Figure 3.10: (a): the cathode plane layout of a quadrant of the Station 1. [160] (b): one chamber of the Station 1. [161] (c): segmentation of a station with a slat architecture. [160] (d): an overview of a station with a slat architecture. [131].

For all the stations the front-end electronics (FEE) are based on a 16-channel chip called MANAS (Multiplexed ANAlogic Signal processor) including the functionality of charge amplifier, filter, shaper and track and hold. The signal digitization is performed on board. The channels of four of these chips are fed into a 12-bits ADC, read out by the Muon Arm Readout Chip (MARC), whose functionalities include zero suppression. The entire chain is mounted on a front-end board, the MAnas NUmerical (MANU): the 1.08 million channels of the tracking system are treated by about 17000 MANU cards.

The Protocol for the ALICE Tracking CHamber (PATCH) buses provides the connection between the MANUs and the Cluster ReadOut Concentrator Unit System (CROCUS) crate. Each chamber is readout by two CROCUS, which concentrate and format the data, transfer them to the DAQ and dispatch the trigger signals, coming from the Central Trigger Processor (CTP). These crates allow also the control of the FEE and of the calibration processes.

The tracking capability of the chambers depends strongly on the precision of their position knowledge. The measurement of the deformations and of the relative displacements of the rigid modules (the frames and the intermediate supports) of the tracking system is carried out by the Geometry Monitoring System (GMS) and used to correct the track coordinates in the offline analysis. The GMS evaluates the in-plane deformations and the displacements of stations 1 and 2, and the displacements of stations 3, 4 and 5 (the carbon fiber material of these stations frames result on a very weak thermal expansion).

3.5.3.1 Alignment of tracking chambers

The alignment of the tracking chambers is a crucial step in the analysis of muons at high transverse momentum. It is ensured by a method using the information of straight tracks from dedicated runs with the magnetic field switched off, as well as standard runs with the magnetic field on. In particular, the mean residual distance between the reconstructed track extrapolation and the measured track impact (hit) is used to correct the alignment parameters of the current detection element. However, the precision of the method is biased by the ignorance on the initial parameters of the track. The bias can be reduced with an iterative approach, but can not be completely avoided. The absolute position of the chambers was measured before data taking with photogrammetry. Their relative position is estimated with a precision of about 100 mm, using a modified version of the MILLIPEDE [162] package, which combines data taken with and without the magnetic field. The residual misalignment of the tracking chambers is taken into account

in the simulations to estimate the acceptance and efficiency (Acc.×Eff.) of the detector. In particular, one residual alignment file was available until January 2014. However, the MC production obtained with this alignment file ("alignment_5") was found to provide a better resolution on the Υ mass peak than the one observed on data. Hence, another set of residual alignment file was produced, with the aim to degrade the mass resolution to the one observed in data. This new set is called "alignment_6" in the following and shows indeed results which are more different from the other considered alignments. While the method provides the most accurate estimation of the relative chamber position, it is not sensitive to a global misalignment of the entire spectrometer.

A data-driven method (called as "resolution task" in the following) was hence developed, in which the simulation of the tracker response is based on a parameterisation of the measured resolution of the clusters associated to a track. The distribution of the difference between the cluster and the reconstructed track positions on each chamber is parameterised with a Gaussian function and utilised to simulate the smearing of the track parameters. The effect of a global misalignment of the muon spectrometer is mimicked by shifting the distribution of the track deviation in the magnetic field in opposite directions for positive and negative tracks. This shift is tuned so as to reproduce the observed difference in the ratio of the p_{T} distributions of positive and negative tracks, corrected for acceptance and efficiency, in two periods of data taking differing only by the magnetic field polarity. The values of the Acc.×Eff. corrections are obtained using either the standard simulations with the residual misalignment, or the data-driven simulations. It is worth noting that the limited momentum resolution of the detector can also result in positive muons wrongly reconstructed as negative muons and viceversa. The resulting loss of efficiency is small (smaller than 1% for muons with $p_{\mathrm{T}} > 10$ GeV/c) and taken into account in the simulations.

3.5.4 The trigger chambers

The muon trigger system (Figure 3.11) consists of two stations (Figure 3.12), with two planes of 18 single-gap Resistive Plate Chambers (RPC) each (Figure 3.13). They are located at 16 m (MT1) and 17 m (MT2) from the interaction point behind the iron muon filter. The size of each plane is 6×6 m^2 and the distance between the two stations is 1 m.

Each RPC is made of two low-resistive bakelite electrodes, separated by a 2 mm gas gap, two graphite films under high voltage and readout strip planes in the x and y direction. The chamber response is fast with a signal rise time of approximately 2 ns and a time resolution of the order of 1-2 ns. The signal is picked up by read-out strips connected with the Front-End Electronics

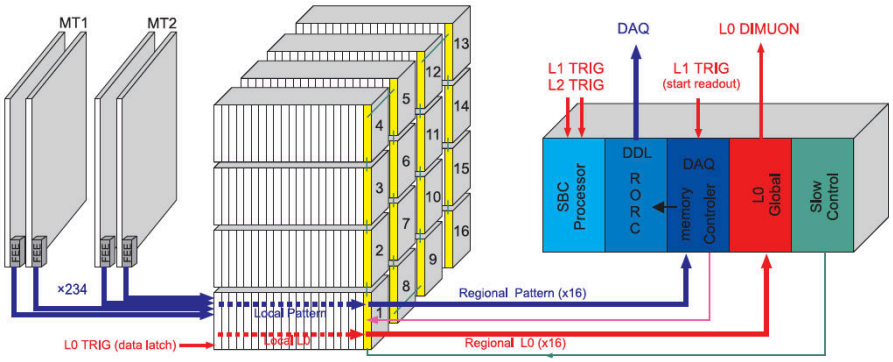

Figure 3.11: Overview of the trigger system. [160].

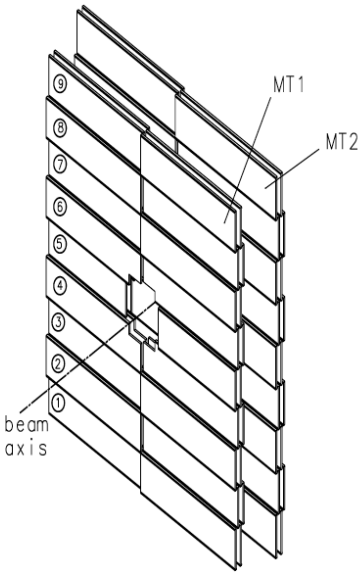

Figure 3.12: Structure of the trigger detector. [160].

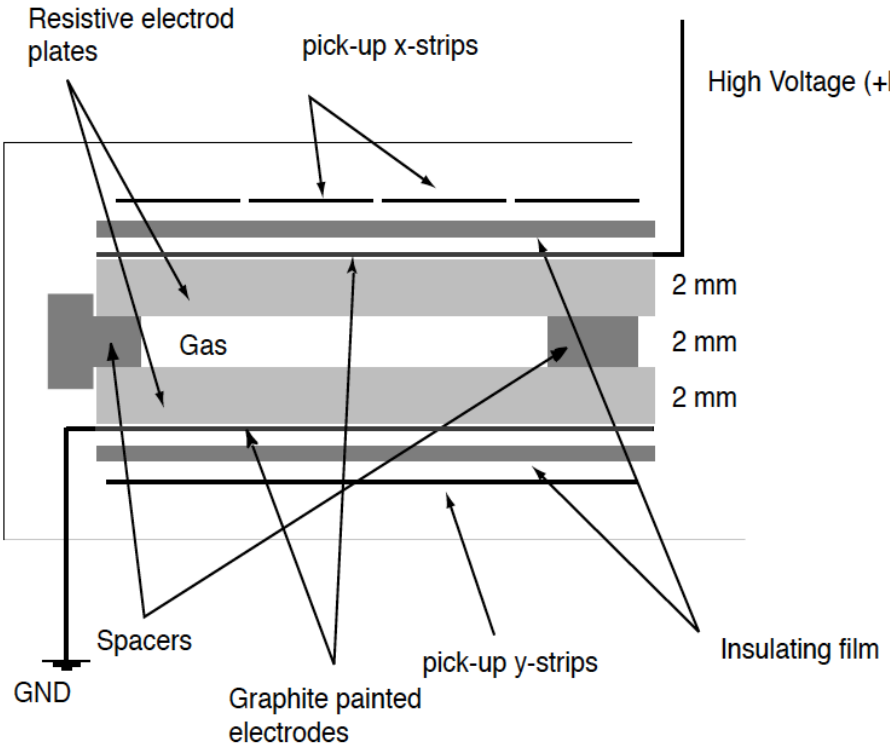

Figure 3.13: Schematic view of an RPC equipped with readout strips. [160].

(FEE), which basically consists of a leading-edge discriminator stage followed by a shaper. The strips are placed on both sides, orthogonally to each others, in order to provide a bi-dimensional information. The horizontal strips measure the bending deviation due to the dipole magnetic field, while vertical strips measure the non-bending direction. The two layers of read-out pads are therefore called "bending" and "non-bending" plane respectively.

The signals coming from the FEE, consisting in the x and y fired strip patterns of the four detection planes, are sent to the local trigger electronics. The whole system is divided into 234 detection areas, each of them associated with a local trigger board. Figure 3.14 presents a schematic view of the local board position in one plane of trigger chambers as seen from the interaction point. The local board density reflects the strip segmentation which is finer in the region close to the beam pipe, where a higher particle multiplicity is expected: in particular, moving from the beam pipe outwards, the strip pitch is about 1, 2 and 4 cm in the bending plane and about 2 and 4 cm in the non-bending plane. [163]

The trigger system is designed to provide muon identification and to trigger single or di-muon tracks above a p_{T} threshold. The track parameters are roughly estimated from the impact point of the track in the two trigger stations, assuming that the track comes from the interaction

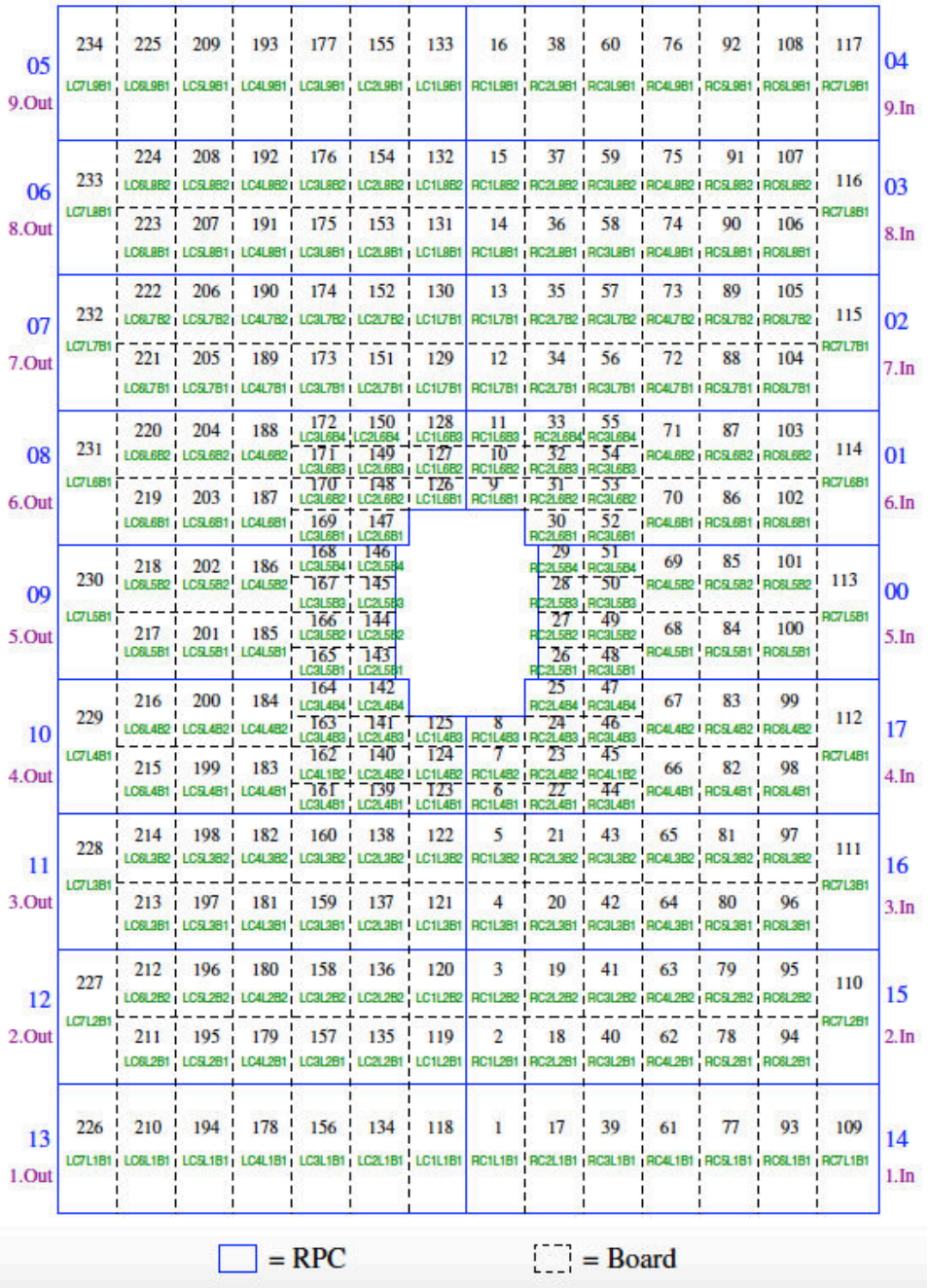

Figure 3.14: View of one of the trigger chambers (looking from the interaction point) showing the 18 RPCs and the 234 trigger boards. The board enumeration, both in labels and numbers (more suitable for interfacing with the analysis software) is also shown. [163].

vertex. The size of the deviation with respect to an infinite momentum track provides information on the track p_T while its direction provides information on the charge of the particle. This allows to provide a like and unlike sign di-muon trigger signal. The trigger system can therefore provide up to six trigger types:

- Muon single low p_T (MSL): at least one single muon above low p_T threshold
- Muon single high p_T (MSH): at least one single muon above high p_T threshold
- Unlike-sign dimuon low p_T (MUL): at least two muons with opposite sign, each of them above low p_T threshold
- Unlike-sign dimuon high p_T (MUH): at least two muons with opposite sign, each of them above high p_T threshold
- Like-sign dimuon low p_T (MLL): at least two muons with same sign, each of them above low p_T threshold
- Like-sign dimuon high p_T (MLH): at least two muons with same deviation sign, each of them above high p_T threshold

The Central Trigger Processor can be configured to read at most 5 of the six signals that the muon trigger system can dispatch. For the study of W boson production an MSH trigger with a threshold of about 4.2 GeV/c was used.

Anyone who has never made a mistake has never tried anything new.

Albert Einstein

4

Data taking in ALICE

ALICE takes data in Pb-Pb collisions as well as in pp and p-Pb collisions, in order to provide a reference and a cold nuclear matter baseline. Table 1 presents a summary of the different running conditions experienced so far. The question you may ask is how does ALICE take and deal with these data. The process is mainly comprised of the online control system, which implements selections in a form of triggers, and the offline system, which performs event reconstruction and enables data analysis offline. During the data taking period, the Trigger System (TRG) receives information of interaction and then transfers to the Data AcQuisition (DAQ). Meanwhile, the High Level Trigger (HLT) is used to select the most relevant data from the large input stream and to reduce the data volume by well over an order of magnitude in order to fit the available storage bandwidth while retaining the interesting physics information. The scheme of the raw data flow from online to offline system interfaced by the DAQ system is shown in Figure 4.1. In this chapter, further details about online and offline system will be provided. After that, i will discuss the selection of good runs for MUON analysis.

4.1 ALICE online control system

The ALICE online control systems, namely, the DCS, the DAQ, the TRG and the HLT interface to each other through a controls layer: the so-called Experiment Control System (ECS),

2010	Low luminosity pp and Pb-Pb collisions Data taking and monitoring for the fine tuning of the system
2011	pp mainly @ $\sqrt{s}$=7 TeV and some fills @ $\sqrt{s}$=2.76 TeV. $L_{MAX}=2\times10^{30}$ cm^{-2}s^{-1} Pb-Pb @ $\sqrt{s_{NN}}$=2.76 TeV. $L_{MAX}=5\times10^{26}$ cm^{-2}s^{-1}
2012	pp @ $\sqrt{s}$=8 TeV. $L_{MAX}=7\times10^{30}$ cm^{-2}s^{-1}
2013	p-Pb and Pb-p @ $\sqrt{s_{NN}}$=5.02 TeV. $L_{MAX}=10^{29}$ cm^{-2}s^{-1} pp @ $\sqrt{s}$=2.76 TeV. $L_{MAX}=4\times10^{30}$ cm^{-2}s^{-1}
2015	pp @ $\sqrt{s}$=13 TeV. $L_{MAX}=5\times10^{30}$ cm^{-2}s^{-1} pp @ $\sqrt{s}$=5 TeV. $L_{MAX}=2\times10^{30}$ cm^{-2}s^{-1} Pb-Pb @ $\sqrt{s}$=5 TeV. $L_{MAX}=10^{27}$ cm^{-2}s^{-1}

Table 4.1: Summary of the ALICE running conditions in 2010-2015. [164].

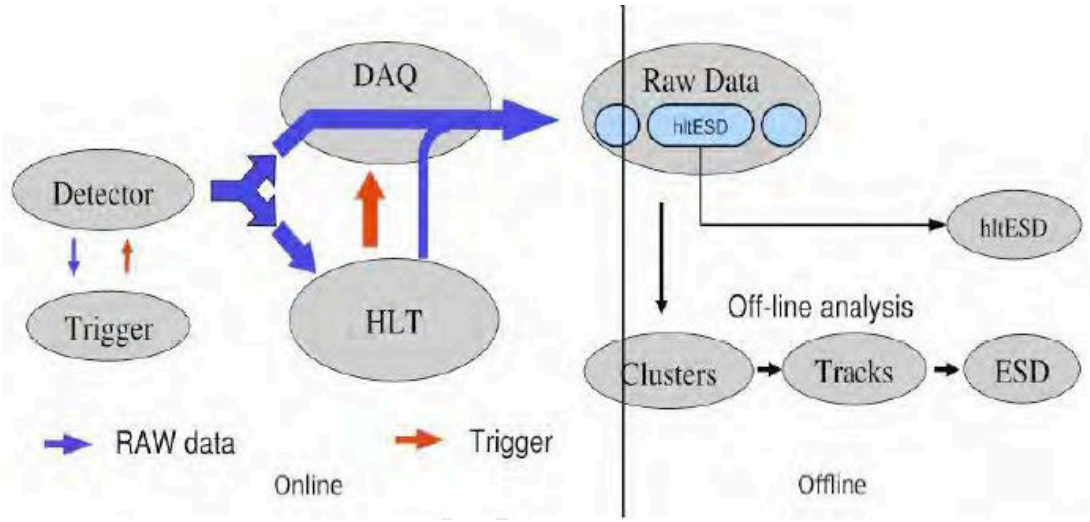

Figure 4.1: The scheme of raw data flow from online to offline.

as shown in Figure 4.2.

4.1.1 Trigger (TRG) system

The ALICE Central Trigger Processor (CTP) [165, 166, 167] is designed to select events having different features at rates which can be scaled down to suit physics requirements and the restrictions due to the bandwidth of the DAQ and HLT system. The challenge for the ALICE trigger is to make optimum use of the component detectors, which are busy for widely different periods following a valid trigger, and to perform trigger selections in a way which is optimised for several different running modes: Pb–Pb, p–Pb and pp, varying by almost two orders of magnitude in counting rate. [131]

The triggers in ALICE are based on the following operational principle: a number of detector

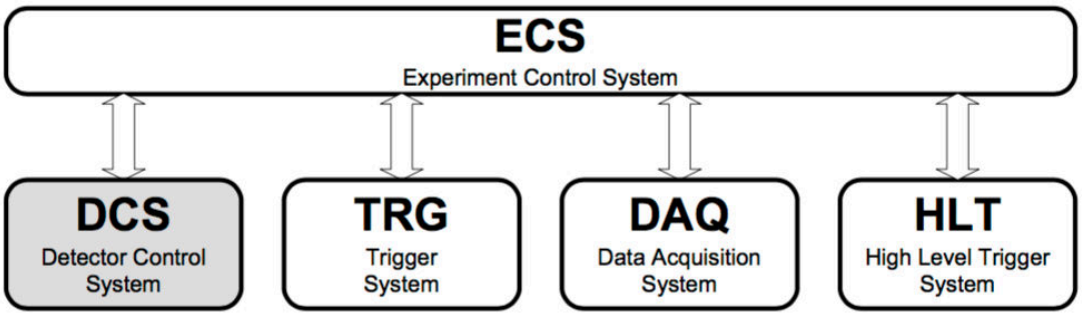

Figure 4.2: The ALICE online control systems. [165].

systems (currently V0, T0, PHOS, TRD, MUON spectrometer, etc.) each provide a number of logic trigger signals which characterize a specific measurement in this particular detector (e.g. multiplicity, high-p_T, muon pair). These logical signals are sent to the CTP as trigger inputs. There they are combined by logical operations inside a Field-Programmable Gate Array (FPGA) to form the different physics triggers (e.g. minimum-bias or central collision, single muon high-p_T event). The CTP in addition takes care of downscaling, pile-up protection, ready status of different detectors and read-out memories, trigger priority, and finally synchronization with the LHC clock cycle, as distributed by the RD12 Trigger Timing and Control (TTC) system [168, 169].

Another particular feature of the ALICE trigger is the possibility to dynamically configure groups of detectors that participate in the readout of any given event. For instance, the TPC is constrained to relatively low trigger rates, because of drift time and data volume, while the MUON spectrometer can record events at a much higher rate. Where it makes sense to do so in order to improve statistics for specific physics channels, groups of detectors, called trigger clusters, are read out separately and at higher rate. The output trigger signal is sent to the Local Trigger Units (LTUs) of each sub-detector to be further processed and finally sent back to the detector Front-End Electronics (FEE). The trigger is divided into three levels (L0, L1 and L2) to take care of different process time of sub-detectors. The faster trigger signal L0 is sent by faster detectors (V0, T0, SPD and MUON trigger) to the CTP within 1.2 μs, the L1 trigger signal is sent within 6.5 μs and the slower L2 trigger signal waits for the end of the past-future protection interval (88 ms) to verify that the event can be taken.

4.1.2 Data AcQuisition (DAQ) system

The function of the DAQ system is to realize the data flow from the detector up to the data storage, including the data flow to and from the HLT farm as well as sub-event and complete event building. The DAQ system also includes software packages for raw data integrity and system performance monitoring and overall control of the DAQ system. [165] The architecture of the DAQ is shown in Figure 4.3. The detectors receive the trigger signals and the associated information from the CTP, through a dedicated LTU interfaced to a TTC system. The Front-End Read-Out (FERO) electronics of the detectors are interfaced to the ALICE-standard Detector Data Links (DDL). Event fragments produced by the detectors are injected on the DDLs using the same standard protocol. Using the DDL by all the detectors is one of the major features of the ALICE DAQ.

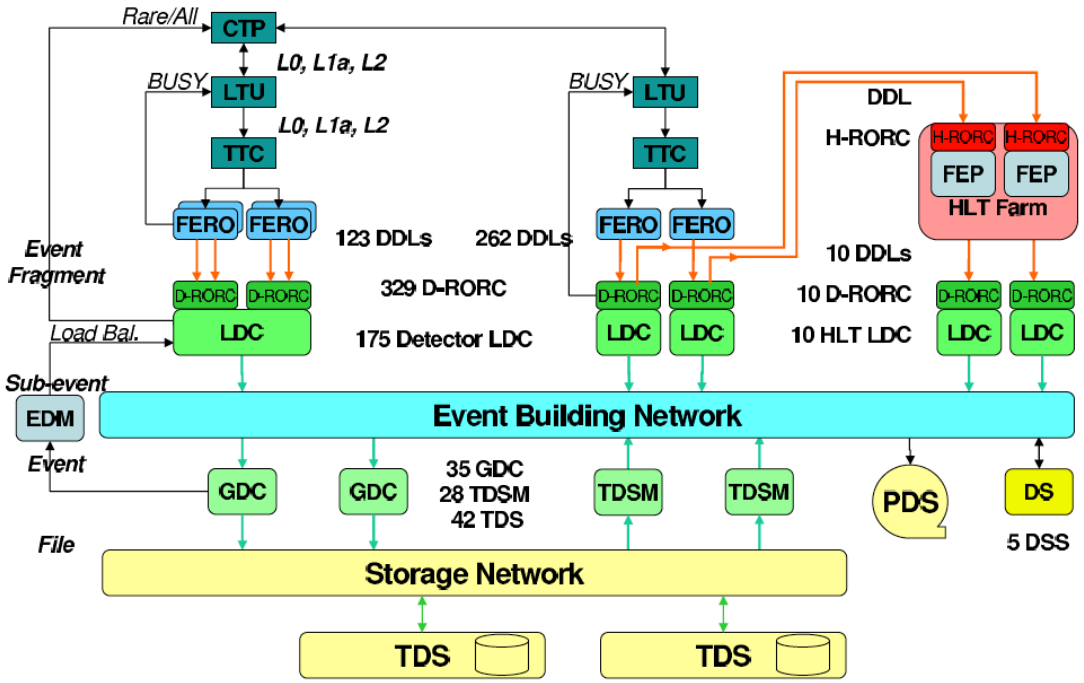

Figure 4.3: The overall architecture of the ALICE DAQ and the interface to the HLT system. [131].

At the receiving side of the DDLs there are PCI-X based electronic modules, called "DAQ Readout Receiver Card" (D-RORC). They are hosted by the front-end machines (commodity PCs), called Local Data Concentrators (LDCs). In the LDCs the event fragments originated by the different D-RORCs are logically assembled into sub-events. The role of the LDCs is to ship the sub-events to a farm of machines (also commodity PCs) called Global Data Collectors (GDCs), where the whole events are built and shipped to the Transient Data Storage (TDS). The

data files on the TDS are migrated to the Permanent Data Storage (PDS) at the computing centre by the TDS Managers (TDSM).

The Data Acquisition and Test Environment (DATE) [170] is the DAQ software framework. It controls and synchronises the processes running in the LDCs and the GDCs. The monitoring programs receive data from the LDC or GDC streams. They can be executed on any LDC, GDC or any other machine accessible via the network. The fundamental requirement for a detailed, real-time assessment of the DAQ machines (LDCs and GDCs), for the usage of the systems resources, and for the DATE performance is addressed by the AFFAIR package, which gathers performance metrics from the LDCs and GDCs and performs the centralised handling of them [165]. The Data Quality Monitoring includes also online monitoring using Monitoring Of Online Data (MOOD) and environment monitoring using Automatic MOnitoRing Environment (AMORE), which are used to handle the detector status, online and offline data stream, etc. These programs monitor the physics data during physics run and accumulate plots that can be inspected to check the DAQ performance.

4.1.3 High-Level Trigger (HLT)

The High-Level Trigger combines and processes the full information from all major detectors of ALICE in a large computer cluster. Its task is to select the relevant part of the huge amount of incoming data and to reduce the data volume by well over one order of magnitude in order to fit the available storage bandwidth while preserving the physics information of interest. This is achieved by a combination of different techniques which require a detailed online event reconstruction:

- trigger: selecting interesting events based on detailed online analysis of its physics observables.
- selection: selecting the Regions of Interests (interesting part of single events).
- compression: reducing the event size by advanced data compression without any loss of the contained physics.

The HLT implements a processing hierarchy as shown in Figure 4.4. The raw data of all detectors are received by 454 Detector Data Links (DDLs) at layer 1. The first processing layer performs basic calibration and extracts hits and clusters (layer 2). The third layer reconstructs the

event for each detector individually. Layer 4 combines the processed and calibrated information of all detectors and reconstructs the whole event. Layer 5 performs the selection of events or regions of interest based on run specific physics selection criteria. The selected data is further handled by complex data compression algorithms. This HLT system will be able to process a data rate of 25 GByte/s online, while the physics content of a large number of events might be small and the DAQ archiving rate is about 1 GByte/s.

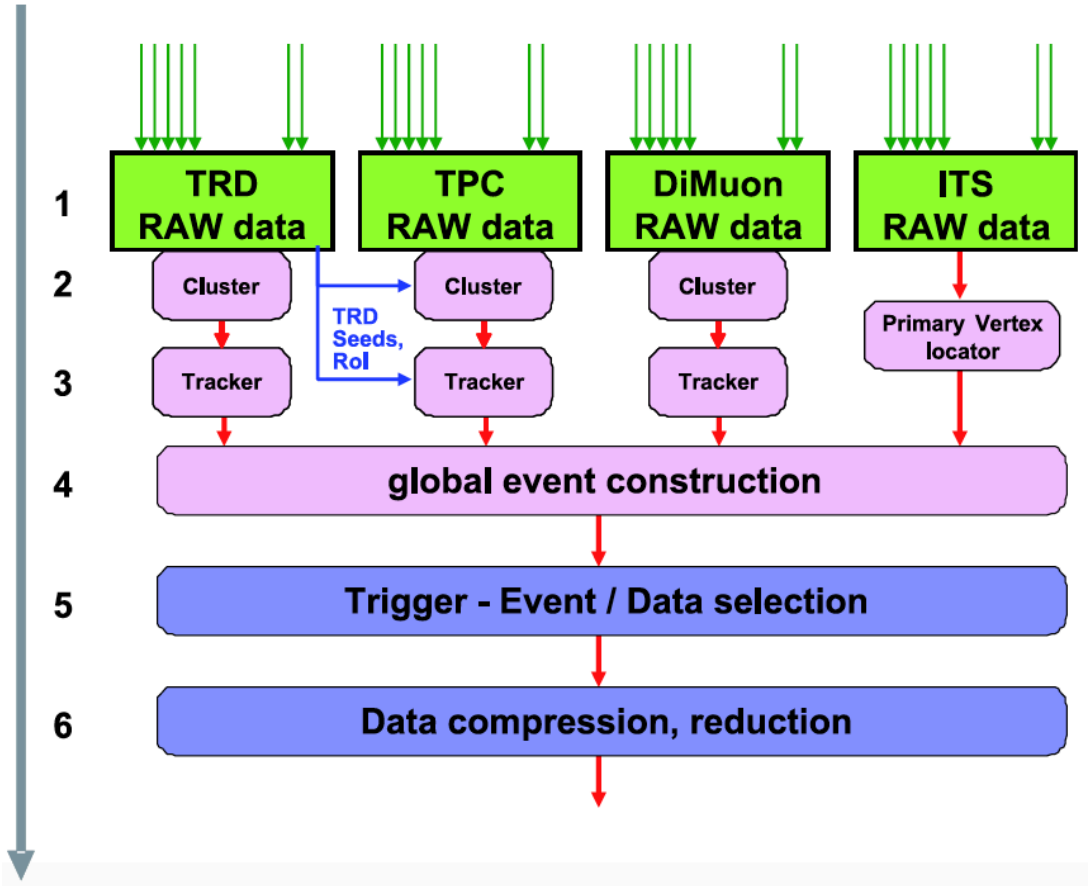

Figure 4.4: The six architectural layers of the HLT. [131].

4.1.4 Detector and experiment control system

The Detector Control System (DCS) is designed to assure a high running efficiency by reducing downtime to a minimum. It provides configuration, remote control, and monitoring of all experimental equipment and maximizes the number of readout channels operational at any time, and measures and stores all parameters necessary for efficient analysis of the physics data.

The control and monitoring is provided in such a way that the whole experiment can be operated from the ALICE Control Room (ACR).

As shown in Figure 4.5 the ALICE control system includes all control activities in the ALICE experiment: the ECS, the DCS and the control of the DAQ, Trigger and HLT. The ALICE control system interfaces through the DCS with the various services (such as electricity, cooling, magnets, etc.) and individual detectors. The Experimental Control System (ECS) is responsible for the synchronization between the various systems. For this it interfaces to the LHC accelerator to obtain operational information and to other systems if needed (such as offline). Many routine operations as well as predefined operation sequences can be programmed in the ECS.

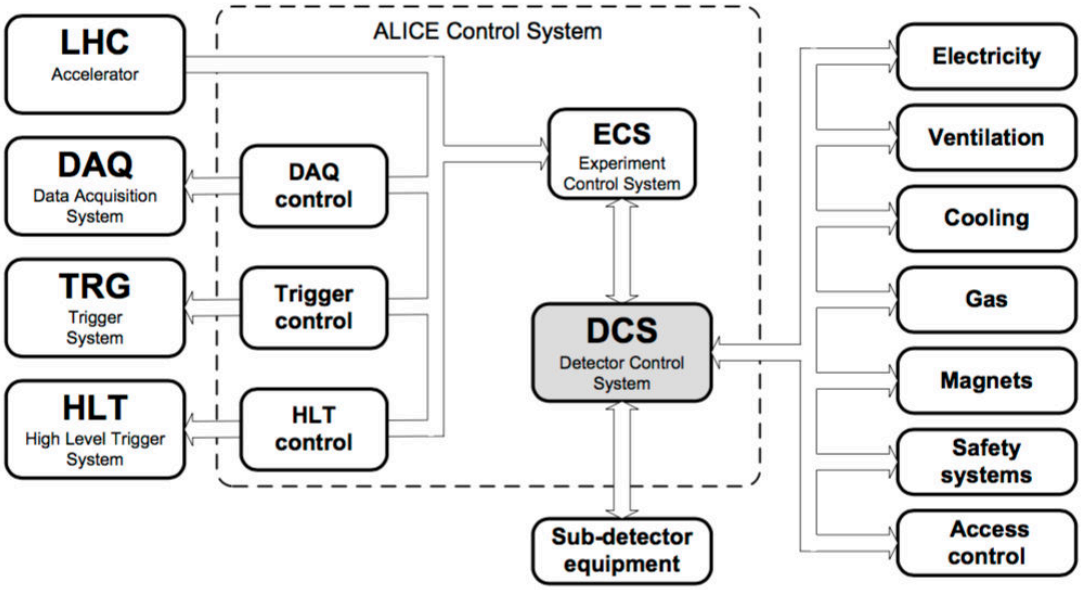

Figure 4.5: The ALICE control system put in context. [165].

The ECS is responsible for the so called "partitioning" of the experiment, whereby a part of the experiment (e.g. a sub-detector) can be operated independently and concurrently from the rest of the experiment. The architecture of the ECS is illustrated in Figure 4.6. The heart of the system is the database, where all the resources are described. The Experiment Control Agent (ECA) is a utility that facilitates the manipulation of the database. Resources are allocated by the Partition Control Agent (PCA), which creates an environment in which only allocated resources are seen by the online systems. The technology of the ECS is based on Finite State Machines (FSMs), which provide an intuitive way of representing the behavioural model of a real object and a natural communication model, based on the control of objects located in remote Activity Domains.

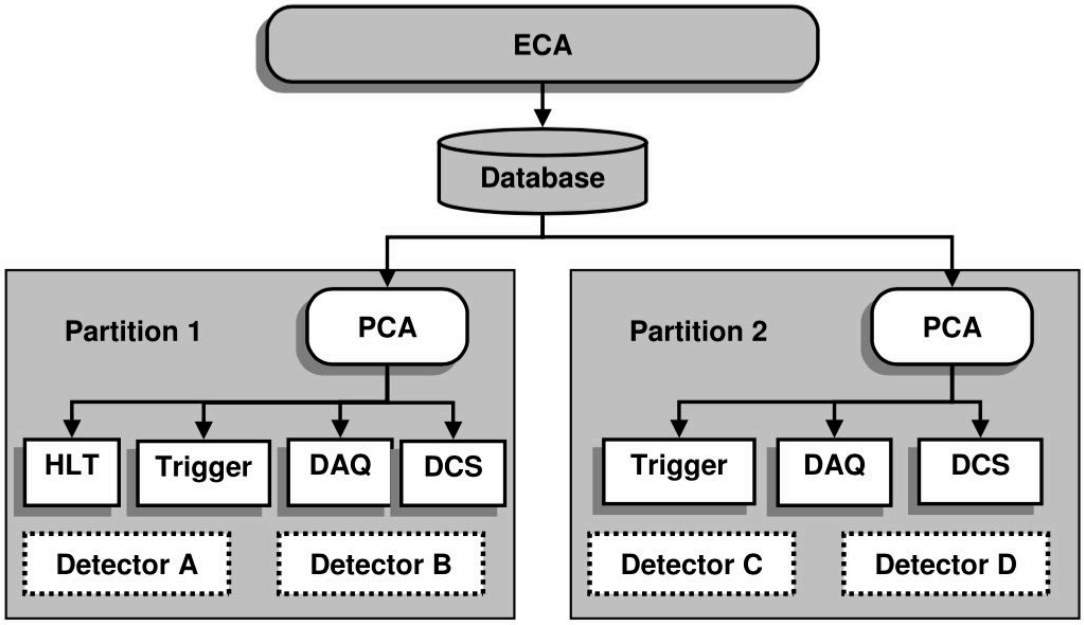

Figure 4.6: ECS architecture. [165].

4.2 ALICE offline framework

The ALICE offline framework, AliRoot [171], whose development started in 1998, is a set of software tools used by the ALICE collaboration to process data. It is based on the Object Oriented technology (C++ [172]) and depends on the ROOT [173] framework, which provides an environment for the development of software packages for event generators, detector simulation, event reconstruction, data acquisition and data analysis (Figure 4.7). The objectives of the AliRoot framework are:

- the simulation of the primary hadronic collisions and the response of the ALICE detectors
- the reconstruction of the physics data from simulated and real interactions
- the analysis of the reconstructed data

The basic principles guided the design of the AliRoot framework are reusability and modularity, which can minimize the amount of unused or rewritten code and maximize the participation of the physicists in the development of the code. A schematic view of the AliRoot framework is shown in Figure 4.8. The main part of the framework is the STEER module, which provides

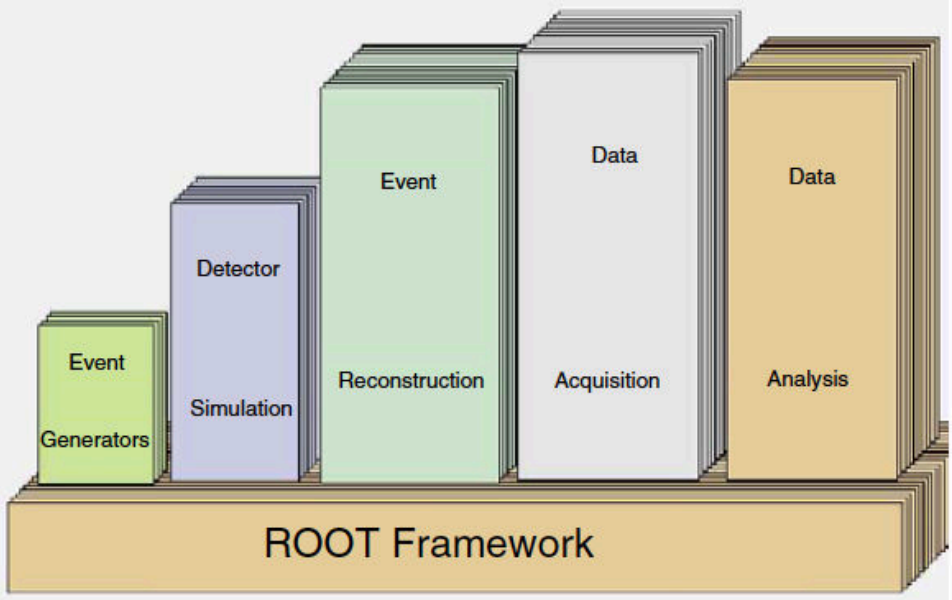

Figure 4.7: The ROOT framework. [141].

steering, run management, interface classes and base classes. The detectors are independent modules which contain the code for simulation and reconstruction while the analysis code is continuously developed and added *. The role of the framework is shown schematically in Figure 4.9. The left and right side represents the simulation and reconstruction stage, respectively.

*Since run 2, the analysis code is moved from AliRoot to AliPhysics.

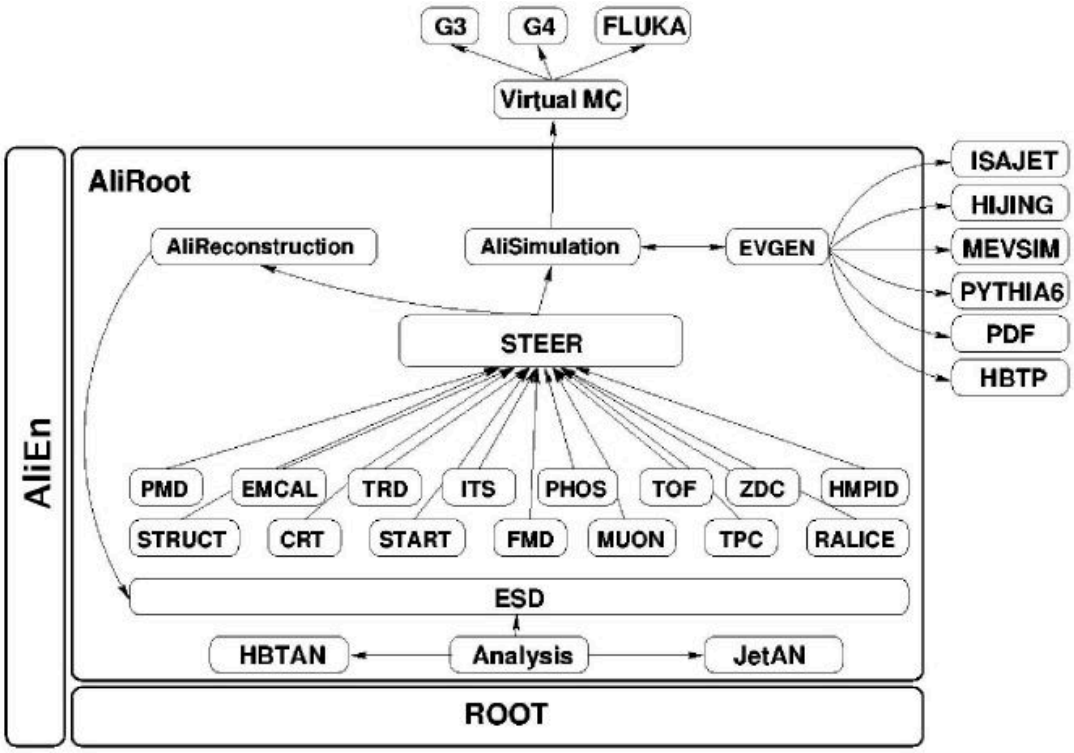

Figure 4.8: Schematic view of the AliRoot framework. [171].

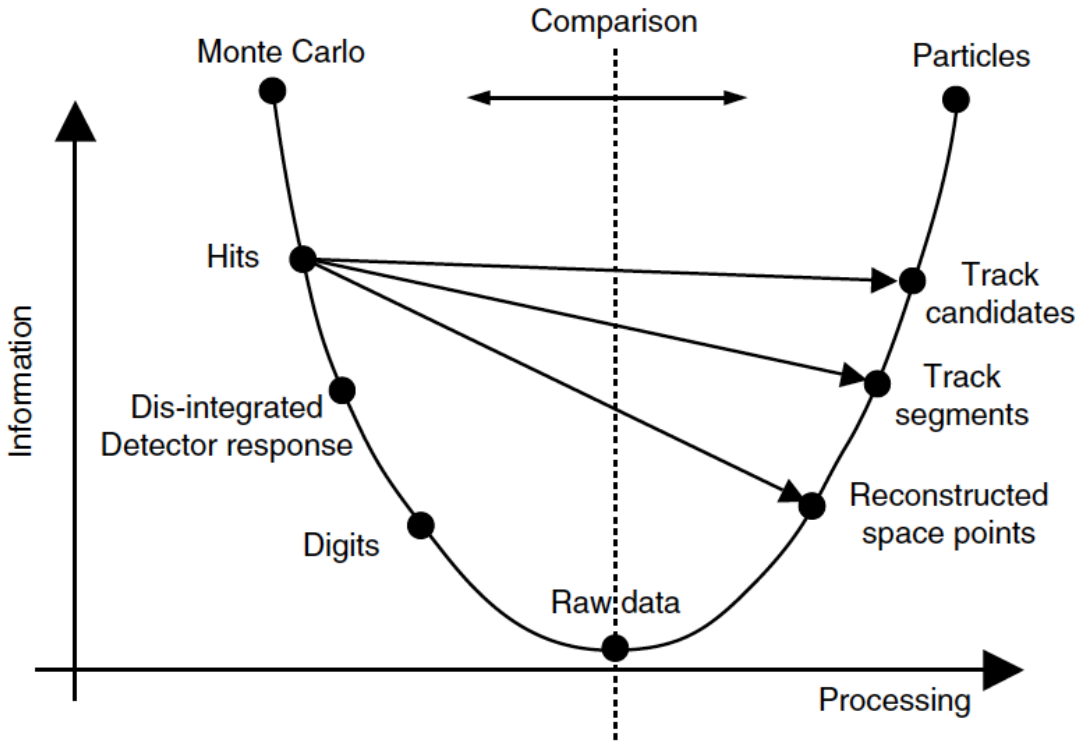

Figure 4.9: Data processing framework. [141].

4.2.1 Simulation

The simulation framework covers the simulation of primary collisions and generation of the emerging particles, the transport of particles through the detector, the simulation of energy depositions (hits) in the detector components, their response in form of so called summable digits, the generation of digits from summable digits with the optional merging of underlying events and the creation of raw data. [174] The hadronic collisions can be simulated with different Monte Carlo event generators, such as PYTHIA [84], POWHEG [86, 87] and HIJING [48], which are interfaced into AliRoot in a transparent way to the users. The simulation of detector response is implemented via switching different transport packages like GEANT3 [175], GEANT4 [176] and FLUKA [177], which are connected to the simulation framework by using the Virtual Monte Carlo (VMC, Figure 4.10), without having to change the code.

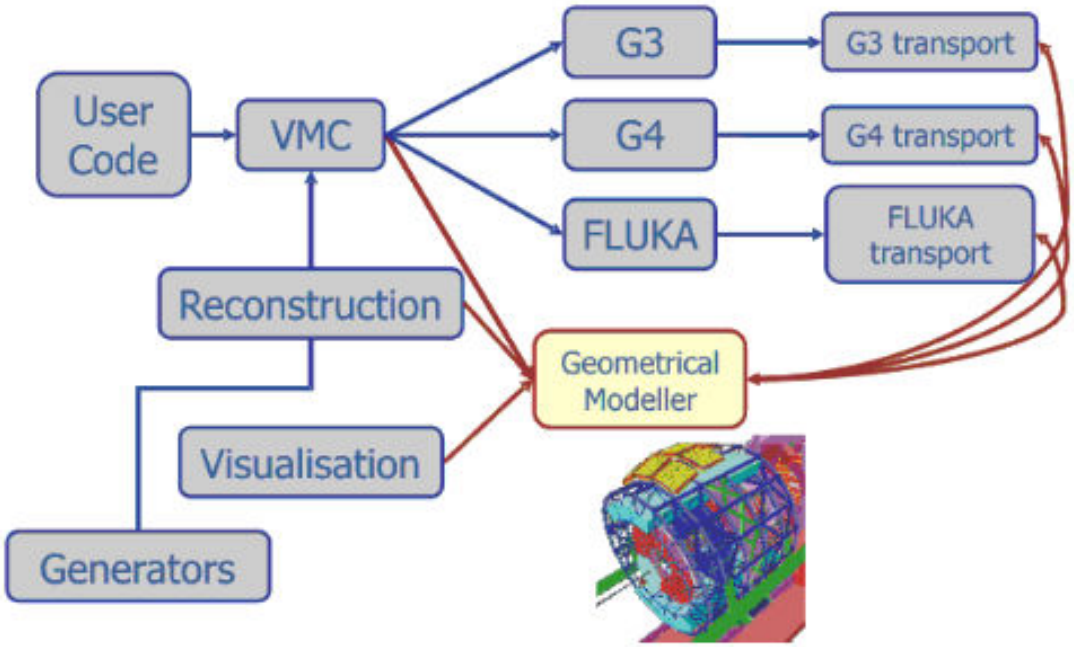

Figure 4.10: The Virtual Monte Carlo. [178].

During the simulation procedure, the primary interactions are simulated by event generators and the resulting kinematic tree, which contains the information of produced particles such as momentum, energy and the decay history (mother-daughters relationship and production vertex), is then used in the transport package. Then each particle is transported into the detectors, where the energy is deposited and causes an hit, which contains also the information ("track label") on the particle that generated it.

At the next step, the detector response is taken into account and the hits are broken down into digits. The information about the parent track is lost and the spatial position is translated into the corresponding detector readout element (e.g. strips, pads, etc.). There are two types of digits: "summable digits", where low thresholds are used and the result is additive, and "digits", where the real thresholds are used and the result is similar to what one would get in the real data taking. In some sense the "summable digits" are precursors of the "digits". The "summable digits" are used for event merging, where a signal event is embedded in a signal-free underlying event. This technique is widely used in heavy-ion physics and allows reusing the underlying events in order to economize computing resources. The "digits" stored in ROOT classes, which still include the information about the Monte Carlo particle that generated it, are eventually converted in raw-data, which are stored in binary format as "payload" in a ROOT structure. The simulation process is highlighted in Figure 4.11.

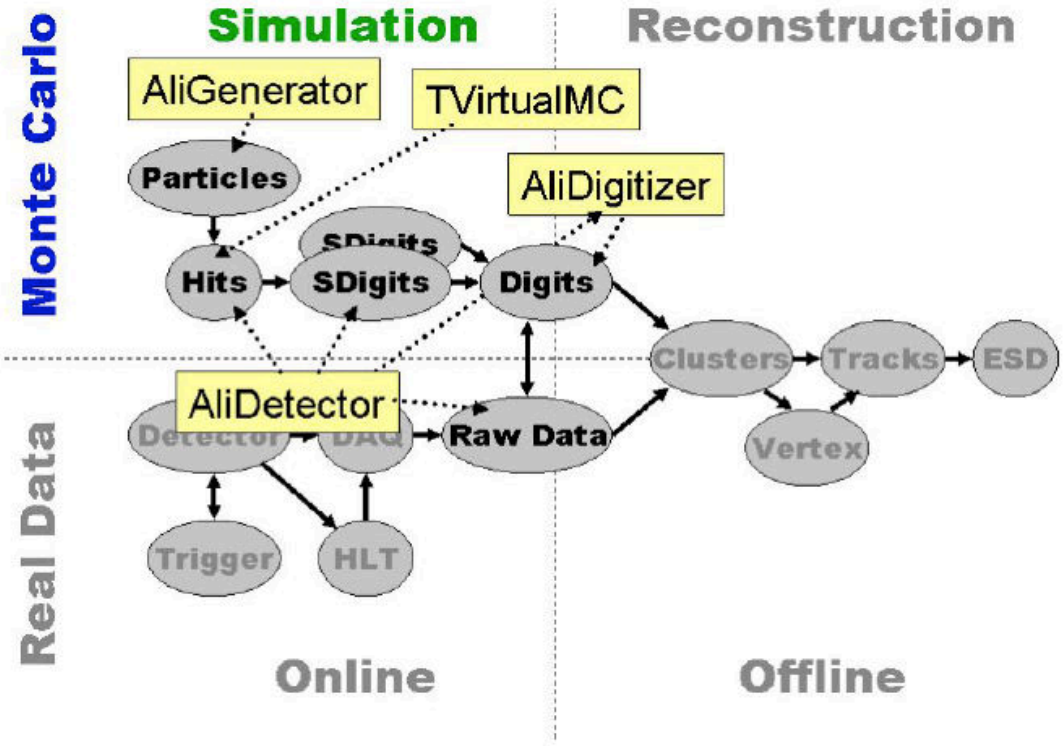

Figure 4.11: Simulation framework. [174].

4.2.2 Reconstruction

The input to the reconstruction framework are digits in ROOT tree format or raw data format. First, a local reconstruction of clusters is performed in each detector. Then vertexes and tracks are reconstructed and the particle identification is executed. The output of the reconstruction is the Event Summary Data (ESD), which is a type of ROOT file including all the necessary reconstruction information for physics studies such as reconstructed tracks/particles and global event properties. Figure 4.12 presents the reconstruction framework and the procedure of digits or raw data to ESD. The reconstruction steps are [131]:

- reconstruction steps that are executed for each detector separately (i.e. the cluster finding)
- primary vertex reconstruction
- track reconstruction and particle identification (PID)
- secondary vertex reconstruction (V°, cascade and kink-decay topologies)

A further selection performed by a train of user-defined analysis tasks, which enables the creation of Analysis Object Data (AOD) files including more compact information and smaller size of data needed for a specific analysis.

4.2.3 Offline conditions database framework

The Offline Conditions Database (OCDB) is the place where the alignment and calibration data is stored. It is a set of entries in the AliEn (ALICE Environment) [179, 180] file catalog that point to the physical entities (ROOT files stored in the various storage elements of the grid [181, 182], see Section 4.2.4) containing the alignment and calibration data. The OCDB was designed under the following principles:

- the calibration and alignment database contains ROOT TObjects stored into ROOT files
- calibration and alignment objects are RUN DEPENDENT objects
- the database is READ-ONLY (automatic versioning of the stored objects)
- the objects in the OCDB are unequivocally identified by: a (logical) path name (path of the file in the AliEn file catalog), a validity expressed as a run range, a main (grid) version number, a local subversion number, only for locally stored objects

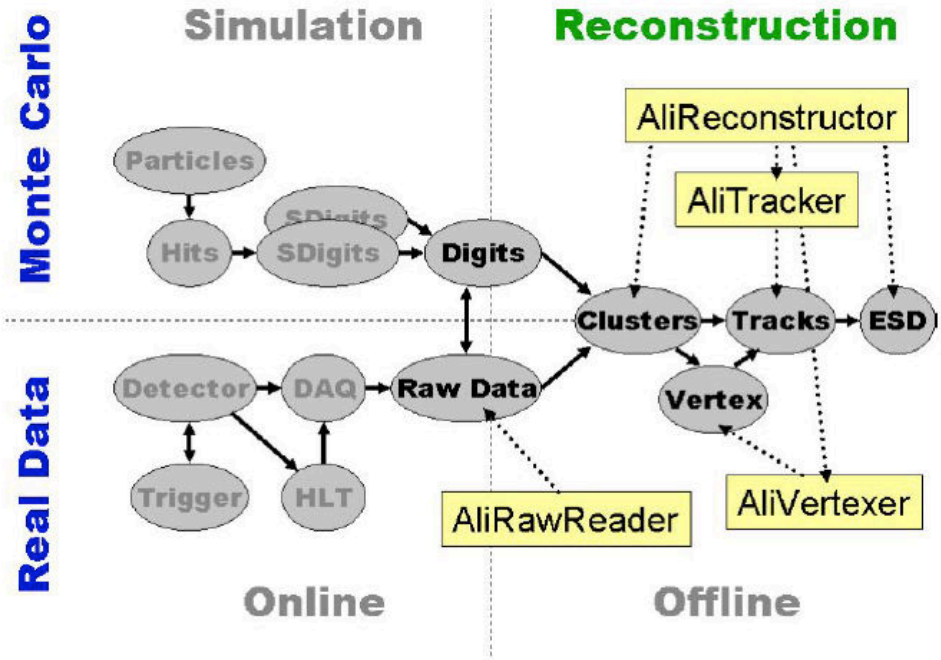

Figure 4.12: Reconstruction framework. [174].

4.2.4 ALICE computing grid

The ALICE experiment collects data at a rate of 1.25 GB/s in heavy-ion mode and approximately 5 PB of data stored on tape each year, producing more than 10^9 files per year which requires massive processing effort for reconstruction. The Worldwide LHC Computing Grid (WLCG) project [181, 182]) was developed to solve this issue. It is a global collaboration of more than 170 computer centers in 42 countries, linking up national and international grid infrastructures. The user interacts with the Grid via the AliEn [179, 180] User Interface (UI). To ease the estimation of required resources, each task has been assigned to a specific Tier, which is a kind of computing center, according to the so-called MONARC model shown in Figure 4.13. This is a distributed model where computing resources are concentrated in a hierarchy of centers called Tiers, where Tier-0 is CERN, Tier-1's are the major computing centers, Tier-2's the smaller regional computing centers, Tier-3's the university departmental computing centers and Tier-4's the user workstations. In such a model the raw data will be stored at CERN, where a Tier-1 center for each experiment will be hosted. Tier-1 centers not at CERN will collectively store a large portion of the raw data, possibly all, providing a natural backup. The reconstruction task is shared by the Tier-1's centers, while subsequent data reduction, analysis and Monte Carlo production is a collective operation where all Tiers participate, with Tier-2's being particularly active for Monte

Carlo and analysis. [141]

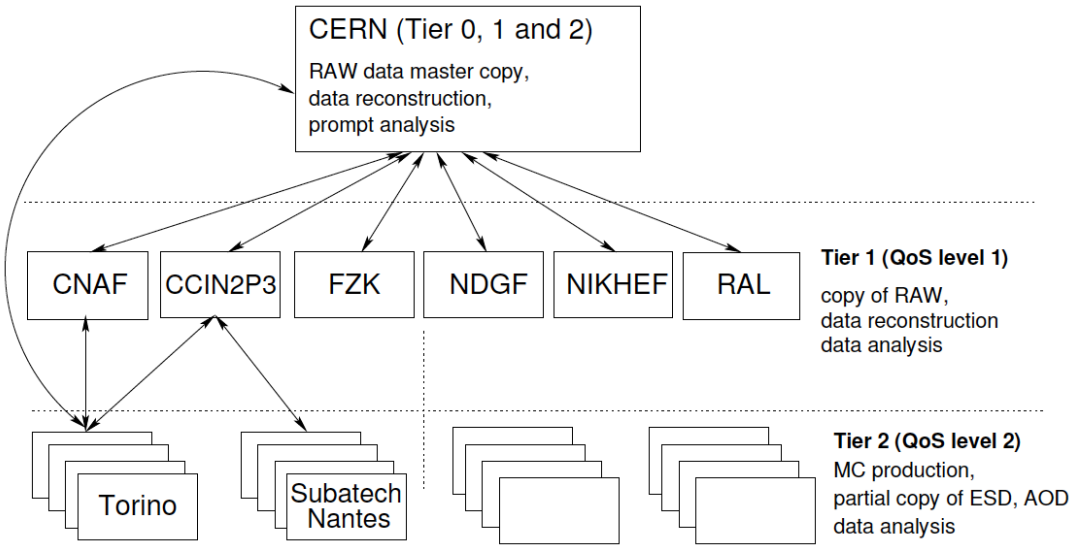

Figure 4.13: Schematic view of the ALICE offline computing tasks in the framework of the tiered MONARC model. [183].

The ALICE monitoring from CERN is performed by MonALISA (Monitoring Agents using a Large Integrated Services Architecture) [184]. The production of real data and Monte Carlo simulations is triggered by AliEn and submitted to the Grid using Job Agents (JA). The interesting job-related parameters are available while the job is running. Monitored parameters include:

- run_time, running time of the job
- cpu_time, effectively consumed cpu time
- cpu_usage, percentage of the instant usage of the cpu(s)
- memory

The values per job are available using the MonALISA GUI client.

4.3 MUON quality assurance

The quality assurance (QA) of data is quite important since it is the basis of all physics analysis. The experts check the status of each detector and give a summary in the ALICE QA meeting once every week. The data taking is subdivided into small periods of time, ranging from few minutes to few hours, called run. Each run is characterized by a fixed configuration and detector

status. The run can be stopped in case of problems with the detector, when the detector needs calibration, when the machine operation changes, to change the trigger configuration, etc.

Different kind of runs can be recorded. In particular, one can have calibration runs, which can be used for example to build the pedestals, runs to measure luminosity, etc. The quality assurance is performed on runs which are dedicated to physics, which are characterized by a stable beam. In order to check the quality, a minimum amount of data should be analyzed. So the QA is performed only if the data taking lasts at least 10 minutes and at least 5000 events are recorded.

For MUON QA, these additional selections are applied:

- Check the status of MUON only for runs where all of the basic detectors needed for the MUON analysis (which includes not only the muon tracker and trigger, but also the VZERO for triggering and SPD for the determination of the primary vertex, which is required for muon tracking) are in the readout.
- The configuration of these readout detectors should be checked by the detector experts and the status should not be labeled as "bad" in the ALICE electronic logbook to ensure detectors work properly.

The quality assurance consists in checking some observables that provide information on the status of the detector and of the reconstruction, such as trigger chamber efficiencies, number of tracks per event, number of clusters per chamber, etc. One thing to be noted is that the muon tracking stations and trigger stations record the data independently. Then the reconstructed tracks in the MUON spectrometer are divided into three categories:

- Tracking (only) tracks: tracks which are reconstructed in the tracking stations and they are not detected by the trigger stations.
- Trigger (only) tracks: tracks which are detected by the trigger stations and they are not reconstructed in the tracking stations.
- Matched tracks: tracks are reconstructed and labeled by both tracking stations and trigger stations.

Here, it is not necessary to show all of the QA plots and some typical examples for LHC13d period are shown in Figure 4.14 to illustrate how to select the correct data samples for our physics analysis. First of all, the list of run number is extracted according to the basic selection mentioned

above in the ALICE electronic logbook. Then some distributions as a function of these run number are checked. In Plot (a), the efficiency distributions of muon trigger chamber as a function of run number are stable and are more than 95%, which is normal for analysis. In Plot (b), the number of tracking tracks, trigger tracks and matched tracks per MSH event are flat and stable except two runs (195681 and 195721). Then check further information in the ALICE electronic logbook and find that there are no MUON triggers in these two runs. Thus, we can decide to remove them from the run list of QA. Plot (c) shows the average number of clusters per chamber associated to a track. The passage of particles in the chambers results in a ionization of the gas and eventually the generated electric signal is collected by the cathode pads. Clusters can be determined from the charge deposition on adjacent pads, and used to reconstruct the tracks. When a module is not efficient, no cluster is formed, and the average number of clusters of the corresponding chamber decreases. The most common cause of inefficiency is the automatic switch-off of the high voltage of a module occurring when the module is drawing too much current (HV trip). The module is inefficient until the high voltage is restored. If the inefficiency is too large or if the faulty module cannot be correctly reproduced in simulations, the run should be declared as bad. Plot (c) shows that the chamber 3 is the most affected by the HV trips. However, the cause of the inefficiency is well identified, and the runs can be declared as good for physics. Some details in the ALICE electronic logbook to remove runs from the QA are listed as follows:

- 195720: rare trigger test
- 195722: TRD trigger test run
- 195723: TRD trigger test run
- 195761: bad VZERO information

After MUON QA analysis, there are still 20 runs in LHC13d period (see Appendix A.1).

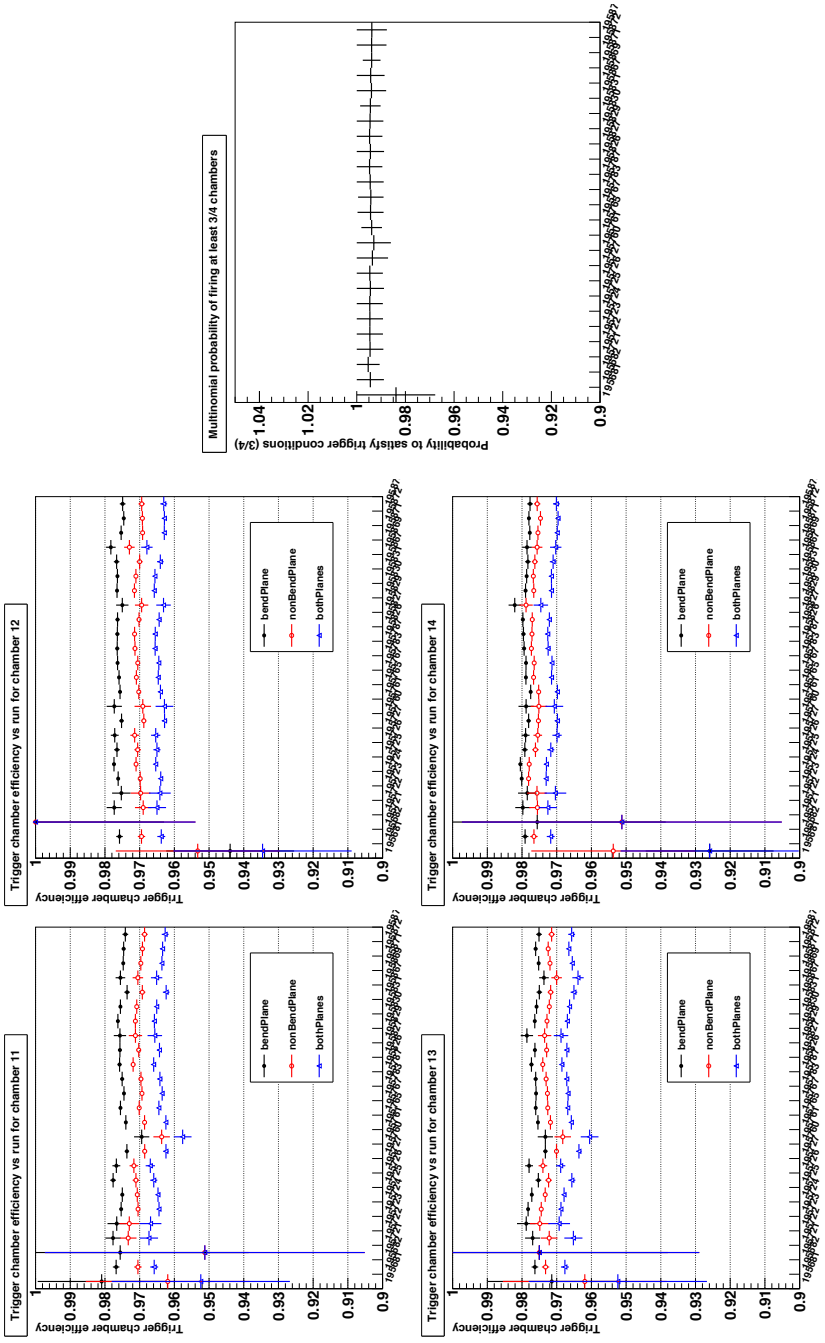

(a)

Figure 4.14: (a) QA plots of muon trigger chamber efficiencies per run in LHC13d period. (b) A QA plot of number of tracks including tracker tracks, trigger tracks, matched tracks and all tracks for MSH trigger per run in LHC13d period. (c) A QA plot of average number of clusters per muon chamber in LHC13d period.

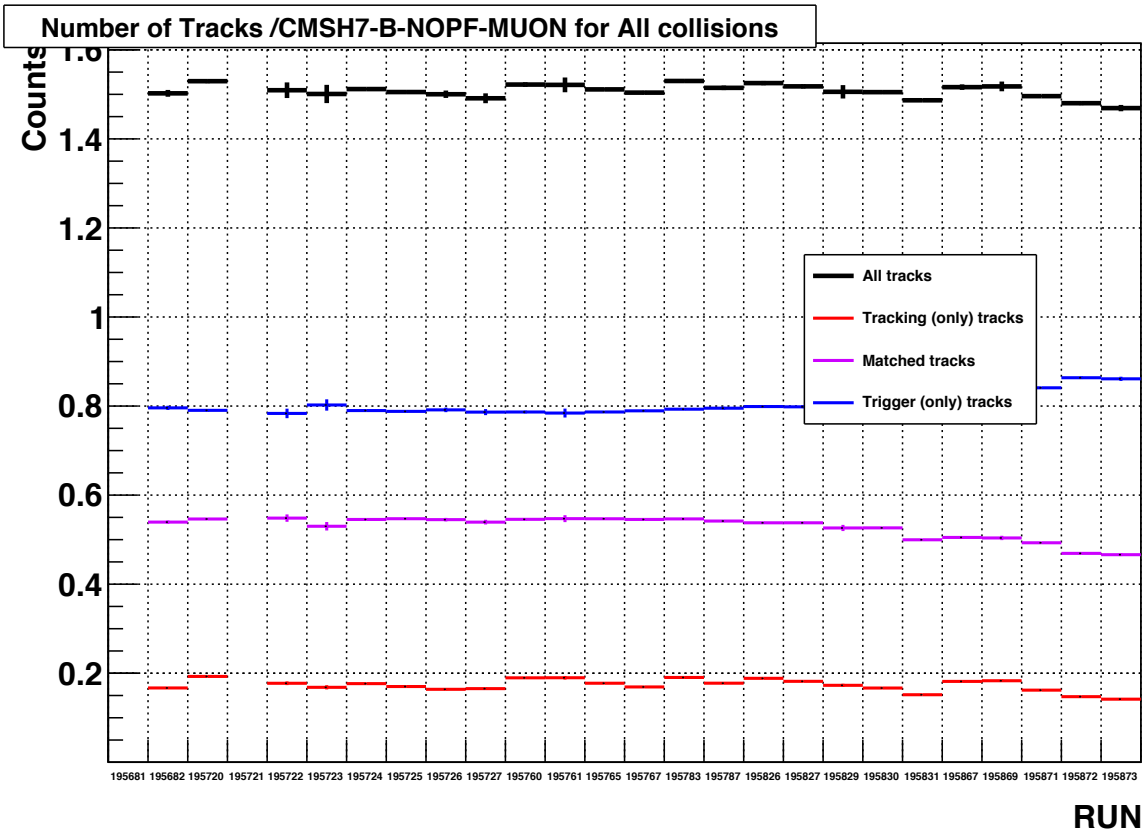

(a)

Figure 4.14: (a) QA plots of muon trigger chamber efficiencies per run in LHC13d period. (b) A QA plot of number of tracks including tracker tracks, trigger tracks, matched tracks and all tracks for MSH trigger per run in LHC13d period. (c) A QA plot of average number of clusters per muon chamber in LHC13d period.

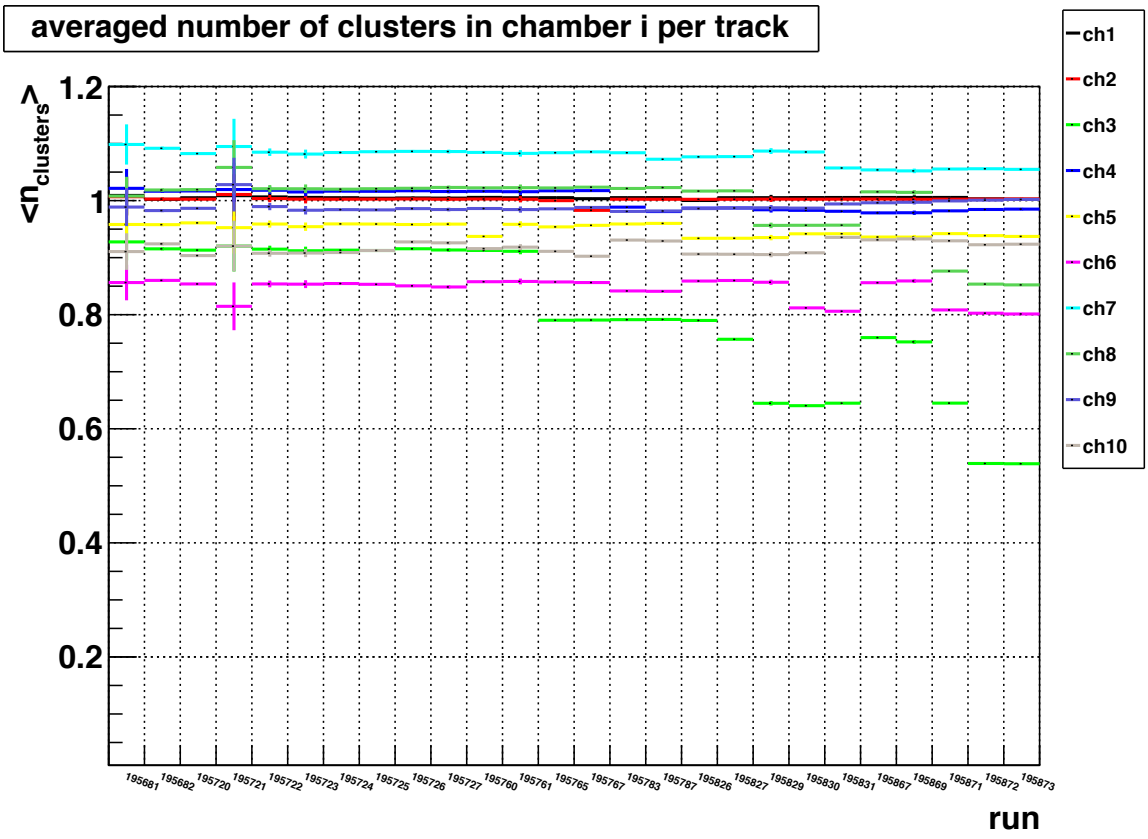

(b)

Figure 4.14: (a) QA plots of muon trigger chamber efficiencies per run in LHC13d period. (b) A QA plot of number of tracks including tracker tracks, trigger tracks, matched tracks and all tracks for MSH trigger per run in LHC13d period. (c) A QA plot of average number of clusters per muon chamber in LHC13d period.

Part III

W-boson Measurement

Equations are more important to me, because politics is for the present, but an equation is something for eternity.

Albert Einstein

5

W-boson measurement in p–Pb collisions

The measurement of the W boson production in p-Pb collisions with the ALICE experiment is based on a feasibility study by Z. Conesa del Valle [30]. From it, we know that the measurement on W-boson can be done via extracting the signal from the inclusive single muon p_{T} spectrum. At high p_{T}, the main contributions to the yield of inclusive muons come from the muonic decays of W bosons, the di-muon decays of $\mathrm{Z}^{\circ}/\gamma^{*}$ bosons and the semi-muonic decays of beauty hadrons. The yield of muons from W-boson decays can be obtained through a fit based on suitable parameterizations of the different components. However, muons from W-boson decays have large momentum, which means the deflection angle in tracking system is very small. In this case, the precision of the measurement on W boson production is limited by the resolution of muon track and alignment in high-p_{T} region.

The ALICE experiment has collected data in pp collisions at $\sqrt{s} = 7$ TeV (2011), 8 TeV (2012) and 13 TeV (2015+2016), p–Pb collisions at $\sqrt{s_{\mathrm{NN}}} = 5.02$ TeV (2013 and 2016) and Pb–Pb collisions at $\sqrt{s_{\mathrm{NN}}} = 2.76$ TeV (2011) and 5.02 TeV (2016) with high luminosity. The measurement of the W boson production in p–Pb collisions at 5.02 TeV will be presented in this chapter. The analogous measurement in pp collisions at 8 TeV will be presented in the following Sections.

5.1 Data samples and standard cuts

The LHC consists of two rings, with beams circulating in opposite directions. Since the rigidity of the magnets is the same, the energy depends on the mass-to-charge ratio of the accelerated particles. When protons are accelerated to 4 TeV, the Pb ion would therefore be accelerated to $Z/A * 4 = 1.58$ TeV. Therefore, the rapidity of the center-of-mass system (cms) is shifted with respect to the laboratory frame by $\Delta y = \frac{1}{2}\ln(\frac{Z_p A_{Pb}}{Z_{Pb} A_p}) \approx 0.465$. The muon spectrometer covers the pseudo-rapidity range $-4.0 < \eta_{lab} < -2.5$ (in the official LHC coordinate system *), thus being sensitive to different regions of the Bjorken x values for the incoming hadron moving towards positive rapidities and the one moving towards negative rapidities. In order to explore both sides of this asymmetric collision system, one should hence collect data with two configurations: one with the proton moving from the interaction point towards the muon spectrometer and the other with the proton moving in the opposite direction. In this case, the data taking is divided into periods with similar data taking conditions. If one adopts the convention that the proton travels towards positive rapidity, the two configurations allow to probe different rapidity regions:

- p–Pb collisions (forward, p-going direction): $2.03 < y^{\mu}_{cms} < 3.53$
- Pb–p collisions (backward, Pb-going direction): $-4.46 < y^{\mu}_{cms} < -2.96$

In the ALICE experiment, the data taking is divided into periods, which are conventionally denoted as LHC+year+sequential letter. The Pb-going direction corresponds therefore to the LHC13f period. On the other hand the p-going direction is divided in two sub-periods, with inverted field polarity: LHC13d and LHC13e. The latter has the same polarity as LHC13f. The run number lists can be found in Appendix A.1.

The data have been collected at $\sqrt{s_{NN}} = 5.02$ TeV with minimum bias (MB), muon single-low p_T (MSL) and muon single-high p_T (MSH) triggers. The MB trigger is defined requiring hits in both sides of the VZERO detector in coincidence with the beam counters. The MSL (MSH) trigger is defined by asking, in addition to the MB condition, for a low (high) transverse momentum muon with an associated p_T trigger threshold set at around 0.5 (4.2) GeV/c. The integrated luminosity for the forward and backward rapidity measurements are 5.03 ± 0.18 and 5.81 ± 0.20 nb^{-1} [185], respectively.

*The official LHC coordinate system is an orthogonal coordinate system with the x axis pointing to the center of the accelerator and the y axis pointing upward.

The offline physics event selection or the so-called physics selection was implemented by reproducing the trigger conditions, cutting on the event leading time of V0A and V0C and identifying background according to the correlation between the tracklets and clusters in SPD. Moreover, the events without reconstructed primary vertex from SPD were rejected from the analysis. Various kinematic cuts were applied for the muon track selection. Tracks were required to be reconstructed within the acceptance of the muon spectrometer ($-4.0 < \eta_{\rm lab} < -2.5$) and to have a polar angle at the end of the absorber ($\theta_{\rm abs}$) from 170^o to 178^o. The track candidate in the tracking system was required to match the track reconstructed in the trigger system. Finally, the contamination from beam-induced background tracks, which do not point to the interaction vertex, can be efficiently removed by exploiting the correlation between the momentum (p) of the track and its Distance of Closest Approach (DCA) to the vertex. Due to the multiple scattering in the front absorber, the DCA distribution of particles produced in the collision can be described with a Gaussian function, whose width depends on the material crossed and is proportional to $1/p$. On the other hand, the background tracks have a DCA larger than about 40 cm, independent of $p_{\rm T}$. They can therefore be rejected by selecting particles with a $p \cdot DCA$ smaller than 6 times the width of the distribution, extracted from a Gaussian fit.

Data selected after the Quality Assurance for both MSL and MSH triggered events are considered.

Table 5.1 summarizes the statistics of the events that pass the offline trigger selection.

		+ Phys. Sel.
LHC13d	MSL	5.78M
	MSH	4.61M
LHC13e	MSL	9.04M
	MSH	5.51M
LHC13f	MSL	26.41M
	MSH	15.67M

Table 5.1: Summary of the statistics after applying physics selection at event level.

The centrality of the collision is measured from the amplitude of the VZERO, the number of clusters in the outer layer of the SPD detector (CL1) or the energy deposited in the ZN in the direction of the fragmenting lead ion. The average number of binary collisions $\langle N_{\rm coll} \rangle$ is determined from a Glauber-model [28] based analysis in the case of VZERO and CL1 estimators, while for the ZN estimator it is computed with a hybrid approach, assuming that the particle density at mid-rapidity is proportional to the average number of nucleons participating in the

collision, $< N_{\text{part}} >$ [186]. The value of $< N_{\text{part}} >$ for a given ZN-centrality class are calculated by scaling the average number of participants in MB collisions $< N_{\text{part}}^{\text{MB}} >$, estimated with a Glauber model, by the ratio of the average charged-particle multiplicity measured at mid-rapidity for the ZN-centrality class and that of MB. The corresponding number of binary collisions is then obtained as: $< N_{\text{coll}} >=< N_{\text{part}}^{\text{MB}} > -1$. The systematic uncertainties are estimated by using different approaches as described in [186]. The resulting values of $< N_{\text{coll}} >$ and their uncertainties are summarized in Table 5.2.

	VoA		CL1		VoC		Hybrid ZNA/ZNC	
Centrality	$\langle N_{\text{coll}} \rangle$	syst	$\langle N_{\text{coll}} \rangle$	syst	$\langle N_{\text{coll}} \rangle$	syst	$\langle N_{\text{coll}} \rangle$	syst
2–20%	12.50	10%	12.90	10%	12.50	10%	11.31	3%
20–40%	9.36	9%	9.49	9%	9.39	9%	9.56	2%
40–60%	6.42	7.2%	6.18	7.2%	6.40	7.2%	7.08	4%
60–100%	2.86	6.2%	2.60	6.2%	2.86	6.2%	3.20	4%
0–100%	6.87	8%	6.83	8%	6.87	8%	6.88	-

Table 5.2: $\langle N_{\text{coll}} \rangle$ with different centrality estimators in different centrality bins.

Since we need to access the high-p_{T} range for the W-boson signal extraction, in the following we will focus on the analysis of MSH events. Figure 5.1 shows the raw transverse momentum distribution with MSH trigger in the period LHC13d+LHC13e (left panel) and LHC13f (right panel) after applying the standard cuts mentioned above.

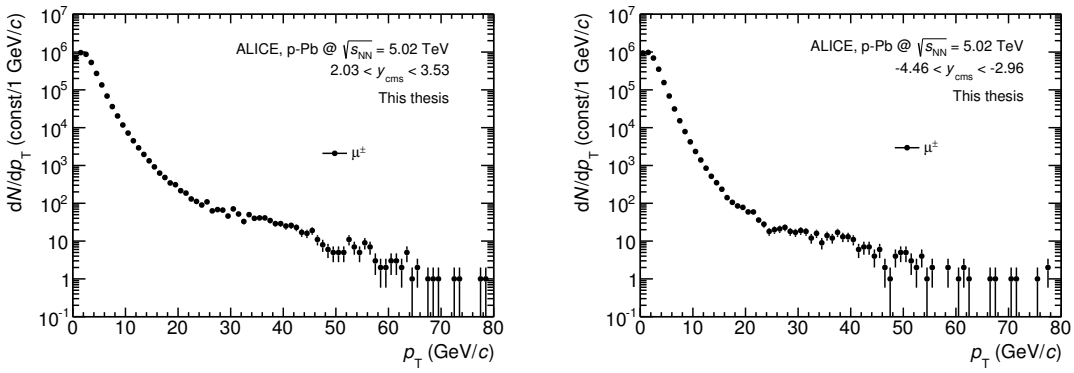

Figure 5.1: Raw p_{T} distributions of muons in MSH events in the periods LHC13d+LHC13e (left panel) and LHC13f (right panel).

5.2 Analysis strategy

The W-boson contributes to the transverse momentum distribution of inclusive muons through the muonic decay channels ($W^+ \rightarrow \mu^+\nu_\mu$, $W^- \rightarrow \mu^-\bar{\nu}_\mu$). The decay kinematic provides two final state particles with $p_T \sim \frac{M_W}{2} \sim 40$ GeV/c. Since the neutrino can not be detected, the signature would be a high-p_T muon with large missing transverse energy (E_T^{miss}). Unfortunately, ALICE is not equipped with an hermetic calorimeter, hence the only information is the presence of a muon with high p_T. The contribution from W-boson decays to the raw p_T muon spectrum must be estimated through a suitable fit of the distribution. The main steps are:

- signal extraction via combined fit
- acceptance $\times$ Efficiency (Acc. $\times$ Eff.) correction
- normalisation to minimum bias event to obtain the cross section

Both the signal extraction and the Acc. $\times$ Eff. correction require the determination of the shape of the p_T-distribution of muons from W-boson decays. This is performed by simulations, which will be described in Section 5.3.

5.3 Monte Carlo simulations

The detector response for muons from W boson decays was determined through Monte Carlo (MC) simulations, which are based on a POWHEG [86, 87, 187], a NLO particle generator, paired with PYTHIA 6.4.25 [84] for parton shower. The version of POWHEG is the POWHEG-BOX v1 modified in order to allow using the EPS09 [119] parameterization of the nuclear modification factor of the PDFs. The W bosons are forced to decay into muons with a polar angle of $168^\circ < \theta_\mu < 178.5^\circ$, slightly larger than the muon spectrometer acceptance in order to account for edge effects. The configurations for W-boson and Z-boson production can be found in Appendix A.3.

The simulations are anchored to the Offline Conditions Database (OCDB) of LHC13d, LHC13e and LHC13f, where the calibration and alignment data is stored, according to the standard procedure for MUON analyses. This can reproduce the condition of the detectors to a certain extent. The alignment file is ideal in simulation, while a custom residual alignment, produced for

all MUON analyses, is used in reconstruction. The simulations are performed by generating a number of events per run proportional to the number of MSH triggers in that run, in order to correctly account for the modification of the status of the detector with time.

The isospin dependence of the W-boson differential cross section [30] is accounted for by simulating separately the proton-proton (pp) and proton-neutron (pn) collisions and then summing the results together with the formula:

$$\frac{1}{N_{\text{p-Pb}}}\frac{dN_{\text{p-Pb}}}{dp_{\text{T}}} = \frac{Z}{A}\frac{1}{N_{\text{pp}}}\frac{dN_{\text{pp}}}{dp_{\text{T}}} + \frac{A-Z}{A}\frac{1}{N_{\text{pn}}}\frac{dN_{\text{pn}}}{dp_{\text{T}}} \tag{5.1}$$

where $A = 208$ and $Z = 82$.

The resulting W-boson and muon generated distributions for pp and pn collisions by POWHEG are shown in Figure 5.2. The shape of the rapidity distribution of W-boson is mainly due to the acceptance cuts on the produced muons. In particular, the W-boson production is shifted in the direction of the valence quark, as explained in Section 2.2.3.

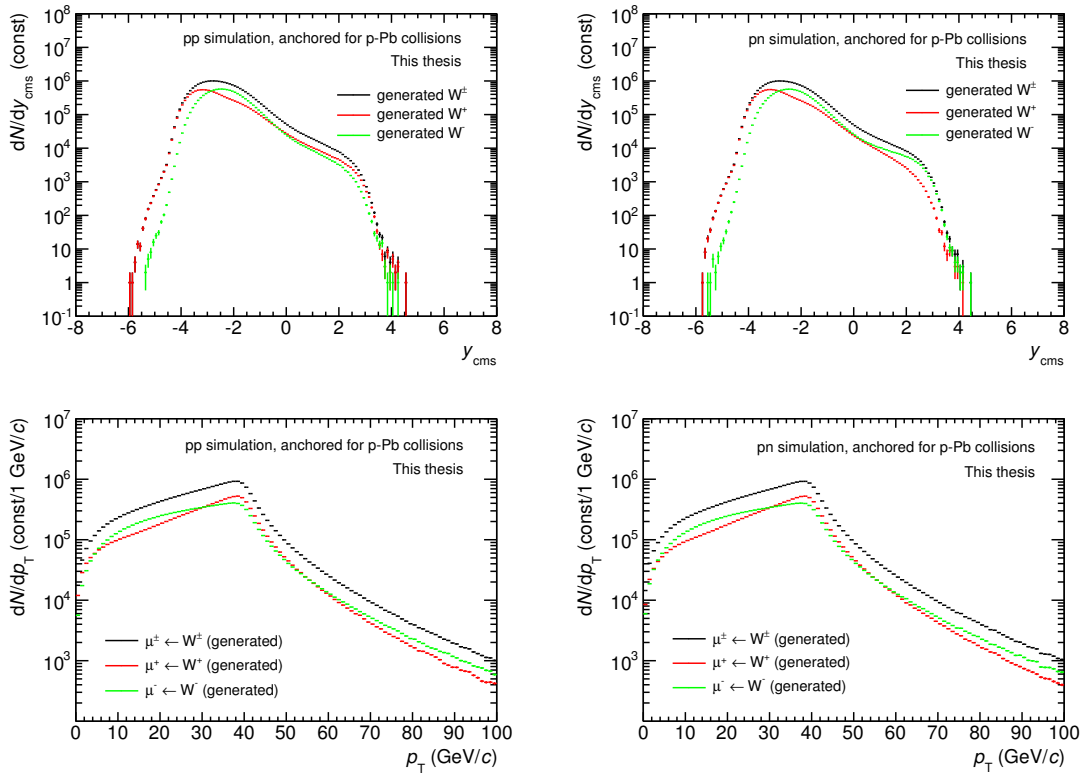

Figure 5.2: Generated distributions with POWHEG, CT10 and EPS09. Top panels: rapidity distributions of generated W bosons. Bottom panels: Transverse momentum distributions of generated muons from W bosons decay. Results are shown for simulations of pp (left panels) and pn (right panels) nucleon-nucleon interactions.

The generation of muons from Z°/γ^{*} decays is performed in an equivalent way, forcing the decay $Z^{\circ}/\gamma^{*} \rightarrow \mu^{+}\mu^{-}$. The interference terms between Z° and γ^{*} production are accounted for in the POWHEG generator.

5.4 Signal extraction

In order to implement the combined fit to the raw p_{T} distribution of inclusive muons to extract the signal of muons from W boson decays, we need to prepare the MC templates of muons from vector bosons and heavy-flavour (HF) decay. The different contributions are summed together in the final fit function, which is defined as:

$$f(p_{T}) = N^{raw}_{bkg} \cdot f_{bkg}(p_{T}) + N^{raw}_{\mu\leftarrow W} \cdot (f_{\mu\leftarrow W}(p_{T}) + R \cdot f_{\mu\leftarrow Z^{\circ}/\gamma^{*}}(p_{T})) \tag{5.2}$$

where f_{bkg}, $f_{\mu\leftarrow W}$ and $f_{\mu\leftarrow Z^{\circ}/\gamma^{*}}$ are the MC templates for muons from heavy-flavoured hadrons, W- and Z-boson decays, respectively. The number of muons from heavy-flavour decays (N^{raw}_{bkg}) and the number of muons from W decays ($N^{raw}_{\mu\leftarrow W}$) are free parameters, while the ratio (R) of the number of muons from Z decays and that from W decays is fixed from MC simulation using POWHEG. The detector response is included in all simulations. The MC templates of muons from vector bosons decay were discussed in Section 5.3. Thus, the background subtraction of muons from heavy-flavour decays will be introduced as well as the fit procedure.

5.4.1 Heavy-flavour decay background description

The distribution of background muons, which basically comes from the decay of heavy flavours, was described with simulations using as input the FONLL predictions for pp collisions at 4+1.58 TeV (i.e. 5.02 TeV in the centre of mass) [188]. The calculations have been obtained using the CTEQ6.6 parton distribution functions [189], without accounting for any nuclear modification of the PDFs. Such modifications, however, are expected to be dominant at low p_{T}, with a negligible contribution in the p_{T} region of interest for this study [190].

Several sources of uncertainties affecting the shape of the MC templates were taken into account. For the background, different MC templates were obtained by varying the FONLL calculations within uncertainties. In particular, six additional templates were produced, corresponding to the upper and lower limits of the calculations obtained by i) varying the factorisation and renormalisation scales, and considering the uncertainties on ii) the quark masses and iii) the PDFs.

The ratio of the FONLL calculations with modified scale, mass and PDFs and the central value are shown in Figure 5.3. The variation of the PDFs provides the largest modification of the shape compared to the central value.

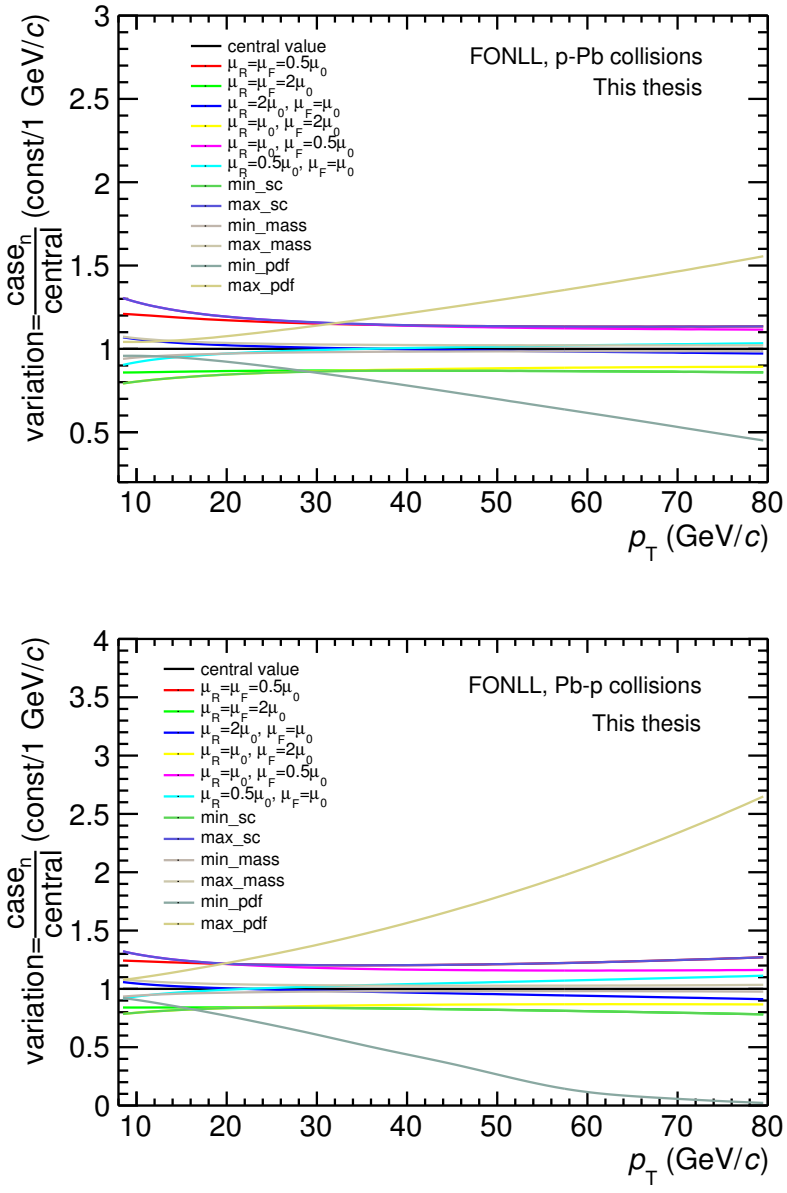

Figure 5.3: The left panel is for p-going direction and the right panel is for Pb-going direction. The variation of the p_T distribution of muons from heavy-flavour decays calculated with FONLL by varying the factorization and renormalisation scales, and considering the uncertainties on the quark masses and the PDFs. The first black benchmark line "central value" represents central value of FONLL prediction. Lines with "μ_R" and "μ_F" indicate different sets of factorisation and renormalisation scales, "min_sc" and "max_sc" mean the minimum and maximum values obtained via varying the factorisation and renormalisation scales, "min_mass" and "max_mass" mean the minimum and maximum value obtained via varying quark masses, "min_pdf" and "max_pdf" mean the minimum and maximum value obtained via varying PDFs.

5.4.2 Fitting procedure

The procedure of the combined fit is listed as following:

- choose a certain p_{T} range
- normalize each of MC templates of muons from vector bosons and heavy-flavour decay to unity
- fix the value of "R" in Eq. 5.2 according to POWHEG
- sum the normalized MC templates together to create a function to implement fit

The yield of muons from W boson decays ($N_{\mu\leftarrow \mathrm{W}}$) is extracted from the fit which pass the criteria below:

- fits must be successful and the minimizer succeeded in finding the minimum (`TFitResult::IsValid()`)
- fits must converge (`gMinuit->fCstatus` has to be "CONVERGED")
- the covariant matrix is required to be accurate (`TFitResult::CovMatrixStatus()==3`)
- fits must have $\chi^2/ndf < 2$, where ndf is the number of degree of freedom

Since there are empty bins, the log-likelihood method was used in the fit. The difference with respect to the chi-square method, however, was tested to be small, since the fit results are driven by data points with $p_{\mathrm{T}} \lesssim 60$ GeV/c.

5.4.3 Optimization of fit p_{T} range

The choice of the p_{T} range of the fit is somehow arbitrary and needs to be tuned. In particular, if one fits at very low-p_{T}, the fit results will be dominated by the background description at very low momenta. On the other hand, if the minimum p_{T} is too large, the heavy-flavor background will not be sufficiently constrained. The determination of the best fitting range is done through MC simulations. The fit p_{T} range matters when the background shape used in the fit does not fully reproduce the data over all the range considered. In order to simulate this, one can generate pseudo-data using a specific background shape, and reconstruct with a modified one (within uncertainties). The steps are:

- fit to raw data with FONLL central value template according to Eq. 5.2 and extract the number of muons from heavy-flavour, W and Z decays with "alignment_5". The number of muons from W decays is called "N_{input}".
- build some "simulated-data", by randomly sampling from the three templates above, assuming a poisson distribution of the number of extracted muons.
- for a fixed p_{T} range, fit "simulated-data" according to the strategy mentioned in Section 5.7.6 to obtain the final number of muons from W decays (N_{W})
- compare N_{W} with N_{input} in different fit p_{T} range

The examples of this test in different fit p_{T} range can be found in Figures 5.4 and 5.5. In $15 < p_{\text{T}} < 50$ GeV/c, the number of N_{W} is closest to the number of N_{input}. It means that the best fit p_{T} range is at around $15 < p_{\text{T}} < 50$ GeV/c. The high p_{T} limit is mainly due to the low statistics (and large number of empty bins). A further test on lower limit of the fit p_{T} range was done with step size of 1 GeV/c and we found that the best fitting p_{T} range is $15 \sim 17 < p_{\text{T}} < 50$ GeV/c.

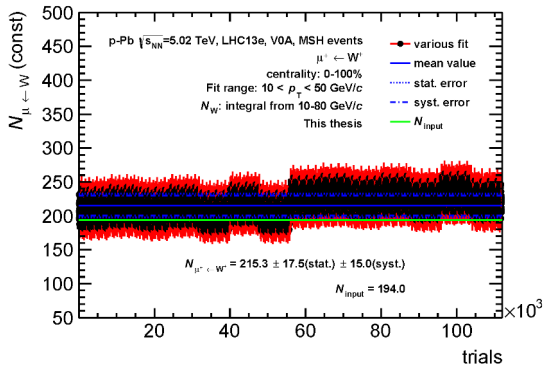

(a) $10 < p_T < 50$ GeV/c

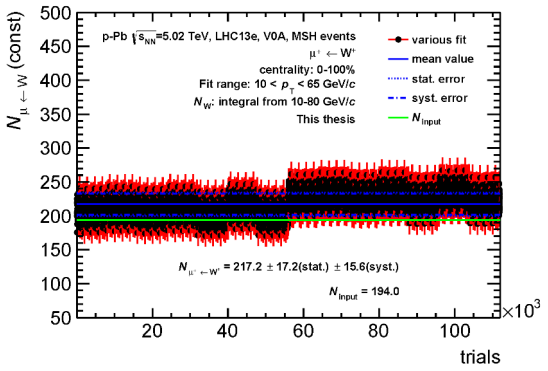

(b) $10 < p_T < 65$ GeV/c

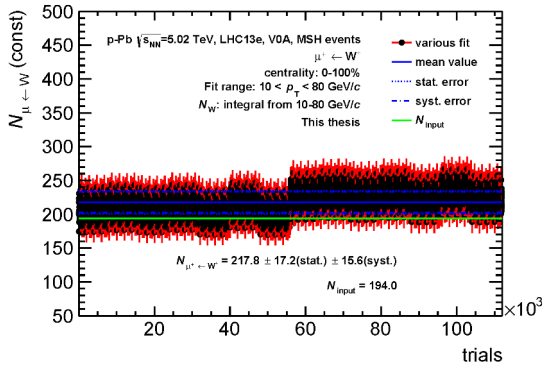

(c) $10 < p_T < 80$ GeV/c

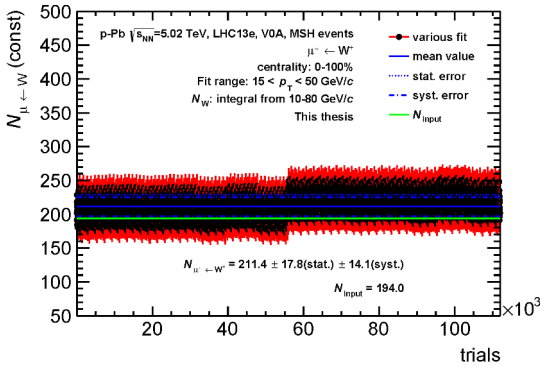

(d) $15 < p_T < 50$ GeV/c

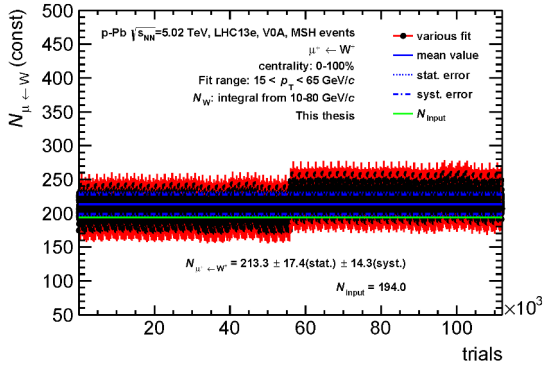

(e) $15 < p_T < 65$ GeV/c

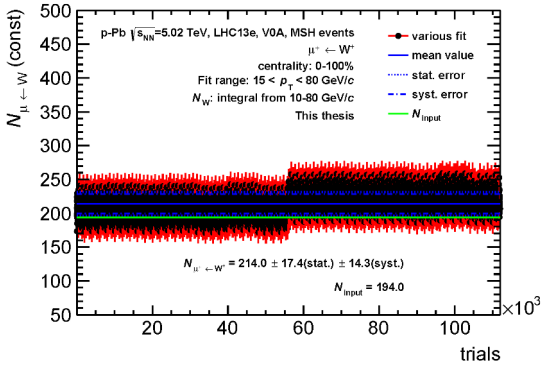

(f) $15 < p_T < 80$ GeV/c

Figure 5.4: The yield of $\mu^+ \leftarrow W^+$ as a function of trials (each "simulated-data") in different fixed fit p_T range for LHC13e period. The lower limit increases with step size of 5 GeV/c and the higher limit increases with step size of 15 GeV/c.

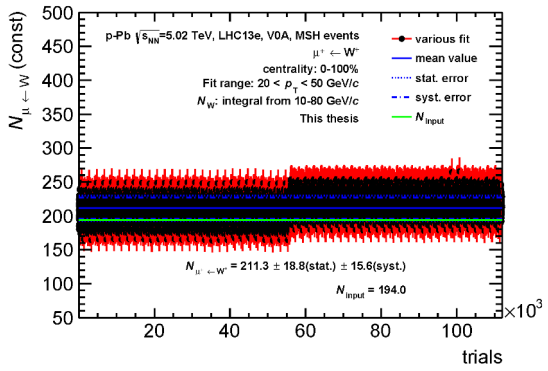

(g) $20 < p_T < 50$ GeV/c

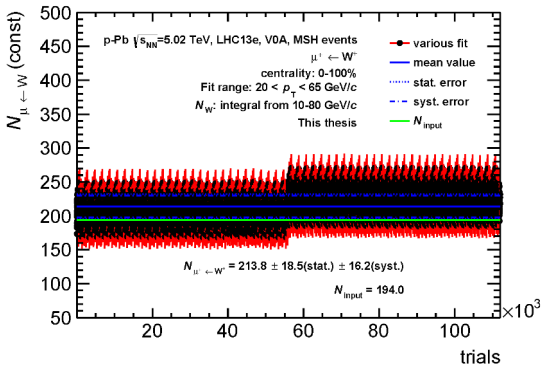

(h) $20 < p_T < 65$ GeV/c

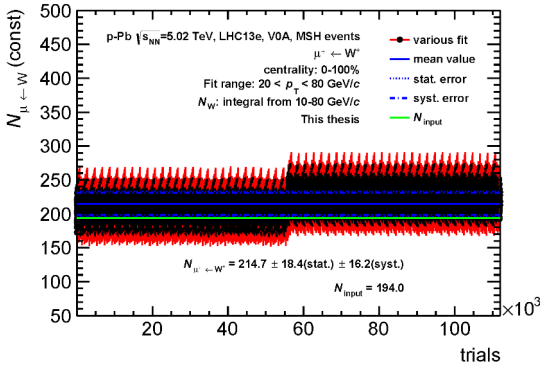

(i) $20 < p_T < 80$ GeV/c

Figure 5.4: The yield of $\mu^+ \leftarrow W^+$ as a function of trials (each "simulated-data") in different fixed fit p_T range for LHC13e period. The lower limit increases with step size of 5 GeV/c and the higher limit increases with step size of 15 GeV/c.

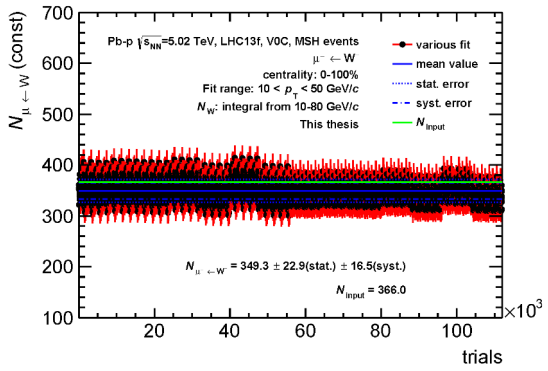

(a) $10 < p_T < 50$ GeV/c

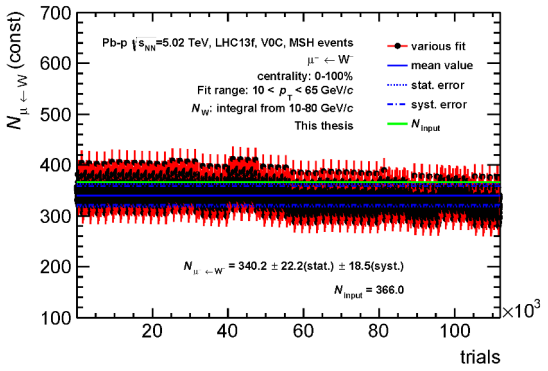

(b) $10 < p_T < 65$ GeV/c

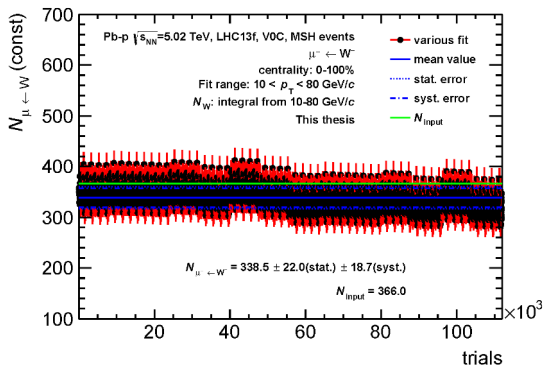

(c) $10 < p_T < 80$ GeV/c

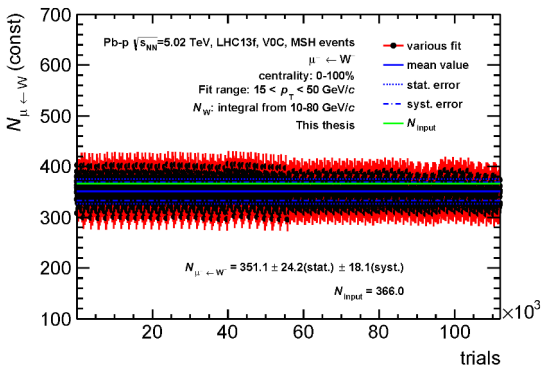

(d) $15 < p_T < 50$ GeV/c

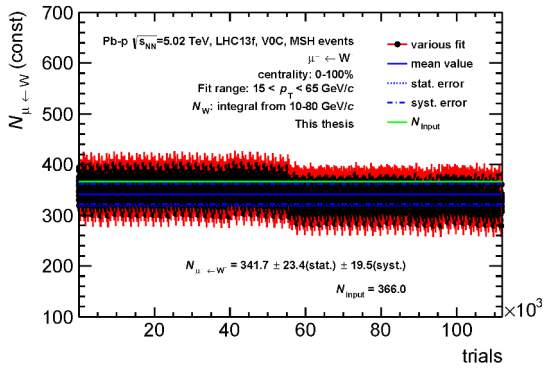

(e) $15 < p_T < 65$ GeV/c

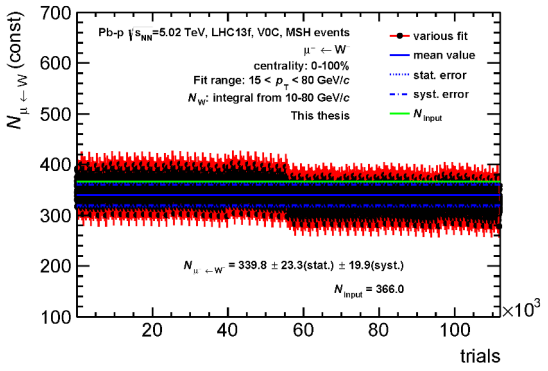

(f) $15 < p_T < 80$ GeV/c

Figure 5.5: The yield of $\mu^- \leftarrow W^-$ as a function of trials (each "simulated-data") in different fixed fit p_T range for LHC13f period. The lower limit increases with step size of 5 GeV/c and the higher limit increases with step size of 15 GeV/c.

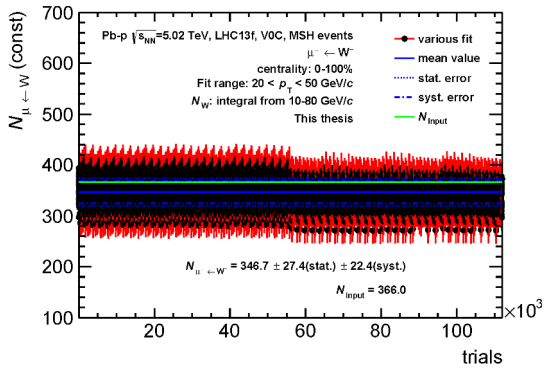

(g) $20 < p_T < 50$ GeV/c

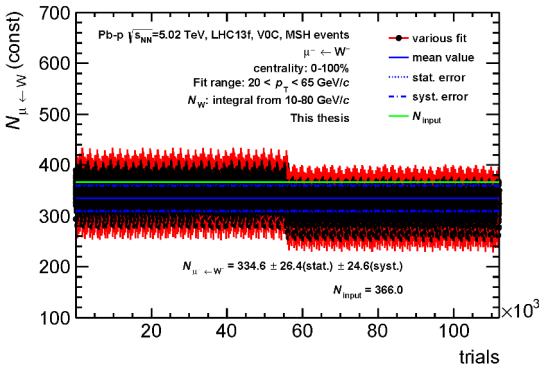

(h) $20 < p_T < 65$ GeV/c

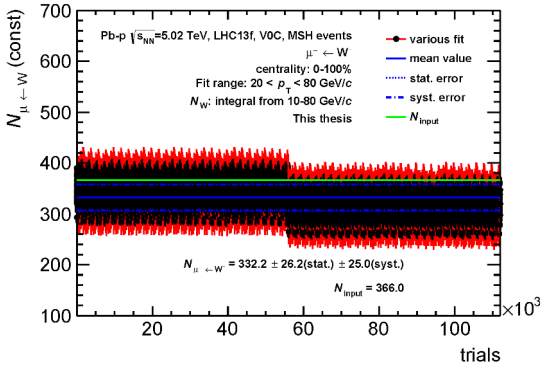

(i) $20 < p_T < 80$ GeV/c

Figure 5.5: The yield of $\mu^- \leftarrow W^-$ as a function of trials (each "simulated-data") in different fixed fit p_T range for LHC13f period. The lower limit increases with step size of 5 GeV/c and the higher limit increases with step size of 15 GeV/c.

Fit examples to p_T distribution of inclusive muons in one of optimized fit p_T ranges are shown in Figures 5.6 for the LHC13d+LHC13e period and Figures 5.7 for the LHC13f period.

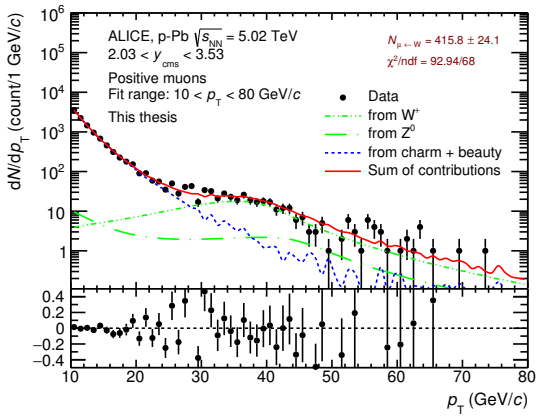

(a) $\mu^+ \leftarrow W^+$

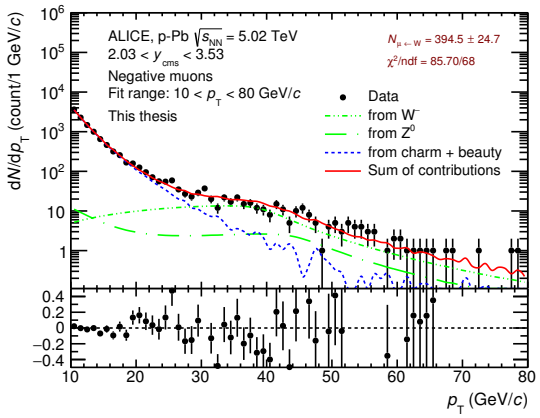

(b) $\mu^- \leftarrow W^-$

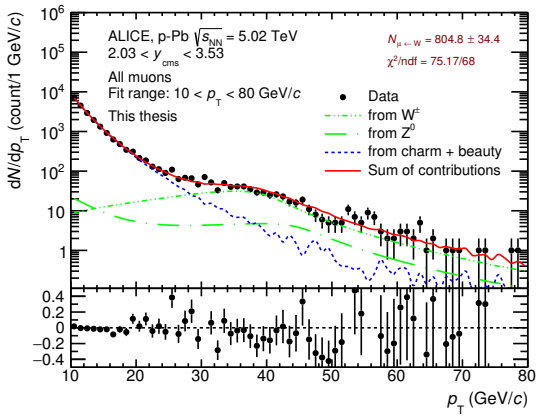

(c) $\mu^\pm \leftarrow W^\pm$

Figure 5.6: The examples of the combined fit for signal extraction of $\mu \leftarrow W$ in LHC13de.

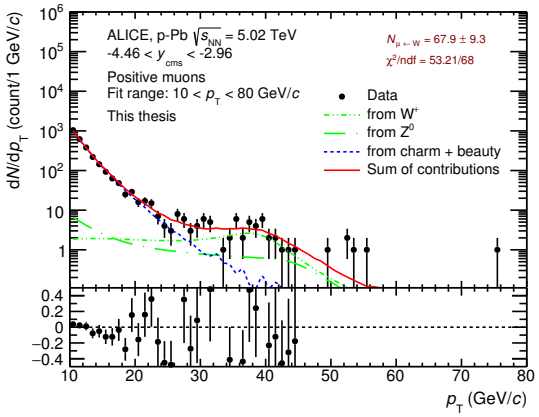

(a) $\mu^+ \leftarrow \mathrm{W}^+$

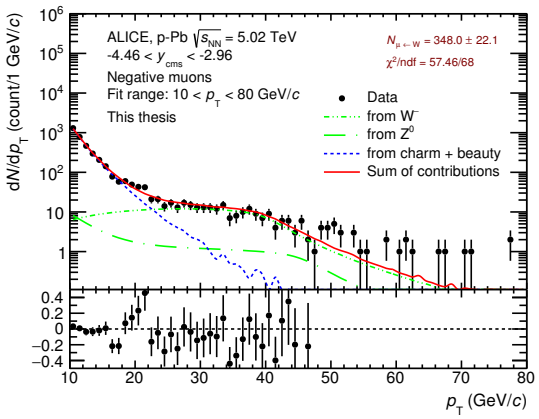

(b) $\mu^- \leftarrow \mathrm{W}^-$

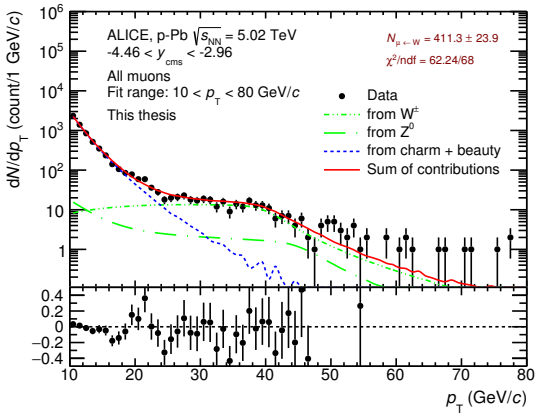

(c) $\mu^\pm \leftarrow \mathrm{W}^\pm$

Figure 5.7: The examples of the combined fit for signal extraction of $\mu \leftarrow \mathrm{W}$ in LHC13f.

5.5 Acceptance × efficiency correction

The Acc.×Eff. corrections are obtained from the simulations described in Section 5.3. The efficiency is defined by the number of muons reconstructed with the same cuts used in the analysis, divided by the number of generated muons coming from $W^{\pm}$ boson decay and with $-4.0 < \eta_{lab}^{\mu,MC} < -2.5$.

The efficiency is provided integrated over the p_T range of the $\mu \leftarrow W$ measurement ($p_T^{\mu} > 10$ GeV/c), in such a way to minimize the bias related to the bin cross-talk caused by the alignment. This bias can be estimated by calculating the Acc.×Eff. in simulations reconstructing with different residual mis-alignment files as well as the resolution task (see Section 3.5.3). The results are summarized in Table 5.3: the effect is lower than 1%.

(a) LHC13d

	μ^+	μ^-
Alignment_6	0.8932 ± 0.0001	0.8931 ± 0.0001
Resoultion	0.8830 ± 0.0003	0.8870 ± 0.0003

(b) LHC13e

	μ^+	μ^-
Alignment_6	0.8837 ± 0.0001	0.8776 ± 0.0001
Resoultion	0.8783 ± 0.0003	0.8654 ± 0.0004

(c) LHC13f

	μ^+	μ^-
Alignment_6	0.7711 ± 0.0001	0.7541 ± 0.0001
Resoultion	0.7579 ± 0.0005	0.7440 ± 0.0005

Table 5.3: Acc.×Eff. for muons from $W^{\pm}$ decays with $p_T^{\mu} > 10$ GeV/c and $-4.0 < \eta_{lab} < -2.5$ obtained from simulations reconstructed with different residual mis-alignment files and resolution task.

5.6 Normalisation to the number of minimum bias events

The normalization procedure is the same used for the measurement of heavy-flavour decay muons [191]. The general strategy is explained in the following.

The results obtained with the high-p_{T} muon trigger events, must be normalized to the number of equivalent Minimum Bias events. This is performed with a suitable normalization factor (F_{norm}), which can be obtained with two different methods.

The first one uses the trigger outputs and the CTP trigger inputs and it is called "offline method" in the following [192]. The corresponding normalization factor for MSH triggers are defined as:

$$F_{\mathrm{norm}}^{\mathrm{MSH}} = \frac{N_{\mathrm{MB}} \times F_{\text{pile-up}}}{N_{(\mathrm{MB\&\&oMSL})}} \times \frac{N_{\mathrm{MSL}}}{N_{(\mathrm{MSL\&\&oMSH})}} \tag{5.3}$$

where $F_{\text{pile-up}}$ is the pile-up correction factor for minimum bias events (see later), N_{MB}, N_{MSL} and N_{MSH} are the number of MB, MSL and MSH triggers, while oMSL and oMSH are the Lo trigger inputs for the single low and high p_{T} triggers, respectively.

The second method is called scaler method [193], and uses the information of Lob counters to avoid statistical fluctuations. The corresponding normalization factor is:

$$F_{\mathrm{norm}}^{\mathrm{MSH}} = \frac{\mathrm{Lob}_{\mathrm{MB}} \times \mathrm{purity}_{\mathrm{MB}} \times F_{\text{pile-up}}}{\mathrm{Lob}_{\mathrm{MSH}} \times PS_{\mathrm{MSH}}} \tag{5.4}$$

where $\mathrm{Lob}_{\mathrm{MB}}$ and $\mathrm{Lob}_{\mathrm{MSH}}$ are the scaler values recorded for minimum bias and single-muon high-p_{T} triggers, respectively and $\mathrm{purity}_{\mathrm{MB}}$ is the fraction of events which satisfy the VZERO timing cut. The purity is better than 99% for most of the runs. PS_{MSH} is the fraction of (accepted) MSH trigger events that pass the Physics Selection mentioned in Section 5.1.

The pile-up correction factor $F_{\text{pile-up}}$ is defined as:

$$F_{\text{pile-up}} = \mu/(1 - e^{-\mu}) \tag{5.5}$$

with

$$\mu = \ln\left(1 - \mathrm{purity}_{\mathrm{MB}} \times \frac{\mathrm{LobRate}_{\mathrm{MB}}}{N_{\mathrm{colliding}} \times f_{\mathrm{LHC}}}\right). \tag{5.6}$$

μ is the mean value of the Poisson distribution which describes the probability to have n collisions when the beams cross each other. $\mathrm{LobRate}_{\mathrm{MB}}$ is the number of minimum bias events recorded by the Lob counter per data taking time. $f_{\mathrm{LHC}} = 11245$ Hz is the collision frequency of the LHC. The

mean values of the pile-up correction factors are about 1.02 for both the LHC13de and LHC13f data samples.

The correction factor F_{norm} is calculated run by run. Their mean value obtained with the two methods are reported in Table 5.4: the results with the two methods differ by about 1% from each other. In the following, the value obtained with the trigger scaler method, which is statistically more precise, will be used as a central value, while the difference between the two methods is used as a systematic uncertainty.

	LHC13de		LHC13f	
F_{norm}	Offline	Scaler	Offline	Scaler
MSH	1021.1	1032.8	794.5	798.3

Table 5.4: Mean values of the normalisation factors for muon single high triggers obtained with the two methods described in the text.

5.7 Systematic uncertainties

5.7.1 W and Z boson generation

The MC templates of muons from $W^{\pm}$ and Z°/γ^{*} boson decays have been obtained from the realistic simulations described in Section 5.3. The generator used is POWHEG with the CT10 Parton Distribution Functions and the EPS09 nuclear modification of PDFs. The systematic uncertainties on the template inputs can be assessed by varying the settings of the PDFs.

The effect of a change in the input PDFs set can be first estimated at the generation level, by comparing the MC kinematic distributions of muons from the decay of $W^{\pm}$ bosons produced with different PDF sets. The results are shown in Figures 5.8 and 5.9. The effect, however, is small compared to the statistical and other systematic uncertainties.

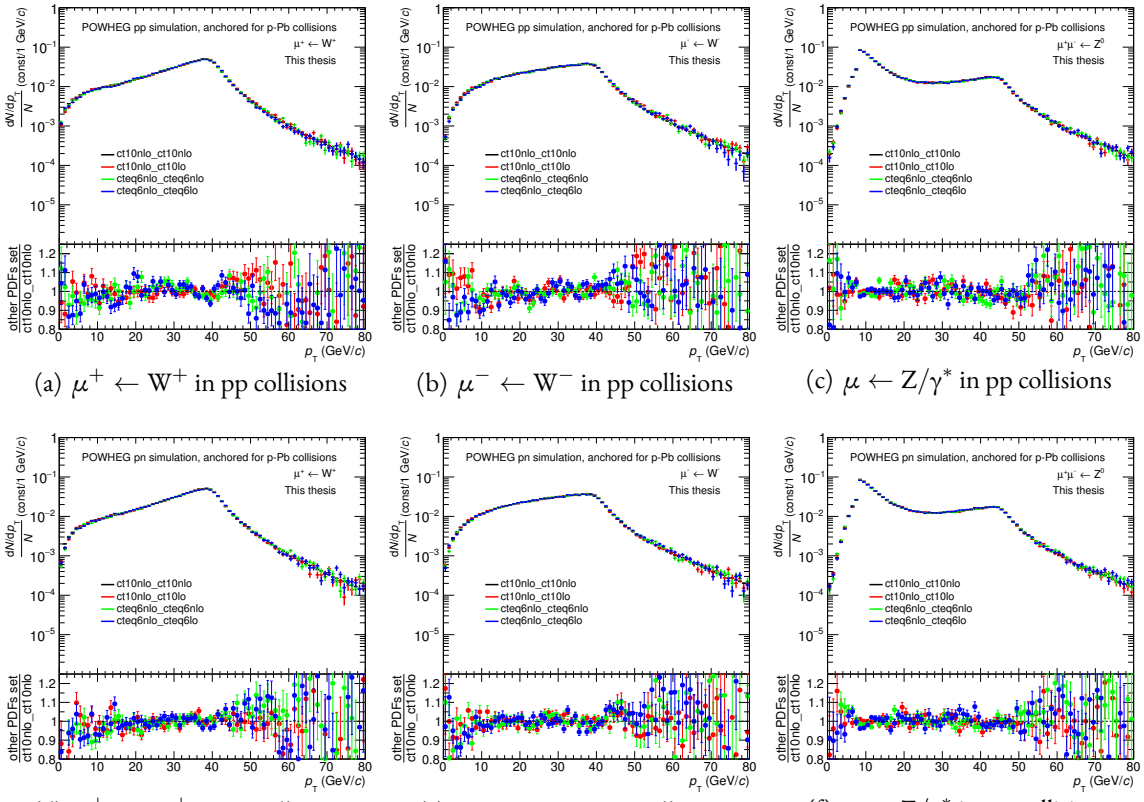

(a) $\mu^+ \leftarrow \mathrm{W}^+$ in pp collisions (b) $\mu^- \leftarrow \mathrm{W}^-$ in pp collisions (c) $\mu \leftarrow \mathrm{Z}/\gamma^*$ in pp collisions

(d) $\mu^+ \leftarrow \mathrm{W}^+$ in pn collisions (e) $\mu^- \leftarrow \mathrm{W}^-$ in pn collisions (f) $\mu \leftarrow \mathrm{Z}/\gamma^*$ in pn collisions

Figure 5.8: Ratio of p_{T}MC kinematic distributions of muons from $\mathrm{W}^{\pm}$ and $\mathrm{Z}^{\circ}/\gamma^*$ decay produced with POWHEG using different PDFs for p-Pb collisions.

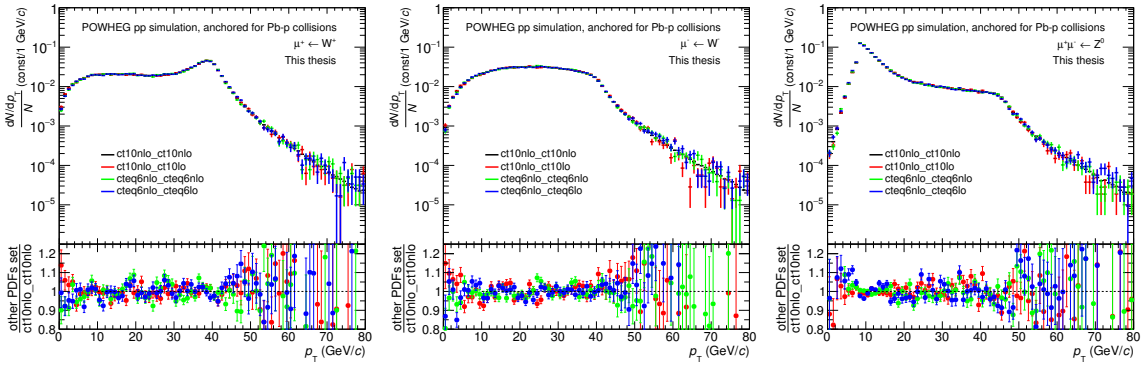

(a) $\mu^+ \leftarrow \mathrm{W}^+$ in pp collisons

(b) $\mu^- \leftarrow \mathrm{W}^-$ in pp collisions

(c) $\mu \leftarrow \mathrm{Z}/\gamma^*$ in pp collisions

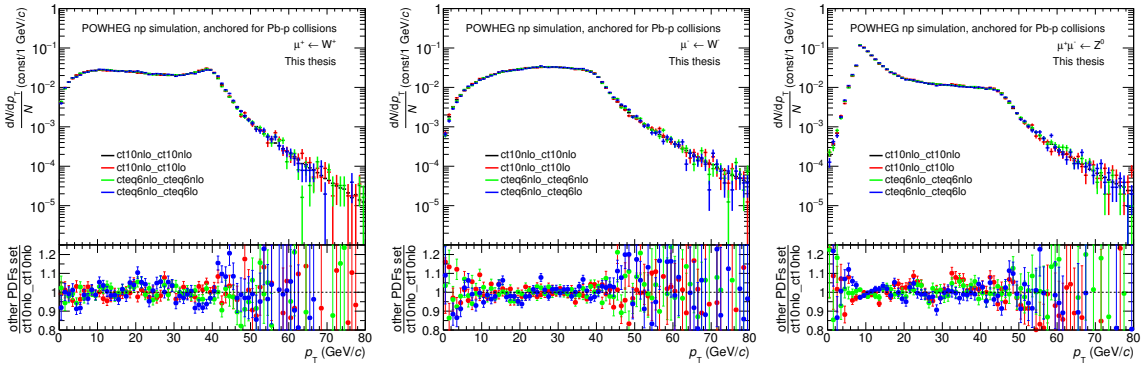

(d) $\mu^+ \leftarrow \mathrm{W}^+$ in np collisions

(e) $\mu^- \leftarrow \mathrm{W}^-$ in np collisions

(f) $\mu \leftarrow \mathrm{Z}/\gamma^*$ in np collisions

Figure 5.9: Ratio of p_{T} MC kinematic distributions of muons from $\mathrm{W}^{\pm}$ and $\mathrm{Z}^{\circ}/\gamma^*$ decay produced with POWHEG using different PDFs for Pb-p collisions.

5.7.2 The component of $Z^{\circ}/\gamma^{*} \rightarrow \mu$

The ratio "R" between the component of $Z^{\circ}/\gamma^{*}$and $W^{\pm}$ in Eq. 5.2 is not a free parameter, but it is rather fixed according to the values of cross section provided by POWHEG. The use of different PDFs sets affects both the shapes of the templates and the cross sections, thus resulting in a variation of the parameter "R". The uncertainty on the contribution of muons from Z°/γ^{*} decays is accounted for automatically by extracting the signal using the values of $N_{\mu\leftarrow Z/\gamma^{*}}/N_{\mu\leftarrow W}$ obtained with POWHEG.

5.7.3 Alignment effect

An example of the modification of the p_{T} distributions can be seen in Figure 5.10, showing the ratio of the p_{T} distributions of muons from W boson decays obtained with two different residual alignment files (see Section 3.5.3). But these two alignment files seem underestimate the alignment effect. In this case, we consider to implement resolution task provided by Philippe Pillot, which use Breit Wigner function to parameterize resolution of clusters in tracking chambers and propagate them to reconstructed tracks. An example of the modification of the p_{T} distributions after applying resolution task can be seen in Figure 5.11.

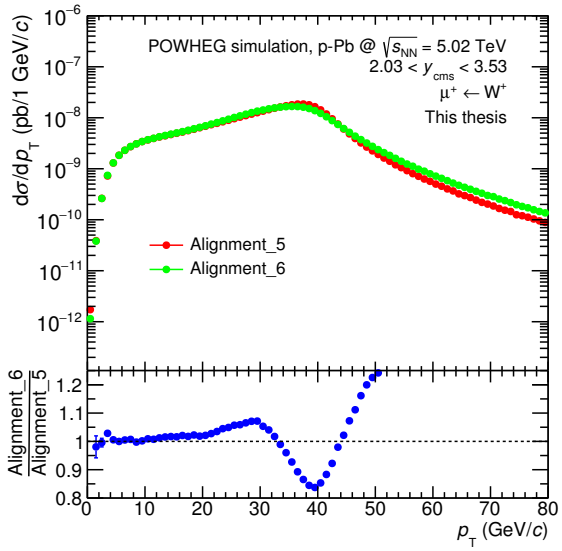

(a) $\mu^+ \leftarrow W^+$, anchored to LHC13d+LHC13e

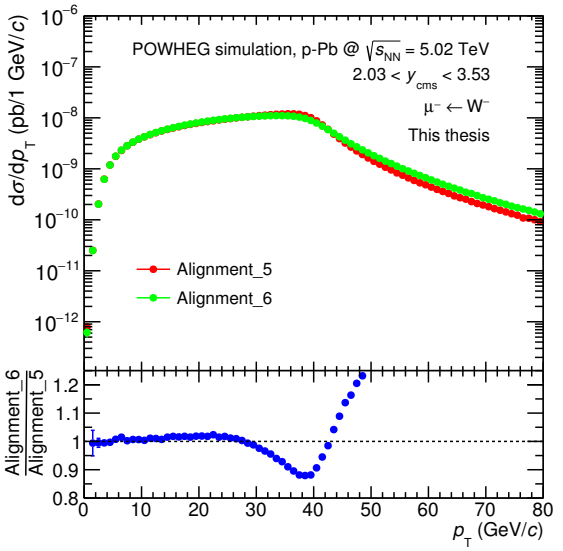

(b) $\mu^- \leftarrow W^-$, anchored to LHC13d+LHC13e

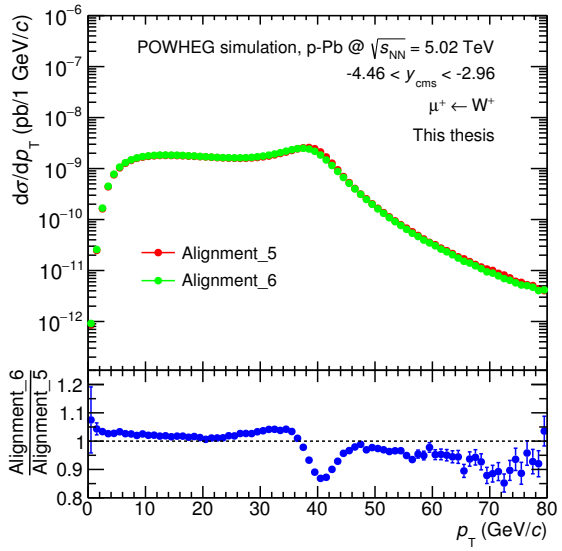

(c) $\mu^+ \leftarrow W^+$, anchored to LHC13f

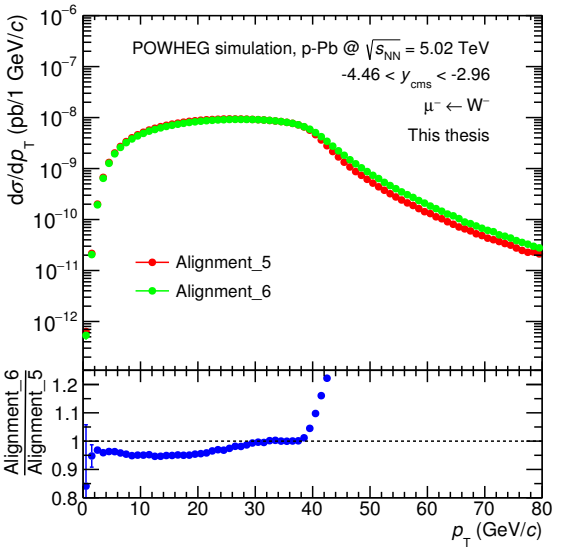

(d) $\mu^- \leftarrow W^-$, anchored to LHC13f

Figure 5.10: Ratio of transverse momentum distributions of muons from $W^{\pm}$ decays reconstructed with different residual alignment files.

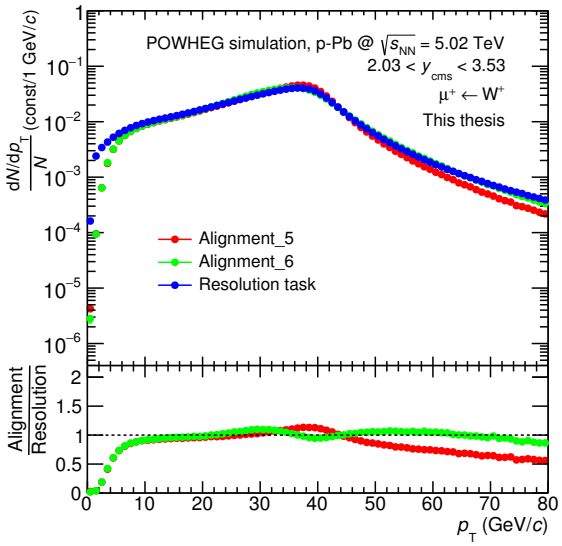

(a) $\mu^+ \leftarrow W^+$, anchored to LHC13d+LHC13e

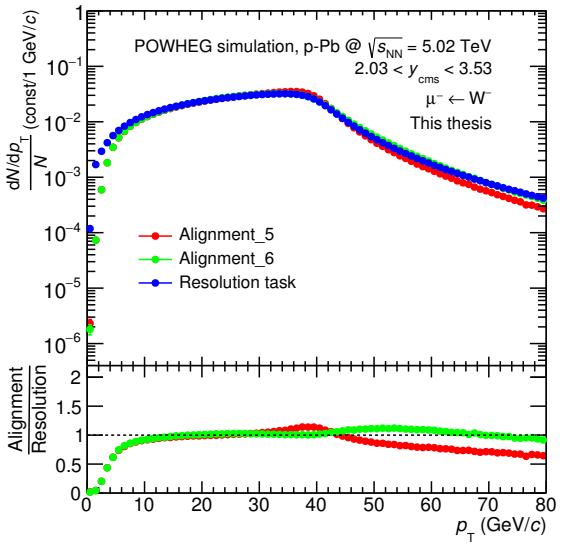

(b) $\mu^- \leftarrow W^-$, anchored to LHC13d+LHC13e

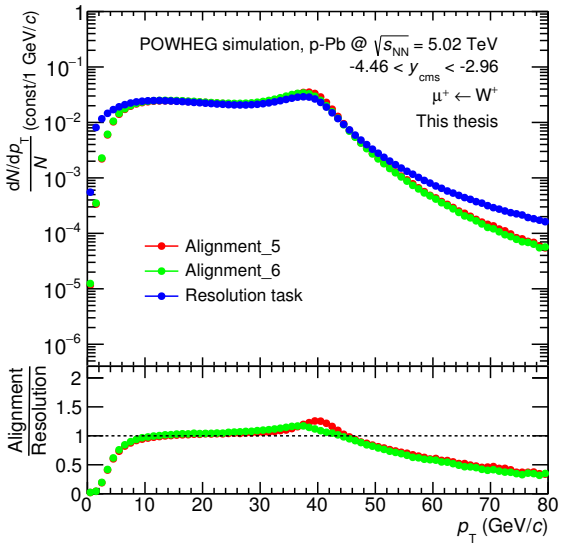

(c) $\mu^+ \leftarrow W^+$, anchored to LHC13f

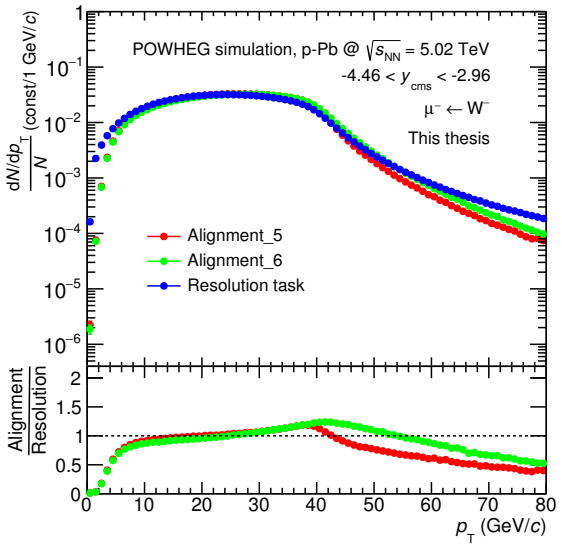

(d) $\mu^- \leftarrow W^-$, anchored to LHC13f

Figure 5.11: Ratio of transverse momentum distributions of muons from $W^{\pm}$ decays reconstructed after applying resolution task.

5.7.3.1 Choice of description function

Figure 5.12 presents the distribution of the distance between cluster and reconstructed track per chamber in y direction. It shows that alignments can not reproduce the large tails of the measured cluster resolution. Thus the fast simulation based on the propagation of the measured cluster resolution (resolution task) was done in order to further study the alignment. In resolution task, one need to choose an appropriate function to describe this cluster resolution distribution. From Figure 5.13, we can find that the Gaussian function can not describe the large tail and Breit-Wigner function overestimates it. While Crystal-Ball function situates between them. The effects of different functions on p_{T} distribution are shown in Figure 5.14. It also indicates that the Crystal-Ball function is the best choice.

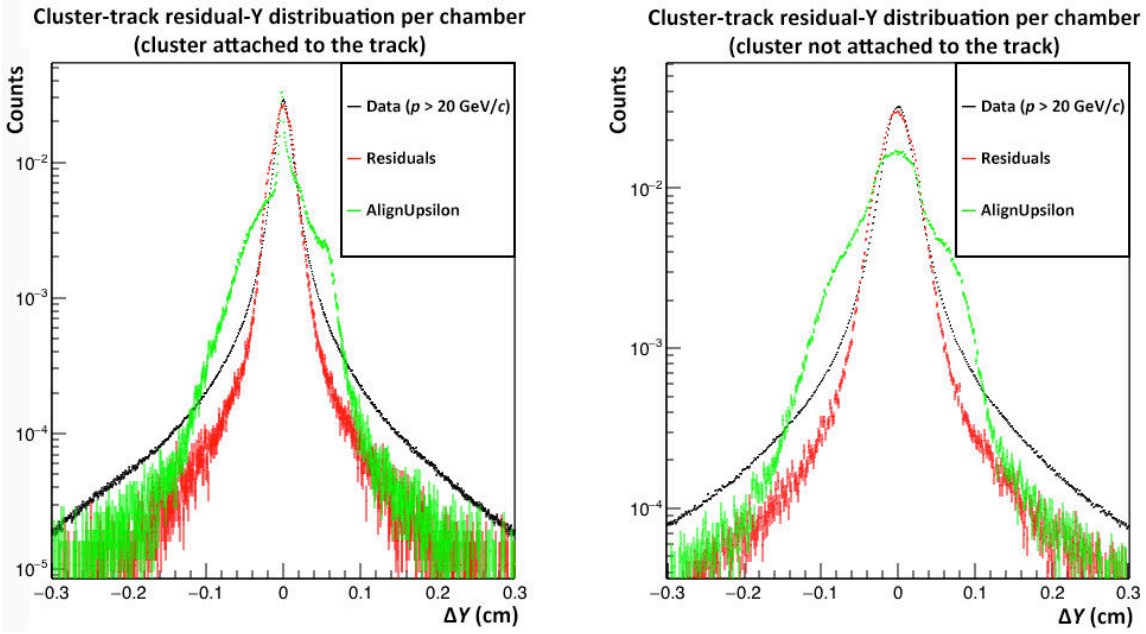

Figure 5.12: The distribution of the distance between cluster and reconstructed track per chamber in y direction in Data and alignments. The cut of momentum $p > 20$ GeV/c is added.

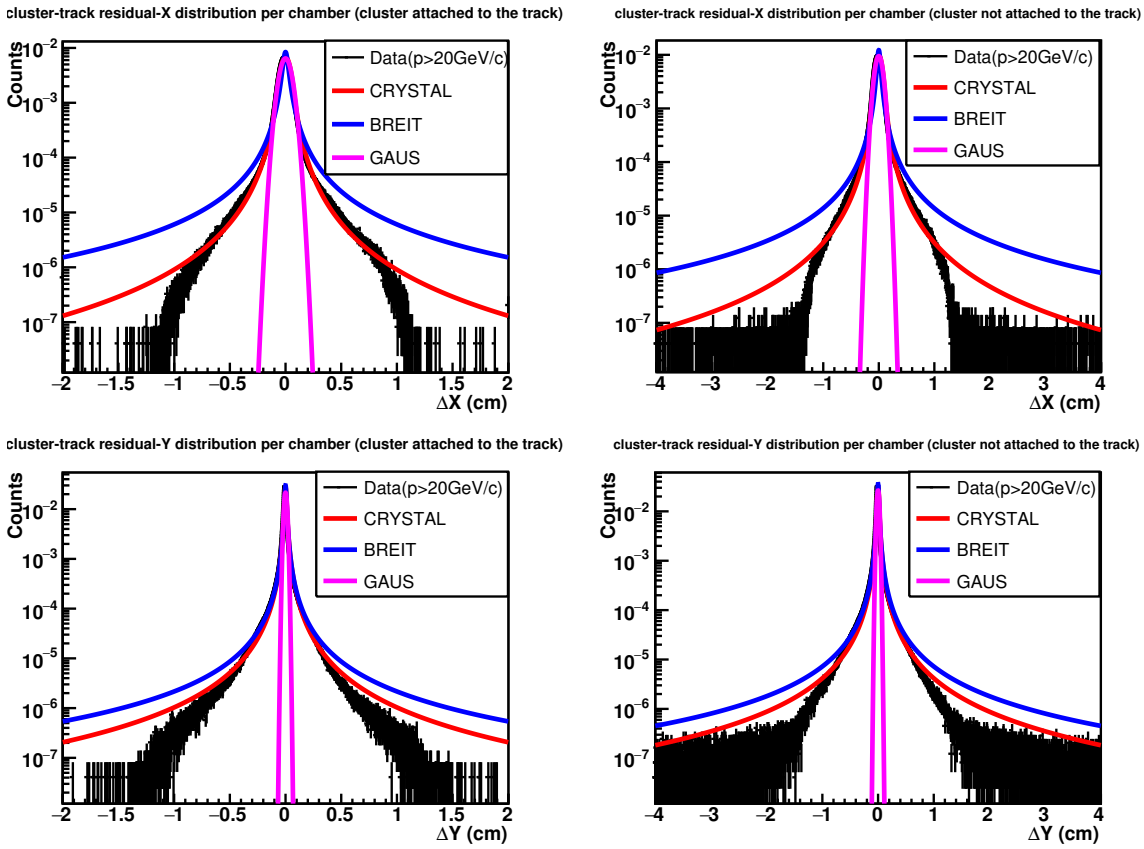

Figure 5.13: The distribution of the distance between cluster and reconstructed track per chamber in x and y direction in Data and resolution task with different description functions. The cut of momentum $p > 20$ GeV/c is added. The blue line represents Breit-Wigner function, the red line represents Crystal-Ball function and the pink line represents Gaussian function.

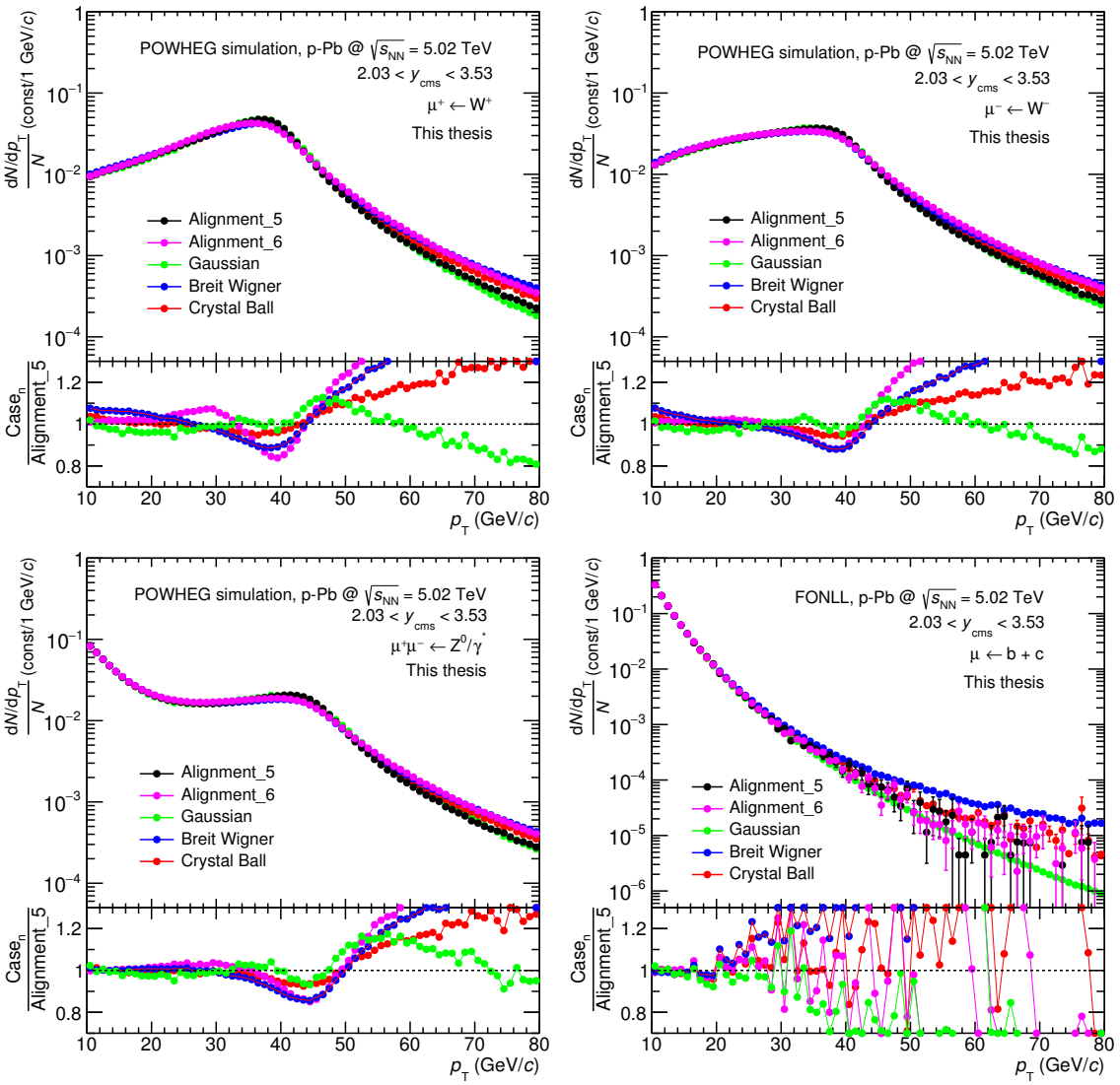

Figure 5.14: The effects of two alignment files and three functions on p_T distribution for muons from $W^{\pm}$, Z°/γ^* and FONLL decay.

5.7.3.2 Add "global shift" effect

As we know, from LHC13d to LHC13e period, the direction of magnetic field changed. This may cause a global shift of tracking chamber, which is expected to affect in opposite directions for the positive and negative charged particles. For instance, there is negative direction shift for positive charged particles and positive direction shift for negative charged particle in LHC13d period, while in LHC13e period there should be positive direction shift for positive charged particles and negative direction shift for negative charged particles. The question is how much is this global shift and how to make sure the direction? One possibility is to check muon charge ratio ($\frac{\mu^+}{\mu^-}$) in each period and double charge ratio ($\frac{(\mu^+/\mu^-)_{\text{LHC13d}}}{(\mu^+/\mu^-)_{\text{LHC13e}}}$) between data and MC simulations.

In Section 5.4.3, from the example of combined fit, we can find that in $10 < p_{\text{T}} < 15$ GeV/c, the dominated contribution is muons from heavy-flavour decays. The fraction of muons from weak bosons decay is negligible and can be ignored. Thus we can tune the parameter of global shift to make the muon charge ratio and double charge ratio consistent between FONLL–based MC simulations and data. Table 5.5 lists results with different shift σ. After comparison, the value of 2.6σ is decided to be used in the resolution task. A further cross-check with 2.6σ shift was done in Figure 5.15, Figure 5.16 and Figure 5.17. The distributions of muon charge ratio and double charge ratio ($\frac{(\mu^+/\mu^-)_{\text{MC}}}{(\mu^+/\mu^-)_{\text{data}}}$) as a function of p_{T} are compatible between data and FONLL-based MC simulations in each period.

	Data	MC (1σ)	MC (2σ)	MC (3σ)
Charge ratio in LHC13d	1.198±0.026	1.079±0.010	1.153±0.011	1.233±0.011
Charge ratio in LHC13e	0.828±0.017	0.928±0.009	0.868±0.008	0.812±0.008
Double charge ratio	1.446±0.044	1.162±0.015	1.328±0.017	1.518±0.020

MC (2.5σ)	MC (2.6σ)	MC (2.7σ)	MC (2.8σ)	MC (2.9σ)
1.192±0.011	1.199±0.011	1.207±0.011	1.215±0.011	1.224±0.011
0.840±0.008	0.835±0.008	0.830±0.008	0.824±0.008	0.818±0.008
1.420±0.019	1.436±0.019	1.455±0.019	1.475±0.019	1.496±0.020

Table 5.5: The muon charge ratio and double charge ratio in $10 < p_{\text{T}} < 15$ GeV/c in data and FONLL–based MC simulations with different value of shift.

The examples of combined fit with FONLL, W, Z templates obtained by resolution task after adding "global shift" effect are shown in Figure 5.18. The number of extracted W^+ yield decreases 10.95% in LHC13d and increases 28.12% in LHC13d. The number of extracted W^- yield increase 38.33% and decrease 12.52% in LHC13e. Considering this different effects of the "global shift" on

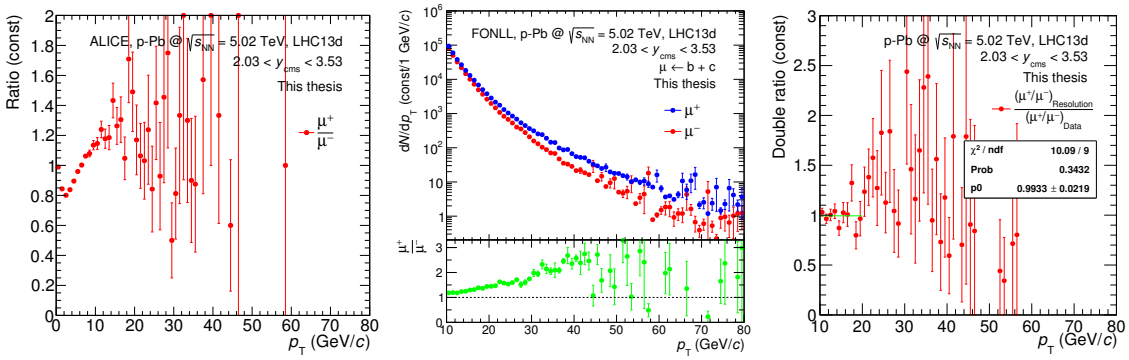

(a) LHC13d: $\frac{\mu^+}{\mu^-}$ vs. p_T in data (b) LHC13d: $\frac{\mu^+}{\mu^-}$ vs. p_T in FONLL (c) LHC13d: $\frac{(\mu^+/\mu^-)_{MC}}{(\mu^+/\mu^-)_{data}}$

Figure 5.15: The distributions of muon charge ratio and double charge ratio ($\frac{(\mu^+/\mu^-)_{MC}}{(\mu^+/\mu^-)_{data}}$) as a function of p_T in LHC13d.

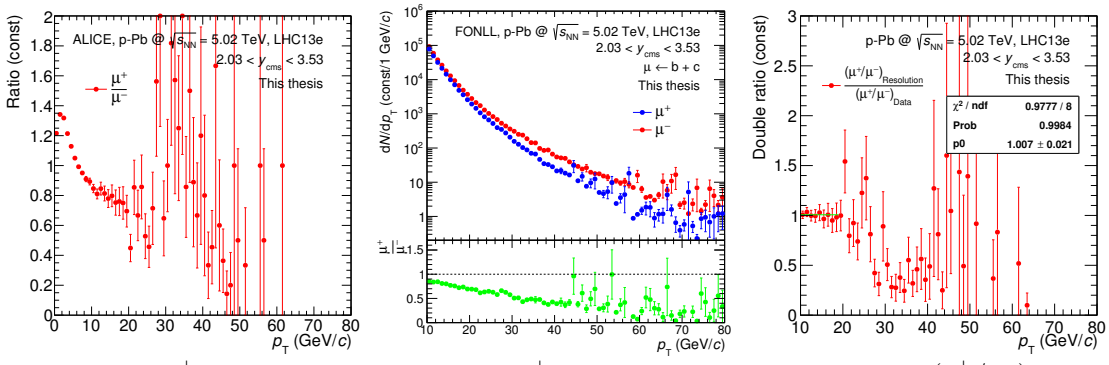

(a) LHC13e: $\frac{\mu^+}{\mu^-}$ vs. p_T in data (b) LHC13e: $\frac{\mu^+}{\mu^-}$ vs. p_T in FONLL (c) LHC13e: $\frac{(\mu^+/\mu^-)_{MC}}{(\mu^+/\mu^-)_{data}}$

Figure 5.16: The distributions of muon charge ratio and double charge ratio ($\frac{(\mu^+/\mu^-)_{MC}}{(\mu^+/\mu^-)_{data}}$) as a function of p_T in LHC13e.

W^+ and W^- between LHC13d and LHC13e, we decide to extract W yield in LHC13d and LHC13e separately, then sum them together.

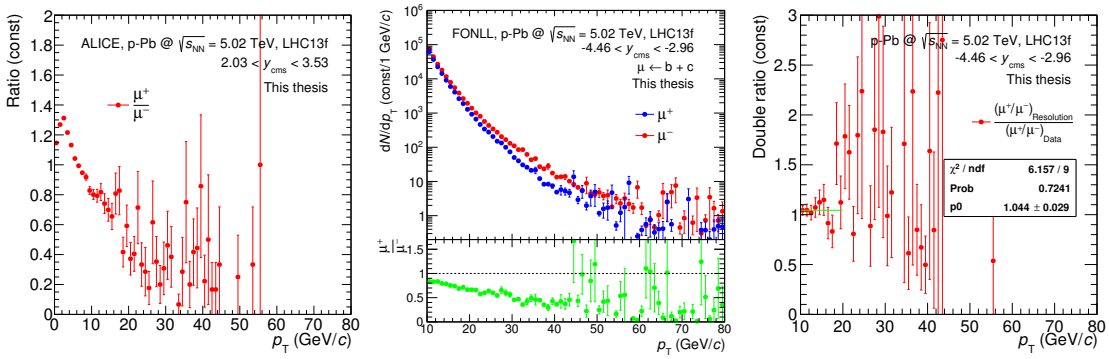

(a) LHC13f: $\frac{\mu^+}{\mu^-}$ vs. p_{T} in data (b) LHC13f: $\frac{\mu^+}{\mu^-}$ vs. p_{T} in FONLL (c) LHC13f: $\frac{(\mu^+/\mu^-)_{\mathrm{MC}}}{(\mu^+/\mu^-)_{\mathrm{data}}}$

Figure 5.17: The distributions of muon charge ratio and double charge ratio ($\frac{(\mu^+/\mu^-)_{\mathrm{MC}}}{(\mu^+/\mu^-)_{\mathrm{data}}}$) as a function of p_{T} in LHC13f.

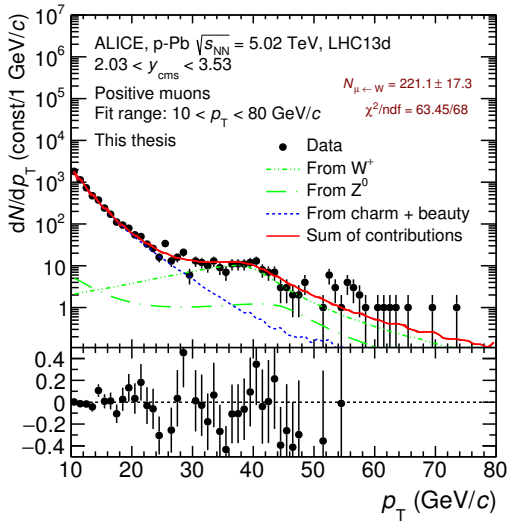

(a) LHC13d, μ^+: fit without "global shift"

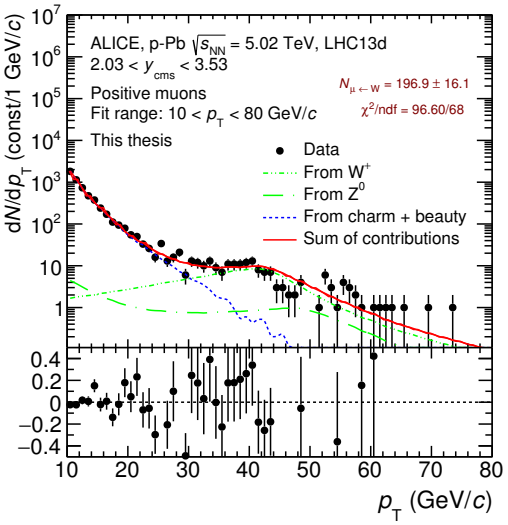

(b) LHC13d, μ^+: fit with "global shift"

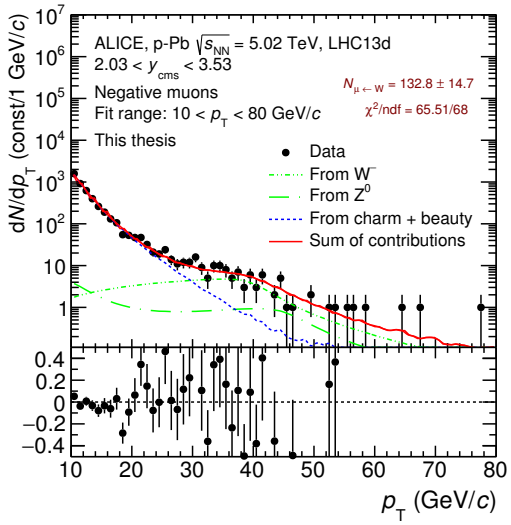

(c) LHC13d, μ^-: fit with "global shift"

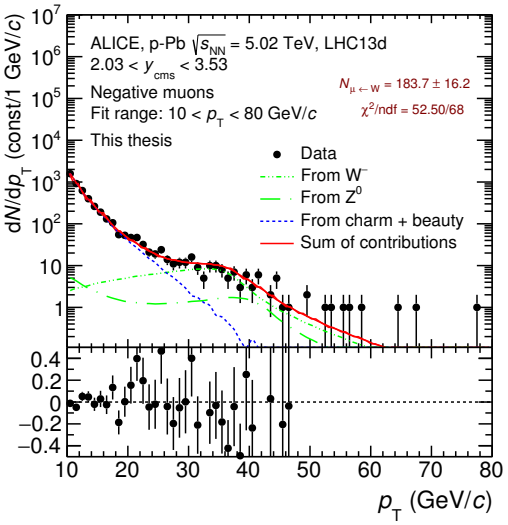

(d) LHC13d, μ^-: fit without "global shift"

Figure 5.18: The combined fit to raw data with FONLL, W, Z templates obtained by resolution task with and without "global shift".

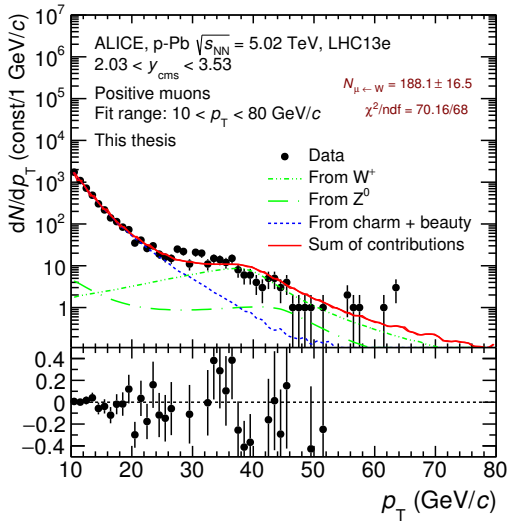

(e) LHC13e, μ^+: fit without "global shift"

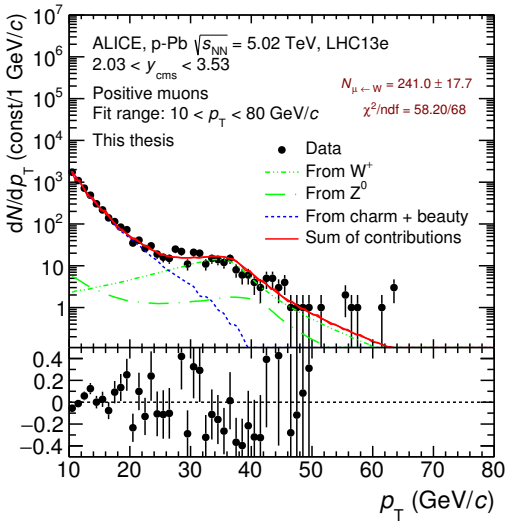

(f) LHC13e, μ^+: fit with "global shift"

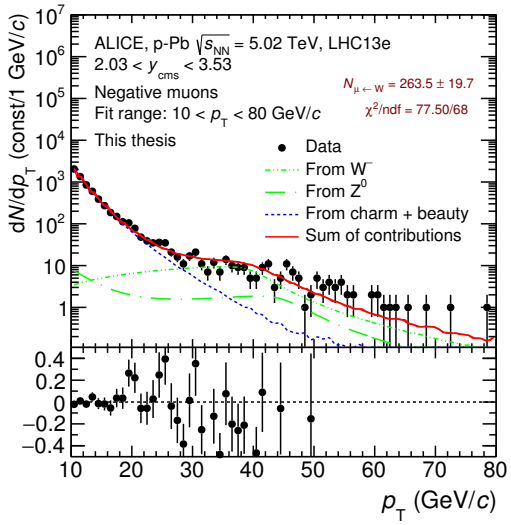

(g) LHC13e, μ^-: fit with "global shift"

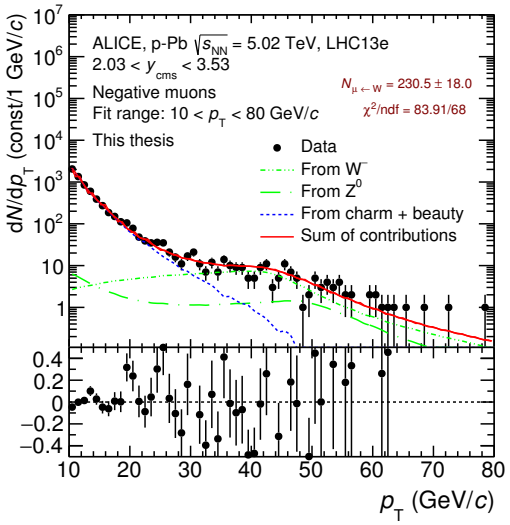

(h) LHC13e, μ^-: fit without "global shift"

Figure 5.18: The combined fit to raw data with FONLL, W, Z templates obtained by resolution task with and without "global shift".

5.7.3.3 Add detector efficiency

In the fast simulation, the momentum resolution is estimated from the parameterized cluster resolution. The effect of the detector efficiency is instead accounted for by using an Acc. × Eff. matrix as a function of the generated muon p_{T} and η. The matrix is built using the full simulations described in Section 5.5. The Acc. × Eff. matrix for μ^+ and μ^- from W boson decays is shown in Figure 5.19. It should be done for the simulations of muons from heavy-flavour, W-boson and Z-boson decay respectively.

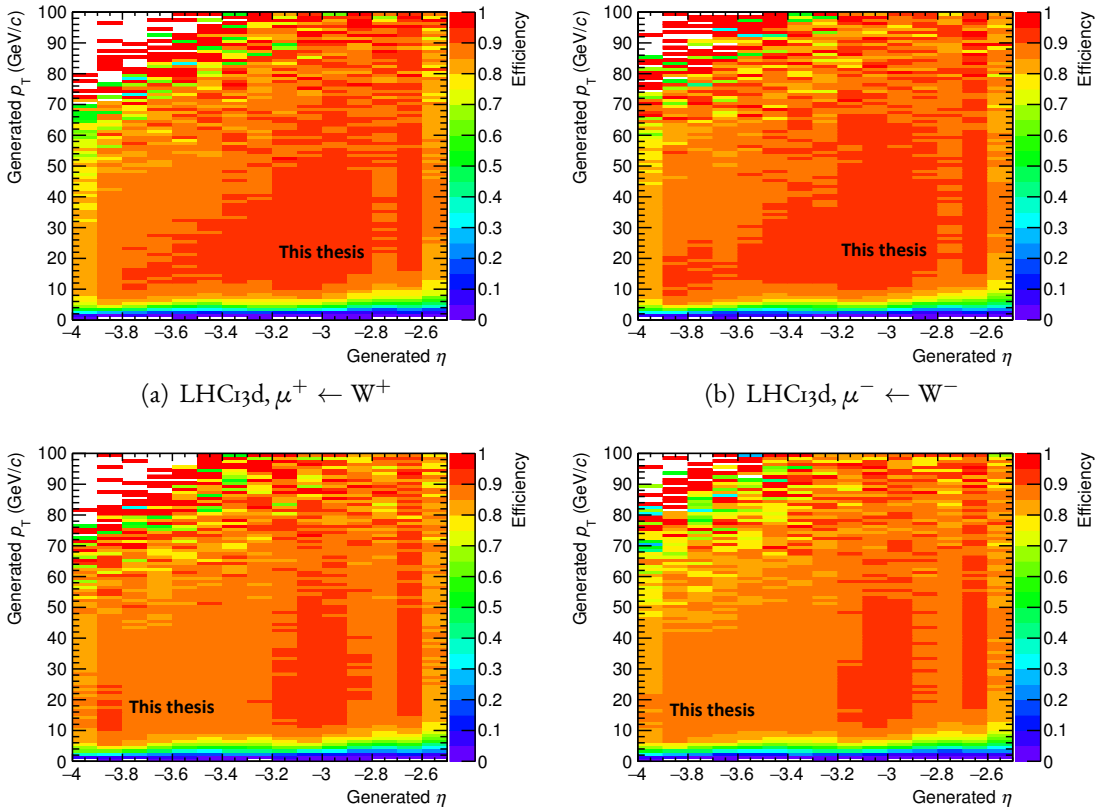

(a) LHC13d, $\mu^+ \leftarrow \mathrm{W}^+$ (b) LHC13d, $\mu^- \leftarrow \mathrm{W}^-$

(c) LHC13e, $\mu^+ \leftarrow \mathrm{W}^+$ (d) LHC13e, $\mu^- \leftarrow \mathrm{W}^-$

Figure 5.19: The Acc. × Eff. matrix of generated p_{T} and η for $\mu^+ \leftarrow \mathrm{W}^+$ and $\mu^- \leftarrow \mathrm{W}^-$ in LHC13d and LHC13e.

The number of muons from $W^{\pm}$ decays is then extracted according to the fit procedure described in Section 5.4.2, but using the Z°/γ^{*} and $W^{\pm}$ boson templates, as well as the FONLL-based MC template (when used to describe the background) obtained with "alignment_6" and resolution task. The results are shown in Figure 5.20 and Figure 5.21.

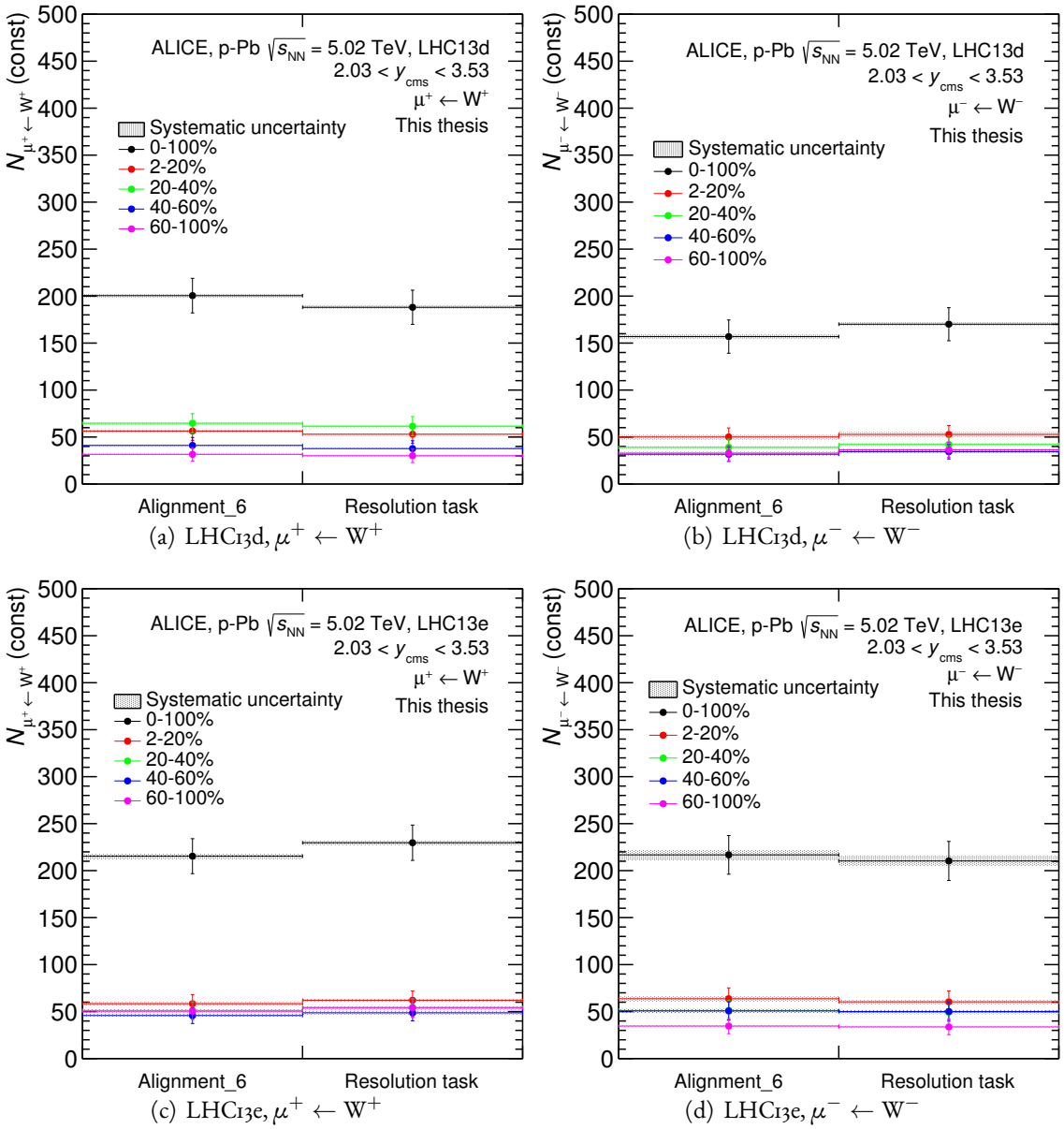

Figure 5.20: Number of muons from $W^{\pm}$ decays extracted with templates obtained from simulations reconstructed from residual alignment file "alignment_6" and resolution task in p–Pb collisions.

The systematic on alignment can be assessed by extracting the number of muons from $W^{\pm}$ decays using templates obtained with the new alignment file and resolution task, thus putting all

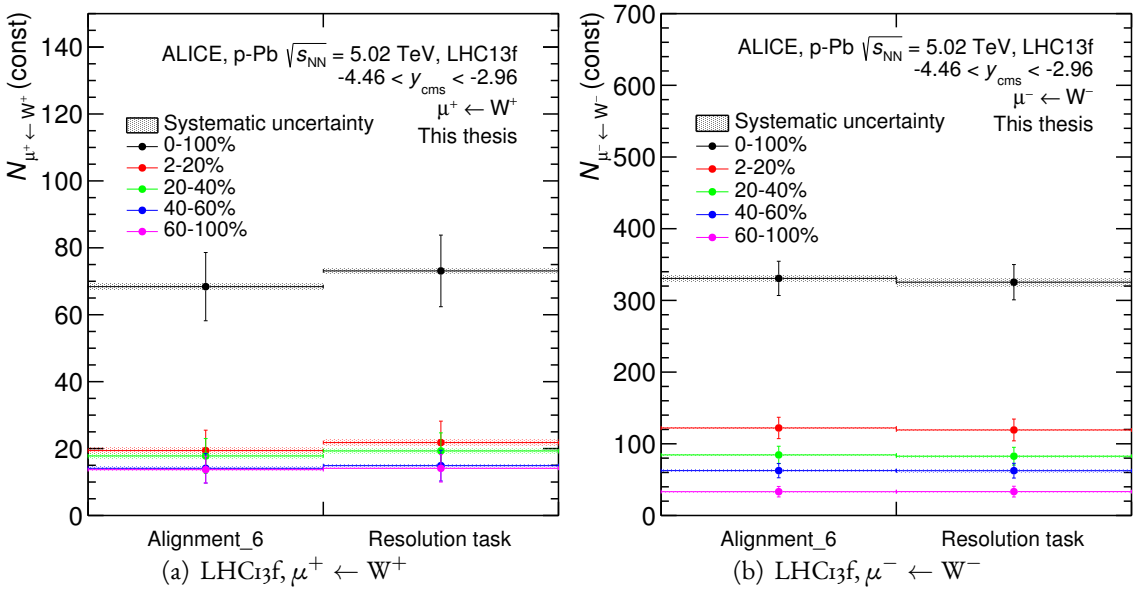

(a) LHC13f, $\mu^+ \leftarrow W^+$ (b) LHC13f, $\mu^- \leftarrow W^-$

Figure 5.21: Number of muons from $W^{\pm}$ decays extracted with templates obtained from simulations reconstructed from different residual alignment file "alignment_6" and resolution task in Pb–p collisions.

of the values together with equations 5.7, 5.8 and 5.9. Please note that here and in the following analysis, the resolution task is used to calculate the central value and statistic uncertainty of W yield, while the new alignment file ("alignment_6") is only used to the systematic uncertainty estimation.

5.7.4 Tracking/trigger efficiency

The uncertainty on the muon tracking efficiency is estimated from the difference between the muon tracking efficiency in MC and that from a data-driven approach based on the redundancy of the tracking stations [139]. It amounts to 2% (3%) for the p-going (Pb-going) period. The uncertainty on trigger efficiency, which is mainly due to the systematic uncertainty in the determination of the efficiency of each trigger chamber from data, amounts to 1%. An additional systematic uncertainty of 0.5% results from the choice of the χ^2 cut in the matching of the tracks reconstructed in the tracker with those in the trigger. The systematic are summarised in Table 5.6.

The trigger systematic only accounts for the effect of the uncertainty on the trigger chamber efficiency. The uncertainty related to the trigger response function affects only the transverse momenta close to the p_T threshold of about 4.2 GeV/c, and has hence a negligible impact in the p_T region of interest for this analysis.

The tracking and trigger uncertainties affect the yields of the reconstructed particles. We

	Systematic
Tracking	2% (p–Pb), 3% (Pb–p)
Trigger	1%
Tracker-trigger matching	0.5%

Table 5.6: Tracking, trigger and tracker-trigger matching systematic uncertainties for muon tracks in the LHC13d and LHC13e periods.

assume that they are uncorrelated versus p_T which would hence lead to an uncertainty of the shape of the measured transverse momentum distribution.

Ideally, the effect should be studied by applying the uncertainties to the MC templates of Section 5.3 and taking them properly into account during the fit. Technically, this is equivalent to add the systematic uncertainty in quadrature to the statistical uncertainty of the raw p_T distributions, which will then be taken into account in the fit.

The procedure to estimate the resulting systematic uncertainties on $N_{\mu\leftarrow W}$ can be summarised as:

- Extract $N_{\mu\leftarrow W}$ without accounting for the tracking/trigger systematic uncertainties. The obtained value is $N^{\text{bias}}_{\mu\leftarrow W} \pm \sigma_{\text{stat}}$
- Sum the systematic uncertainties of Table 5.6 to the statistical uncertainties of the raw data, for each bin in p_T .
- Extract $N_{\mu\leftarrow W}$: the obtained value is $N_{\mu\leftarrow W} \pm \sigma_{\text{stat+syst}}$
- Get the contribution of the systematic uncertainties on tracking/trigger as: $\sigma^2_{\text{track/trig}} = \sigma^2_{\text{stat+syst}} - \sigma^2_{\text{stat}}$

The resulting systematic error on $N_{\mu\leftarrow W}$ is summarised in Table 5.7. It is worth noting that the

Multiplicity	$\sigma_{\text{track/trig}}$
0–100%	2.65%
5–20%	-
20–40%	1.43%
40–60%	-
60–80%	1.77%

Table 5.7: Systematic error on $N_{\mu\leftarrow W}$ due to the uncertainties on tracking and trigger efficiencies as well as tracker/trigger matching. The"-" means that the procedure described in the text returned a negative quadratic uncertainty.

square of the systematic uncertainty obtained from the quadratic difference of $\sigma_{\text{stat+syst}}$ and σ_{stat}

may return negative values for certain bins in multiplicity. This is mainly due to the fact that the systematic effect is small compared to the large fluctuations due to the fit. A conservative estimation of the systematic error, may be obtained by considering the uncertainties as fully correlated versus p_T . In this case, the three values of systematic uncertainties of Table 5.6, would sum quadratically to the systematic error on the extracted number of muons from $W^{\pm}$ decay. The error would hence be 2.3% for p–Pb and 3.2% for Pb–p, which are in fairy good agreement with the value extracted with the previously described procedure in the bin 0–100%.

5.7.5 Pile-up effect

In p-Pb data taking, the bunch spacing is 200 ns. In the data selection, since the muon tracks are requested to match with the muon trigger which has a time resolution of 25 ns, the reconstructed muon events are not sensitive to pile-up from different bunches. V0A has also a small timing resolution and the SPD has an integration time of $\pm$150 ns and a very small contribution from pile-up from different bunches is expected. Therefore pile-up events from other bunches are expected to be negligible for the detectors used for this analysis. In the following, pile-up will always refer to pile-up from the same bunch crossing.

Due to the effect of pile-up, the particle multiplicity and the energy deposit in ZN of two separate events sum up, thus biasing the centrality determination towards the most central collisions. The pile-up bias was estimated as described here [194]. The pile-up events are flagged using the information of the SPD. In particular, it is possible to check if more than one vertex is reconstructed per event. A pile-up vertex is considered if it is estimated from a minimum number of contributors (n) and if the distance with respect to the primary vertex (d) is larger than a given value. Figure 5.22 shows the plots of the pile-up fraction as function of run number. MV stands for Multi-Vertexer. The MV option was proved to be efficient when using full tracks (measured with the full ITS and in addition the TPC). However the muon production uses SPD tracklets and this can affect the purity and efficiency of the MV pile-up option. As seen in the plots, the hardware level pile-up rejection, which is estimated as explained in Section 5.6, is compared with the software level pile-up tagging using the SPD. In order to estimate the effect of pile-up on the number of events the n = 4 option was chosen since it exhibits the highest efficiency $\sim$0.85. For ZN, this method was found to provide consistent results with respect to a toy MC, where the deposited energy fraction in the ZN is sampled from a measurement at low multiplicity, and the pile-up probability is simulated assuming a Poisson distribution.

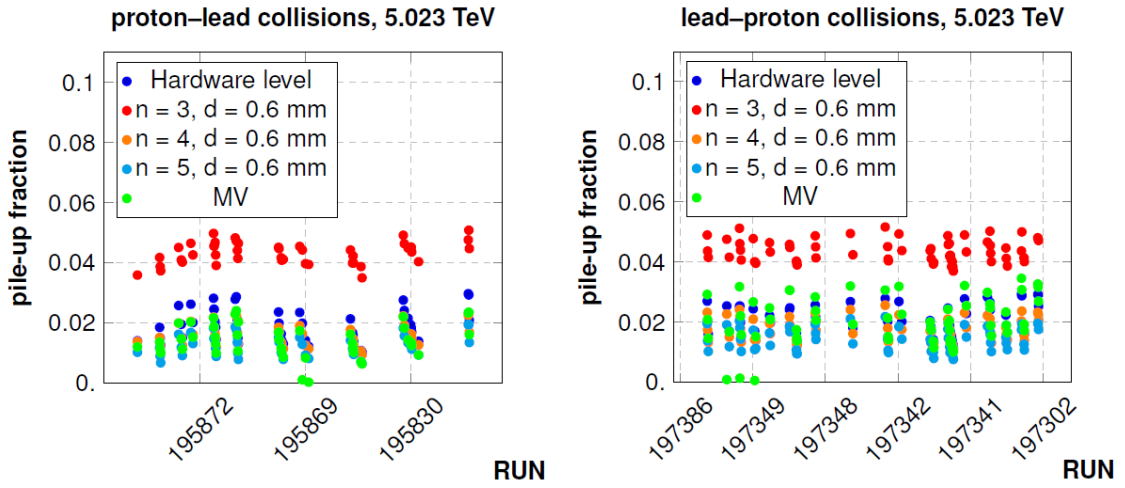

Figure 5.22: Pile-up fractions as function of run number. Hardware level compared to software level pile up based on SPD.

The estimated contamination for different centrality estimators is shown in Figure 5.23: the contamination decreases from central to peripheral collisions. It is very large in the 0-2% centrality class, while it becomes of the order of few percent for 2-20%. The 0-2% centrality class was therefore excluded from the analysis.

The systematics of pile-up effect based on the events tagged with SPD for p-going and Pb-going period are summarized in Table 5.8. In centrality 2-20%, the systematic of pile-up effect from VZERO and SPD are larger than ZN.

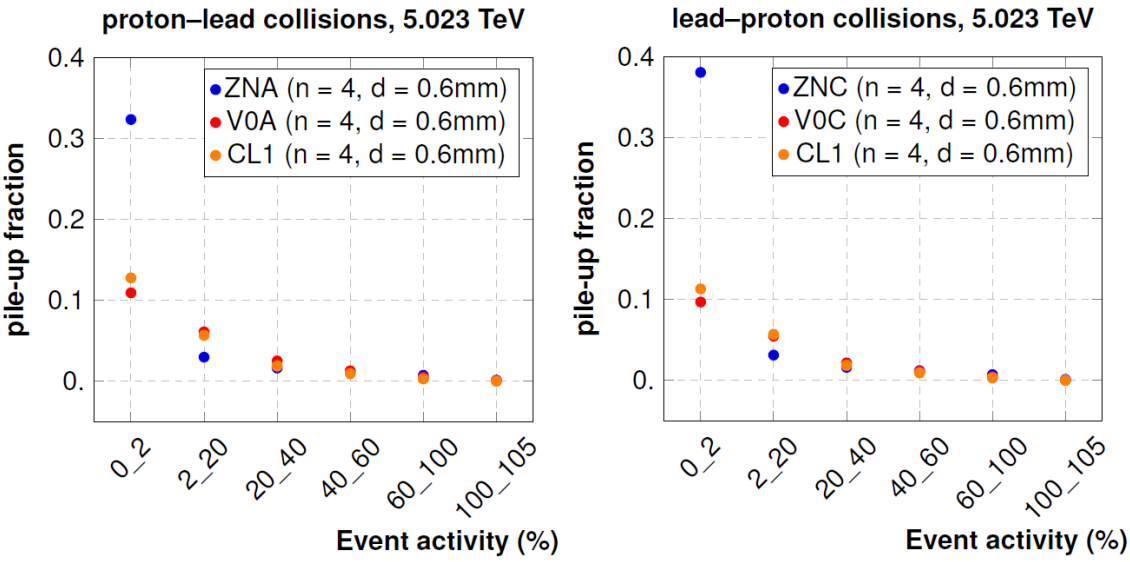

Figure 5.23: Pile-up fractions as function of event activity for different estimators. Pile-up events are tagged with the SPD requiring at least 4 tracks to come from a secondary vertex located 0.6 mm away from the primary vertex.

Estimator	Centrality (%)	Systematics(%)	Estimator	Centrality (%)	Systematics(%)
ZNA		3.35	ZNC		3.65
VoA	0_100	3.31	VoC	0_100	3.62
CL1		3.31	CL1		3.62
ZNA		2.96	ZNC		3.13
VoA	2_20	6.09	VoC	2_20	5.45
CL1		5.66	CL1		5.68
ZNA		1.62	ZNC		1.61
VoA	20_40	2.50	VoC	20_40	2.15
CL1		1.89	CL1		1.85
ZNA		1.21	ZNC		1.19
VoA	40_60	1.27	VoC	40_60	1.10
CL1		0.93	CL1		0.921
ZNA		0.726	ZNC		0.711
VoA	60_100	0.454	VoC	60_100	0.396
CL1		0.28	CL1		0.290

Table 5.8: Summary of pile-up systematics based on the events tagged with SPD for p-going and Pb-going period, respectively.

5.7.6 Combination of fit results

The fit is performed many times by varying the p_T range, the templates, the ratio $N_{\mu\leftarrow Z/\gamma^*}/N_{\mu\leftarrow W}$ etc., as explained above in this section. The number of muons extracted in each trial is then plotted as a function of the test number:

- (7 MC templates for background described in Section 5.4.1) × (4 PDFs sets for signal) × (different p_T ranges) × (1 alignment file ("alignment_6") + 1 resolution task (see Section 5.7.3))

The final number of muons from W-boson decays is the arithmetic average of the $N_{\mu\leftarrow W}$ extracted in each fit, defined as:

$$\langle N_{\mu\leftarrow W}\rangle = \frac{\sum_{i=1}^{n} N_{\mu\leftarrow W,i}}{n} \tag{5.7}$$

where i runs over the number of n trials performed and $N_{\mu\leftarrow W,i}$ is the number of muons from W decays extracted in each trial. The statistical error is given by the arithmetic average of the error on each trial:

$$\sigma_{\langle N_{\mu\leftarrow W}\rangle} = \frac{\sum_{i=1}^{n} \sigma_{\mu\leftarrow W,i}}{n} \tag{5.8}$$

Finally, the RMS of the distribution:

$$RMS = \sqrt{\frac{\sum_{i=1}^{n} N^2_{\mu\leftarrow W,i}}{n} - \langle N_{\mu\leftarrow W}\rangle^2} \tag{5.9}$$

is the systematic error. The results of extracted W yields are shown in Figures 5.24, 5.25, 5.26. The significant difference is caused by the misalignment of detector.

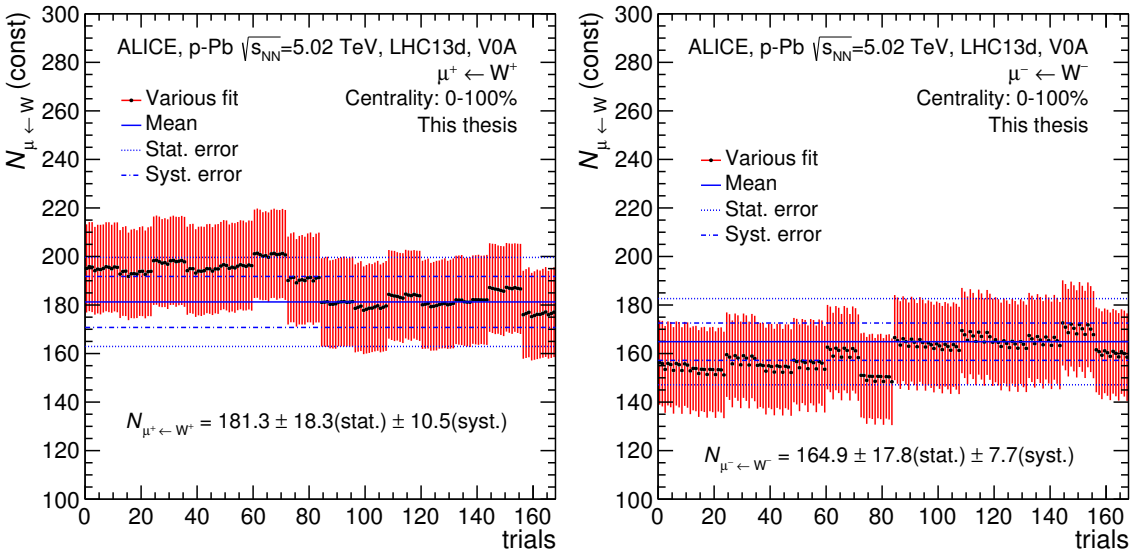

(a) $\mu^+ \leftarrow W^+$ (b) $\mu^- \leftarrow W^-$

Figure 5.24: LHC13d. Centrality: 0–100%, estimated with V0A. Raw number of muons from $W^{\pm}$ decays as a function of the trial. The solid line is the average number of muons from $W^{\pm}$ decays, estimated through Eq. 5.7 while the dashed (dot-dashed) line represent the statistical (systematic) uncertainty band, obtained with Eq. 5.8 (Eq. 5.9).

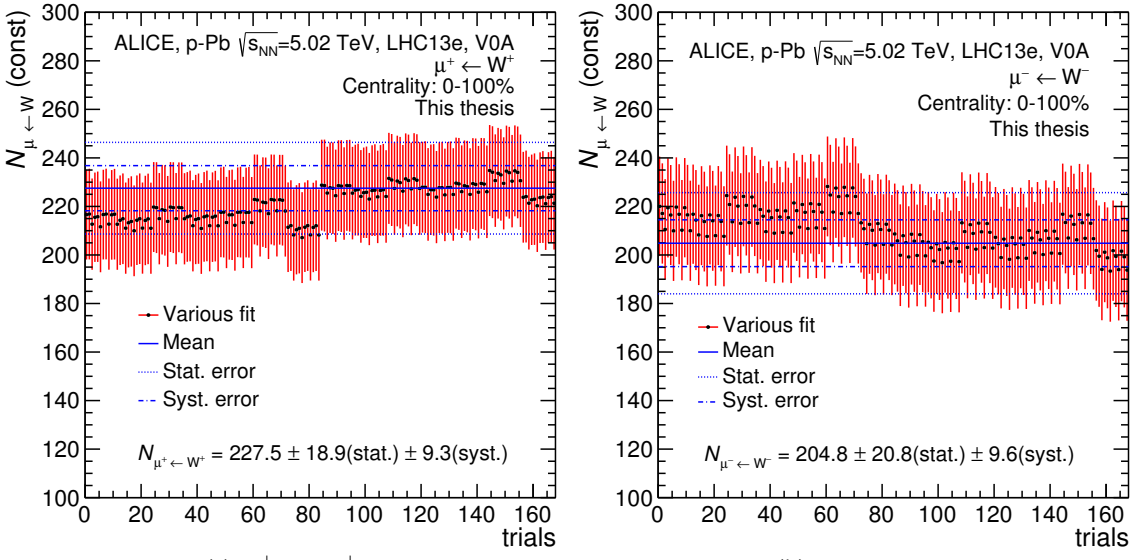

(a) $\mu^+ \leftarrow W^+$ (b) $\mu^- \leftarrow W^-$

Figure 5.25: LHC13e. Centrality: 0–100%, estimated with V0A. Raw number of muons from $W^{\pm}$ decays as a function of the trial. The solid line is the average number of muons from $W^{\pm}$ decays, estimated through Eq. 5.7 while the dashed (dot-dashed) line represent the statistical (systematic) uncertainty band, obtained with Eq. 5.8 (Eq. 5.9).

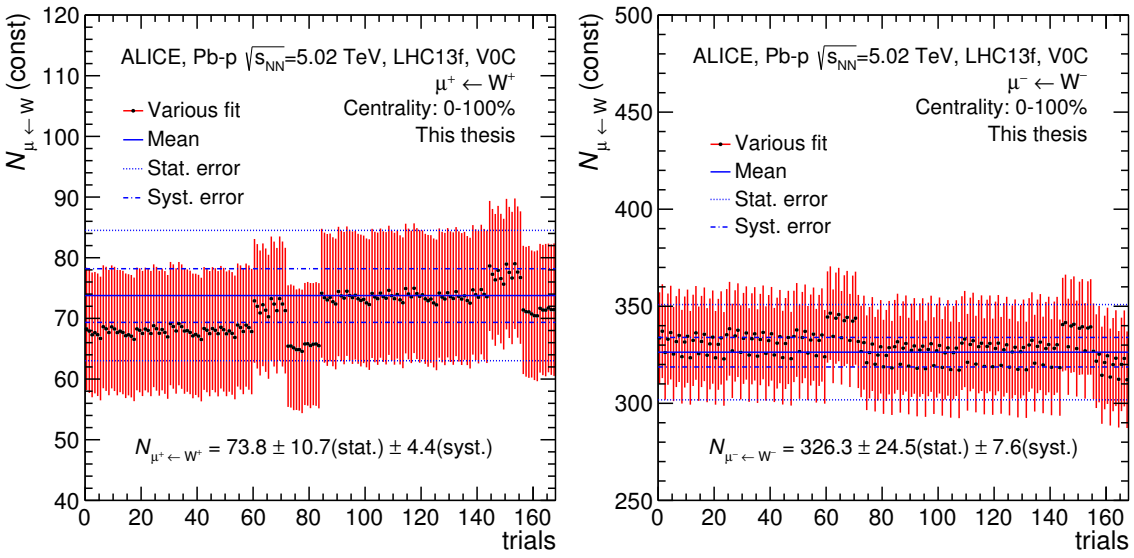

(a) $\mu^+ \leftarrow W^+$ (b) $\mu^- \leftarrow W^-$

Figure 5.26: LHC13f. Centrality: 0–100%, estimated with V0C. Raw number of muons from $W^{\pm}$ decays as a function of the trial. The solid line is the average number of muons from $W^{\pm}$ decays, estimated through Eq. 5.7 while the dashed (dot-dashed) line represent the statistical (systematic) uncertainty band, obtained with Eq. 5.8 (Eq. 5.9).

5.7.7 Summary of systematic uncertainties

The systematic uncertainties on the measurement are summarized in Table 5.9.

Signal extraction	
(includes alignment, fit stability/shape, etc.)	from 2% to 6%
– vs. centrality	from 5% to 15%
Acc.$\times$Eff.	
– tracking efficiency	2% (p-going) 3% (Pb-going)
– trigger efficiency	1%
– tracker/trigger matching	0.5%
– alignment	1%
Normalisation to MB	
– F_{norm}	1%
– σ_{MB}	3.3%
Pile-up	from 1% to 3%
$\langle N_{\mathrm{coll}} \rangle$	from 2% to 8%

Table 5.9: Summary of systematic uncertainties.

5.8 Results

5.8.1 Production cross section

The production cross section of muons from W^+ and W^- boson decays with $p_T^\mu > 10$ GeV/c measured at forward and backward rapidities in p–Pb collisions at $\sqrt{s_{NN}} = 5.02$ TeV are shown in the left and right panels of Figure 5.27, respectively. The vertical bars represent the statistical uncertainties while the open boxes are the systematic ones. The smaller cross section of positive W bosons at backward rapidity is the combined effect of the parity violation of the weak interaction, which only couples left-handed fermions with right-handed anti-fermions, and of the helicity conservation in the semi-leptonic decay. This results in an anisotropic emission of the muons. In particular, the μ^- is preferably emitted in the same direction of the W^-, while the μ^+ is emitted in the opposite direction with respect to the W^+ [30]. This implies that the μ^+ measured in $-4.46 < y_{cms} < -2.96$ mainly comes from the decay of W^+ at even more backward rapidities, where the production cross section rapidly decreases.

The experimental measurement and theoretical calculation are summarized in Tables 5.10 and 5.11 for $2.03 < y_{cms} < 3.53$ and $-4.46 < y_{cms} < -2.96$, respectively. The results are compared with NLO and NNLO theoretical calculations including or not the nuclear modification of the parton distribution functions. The NLO pQCD calculations [195] with CT10 [95] parton distribution functions and the NNLO calculations with FEWZ [89] with the MSTW2008 [96] PDF set both describe data within uncertainties. The inclusion of a parameterisation of the nuclear modification of the parton distribution function in the calculations results in a slightly lower value of the cross section, especially at forward rapidity. This variation, however, is of the same order of the uncertainties in the theoretical calculations, thus limiting the discriminating power of the cross section alone.

	$d\sigma/dy\,(\mu^+ \leftarrow W^+)$	$d\sigma/dy\,(\mu^- \leftarrow W^-)$
Measured (nb)	$61.6 \pm 4.0(\text{stat.}) \pm 3.4(\text{syst.})$	$55.9 \pm 4.2(\text{stat.}) \pm 3.0(\text{syst.})$
pQCD w/ EPS09 (nb)	58.9 ± 4.9	48.7 ± 4.0
pQCD w/o EPS09 (nb)	67.5 ± 3.0	55.6 ± 2.7
FEWZ w/ EPS09 (nb)	64.7 ± 1.2	52.3 ± 1.1
FEWZ w/o EPS09 (nb)	70.8 ± 1.4	56.9 ± 1.1

Table 5.10: Cross section of muons from $W^\pm$ decays with $2.03 < y_{cms} < 3.53$ and $p_T^\mu > 10$ GeV/c in p–Pb collisions at $\sqrt{s_{NN}} = 5.02$ TeV.

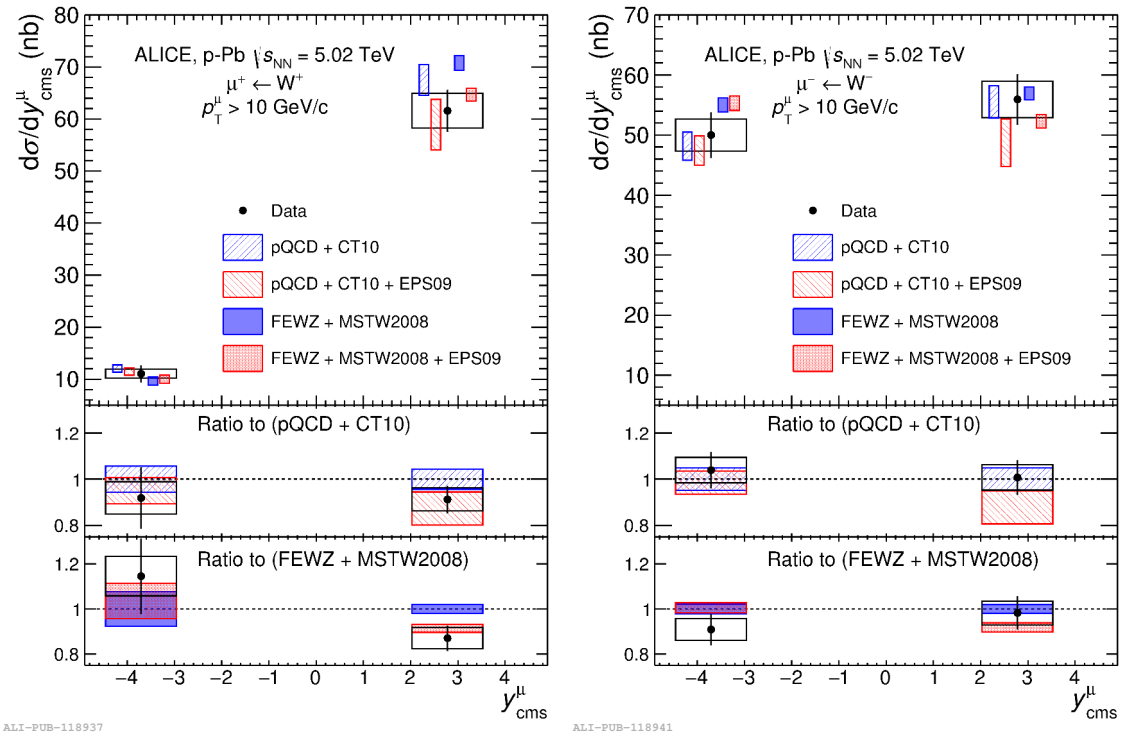

Figure 5.27: Left (right) panel: cross section of μ^+ (μ^-) from W^+ (W^-) boson decays at backward and forward rapidities measured in p–Pb collisions at $\sqrt{s_{NN}} = 5.02$ TeV. The vertical error bars (open boxes) represent the statistical (systematic) uncertainties. The horizontal width of the boxes corresponds to the measured rapidity range. The results are compared with theoretical calculations [195, 89] performed both including and without including the nuclear modification of the parton distribution functions. In the top panels, the calculations are shifted along the rapidity axis to improve the visibility. The middle (bottom) panel shows the data and pQCD (FEWZ) calculations divided by the pQCD (FEWZ) calculations without nuclear modification of the PDFs.

	$d\sigma/dy\,(\mu^+ \leftarrow W^+)$	$d\sigma/dy\,(\mu^- \leftarrow W^-)$
Measured (nb)	$11.1 \pm 1.6(\text{stat.}) \pm 0.8(\text{syst.})$	$50.0 \pm 3.8(\text{stat.}) \pm 2.7(\text{syst.})$
pQCD w/ EPS09 (nb)	11.4 ± 0.7	47.4 ± 2.4
pQCD w/o EPS09 (nb)	12.0 ± 0.7	48.1 ± 2.3
FEWZ w/ EPS09 (nb)	10.0 ± 0.8	55.3 ± 1.2
FEWZ w/o EPS09 (nb)	9.7 ± 0.7	55.0 ± 1.2

Table 5.11: Cross section of muons from $W^{\pm}$ decays with $-4.46 < y_{cms} < -2.96$ and $p_T^{\mu} > 10$ GeV/c in p–Pb collisions at $\sqrt{s_{NN}} = 5.02$ TeV.

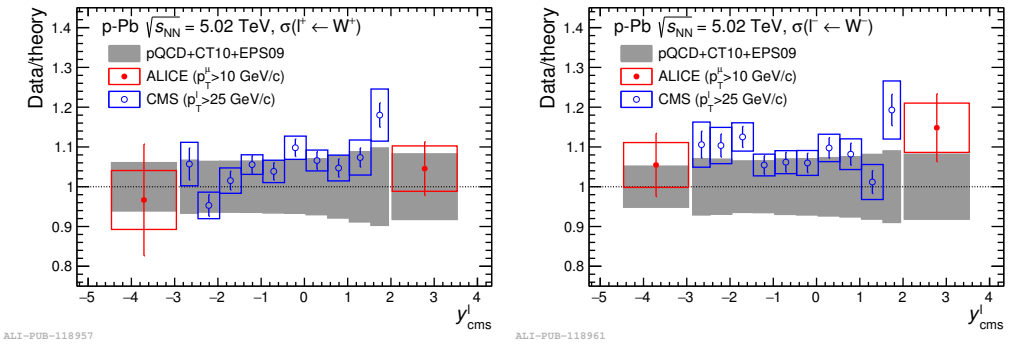

Figure 5.28: Ratio of data over theoretical calculations for the production cross section of positive (top panel) and negative (bottom panel) muons and leptons from W-boson production measured by the ALICE and CMS experiments [66], respectively. The luminosity uncertainty of 3.5% for CMS is not shown. The pQCD calculations are obtained with CT10 NLO PDF set and with the EPS09NLO parameterisation of the nuclear modifications.

The production of electrons and muons from W-boson decays was measured at mid-rapidity in p–Pb collisions at $\sqrt{s_{NN}} = 5.02$ TeV by the CMS experiment [66]. The cross section results, each divided by the corresponding NLO pQCD expectation including nuclear modification of the PDFs, are shown together with the analogous ALICE results in Figure 5.28: the calculations are found to describe data over the full explored rapidity interval.

5.8.2 Charge asymmetry

The charge asymmetry in the production of the W^+ and W^- bosons can be used to gain sensitivity in the study of the nuclear modification of the PDFs [66]. It is defined as:

$$A = \frac{N^{\text{corr}}_{\mu^+\leftarrow W^+} - N^{\text{corr}}_{\mu^-\leftarrow W^-}}{N^{\text{corr}}_{\mu^+\leftarrow W^+} + N^{\text{corr}}_{\mu^-\leftarrow W^-}} = \frac{R-1}{R+1} \tag{5.10}$$

where $N^{\text{corr}}_{\mu^+\leftarrow W^+}$ and $N^{\text{corr}}_{\mu^-\leftarrow W^-}$ are the yields of muons from, respectively, the W^+ and W^- decays, corrected by the detector acceptance and efficiency.

Part of the theoretical uncertainties, such as those on the scale that are of the order of 5%,

and the experimental uncertainties on the tracking and trigger efficiency, normalisation factors and MB cross section, whose quadratic sum amounts to 4.3% (4.8%) in the p-going (Pb-going) period, cancel when measuring the relative yield of muons from W^+ and W^- decays.

We use the same scheme as the W-boson signal extraction and calculate the charge asymmetry in each trial, thus combine them together according to the method introduced in Section 5.7.6. Figure 5.29 shows the charge asymmetry as a function of trials.

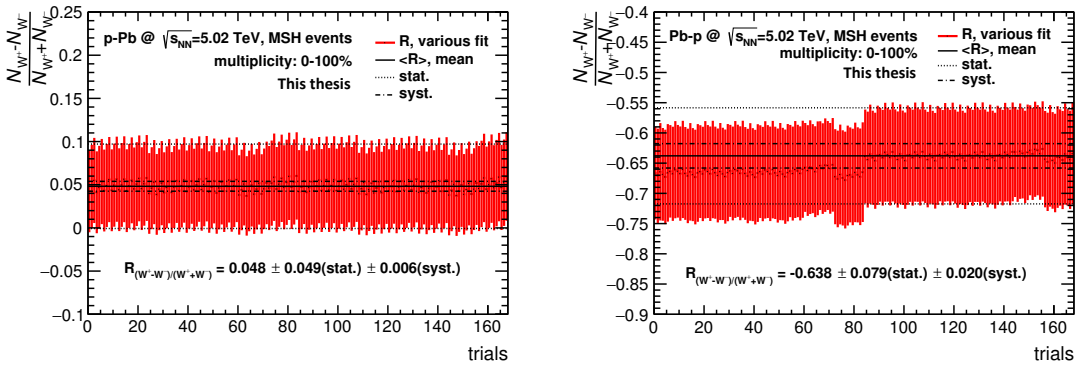

(a) charge asymmetry in p-Pb collisions

(b) charge asymmetry in Pb-p collisions

Figure 5.29: Charge asymmetry as a function of trials in p-Pb and Pb-p collisions.

Figure 5.30 shows the lepton charge asymmetry, compared with theory calculation. The relative systematic uncertainties in the pQCD and FEWZ calculations are strongly reduced in the ratio. However, the results with and without nuclear modification are very similar in this kinematic range, and the measurement cannot discriminate between them.

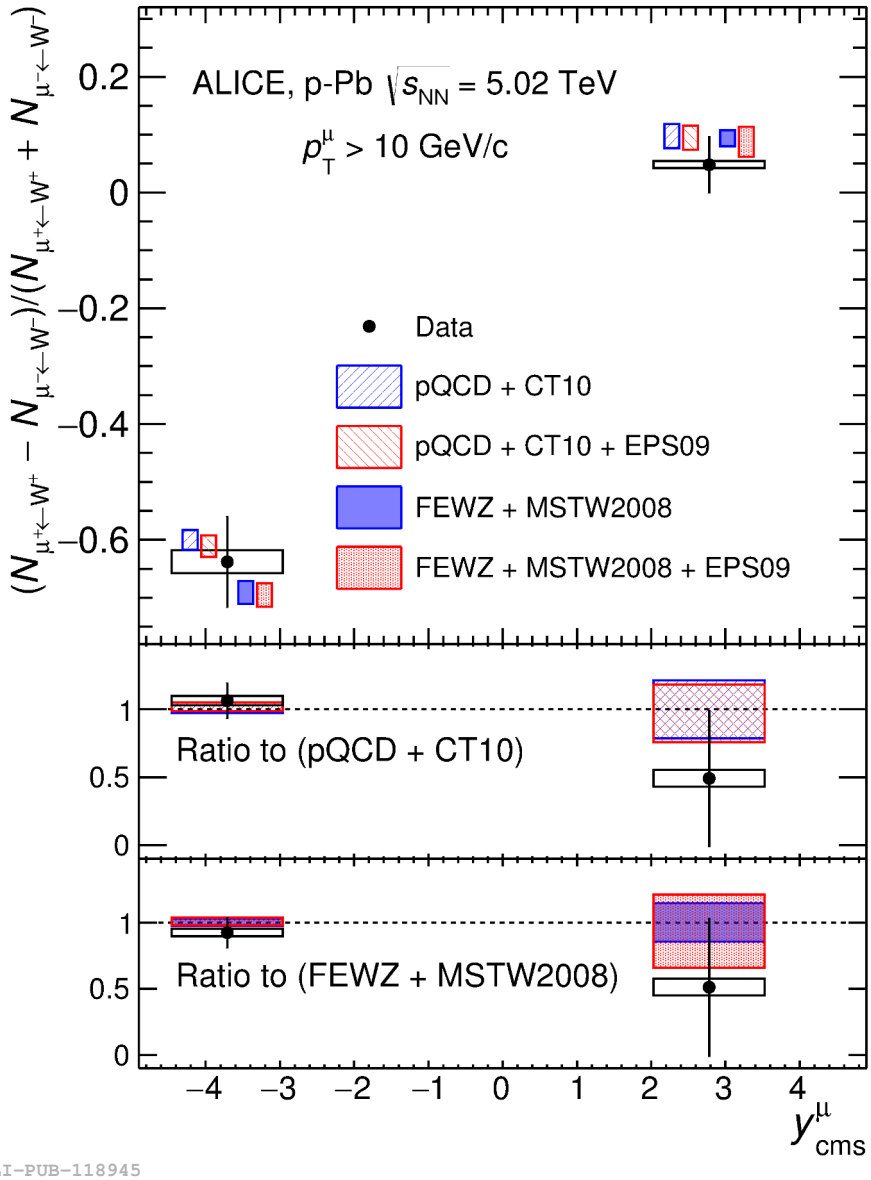

Figure 5.30: Lepton charge asymmetry of muons from W-boson decays at backward and forward rapidities measured in p–Pb collisions at $\sqrt{s_{NN}} = 5.02$ TeV. The vertical error bars (open boxes) represent the statistical (systematic) uncertainties. The horizontal width of the boxes corresponds to the measured rapidity range. The results are compared with theoretical calculations [195, 89] performed both including and without including the nuclear modification of the parton distribution functions. In the top panel, the calculations are shifted along the rapidity axis to improve the visibility. The middle (bottom) panel shows the data and pQCD (FEWZ) calculations divided by the pQCD (FEWZ) calculations without nuclear modification of the PDFs.

5.8.3 Cross section vs. centrality

Besides the measurement of the production of muons from W-boson decays in whole centrality (0-100%), the cross section of muons from W-boson decays can also be extracted per event activity interval. The yield is corrected by acceptance times efficiency and normalized to the number of equivalent MB event. Thus the normalized yield can be used to calculate the cross section. The cross section is divided by the average number of binary nucleon-nucleon collisions $\langle N_{\rm coll} \rangle$ in each event activity interval, in order to obtain the cross section per binary collision.

The muon trigger efficiency is found to be independent of centrality in p-Pb collisions. The normalisation factor of muon-triggered to MB events per centrality class can be obtained from the centrality integrated value $F_{\mu-{\rm trig}/{\rm MB}}$ scaled by the fraction of the MB events in the given centrality class. The 0-2% most central collisions are excluded in the centrality-dependent analysis, because of the large pile-up contamination in this event class (of the order of 20-30%). In pile-up events the ZN energies of two (or more) interactions sum up, thus biasing the centrality determination towards the most central classes. The contamination is reduced with decreasing centrality, and is about 3% in the 2-20% event classes in both the p-going and Pb-going data sample. These values are taken into account in the systematic uncertainties on the normalisation.

Due to the limited statistics, the μ^+ and μ^- results are summed together. In the sum, the systematic uncertainties on signal extraction are considered as uncorrelated and summed in quadrature. The uncertainties on the normalisation factor and tracking and trigger uncertainties tracking and trigger efficiency are fully correlated among μ^+ and μ^- and among the different centrality bins. The uncertainties on Acc.$\times$Eff. are uncorrelated for μ^+ and μ^-, but correlated with centrality. The uncertainties on pile-up and on $\langle N_{\rm coll} \rangle$ are correlated among μ^+ and μ^-, but uncorrelated in centrality. The production of muons from W-boson decays with $p_{\rm T}^{\mu} > 10$ GeV/c as a function of the collision centrality in $2.03 < y_{\rm cms} < 3.53$ and $-4.46 < y_{\rm cms} < -2.96$ determined by ZN centrality estimator are shown in Figures 5.31 and 5.32, respectively. The vertical bars represent the statistical uncertainties while the open boxes are the uncorrelated systematic ones. The quadratic sum of the correlated systematic uncertainties on the MB cross section, normalisation, Acc.$\times$Eff. correction and tracking and trigger efficiency, which amounts to 4.3% (4.8%) in the p-going (Pb-going) sample, are quoted in the figure.

If the W boson production rate is consistent with geometric expectation, the production cross-section is expected to scale with the number of binary collisions for all centrality classes, provided that the centrality determination is not biased. The measured centrality dependence is

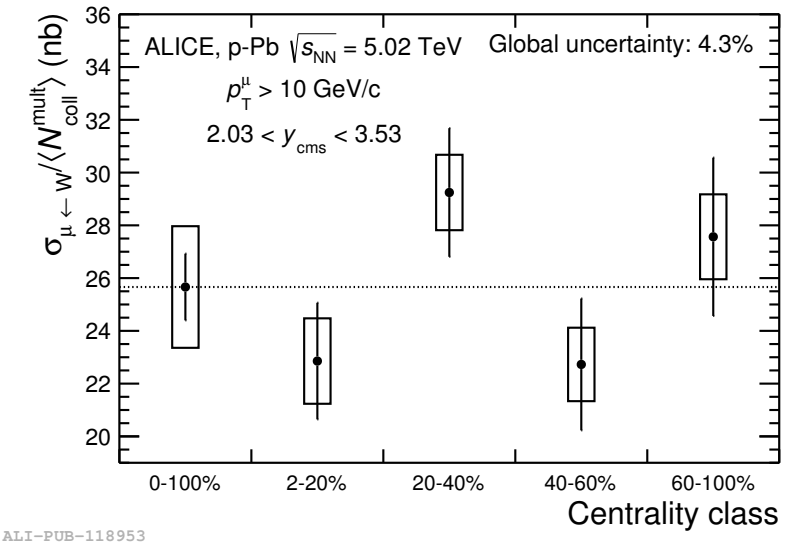

Figure 5.31: Cross section of muons from $W^{\pm}$ decays with $p_T^\mu > 10$ GeV/c and $2.03 < y_{cms} < 3.53$ divided by the average number of binary collisions as a function of the centrality class for ZNA estimator.

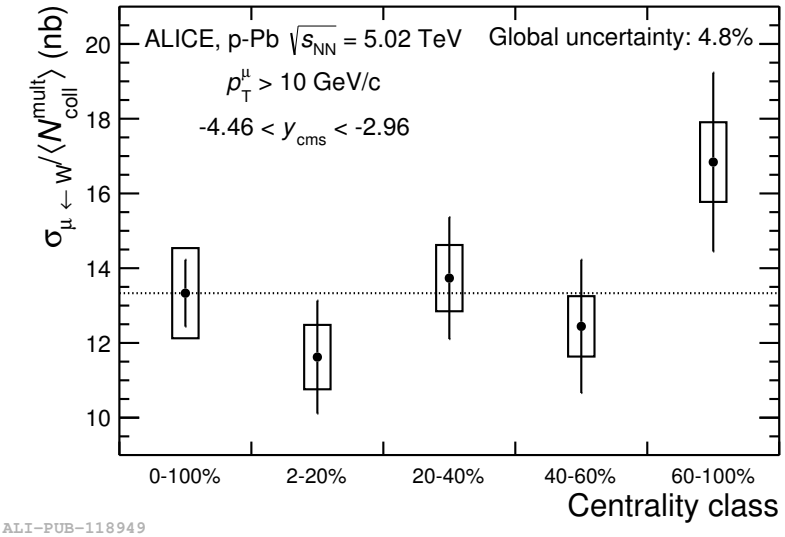

Figure 5.32: Cross section of muons from $W^{\pm}$ decays with $p_T^\mu > 10$ GeV/c and $-4.46 < y_{cms} < -2.96$ divided by the average number of binary collisions as a function of the centrality class for ZNC estimator.

found to be compatible with a constant within uncertainties.

If A is a success in life, then A equals x plus y plus z. Work is x; y is play; and z is keeping your mouth shut.

Albert Einstein

6

W-boson measurement in pp collisions

The W production is extensively studied at hadron colliders since it represents an important benchmark of the SM. The measurements in pp collisions at different energies are well described by Electroweak theory and Quantum Chromodynamics (QCD) calculations at Next-to-Leading Order (NLO) and Next-to-Next-to-Leading Order (NNLO) in perturbation theory. The ALICE experiment has a limited luminosity in pp collisions compared to other LHC experiments. The resulting statistical error is therefore too large to further constrain the theory. However, the measurement of W boson production in pp collisions provide a valuable test bench for the validation of the analysis strategy in p-Pb collisions. In the following, the measurement of pp collisions at $\sqrt{s} = 8$ TeV is discussed. It is worth noting that this data sample was collected just before the p-Pb run and therefore has the same alignment conditions.

6.1 Data sample

Data are collected in pp collisions at $\sqrt{s} = 8$ TeV and the associated period is LHC12h. The run number lists can be found in Appendix A.2. The muon trigger is a coincidence of a VZERO and muon trigger signal. The MSH trigger has the same minimum p_{T} threshold ($p_{\mathrm{T}} \gtrsim 4.2\,\mathrm{GeV}/c$) as in p–Pb collisions at $\sqrt{s} = 5.02$ TeV. The integrated luminosity (L_{int}) for the LHC12h period is of 510 nb^{-1}. The same offline physics selection was used to refine the events as was done in the

p–Pb collisions.

Figure 6.1 shows the transverse momentum distribution of muon tracks after applying the same analysis cuts as in p–Pb collisions (Section 5.1).

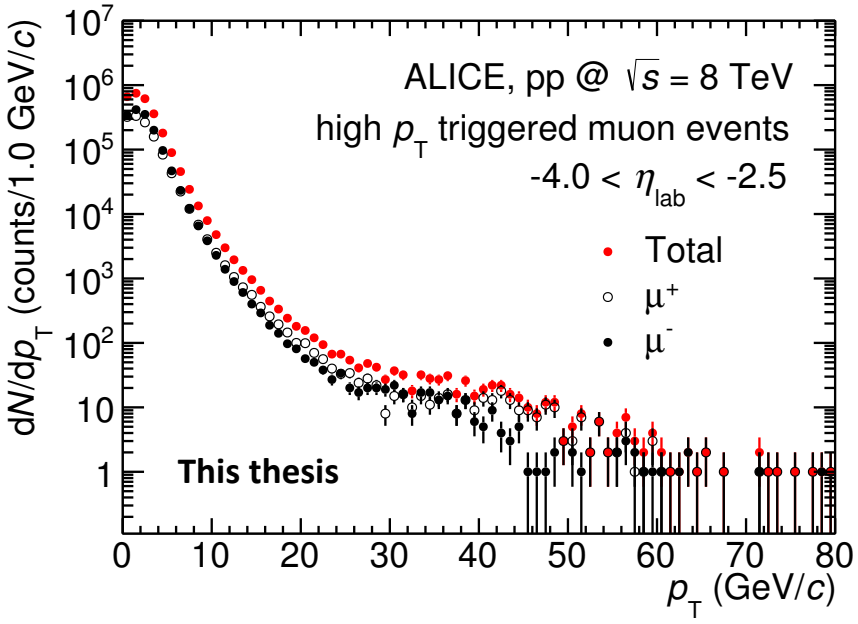

Figure 6.1: Raw p_T distribution of inclusive muon in CMSH7-S-NOPF-MUON events in the periods LHC12h.

The analysis is based on the extraction of the $W^{\pm}$ boson contribution from the transverse momentum muon distributions in Figure 6.1. The same strategy as described in Section 5.2 is implemented in pp collisions.

6.2 Monte Carlo simulations

The simulation of $W^{\pm}$ and Z°/γ^{*} are performed with the next-to-leading-order MC generator (POWHEG) with CT10 PDFs. The heavy flavour background is based on the parameterization of FONLL [188] calculations. The alignment file is ideal in simulation, while a custom residual alignment, produced for all MUON analyses, is used in reconstruction. The simulations are performed by generating a number of events per run proportional to the number of MSH triggers in that run, in order to correctly account for the modification of the status of the detector with time. The templates obtained in these simulations are shown in Figures 6.2 - 6.4. In order to take into account the systematics on the description of heavy flavour background, different shapes were used via varying the factorisation and renormalisation scales. This is different with respect to p–Pb collisions, where the variation of the PDF shape, which provides the largest difference in the templates, was also accounted for.

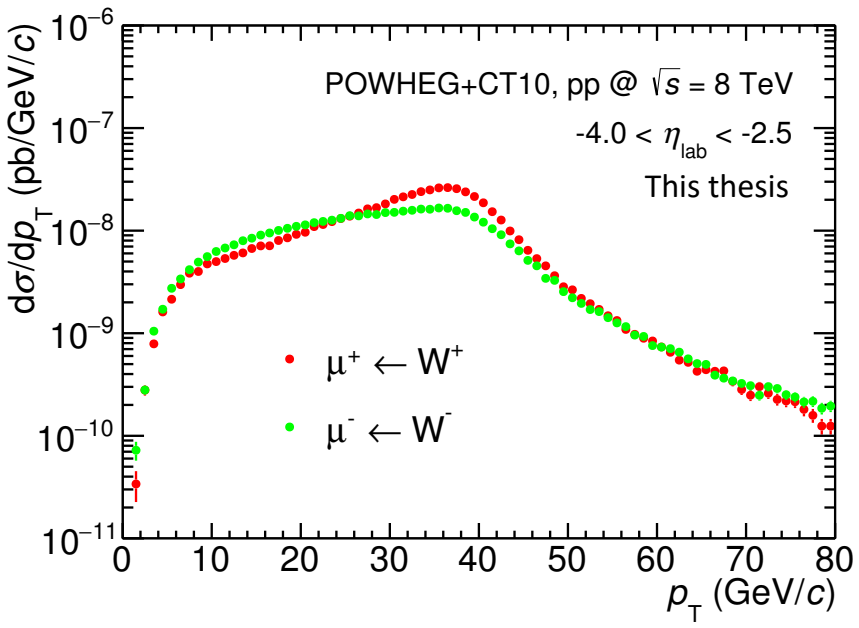

Figure 6.2: MC templates of muons from W-boson decays generated with POWHEG using the CT10 PDF set in pp collisions at 8 TeV.

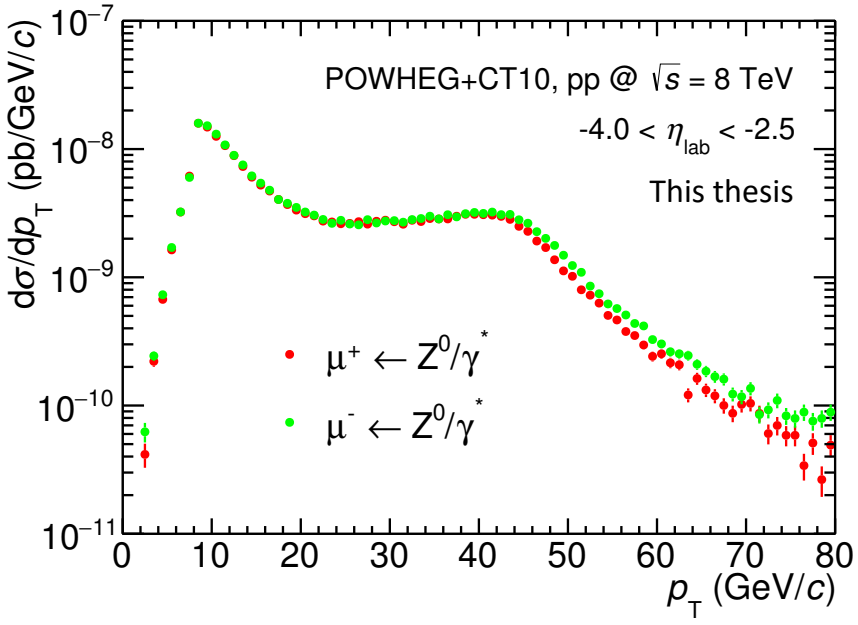

Figure 6.3: MC templates of muons from Z°/γ^{*} decays generated with POWHEG using the CT10 PDF set in pp collisions at 8 TeV.

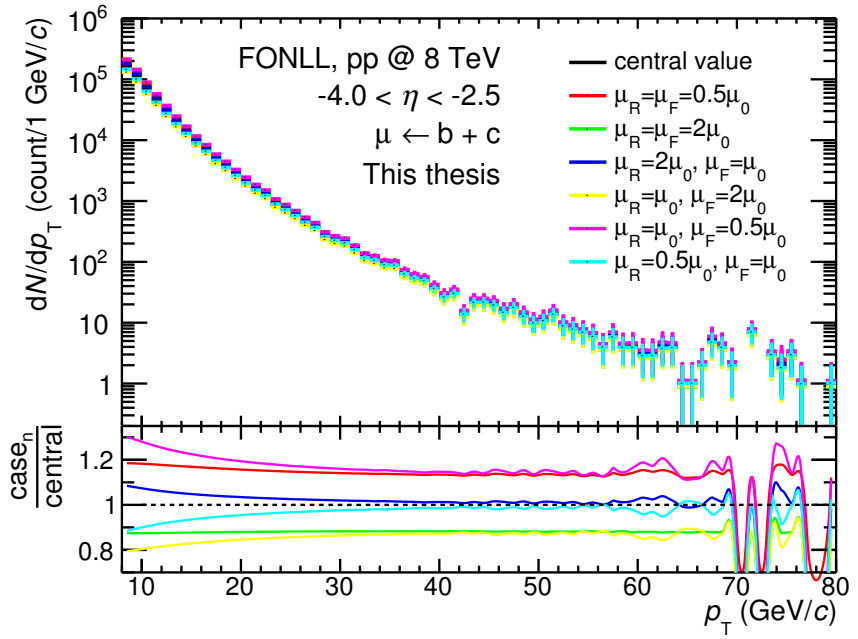

Figure 6.4: MC templates of muons from heavy flavour decays produced according to FONLL in pp collisions at 8 TeV.

6.3 Signal extraction

The same procedure used in p–Pb collisions is employed here. Figure 6.5 show the fit examples based on Equation 5.2.

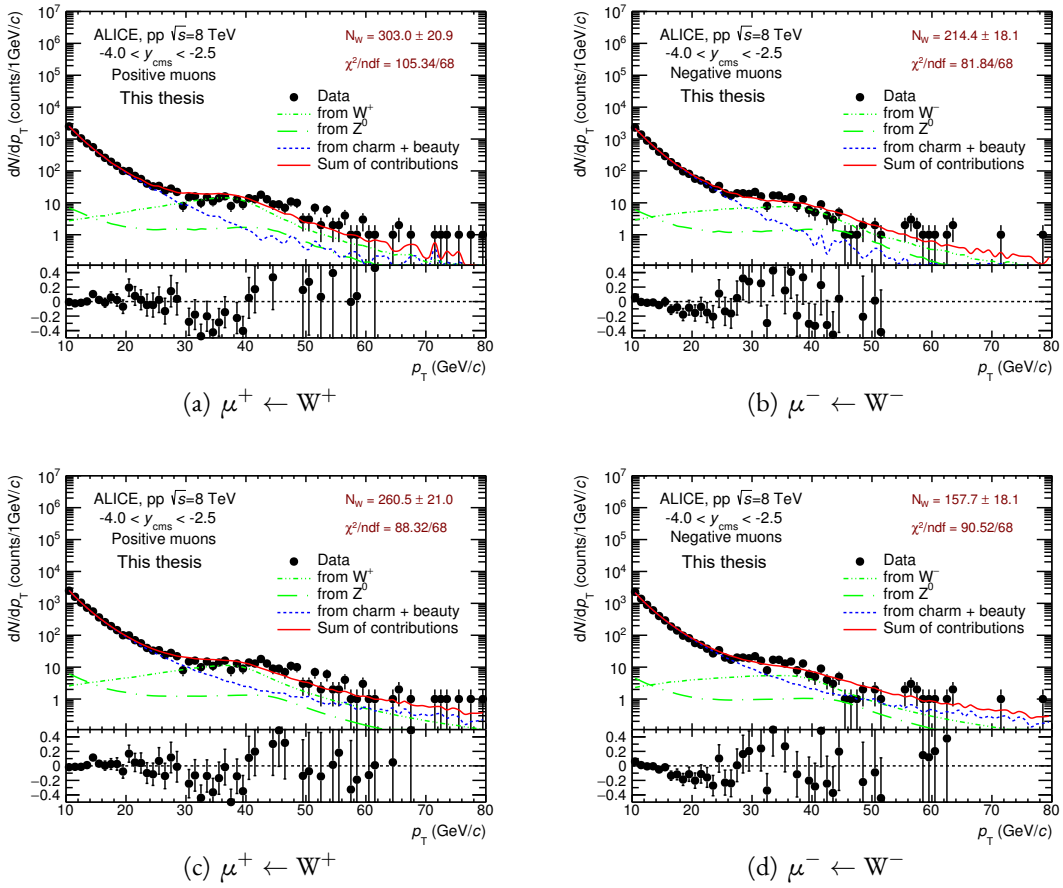

(a) $\mu^+ \leftarrow W^+$ (b) $\mu^- \leftarrow W^-$

(c) $\mu^+ \leftarrow W^+$ (d) $\mu^- \leftarrow W^-$

Figure 6.5: Fit examples in pp collisions at 8 TeV. The left and right are the fit to the positive and negative muon p_T spectrum, respectively. Top plots are based on residual alignment and the bottom plots are based on resolution task.

The fit is performed many times varying the p_T range, MC templates and alignment. The number of muons is then plotted as a function of the number of trials. The different trials include:

- (7 MC templates for heavy-flavour decay background) × (1 PDFs set for $W^{\pm}$ and Z^0/γ^*) × (different p_T ranges) × (1 alignment file + 1 resolution task)

The fitting p_T range and the PDFs set for measurements in pp collisions are different from p-Pb collisions. Here, the fitting p_T range is $10 \sim 20 < p_T < 50 \sim 80$ GeV/c with steps of 1 GeV/c

for the lower limit and steps of 5 GeV/c for the higher limit. Of course, this can be optimised according to what we did in p-Pb collisions. However, we already obtain that the systematic of fitting p_{T} range is small with respect to the one of alignment effect. Thus as the fast cross-check analysis, we decide to use the above fitting p_{T} range. Moreover, there is only one PDFs set used in pp collisions since the systematic caused by different PDFs sets in p-Pb collisions is very small (less than 1%) and neglected.

The final number of muons from W-boson decays is the arithmetic average of the $N_{\mu\leftarrow \mathrm{W}}$ extracted in each fit. The estimation of statistical and systematical uncertainties are the same as p–Pb collisions. The resulting number of muons from W-boson decays as a function of trials are shown in Figure 6.6 for pp collisions at 8 TeV. In these plots one can see that the results obtained with the standard description of the alignment in simulation are systematically larger than the one estimated with the templates obtained with a data-driven description of the alignment. The reason is that the residual alignment tends to under estimate the track smearing at high p_{T}, resulting in a smaller contribution of muons from heavy flavour decay. The results are summarised in Table 6.1.

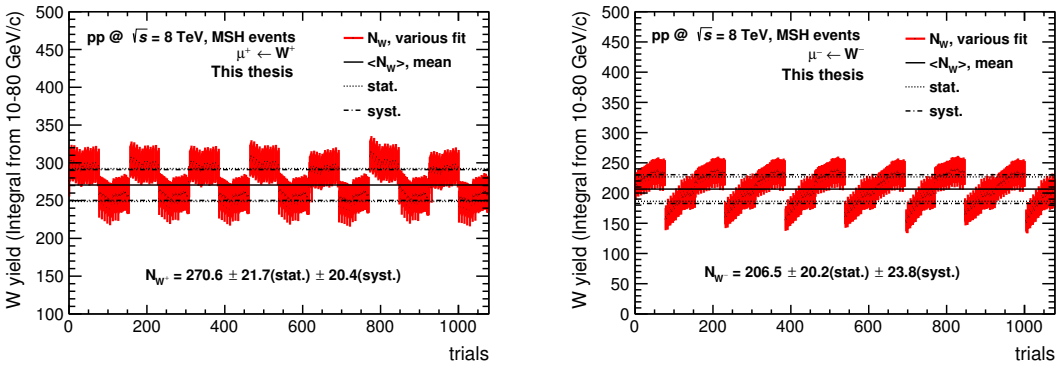

Figure 6.6: Number of muons from W-boson decays as function of the trials in pp collisions at 8 TeV. The top panel is for $N_{\mu^+\leftarrow \mathrm{W}^+}$ and the bottom panel is for $N_{\mu^-\leftarrow \mathrm{W}^-}$.

	pp @ 8 TeV
$\mu^+ \leftarrow \mathrm{W}^+$	$270.6 \pm 21.7\ (\mathrm{stat.}) \pm 20.4\ (\mathrm{syst.})$
$\mu^- \leftarrow \mathrm{W}^-$	$206.5 \pm 20.2\ (\mathrm{stat.}) \pm 23.8\ (\mathrm{syst.})$

Table 6.1: The extracted yield of muons from $\mathrm{W}^{\pm}$ decays with $-4.0 < y^{\mu}_{\mathrm{cms}} < -2.5$ and $p^{\mu}_{\mathrm{T}} > 10$ GeV/c in pp collisions at 8 TeV.

6.4 Acceptance × efficiency correction and normalization

The Acc.×Eff. corrections are obatined from the simulations described in Section 6.2. The efficiency is defined by the number of muons reconstructed with the same cuts used in the analysis, divided by the number of generated muons coming from $W^{\pm}$ boson decay and with $-4.0 < \eta_{lab}^{\mu,MC} < -2.5$. It is provided integrated over the p_T range of the $\mu \leftarrow W$ measurement ($p_T^{\mu} > 10$ GeV/c). The results are summarized in Table 6.2.

	μ^+	μ^-
Acc.×Eff.	0.780	0.783

Table 6.2: Acc.×Eff. for muons from $W^{\pm}$ decays with $p_T^{\mu} > 10$ GeV/c and $-4.0 < \eta_{lab} < -2.5$ obtained from simulations reconstructed with one residual mis-alignment file in pp collisions at 8 TeV.

The normalization used to obtain the cross section is based on the luminosity obtained using trigger scalers of the minimum bias trigger with the known cross section 28 mb [196].

6.5 Results

6.5.1 Production cross section

The production cross section of muons from W-boson decays is obtained with the following equation:

$$\sigma_{\mu^{\pm}\leftarrow W^{\pm}} = \frac{1}{A \times \varepsilon} \cdot \frac{N_{\mu^{\pm}\leftarrow W^{\pm}}}{L_{int}} \tag{6.1}$$

The result for pp collisions at 8 TeV respectively is listed in Table 6.3 and is shown in Figure 6.7. Please note that the effect of alignment in pp collisions at 8 TeV is the same as p–Pb collisions at 5.02 TeV. In the resolution task, all the parameters are tuned according to the data of p–Pb collisions at 5.02 TeV. The measured cross section of muons from $W^{\pm}$ decays is consistent with POWHEG calculation with CT10 PDFs in pp collisions at 8 TeV. It indicates that the strategy of W-boson signal extraction in p–Pb collisions is validated in pp collisions.

	Measured (pb)	POWHEG w/ CT10 (pb)
$\mu^+ \leftarrow \mathrm{W}^+$	$680.1 \pm 54.5\,(\mathrm{stat.}) \pm 51.7\,(\mathrm{syst.})$	707.8
$\mu^- \leftarrow \mathrm{W}^-$	$517.0 \pm 50.6\,(\mathrm{stat.}) \pm 59.8\,(\mathrm{syst.})$	590.2

Table 6.3: Cross section of muons from $\mathrm{W}^{\pm}$ decays with $-4.0 < y^{\mu}_{\mathrm{cms}} < -2.5$ and $p^{\mu}_{\mathrm{T}} > 10$ GeV/c in pp collisions at 8 TeV.

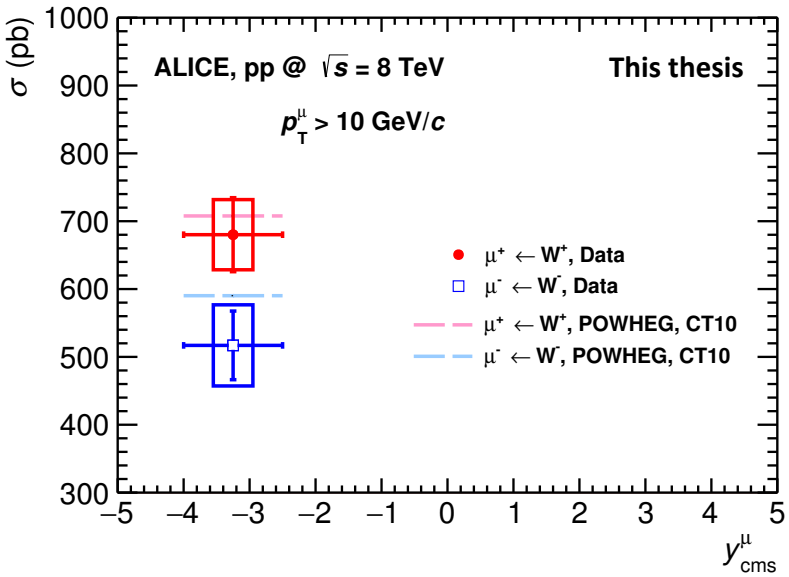

Figure 6.7: Cross section of muons from $\mathrm{W}^{\pm}$ decays with $p^{\mu}_{\mathrm{T}} > 10$ GeV/c compared with POWHEG calculation with CT10 PDFs in pp collisions at 8 TeV.

6.5.2 Charge asymmetry

The charge asymmetry is a good measurement, which gives direct access to the up and down quark PDFs. In this ratio, most of the experimental uncertainties cancel out, for example, correlated uncertainties like luminosity (normalization), pile-up, MB cross section, whereas anti-correlated such as alignment are enhanced. Here we use the same definition and estimation strategy as in p–Pb collisions. The Figure 6.8 show the charge asymmetry as a function of trials. The trials representation that the results obtained via varying the lower fitting range between $10 < p_{\mathrm{T}} < 20$ GeV/c with steps of 1 GeV/c and the higher limit is varied from $50 < p_{\mathrm{T}} < 80$ GeV/c with steps of 5 GeV/c. The comparison between the measurement and the calculation of POWHEG with CT10 PDFs are shown in Figure 6.9. The measured charge asymmetry is in good agreement with model calculations.

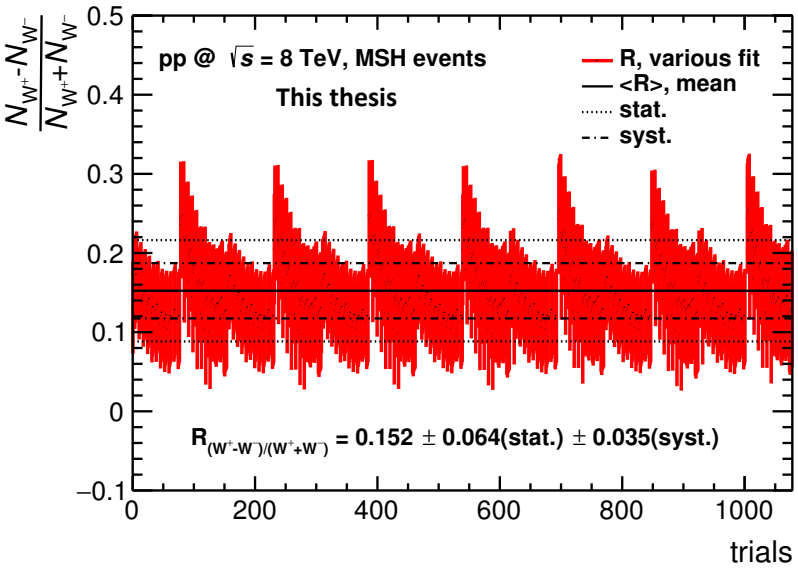

Figure 6.8: The charge asymmetry as a function of trials in pp collisions at 8 TeV.

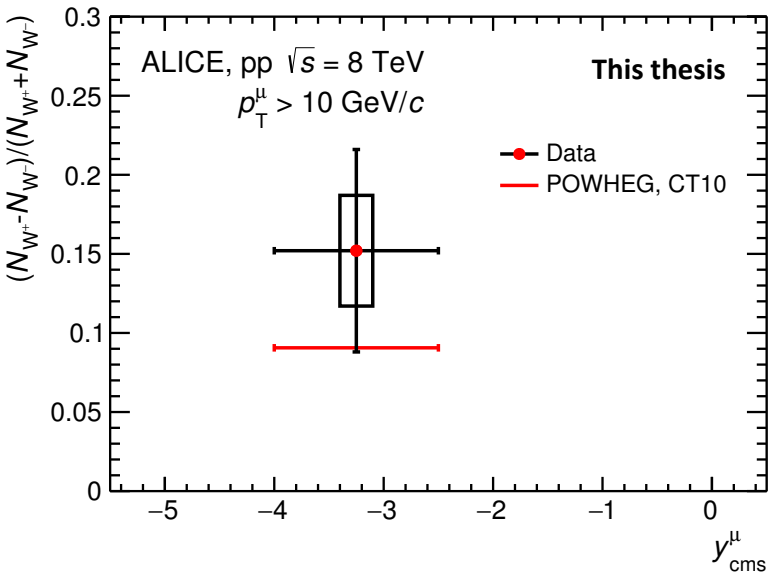

Figure 6.9: The charge asymmetry of muons from W-boson decays in pp collisions at 8 TeV and compared with POWHEG calculations.

Part IV

Discussions and Conclusions

I love to travel, but hate to arrive.

Albert Einstein

7 Conclusion

For anyone in the field of particle physics experimental research, it is important to check the theory with new experimental results. This thesis work is divided into three parts.

In the first part, a general and basic introduction on particle physics in heavy-ion collisions is provided, including the SM, QCD, the formation of QGP, the evolution of heavy-ion collisions and experimental observables. In the second chapter, we focus on the electroweak theory, which is the interaction responsible of the W-boson production in pp and p–Pb collisions. QCD correction to the W-boson production are important for next-to-leading order diagrams. The W-boson is produced in initial hard parton scattering processes and decays before the formation of the QGP, which is a deconfined phase of QCD matter produced in high-energy heavy-ion collisions. Its leptonic decay products do not interact strongly with the QGP. Thus it introduces a way for benchmarking in-medium modifications to colored probes. In Pb–Pb and p–Pb collisions, precise measurements of W-boson production can constrain the nuclear Parton Distribution Functions (nPDFs), which could be modified with respect to the nucleon due to shadowing or gluon saturation, and they can be used to test the scaling of hard particle production with the number of binary nucleon–nucleon collisions. In particular, the measurement of W boson production at forward and backward rapidity allows us to probe the modification of nPDFs at small and large Bjorken-x, respectively. Such measurements can constrain the PDFs in pp collisions, where W-boson production is well described by QCD calculations at NLO and NNLO in

perturbation theory. Also, the charge asymmetry of leptons from W-boson decays is a sensitive probe of up and down quark densities in a nucleon inside a nucleus.

In the second part, the design of the ALICE detector is presented for each sub-detector, especially for the muon spectrometer located at the forward region ($-4.0 < \eta_{\rm lab} < -2.5$). Then, the online data taking, the offline framework (aliroot) and the data quality assurance are introduced.

In the third part, we describe the measurement of the W boson cross section and lepton charge asymmetry in the muonic decay channel with $p_{\rm T} > 10$ GeV/c in p–Pb collisions at $\sqrt{s_{\rm NN}} = 5.02$ TeV at forward rapidity (p-going direction, $2.03 < y_{\rm cms} < 3.53$) and backward rapidity (Pb-going direction, $-4.46 < y_{\rm cms} < -2.96$), respectively, and in pp collisions at $\sqrt{s} = 8$ TeV at backward rapidity ($-4.0 < y_{\rm cms} < -2.5$). The work in this thesis is the first measurement of the W boson in ALICE experiment. The transverse momentum distribution of single muons is dominated at high $p_{\rm T}$ by the semi-leptonic decay of heavy-flavours and the leptionic decay of W and Z bosons. The signal is therefore extracted through a fit of the $p_{\rm T}$ distribution where the different components are described by MC templates. From the results we obtained in p–Pb collisions, theoretical predictions based on NLO pQCD and FEWZ calculations with CT10 PDFs agree with the measurement within uncertainties. Taking into account the EPS09 parametrization of nuclear effects on the PDFs further improves the agreement between theoretical predictions and the measurements at forward rapidity where shadowing is expected to be important. The production of muons from W-boson decays with $p_{\rm T}^{\mu} > 10$ GeV/c is studied as a function of the collision centrality. Due to the limited statistics, the μ^+ and μ^- results are summed together. In the absence of impact-parameter dependent nuclear modifications of PDFs, the cross section of muons from W-boson decays is expected to scale with the number of binary collisions for all centrality classes, provided that the centrality determination is not biased. The measured centrality dependence is found to be compatible with a constant within uncertainties. Further measurements with better precision are however needed to provide more stringent constraints on the nPDFs and on the binary scaling. The method of W-boson extraction used in p–Pb collisions is also validated in pp collisions via comparing the measurements with theoretical calculation.

A

Appendix

A.1 Data samples in p–Pb collisions

Data selected after the Quality Assurance for both MSL and MSH triggered events are considered. The following runs for each period are considered as "good" runs and are used in the analysis. The output of each run is the Event Summary Data (ESD), which contains the list of reconstructed tracks with physical information. Further selections are performed by user defined analysis tasks to create the Analysis Object Data (AOD) files, which contain more compact information used for specific analysis. The related reconstruction pass number, AOD version and total number of runs are listed:

- LHC13d, muon_pass2, AOD134, 20 runs:
  195682, 195724, 195725, 195726, 195727, 195760, 195765, 195767, 195783, 195787
  195826, 195827, 195829, 195830, 195831, 195867, 195869, 195871, 195872, 195873

- LHC13e, muon_pass2, AOD134, 26 runs:
  195949, 195950, 195954, 195955, 195958, 195989, 195994, 196000, 196006, 196085
  196089, 196090, 196091, 196105, 196107, 196185, 196187, 196194, 196199, 196200
  196201, 196203, 196214, 196308, 196309, 196310

- LHC13f, muon_pass2, AOD, 63 runs:

196474, 196475, 196477, 196528, 196535, 196563, 196564, 196566, 196568, 196601
196605, 196608, 196646, 196648, 196701, 196702, 196720, 196721, 196722, 196772
196773, 196774, 196869, 196876, 196965, 196972, 196973, 196974, 197003, 197011
197089, 197091, 197092, 197098, 197099, 197138, 197139, 197142, 197143, 197144
197145, 197147, 197148, 197150, 197152, 197153, 197184, 197189, 197247, 197254
197255, 197256, 197258, 197298, 197299, 197302, 197341, 197342, 197348, 197349
197386, 197387, 197388

A.2 Data sample in pp collisions

The runs after QA checked for MSH trigger [197] have been considered. The related reconstruction pass number, AOD version and total number of runs are listed:

- LHC11c, muon_pass2, AOD118, 44 runs:
  154726, 154732, 154733, 154742, 154745, 154750, 154753, 154789, 154793, 154808
  155135, 155162, 155163, 155164, 155165, 155166, 155167, 155174, 155235, 155237
  155239, 155251, 155277, 155278, 155300, 155302, 155305, 155308, 155314, 155325
  155331, 155333, 155337, 155345, 155346, 155347, 155367, 155368, 155370, 155371
  155375, 155376, 155382, 155384

- LHC11d, muon_pass2, AOD118, 124 runs:
  156889, 156891, 156893, 156896, 157025, 157026, 157028, 157079, 157087, 157091
  157092, 157094, 157096, 157098, 157100, 157209, 157210, 157211, 157214, 157227
  157257, 157261, 157262, 157275, 157277, 157475, 157560, 157562, 157564, 157569
  157770, 157819, 157848, 157975, 158084, 158086, 158111, 158112, 158115, 158118
  158124, 158132, 158136, 158137, 158139, 158171, 158173, 158175, 158176, 158177
  158179, 158189, 158192, 158194, 158196, 158200, 158201, 158252, 158258, 158263
  158271, 158285, 158287, 158288, 158299, 158303, 158304, 158340, 158463, 158466
  158467, 158468, 158471, 158492, 158495, 158496, 158516, 158518, 158520, 158526
  158528, 158533, 158602, 158604, 158611, 158613, 158615, 158617, 158626, 158784
  158790, 158791, 158793, 158868, 158875, 158876, 158877, 158878, 158879, 159090
  159254, 159259, 159283, 159285, 159286, 159318, 159319, 159356, 159378, 159379
  159532, 159535, 159536, 159538, 159539, 159577, 159580, 159581, 159582, 159593
  159595, 159599, 159602, 159606

- LHC12h, muon_calo_pass2, 114 runs:
  189576, 189577, 189578, 189596, 189601, 189603, 189605, 189607, 189608, 189610
  189611, 189612, 189616, 189621, 189623, 189641, 189642, 189647, 189648, 189650
  189654, 189656, 189658, 189659, 189685, 189687, 189694, 189696, 189697, 189698
  190150, 190209, 190212, 190214, 190215, 190216, 190240, 190242, 190244, 190304
  190305, 190307, 190336, 190337, 190340, 190341, 190342, 190386, 190388, 190389
  190390, 190392, 190393, 190416, 190417, 190418, 190419, 190895, 190898, 190903
  190904, 190968, 190969, 190970, 190979, 190981, 190983, 190984, 191129, 191227
  191229, 191230, 191231, 191232, 191234, 191242, 191244, 191245, 191247, 191248
  191450, 191451, 192004, 192072, 192073, 192095, 192128, 192136, 192140, 192141
  192172, 192174, 192177, 192194, 192197, 192199, 192200, 192201, 192202, 192205
  192246, 192468, 192471, 192492, 192499, 192505, 192510, 192534, 192535, 192542
  192548, 192729, 192731, 192732

A.3 POWHEG

The configuration for W-boson production is shown here:

```
!Single vector boson production parameters
idvecbos -24 ! PDG code for vector boson to be produced (W
   +:24 W-:-24 )
vdecaymode 2 !(1:electronic decay, 2: muonic decay, 3:
   tauonic decay)

numevts 1000000 ! number of events to be generated
ih1 1 ! hadron 1 (1 for protons, -1 for antiprotons)
ih2 1 ! hadron 2 (1 for protons, -1 for antiprotons)
ndns1 131 ! pdf set for hadron 1 (mlm numbering)
ndns2 131 ! pdf set for hadron 2 (mlm numbering)
ebeam1 2511do ! energy of beam 1
ebeam2 2511do ! energy of beam 2
! To be set only if using LHA pdfs
lhans1 10050 ! pdf set for hadron 1 (LHA numbering)
lhans2 10050 ! pdf set for hadron 2 (LHA numbering)
```

```
! To be set only if using different pdf sets for the two incoming
    hadrons
! QCDLambda5  0.25 ! for not equal pdf sets

! Parameters to allow or not the use of stored data
use-old-grid    1 ! if 1 use old grid if file pwggrids.dat is
   present (<> 1 regenerate)
use-old-ubound  1 ! if 1 use norm of upper bounding function
   stored in pwgubound.dat, if present; <> 1 regenerate

ncall1 120000   ! number of calls for initializing the
   integration grid
itmx1    5      ! number of iterations for initializing the
   integration grid
ncall2 250000   ! number of calls for computing the integral and
   finding upper bound
itmx2    5      ! number of iterations for computing the integral
   and finding upper bound
foldcsi  1      ! number of folds on csi integration
foldy    1      ! number of folds on  y  integration
foldphi  1      ! number of folds on phi integration
nubound 20000   ! number of bbarra calls to setup norm of upper
   bounding function
icsimax  1      ! <= 100, number of csi subdivision when computing
    the upper bounds
iymax    1      ! <= 100, number of y subdivision when computing
   the upper bounds
xupbound 2do    ! increase upper bound for radiation generation

! OPTIONAL PARAMETERS
withdamp    1       ! (default 0, do not use) use Born-zero
   damping factor
testplots   1       ! (default 0, do not) do NLO and PWHG
   distributions
```

The configuration for Z-boson production is shown here:

```
! Z production parameter
vdecaymode 2       !(1:electronic decay, 2: muonic decay, 3:
   tauonic decay)

numevts 1000000     ! number of events to be generated
ih1    1            ! hadron 1 (1 for protons, -1 for antiprotons)
ih2    1            ! hadron 2 (1 for protons, -1 for antiprotons)
ndns1 131           ! pdf set for hadron 1 (mlm numbering)
ndns2 131           ! pdf set for hadron 2 (mlm numbering)
ebeam1 2511do     ! energy of beam 1
ebeam2 2511do     ! energy of beam 2
! To be set only if using LHA pdfs
lhans1   10050      ! pdf set for hadron 1 (LHA numbering)
lhans2   10050      ! pdf set for hadron 2 (LHA numbering)
! To be set only if using different pdf sets for the two incoming
    hadrons
! QCDLambda5  0.25 ! for not equal pdf sets

! Parameters to allow or not the use of stored data
use-old-grid     1 ! if 1 use old grid if file pwggrids.dat is
   present (<> 1 regenerate)
use-old-ubound   1 ! if 1 use norm of upper bounding function
   stored in pwgubound.dat, if present; <> 1 regenerate

ncall1 100000   ! number of calls for initializing the
   integration grid
itmx1    5      ! number of iterations for initializing the
   integration grid
ncall2 100000   ! number of calls for computing the integral and
   finding upper bound
itmx2    5      ! number of iterations for computing the integral
   and finding upper bound
foldcsi   1     ! number of folds on csi integration
```

```
foldy       1     ! number of folds on y integration
foldphi     1     ! number of folds on phi integration
nubound 20000  ! number of bbarra calls to setup norm of upper
    bounding function
icsimax   1       ! <= 100, number of csi subdivision when computing
     the upper bounds
iymax     1       ! <= 100, number of y subdivision when computing
    the upper bounds
xupbound 2do    ! increase upper bound for radiation generation

! OPTIONAL PARAMETERS
testplots   1         ! (default 0, do not) do NLO and PWHG
    distributions
```

The collisions are simulated in their centre of mass energy. The output of POWHEG is a text file with the product of the hard parton interactions tabulated according to the Les Houches Accords format [198], which is then passed to PYTHIA. PYTHIA applies the ISR, FSR radiation and p_T kick as well as the boost and the cuts on the muon kinematics. Its configuration is the following:

```
AliGenPythia *gener = new AliGenPythia(1);
gener->SetProcess(kPyWPWHG);
gener->SetStrucFunc(kCTEQ6l);
gener->SetReadLHEF("pwgevents.lhe");
gener->SetProjectile("p",208,82);
gener->SetTarget("p",1,1);
gener->SetUseLorentzBoost(kTRUE);
gener->SetPhiRange(0., 360.);
gener->SetCutOnChild(1);
gener->SetChildThetaRange(168.0,178.5);
gener->SetNumberOfAcceptedParticles(1);
gener->SetPdgCodeParticleforAcceptanceCut(13);
gener->SetTrackingFlag(1);
```

B

Publication List

1) W and Z boson production in p–Pb collisions at $\sqrt{s_{\mathrm{NN}}} = 5.02$ TeV, ALICE collaboration, *JHEP 02 (2017) 077*

2) Measurement of W- and Z-boson production in p–Pb collisions at $\sqrt{s_{\mathrm{NN}}} = 5.02$ TeV with ALICE at the LHC, *J. Phys.: Conf. Ser. 770 (2016) 012002*

3) Measurement of W-boson production in p–Pb collisions at $\sqrt{s_{\mathrm{NN}}} = 5.02$ TeV with ALICE at the LHC, *J. Phys.: Conf. Ser. 612 (2015) 012009*

4) Production of muons from $\mathrm{W}^{\pm}$ decays at forward rapidity in p–Pb collisions at $\sqrt{s_{\mathrm{NN}}} = 5.02$ TeV, *ALICE-ANA-2013-1152 (2013)*

5) Production of $\mathrm{W}^{\pm}$ bosons at forward rapidity in pp collisions at $\sqrt{s} = 8$ TeV, *ALICE-ANA-2013-2448 (2013)*

C

Presentation List

Oral presentations and posters at Conferences

1) "Nuclear Modification Factor and Elliptic Flow of Muons from Open Heavy Flavor Decays at Forward Rapidity in Pb–Pb Collisions at $\sqrt{s_{NN}} = 2.76$ TeV with ALICE." Invited talk in the 4th Asian Triangle Heavy Ion Conference (ATHIC 2012), 14-17 November 2012, Pusan, Korea

2) "Heavy-flavour Production in proton-proton Collisions with ALICE." Invited talk in the 6th France China Particle Physics Laboratory (FCPPL 2013), 27-30 March, 2013, Nanjing, China

3) "W Production at Forward Rapidity in p–Pb Collisions." Poster in Hard Probes 2013, 4-8 November, 2013, Stellenbosch, South Africa

4) "Measurement of W Boson at Forward Rapidity in p–Pb collisions at $\sqrt{s_{NN}} = 5.02$ TeV with ALICE." Invited talk in the 7th France China Particle Physics Laboratory (FCPPL 2014), 08-10 April 2014, Clermont-Ferrand, France

5) "Measurement of W-boson production in p–Pb collisions at $\sqrt{s_{NN}} = 5.02$ TeV with ALICE." Invited talk in QGP-France 2014, 15-18 September 2014, Etretat, France

6) "Measurement of W-boson production in p–Pb collisions at $\sqrt{s_{\rm NN}} = 5.02$ TeV with ALICE at the LHC." Presentation in Hot Quarks 2014, 21-28 September 2014, Las Negras, Andalucia, Spain

7) "Measurement of W-boson production in p–Pb collisions with ALICE at the LHC." Invited talk in the 8th France China Particle Physics Laboratory (FCPPL 2015), 08-10 April 2015, Hefei, China

8) "Measurement of W and Z-boson production in p–Pb collisions with ALICE at the LHC." Poster in Quark Matter 2015, 27 September - 3 October 2015, Kobe, Japan

9) "Measurement of W- and Z-boson production in p–Pb collisions at $\sqrt{s_{\rm NN}} = 5.02$ TeV with ALICE at the LHC." Invited talk in XIIth International Conference on Beauty, Charm, and Hyperons in Hadronic Interactions, 12 - 18 June 2016, George Mason University, Fairfax, Virginia, USA

10) "The measurements of open heavy-flavor and electroweak boson via the muonic decay channel with ALICE." Invited talk in the 2nd China LHC Physics workshop (CLHCP), 16 - 19 December 2016, Peking University, Beijing, China

Listing of figures

Listing of tables

References

[1] A. Einstein, "Die Feldgleichungen der Gravitation," *Sitzungsberichte der Koniglich Preubischen Akademie der Wissenschaften* (1915) 844–847.

[2] ATLAS Collaboration, G. Aad *et al.*, "Observation of a new particle in the search for the Standard Model Higgs boson with the ATLAS detector at the LHC," *Phys. Lett.* B716 (2012) 1–29, arXiv:1207.7214 [hep-ex].

[3] CMS Collaboration, S. Chatrchyan *et al.*, "Observation of a new boson at a mass of 125 GeV with the CMS experiment at the LHC," *Phys. Lett.* B716 (2012) 30–61, arXiv:1207.7235 [hep-ex].

[4] M. E. Peskin and D. V. Schroeder, *An Introduction to quantum field theory*. 1995. http://www.slac.stanford.edu/spires/find/books/www?cl=QC174.45%3AP4.

[5] R. D. Field, "Applications of Perturbative QCD," *Front. Phys.* 77 (1989) 1–366.

[6] Particle Data Group Collaboration, K. A. Olive *et al.*, "Review of Particle Physics," *Chin. Phys.* C38 (2014) 090001.

[7] D. J. Gross and F. Wilczek, "Ultraviolet Behavior of Nonabelian Gauge Theories," *Phys. Rev. Lett.* 30 (1973) 1343–1346.

[8] H. D. Politzer, "Reliable Perturbative Results for Strong Interactions?," *Phys. Rev. Lett.* 30 (1973) 1346–1349.

[9] S. Hands, "The phase diagram of QCD," *Contemp. Phys.* 42 (2001) 209–225.

[10] B.-J. Schaefer and M. Wagner, "On the QCD phase structure from effective models," *Prog. Part. Nucl. Phys.* 62 (2009) 381, arXiv:0812.2855 [hep-ph].

[11] F. Karsch, "Lattice results on QCD thermodynamics," *Nucl. Phys.* A698 (2002) 199–208, arXiv:hep-ph/0103314 [hep-ph].

[12] T. D. Lee and G. C. Wick, "Vacuum Stability and Vacuum Excitation in a Spin 0 Field Theory," *Phys. Rev.* D9 (1974) 2291–2316.

[13] J. Silk, *Horizons of Cosmology*. Templaton Press, 2009.

[14] S. Singh, *Big Bang: The Origin of the Universe*. Harper Perennial, 2005.

[15] P. Coles and F. Lucchin, *Cosmology: The Origin and Evolution of Cosmic Structure*. John Wiley And Sons Ltd., 2002.

[16] Y. Chen, "PhD thesis." http://academiccommons.columbia.edu/catalog/ac%3A159130. 2013.

[17] U. W. Heinz, "Concepts of heavy ion physics," in *2002 European School of high-energy physics, Pylos, Greece, 25 Aug-7 Sep 2002: Proceedings*, pp. 165–238. 2004. arXiv:hep-ph/0407360 [hep-ph]. http://doc.cern.ch/yellowrep/CERN-2004-001.

[18] J. Goldhaber, "Bevalac Had 40-Year Record of Historic Discoveries." http://www2.lbl.gov/Science-Articles/Archive/Bevalac-nine-lives.html. 1992.

[19] J. Barale *et al.*, "Performance of the Bevalac," *IEEE Transactions on Nuclear Science* 22 no. 3, (1975) 1672–1674.

[20] R. Stock, "Ultra-relativistic nucleus-nucleus collisions," *J. Phys.* G30 (2004) S633–S648, arXiv:nucl-ex/0405007 [nucl-ex].

[21] PHENIX Collaboration, K. Adcox *et al.*, "Formation of dense partonic matter in relativistic nucleus-nucleus collisions at RHIC: Experimental evaluation by the PHENIX collaboration," *Nucl. Phys.* A757 (2005) 184–283, arXiv:nucl-ex/0410003 [nucl-ex].

[22] ALICE Collaboration, K. Aamodt *et al.*, "Elliptic flow of charged particles in Pb-Pb collisions at 2.76 TeV," *Phys. Rev. Lett.* 105 (2010) 252302, arXiv:1011.3914 [nucl-ex].

[23] ALICE Collaboration, J. Adam *et al.*, "Anisotropic flow of charged particles in Pb-Pb collisions at $\sqrt{s_{\mathrm{NN}}} = 5.02$ TeV," *Phys. Rev. Lett.* 116 (2016) 132302, arXiv:1602.01119 [nucl-ex].

[24] ALICE Collaboration, K. Aamodt *et al.*, "Charged-particle multiplicity density at mid-rapidity in central Pb-Pb collisions at $\sqrt{s_{\mathrm{NN}}} = 2.76$ TeV," *Phys. Rev. Lett.* 105 (2010) 252301, arXiv:1011.3916 [nucl-ex].

[25] ALICE Collaboration, J. Adam *et al.*, "Centrality dependence of the charged-particle multiplicity density at midrapidity in Pb-Pb collisions at $\sqrt{s_{\mathrm{NN}}} = 5.02$ TeV," *Phys. Rev. Lett.* 116 (2016) 222302, arXiv:1512.06104 [nucl-ex].

[26] J. Schukraft, "Heavy ions at the LHC: Physics perspectives and experimental program," *Pramana* 57 no. 2, (2001) 345–354. http://dx.doi.org/10.1007/s12043-001-0044-6.

[27] B. Muller, J. Schukraft, and B. Wyslouch, "First Results from Pb-Pb collisions at the LHC," *Ann. Rev. Nucl. Part. Sci.* 62 (2012) 361–386, arXiv:1202.3233 [hep-ex].

[28] M. L. Miller, K. Reygers, S. J. Sanders, and P. Steinberg, "Glauber modeling in high energy nuclear collisions," *Ann. Rev. Nucl. Part. Sci.* 57 (2007) 205–243, arXiv:nucl-ex/0701025 [nucl-ex].

[29] J. D. Bjorken, "Highly Relativistic Nucleus-Nucleus Collisions: The Central Rapidity Region," *Phys. Rev.* D27 (1983) 140–151.

[30] Z. Conesa Del Valle, *Performance of the ALICE muon spectrometer. Weak boson production and measurement in heavy-ion collisions at LHC.* PhD thesis, SUBATECH, Nantes, 2007. https://inspirehep.net/record/886889/files/CERN-THESIS-2007-102.pdf.

[31] *Hard probes in heavy ion collisions at the LHC: PDFs, shadowing and p-A collisions.* 2004. arXiv:hep-ph/0308248 [hep-ph]. http://doc.cern.ch/cernrep/2004/2004-009/2004-009.html.

[32] ALICE Collaboration, K. Aamodt *et al.*, "Suppression of Charged Particle Production at Large Transverse Momentum in Central Pb-Pb Collisions at $\sqrt{s_{\mathrm{NN}}} = 2.76$ TeV," *Phys. Lett.* B696 (2011) 30–39, arXiv:1012.1004 [nucl-ex].

[33] ALICE Collaboration, J. Adam *et al.*, "Centrality evolution of the charged-particle pseudorapidity density over a broad pseudorapidity range in Pb-Pb collisions at $\sqrt{s_{\mathrm{NN}}} = 2.76$ TeV," *Phys. Lett.* B754 (2016) 373–385, arXiv:1509.07299 [nucl-ex].

[34] ATLAS Collaboration, G. Aad *et al.*, "Measurement of the centrality dependence of the charged particle pseudorapidity distribution in lead-lead collisions at $\sqrt{s_{\mathrm{NN}}} = 2.76$ TeV with the ATLAS detector," *Phys. Lett.* B710 (2012) 363–382, arXiv:1108.6027 [hep-ex].

[35] BRAHMS Collaboration, I. G. Bearden *et al.*, "Pseudorapidity distributions of charged particles from Au-Au collisions at the maximum RHIC energy," *Phys. Rev. Lett.* 88 (2002) 202301, arXiv:nucl-ex/0112001 [nucl-ex].

[36] PHOBOS Collaboration, B. B. Back *et al.*, "Centrality dependence of the charged particle multiplicity near mid-rapidity in Au-Au collisions at $\sqrt{s_{\mathrm{NN}}} = 130$ GeV and 200 GeV," *Phys. Rev.* C65 (2002) 061901, arXiv:nucl-ex/0201005 [nucl-ex].

[37] PHENIX Collaboration, S. S. Adler *et al.*, "Systematic studies of the centrality and $\sqrt{s_{\mathrm{NN}}}$ dependence of the $dE_{\mathrm{T}}/d\eta$ and $dN_{\mathrm{ch}}/d\eta$ in heavy ion collisions at mid-rapidity," *Phys. Rev.* C71 (2005) 034908, arXiv:nucl-ex/0409015 [nucl-ex]. [Erratum: Phys. Rev.C71,049901(2005)].

[38] CMS Collaboration, S. Chatrchyan *et al.*, "Dependence on pseudorapidity and centrality of charged hadron production in Pb-Pb collisions at a nucleon-nucleon centre-of-mass energy of 2.76 TeV," *JHEP* 08 (2011) 141, arXiv:1107.4800 [nucl-ex].

[39] J. D. Bjorken, "Energy Loss of Energetic Partons in Quark-Gluon Plasma: Possible Extinction of High p_{T} Jets in Hadron-Hadron Collisions." 1982.

[40] STAR Collaboration, J. Adams *et al.*, "Evidence from d-Au measurements for final state suppression of high p_{T} hadrons in Au-Au collisions at RHIC," *Phys. Rev. Lett.* 91 (2003) 072304, arXiv:nucl-ex/0306024 [nucl-ex].

[41] STAR Collaboration, C. Adler *et al.*, "Disappearance of back-to-back high p_{T} hadron correlations in central Au-Au collisions at $\sqrt{s_{\mathrm{NN}}} = 200$ GeV," *Phys. Rev. Lett.* 90 (2003) 082302, arXiv:nucl-ex/0210033 [nucl-ex].

[42] D. d'Enterria, "Jet quenching," *Landolt-Bornstein* 23 (2010) 471, arXiv:0902.2011 [nucl-ex].

[43] S. J. Brodsky and H. J. Lu, "Shadowing and Antishadowing of Nuclear Structure Functions," *Phys. Rev. Lett.* 64 (1990) 1342.

[44] B. Z. Kopeliovich, J. Nemchik, A. Schafer, and A. V. Tarasov, "Cronin effect in hadron production off nuclei," *Phys. Rev. Lett.* 88 (2002) 232303, arXiv:hep-ph/0201010 [hep-ph].

[45] F. Gelis, E. Iancu, J. Jalilian-Marian, and R. Venugopalan, "The Color Glass Condensate," *Ann. Rev. Nucl. Part. Sci.* 60 (2010) 463–489, arXiv:1002.0333 [hep-ph].

[46] F. Gelis, "Color Glass Condensate and Glasma," *Int. J. Mod. Phys.* A28 (2013) 1330001, arXiv:1211.3327 [hep-ph].

[47] D. de Florian, R. Sassot, and M. Stratmann, "Global analysis of fragmentation functions for pions and kaons and their uncertainties," *Phys. Rev.* D75 (2007) 114010, arXiv:hep-ph/0703242 [HEP-PH].

[48] M. Gyulassy and X.-N. Wang, "HIJING 1.0: A Monte Carlo program for parton and particle production in high-energy hadronic and nuclear collisions," *Comput. Phys. Commun.* 83 (1994) 307, arXiv:nucl-th/9502021 [nucl-th].

[49] E. L. Simili, *Elliptic flow measurement at ALICE*. PhD thesis, Utrecht U., 2009. http://www.nikhef.nl/pub/services/newbiblio/theses.php.

[50] J.-Y. Ollitrault, "Anisotropy as a signature of transverse collective flow," *Phys. Rev.* D46 (1992) 229–245.

[51] A. M. Poskanzer and S. A. Voloshin, "Methods for analyzing anisotropic flow in relativistic nuclear collisions," *Phys. Rev.* C58 (1998) 1671–1678, arXiv:nucl-ex/9805001 [nucl-ex].

[52] S. Weinberg, "A Model of Leptons," *Phys. Rev. Lett.* 19 (1967) 1264–1266.

[53] Aachen-Annecy-Birmingham-CERN-Paris(CdF)-London(QMC)-Riverside-Rutherford-Saclay Collaboration, C. Rubbia *et al.*, "A 4π solid angle detector for the SPS used as a proton-antiproton collider at a centre of mass energy of 540 GeV," Tech. Rep. CERN-SPSC-78-19. SPSC-P-92-S, CERN, Geneva, 1978. http://cds.cern.ch/record/689679.

[54] M. Banner *et al.* Tech. Rep. CERN/SPS/78-08 (1978) and CERN/SPS/78-54 (1978).

[55] DELPHI, OPAL, ALEPH, LEP Electroweak Working Group, L3 Collaboration, J. Alcaraz *et al.*, "A Combination of preliminary electroweak measurements and constraints on the standard model." 2006.

[56] P. Z. Quintas, "Measurement of W and Z production cross-sections in $p\bar{p}$ collisions at $\sqrt{s} = 1.8$ TeV," arXiv:hep-ex/9412016 [hep-ex].

[57] CDF Collaboration, A. Abulencia *et al.*, "Observation of WZ Production," *Phys. Rev. Lett.* 98 (2007) 161801, arXiv:hep-ex/0702027 [hep-ex].

[58] CMS Collaboration, S. Chatrchyan *et al.*, "Study of W boson production in Pb-Pb and pp collisions at $\sqrt{s_{\mathrm{NN}}} = 2.76$ TeV," *Phys. Lett.* B715 (2012) 66–87, arXiv:1205.6334 [nucl-ex].

[59] CMS Collaboration, S. Chatrchyan *et al.*, "Measurement of the Inclusive W and Z Production Cross Sections in pp Collisions at $\sqrt{s} = 7$ TeV," *JHEP* 10 (2011) 132, arXiv:1107.4789 [hep-ex].

[60] CMS Collaboration, S. Chatrchyan *et al.*, "Measurement of inclusive W and Z boson production cross sections in pp collisions at $\sqrt{s} = 8$ TeV," *Phys. Rev. Lett.* 112 (2014) 191802, arXiv:1402.0923 [hep-ex].

[61] ATLAS Collaboration, G. Aad *et al.*, "Measurement of the inclusive $\mathrm{W}^{\pm}$ and Z/gamma cross sections in the electron and muon decay channels in pp collisions at $\sqrt{s} = 7$ TeV with the ATLAS detector," *Phys. Rev.* D85 (2012) 072004, arXiv:1109.5141 [hep-ex].

[62] ATLAS Collaboration, G. Aad *et al.*, "Measurement of $\mathrm{W}^{\pm}$ and Z-boson production cross sections in pp collisions at $\sqrt{s} = 13$ TeV with the ATLAS detector," *Phys. Lett.* B759 (2016) 601–621, arXiv:1603.09222 [hep-ex].

[63] LHCb Collaboration, R. Aaij *et al.*, "Inclusive W and Z production in the forward region at $\sqrt{s} = 7$ TeV," *JHEP* 06 (2012) 058, arXiv:1204.1620 [hep-ex].

[64] LHCb Collaboration, R. Aaij *et al.*, "Measurement of the forward W boson cross-section in pp collisions at $\sqrt{s} = 7$ TeV," *JHEP* 12 (2014) 079, arXiv:1408.4354 [hep-ex].

[65] LHCb Collaboration, R. Aaij *et al.*, "Measurement of forward W and Z boson production in pp collisions at $\sqrt{s} = 8$ TeV," *JHEP* 01 (2016) 155, arXiv:1511.08039 [hep-ex].

[66] CMS Collaboration, V. Khachatryan *et al.*, "Study of W boson production in p-Pb collisions at $\sqrt{s_{\mathrm{NN}}} = 5.02$ TeV," *Phys. Lett.* B750 (2015) 565–586, arXiv:1503.05825 [nucl-ex].

[67] CMS Collaboration, V. Khachatryan *et al.*, "Study of Z boson production in p-Pb collisions at $\sqrt{s_{\mathrm{NN}}} = 5.02$ TeV," *Phys. Lett.* B759 (2016) 36–57, arXiv:1512.06461 [hep-ex].

[68] ATLAS Collaboration, G. Aad *et al.*, "Z boson production in p-Pb collisions at $\sqrt{s_{\mathrm{NN}}} = 5.02$ TeV measured with the ATLAS detector," *Phys. Rev.* C92 (2015) 044915, arXiv:1507.06232 [hep-ex].

[69] LHCb Collaboration, R. Aaij *et al.*, "Observation of Z production in proton-lead collisions at LHCb," *JHEP* 09 (2014) 030, arXiv:1406.2885 [hep-ex].

[70] CMS Collaboration, S. Chatrchyan *et al.*, "Study of Z boson production in Pb-Pb collisions at $\sqrt{s_{\mathrm{NN}}} = 2.76$ TeV," *Phys. Rev. Lett.* 106 (2011) 212301, arXiv:1102.5435 [nucl-ex].

[71] CDF Collaboration, T. Affolder *et al.*, "Charged jet evolution and the underlying event in $\mathrm{p\bar{p}}$ collisions at 1.8 TeV," *Phys. Rev.* D65 (2002) 092002.

[72] G. G. Barnafoldi, A. G. Agocs, and P. Levai, "Underlying Event Studies for LHC Energies," *AIP Conf. Proc.* 1348 (2011) 124–129, arXiv:1101.4155 [hep-ph].

[73] CDF Collaboration, R. D. Field, "The Underlying event in hard scattering processes," *eConf* C010630 (2001) 501, arXiv:hep-ph/0201192 [hep-ph].

[74] R. Field, "Min-Bias and the Underlying Event at the LHC," in *Proceedings, 31st International Conference on Physics in collisions (PIC 2011)*. 2012. arXiv:1202.0901 [hep-ph].
https://inspirehep.net/record/1087901/files/arXiv:1202.0901.pdf.

[75] M. H. Seymour and M. Marx, "Monte Carlo Event Generators," in *Proceedings, 69th Scottish Universities Summer School in Physics : LHC Phenomenology (SUSSP69)*, pp. 287–319. 2013. arXiv:1304.6677 [hep-ph].
https://inspirehep.net/record/1229804/files/arXiv:1304.6677.pdf.

[76] R. P. Feynman, "Very high-energy collisions of hadrons," *Phys. Rev. Lett.* 23 (1969) 1415–1417.

[77] S. D. Drell and T. M. Yan, "Massive Lepton Pair Production in Hadron-Hadron Collisions at High-Energies," *Phys. Rev. Lett.* 25 (1970) 316–320. [Erratum: Phys. Rev. Lett.25,902(1970)].

[78] J. M. Campbell, J. W. Huston, and W. J. Stirling, "Hard Interactions of Quarks and Gluons: A Primer for LHC Physics," *Rept. Prog. Phys.* 70 (2007) 89, arXiv:hep-ph/0611148 [hep-ph].

[79] M. Kobayashi and T. Maskawa, "CP-Violation in the Renormalizable Theory of Weak Interaction," *Prog. Theor. Phys.* 49 (1973) 652–657.

[80] A. D. Martin, R. G. Roberts, W. J. Stirling, and R. S. Thorne, "Parton distributions and the LHC: W and Z production," *Eur. Phys. J.* C14 (2000) 133–145, arXiv:hep-ph/9907231 [hep-ph].

[81] S. Frixione and M. L. Mangano, "How accurately can we measure the W cross section?," *JHEP* 05 (2004) 056, arXiv:hep-ph/0405130 [hep-ph].

[82] C. Anastasiou, L. J. Dixon, K. Melnikov, and F. Petriello, "High precision QCD at hadron colliders: Electroweak gauge boson rapidity distributions at NNLO," *Phys. Rev.* D69 (2004) 094008, arXiv:hep-ph/0312266 [hep-ph].

[83] S. Hoche, "Introduction to parton-shower event generators," in *Theoretical Advanced Study Institute in Elementary Particle Physics: Journeys Through the Precision Frontier: Amplitudes for Colliders (TASI 2014) Boulder, Colorado, June 2-27, 2014*. 2014. arXiv:1411.4085 [hep-ph]. https://inspirehep.net/record/1328513/files/arXiv:1411.4085.pdf.

[84] T. Sjostrand, S. Mrenna, and P. Z. Skands, "PYTHIA 6.4 Physics and Manual," *JHEP* 05 (2006) 026, arXiv:hep-ph/0603175 [hep-ph].

[85] E. Barberio and Z. Was, "PHOTOS: A Universal Monte Carlo for QED radiative corrections. Version 2.0," *Comput. Phys. Commun.* 79 (1994) 291–308.

[86] C. Oleari, "The POWHEG-BOX," *Nucl. Phys. Proc. Suppl.* 205-206 (2010) 36–41, arXiv:1007.3893 [hep-ph].

[87] P. A. Nason, "Recent Developments in POWHEG," *PoS* RADCOR2009 (2010) 018, arXiv:1001.2747 [hep-ph].

[88] R. Gavin, Y. Li, F. Petriello, and S. Quackenbush, "W Physics at the LHC with FEWZ 2.1," *Comput. Phys. Commun.* 184 (2013) 208–214, arXiv:1201.5896 [hep-ph].

[89] R. Gavin, Y. Li, F. Petriello, and S. Quackenbush, "FEWZ 2.0: A code for hadronic Z production at next-to-next-to-leading order," *Comput. Phys. Commun.* 182 (2011) 2388–2403, arXiv:1011.3540 [hep-ph].

[90] Y. Li and F. Petriello, "Combining QCD and electroweak corrections to dilepton production in FEWZ," *Phys. Rev.* D86 (2012) 094034, arXiv:1208.5967 [hep-ph].

[91] P. Jimenez-Delgado and E. Reya, "Dynamical NNLO parton distributions," *Phys. Rev.* D79 (2009) 074023, arXiv:0810.4274 [hep-ph].

[92] S. Catani, L. Cieri, G. Ferrera, D. de Florian, and M. Grazzini, "Vector boson production at hadron colliders: a fully exclusive QCD calculation at NNLO," *Phys. Rev. Lett.* 103 (2009) 082001, arXiv:0903.2120 [hep-ph].

[93] S. Catani and M. Grazzini, "An NNLO subtraction formalism in hadron collisions and its application to Higgs boson production at the LHC," *Phys. Rev. Lett.* 98 (2007) 222002, arXiv:hep-ph/0703012 [hep-ph].

[94] J. Pumplin, D. R. Stump, J. Huston, H. L. Lai, P. M. Nadolsky, and W. K. Tung, "New generation of parton distributions with uncertainties from global QCD analysis," *JHEP* 07 (2002) 012, arXiv:hep-ph/0201195 [hep-ph].

[95] H.-L. Lai, M. Guzzi, J. Huston, Z. Li, P. M. Nadolsky, J. Pumplin, and C. P. Yuan, "New parton distributions for collider physics," *Phys. Rev.* D82 (2010) 074024, arXiv:1007.2241 [hep-ph].

[96] A. D. Martin, W. J. Stirling, R. S. Thorne, and G. Watt, "Parton distributions for the LHC," *Eur. Phys. J.* C63 (2009) 189–285, arXiv:0901.0002 [hep-ph].

[97] D. Stump, J. Huston, J. Pumplin, W.-K. Tung, H. L. Lai, S. Kuhlmann, and J. F. Owens, "Inclusive jet production, parton distributions, and the search for new physics," *JHEP* 10 (2003) 046, arXiv:hep-ph/0303013 [hep-ph].

[98] A. D. Martin, R. G. Roberts, W. J. Stirling, and R. S. Thorne, "Physical gluons and high E_T jets," *Phys. Lett.* B604 (2004) 61–68, arXiv:hep-ph/0410230 [hep-ph].

[99] S. Alekhin, "Parton distribution functions from the precise NNLO QCD fit," *JETP Lett.* 82 (2005) 628–631, arXiv:hep-ph/0508248 [hep-ph]. [Pisma Zh. Eksp. Teor. Fiz. 82, 710 (2005)].

[100] H1 Collaboration, C. Adloff *et al.*, "Deep inelastic inclusive ep scattering at low x and a determination of α_s," *Eur. Phys. J.* C21 (2001) 33–61, arXiv:hep-ex/0012053 [hep-ex].

[101] H1 Collaboration, C. Adloff *et al.*, "Measurement and QCD analysis of neutral and charged current cross-sections at HERA," *Eur. Phys. J.* C30 (2003) 1–32, arXiv:hep-ex/0304003 [hep-ex].

[102] ZEUS Collaboration, S. Chekanov *et al.*, "A ZEUS next-to-leading-order QCD analysis of data on deep inelastic scattering," *Phys. Rev.* D67 (2003) 012007, arXiv:hep-ex/0208023 [hep-ex].

[103] ZEUS Collaboration, S. Chekanov *et al.*, "An NLO QCD analysis of inclusive cross-section and jet-production data from the ZEUS experiment," *Eur. Phys. J.* C42 (2005) 1–16, arXiv:hep-ph/0503274 [hep-ph].

[104] G. Altarelli and G. Parisi, "Asymptotic Freedom in Parton Language," *Nucl. Phys.* B126 (1977) 298–318.

[105] Y. L. Dokshitzer, "Calculation of the Structure Functions for Deep Inelastic Scattering and e^+e^- Annihilation by Perturbation Theory in Quantum Chromodynamics.," *Sov. Phys. JETP* 46 (1977) 641–653. [Zh. Eksp. Teor. Fiz. 73, 1216 (1977)].

[106] V. N. Gribov and L. N. Lipatov, "Deep inelastic e p scattering in perturbation theory," *Sov. J. Nucl. Phys.* 15 (1972) 438–450. [Yad. Fiz. 15, 781 (1972)].

[107] E. Perez and E. Rizvi, "The Quark and Gluon Structure of the Proton," *Rep. Prog. Phys.* 76 (2013) 046201, arXiv:1208.1178 [hep-ex].

[108] J. Gao, M. Guzzi, J. Huston, H.-L. Lai, Z. Li, P. Nadolsky, J. Pumplin, D. Stump, and C. P. Yuan, "CT10 next-to-next-to-leading order global analysis of QCD," *Phys. Rev.* D89 (2014) 033009, arXiv:1302.6246 [hep-ph].

[109] ZEUS, H1 Collaboration, F. D. Aaron *et al.*, "Combined Measurement and QCD Analysis of the Inclusive ep Scattering Cross Sections at HERA," *JHEP* 01 (2010) 109, arXiv:0911.0884 [hep-ex].

[110] ZEUS, H1 Collaboration, V. Radescu, "Hera Precision Measurements and Impact for LHC Predictions," in *Proceedings, 46th Rencontres de Moriond on QCD and High Energy Interactions*, pp. 27–30. 2011. arXiv:1107.4193 [hep-ex]. https://inspirehep.net/record/919392/files/arXiv:1107.4193.pdf.

[111] S. Alekhin, J. Blumlein, and S. Moch, "Parton Distribution Functions and Benchmark Cross Sections at NNLO," *Phys. Rev.* D86 (2012) 054009, arXiv:1202.2281 [hep-ph].

[112] R. D. Ball *et al.*, "Parton distributions with LHC data," *Nucl. Phys.* B867 (2013) 244–289, arXiv:1207.1303 [hep-ph].

[113] NNPDF Collaboration, R. D. Ball *et al.*, "Parton distributions for the LHC Run II," *JHEP* 04 (2015) 040, arXiv:1410.8849 [hep-ph].

[114] J. Thomas, C. A. Bertulani, N. Brady, D. B. Clark, E. Godat, and F. Olness, "Parton distribution functions probed in ultraperipheral collisions at the CERN Large Hadron Collider." 2016.

[115] J. Rojo, "Parton Distributions and LHC Data," *Nuovo Cim.* C035N1 (2012) 179–186, arXiv:1106.1997 [hep-ph].

[116] W. J. Stirling. http://www.hep.ph.ic.ac.uk/~wstirlin/plots/plots.html.

[117] K. J. Eskola, V. J. Kolhinen, H. Paukkunen, and C. A. Salgado, "Global reanalysis of nPDFs," *PoS* LHC07 (2007) 018, arXiv:0707.0060 [hep-ph].

[118] K. J. Eskola, H. Paukkunen, and C. A. Salgado, "EPS09 - Global NLO analysis of nuclear PDFs and their uncertainties," *PoS* High-p_{T} physics09 (2009) 019, arXiv:0903.1956 [hep-ph].

[119] K. J. Eskola, H. Paukkunen, and C. A. Salgado, "EPS09: A New Generation of NLO and LO Nuclear Parton Distribution Functions," *JHEP* 04 (2009) 065, arXiv:0902.4154 [hep-ph].

[120] P. R. Norton, "The EMC effect," *Rept. Prog. Phys.* 66 (2003) 1253–1297.

[121] A. Bodek and J. L. Ritchie, "Fermi Motion Effects in Deep Inelastic Lepton Scattering from Nuclear Targets," *Phys. Rev.* D23 (1981) 1070.

[122] K. J. Eskola, V. J. Kolhinen, and P. V. Ruuskanen, "Scale evolution of nuclear parton distributions," *Nucl. Phys.* B535 (1998) 351–371, arXiv:hep-ph/9802350 [hep-ph].

[123] K. J. Eskola, V. J. Kolhinen, and C. A. Salgado, "The Scale dependent nuclear effects in parton distributions for practical applications," *Eur. Phys. J.* C9 (1999) 61–68, arXiv:hep-ph/9807297 [hep-ph].

[124] M. Hirai, S. Kumano, and M. Miyama, "Determination of nuclear parton distributions," *Phys. Rev.* D64 (2001) 034003, arXiv:hep-ph/0103208 [hep-ph].

[125] M. Hirai, S. Kumano, and T. H. Nagai, "Nuclear parton distribution functions and their uncertainties," *Phys. Rev.* C70 (2004) 044905, arXiv:hep-ph/0404093 [hep-ph].

[126] D. de Florian and R. Sassot, "Nuclear parton distributions at next-to-leading order," *Phys. Rev.* D69 (2004) 074028, arXiv:hep-ph/0311227 [hep-ph].

[127] V. I. Martinez Outschoorn, *Measurement of the Charge Asymmetry of W Bosons Produced in pp Collisions at $\sqrt{s} = 7$ TeV with the ATLAS Detector*. PhD thesis, Harvard U., 2011. https://inspirehep.net/record/1088185/files/CERN-THESIS-2011-037.pdf.

[128] L. Evans and P. Bryant, "LHC Machine," *JINST* 3 (2008) S08001.

[129] CERN, "Accelerators and Technology Sector." https://espace.cern.ch/acc-tec-sector/default.aspx.

[130] K. Schweda, "ALICE at the Dawn of LHC." http://www.epi.rub.de/EUNPC/programme/schweda.pdf. 2009.

[131] ALICE Collaboration, K. Aamodt *et al.*, "The ALICE experiment at the CERN LHC," *JINST* 3 (2008) S08002.

[132] ATLAS Collaboration, G. Aad *et al.*, "The ATLAS Experiment at the CERN Large Hadron Collider," *JINST* 3 (2008) S08003.

[133] CMS Collaboration, S. Chatrchyan *et al.*, "The CMS experiment at the CERN LHC," *JINST* 3 (2008) S08004.

[134] LHCb Collaboration, A. A. Alves, Jr. *et al.*, "The LHCb Detector at the LHC," *JINST* 3 (2008) S08005.

[135] LHCf Collaboration, O. Adriani *et al.*, "The LHCf detector at the CERN Large Hadron Collider," *JINST* 3 (2008) S08006.

[136] TOTEM Collaboration, G. Anelli *et al.*, "The TOTEM experiment at the CERN Large Hadron Collider," *JINST* 3 (2008) S08007.

[137] ALICE Collaboration. http://alice-collaboration.web.cern.ch/general/index.html.

[138] "Physics Publications of the ALICE Collaboration submitted to Refereed Journals." http://aliceinfo.cern.ch/ArtSubmission/submitted?title=&field_draft_status_value_many_to_one_1%5B%5D=published&field_draft_submission_date_value%5Bmin%5D%5Byear%5D=&field_draft_submission_date_value%5Bmin%5D%5Bmonth%5D=&field_draft_submission_date_value%5Bmin%5D%5Bday%5D=&field_draft_submission_date_value%5Bmax%5D%5Byear%5D=&field_draft_submission_date_value%5Bmax%5D%5Bmonth%5D=&field_draft_submission_date_value%5Bmax%5D%5Bday%5D=.

[139] ALICE Collaboration, B. B. Abelev *et al.*, "Performance of the ALICE Experiment at the CERN LHC," *Int. J. Mod. Phys.* A29 (2014) 1430044, arXiv:1402.4476 [nucl-ex].

[140] ALICE Collaboration, P. Cortese *et al.*, "ALICE: Physics performance report, volume II," *J. Phys.* G32 (2006) 1295–2040.

[141] ALICE Collaboration, P. Cortese *et al.*, "ALICE: Physics performance report, volume I," *J. Phys.* G30 (2004) 1517–1763.

[142] ALICE Collaboration. https://alice-collaboration.web.cern.ch/documents/tdr/index.html.

[143] J. Allen *et al.*, "ALICE DCal: An Addendum to the EMCal Technical Design Report Di-Jet and Hadron-Jet correlation measurements in ALICE," Tech. Rep. CERN-LHCC-2010-011. ALICE-TDR-14-add-1, Jun, 2010. https://cds.cern.ch/record/1272952.

[144] P. G. Kuijer, "Com sioning and Prospects for Early Physics with ALICE," *Nucl. Phys.* A830 (2009) 81C–88C, arXiv:0907.5060 [hep-ex].

[145] ALICE Collaboration, G. Dellacasa *et al.*, "ALICE technical design report of the zero degree calorimeter (ZDC)." 1999.

[146] ALICE Collaboration, G. Dellacasa *et al.*, "ALICE technical design report: Photon multiplicity detector (PMD)." 1999.

[147] ALICE Collaboration, P. Cortese *et al.*, "ALICE technical design report on forward detectors: FMD, To and Vo." 2004.

[148] ALICE Collaboration, G. Dellacasa *et al.*, "ALICE technical design report of the inner tracking system (ITS)." 1999.

[149] ALICE Collaboration, G. Dellacasa *et al.*, "ALICE: Technical design report of the time projection chamber." 2000.

[150] ALICE Collaboration, P. Cortese, *ALICE transition-radiation detector: Technical Design Report*. Technical Design Report ALICE. CERN, Geneva, 2001. http://cds.cern.ch/record/519145.

[151] G. Dellacasa and P. Braun-Munzinger, "ALICE: a transition radiation detector for electron identification within the ALICE central detector - an addendum to the Technical Proposal," Tech. Rep. CERN-LHCC-99-013. LHCC-P-3-Add-2, CERN, Geneva, May, 1999. http://cds.cern.ch/record/401988.

[152] ALICE Collaboration, G. Dellacasa *et al.*, "ALICE technical design report of the time-of-flight system (TOF)." 2000.

[153] ALICE Collaboration, P. Cortese *et al.*, "ALICE: Addendum to the technical design report of the time of flight system (TOF)." 2002.

[154] ALICE Collaboration, F. Piuz, W. Klempt, L. Leistam, J. De Groot, and J. Sch□kraft, *ALICE high-momentum particle identification: Technical Design Report*. Technical Design Report ALICE. CERN, Geneva, 1998. http://cds.cern.ch/record/381431.

[155] ALICE Collaboration, V. I. Man'ko, W. Klempt, L. Leistam, J. De Groot, and J. Schukraft, *ALICE Photon Spectrometer (PHOS): Technical Design Report*. Technical Design Report ALICE. CERN, Geneva, 1999. http://cds.cern.ch/record/381432.

[156] T. Cormier, C. W. Fabjan, L. Riccati, and H. de Groot, "ALICE electromagnetic calorimeter: addendum to the ALICE technical proposal," Tech. Rep. CERN-LHCC-2006-014. CERN-LHCC-96-32-ADD-3, CERN, Geneva, Mar, 2006. http://cds.cern.ch/record/932676.

[157] "Dimuon Forward Spectrometer : Tracking chambers." https://twiki.cern.ch/twiki/bin/viewauth/ALICE/MuonTracking.

[158] ALICE Collaboration, N. Bastid *et al.*, "Test Experiment for the Beam Shielding in ALICE," Tech. Rep. ALICE-INT-1996-14. CERN-ALICE-INT-1996-14, CERN, Geneva, 1996. https://cds.cern.ch/record/689402.

[159] ALICE Collaboration, S. Beole *et al.*, "The forward muon spectrometer of ALICE." 1996.

[160] ALICE Collaboration, "ALICE technical design report of the dimuon forward spectrometer." 1999.

[161] C. Suire, "Installation of station 1 of the tracking chambers of the ALICE Muon Spectrometer." ALICE Collection., Mar, 2007.

[162] V. Blobel and C. Kleinwort, "A New method for the high precision alignment of track detectors," in *Advanced Statistical Techniques in Particle Physics. Proceedings, Conference, Durham, UK, March 18-22, 2002*, pp. URL–STR(9). 2002. arXiv:hep-ex/0208021 [hep-ex]. http://www.ippp.dur.ac.uk/Workshops/02/statistics/proceedings//blobel1.pdf.

[163] D. Stocco, *Development of the ALICE Muon Spectrometer: Preparation for data taking and heavy flavor measurement*. PhD thesis, Turin U., 2008. http://dottorato.ph.unito.it/Studenti/Tesi/XXI/stocco.pdf.

[164] G. G. Fronze, "Performance of the ALICE muon trigger system in pp and Pb-Pb collisions at the LHC," *JINST* 11 (2016) C06003, arXiv:1605.03461 [physics.ins-det].

[165] ALICE Collaboration, C. W. Fabjan *et al.*, *ALICE trigger data-acquisition high-level trigger and control system: Technical Design Report*. Technical Design Report ALICE. CERN, Geneva, 2004. https://cds.cern.ch/record/684651.

[166] ALICE Collaboration, O. Villalobos Baillie *et al.*, "The ALICE Central Trigger Processor." 2005.

[167] ALICE Collaboration, O. Villalobos Baillie *et al.*, "Recent developments on the ALICE central Trigger processor." 2007.

[168] RD12 Collaboration, B. G. Taylor, "Timing distribution at the LHC." 2002.

[169] S. Baron and A. Monera-Martinez, "Status of the TTC upgrade." 2007.

[170] W. Carena *et al.*, "ALICE DAQ and ECS User's Guide," Tech. Rep. ALICE-INT-2005-015. CERN-ALICE-INT-2005-015, CERN, Geneva, 2005. http://cds.cern.ch/record/960457.

[171] "ALICE Offline Pages." http://aliweb.cern.ch/Offline.

[172] "C++." http://www.cplusplus.com/info/.

[173] "ROOT: A Data Analysis Framework." http://root.cern.ch.

[174] ALICE Collaboration, "The ALICE Offline Bible." http://aliweb.cern.ch/Offline.

[175] R. Brun, F. Bruyant, M. Maire, A. C. McPherson, and P. Zanarini, *GEANT 3: user's guide Geant 3.10, Geant 3.11; rev. version*. CERN, Geneva, 1987. https://cds.cern.ch/record/1119728.

[176] GEANT4 Collaboration, S. Agostinelli *et al.*, "GEANT4: A Simulation toolkit," *Nucl. Instrum. Meth.* A506 (2003) 250–303.

[177] A. Ferrari, P. R. Sala, A. Fasso, and J. Ranft, *FLUKA: A multi-particle transport code (program version 2005)*. CERN, Geneva, 2005. https://cds.cern.ch/record/898301.

[178] ALICE Collaboration, "Particle Transport and Detector Simulation." http://aliweb.cern.ch/Offline/Activities/Simulation/ParticleTransport.html.

[179] ALICE Collaboration, "AliEn home page." http://alien.web.cern.ch.

[180] ALICE Collaboration, P. Saiz, L. Aphecetche, P. Buncic, R. Piskac, J. E. Revsbech, and V. Sego, "AliEn - ALICE environment on the GRID," *Nucl. Instrum. Meth.* A502 (2003) 437–440.

[181] CERN, "WLCG." http://wlcg.web.cern.ch.

[182] CERN, "The Worldwide LHC Computing Grid." http://home.cern/about/computing/worldwide-lhc-computing-grid.

[183] ALICE Collaboration, P. Cortese *et al.*, *ALICE computing: Technical Design Report*. Technical Design Report ALICE. CERN, Geneva, 2005. http://cds.cern.ch/record/832753.

[184] "MonALISA: Monitoring Agents using a Large Integrated Services Architecture." http://monalisa.cacr.caltech.edu/monalisa.htm.

[185] ALICE Collaboration, B. B. Abelev *et al.*, "Measurement of visible cross sections in proton-lead collisions at $\sqrt{s_{\mathrm{NN}}} = 5.02$ TeV in van der Meer scans with the ALICE detector," *JINST* 9 (2014) P11003, arXiv:1405.1849 [nucl-ex].

[186] ALICE Collaboration, J. Adam *et al.*, "Centrality dependence of particle production in p-Pb collisions at $\sqrt{s_{\mathrm{NN}}} = 5.02$ TeV," *Phys. Rev.* C91 (2015) 064905, arXiv:1412.6828 [nucl-ex].

[187] S. Alioli, P. Nason, C. Oleari, and E. Re, "NLO vector-boson production matched with shower in POWHEG," *JHEP* 07 (2008) 060, arXiv:0805.4802 [hep-ph].

[188] M. Cacciari, S. Frixione, N. Houdeau, M. L. Mangano, P. Nason, and G. Ridolfi, "Theoretical predictions for charm and bottom production at the LHC," *JHEP* 10 (2012) 137, arXiv:1205.6344 [hep-ph]. http://www.lpthe.jussieu.fr/~cacciari/fonll/fonllform.html.

[189] P. M. Nadolsky, H.-L. Lai, Q.-H. Cao, J. Huston, J. Pumplin, D. Stump, W.-K. Tung, and C. P. Yuan, "Implications of CTEQ global analysis for collider observables," *Phys. Rev.* D78 (2008) 013004, arXiv:0802.0007 [hep-ph].

[190] ALICE Collaboration, B. B. Abelev *et al.*, "Measurement of prompt D-meson production in p-Pb collisions at $\sqrt{s_{\rm NN}} = 5.02$ TeV," *Phys. Rev. Lett.* 113 (2014) 232301, arXiv:1405.3452 [nucl-ex].

[191] N. Bastid, P. Crochet, S. Li, and X. Zhang, "Production of muons from heavy-flavour decays at forward rapidity in p-Pb and Pb-p collisions at $\sqrt{s_{\rm NN}} = 5.02$ TeV." https://aliceinfo.cern.ch/Notes/node/196. 2013.

[192] C. Hadjidakis. Jpis2MuMu PAG meeting, February 22nd 2013.

[193] M. Gagliardi. Jpsi2MuMu PAG meeting, March 8th 2013.

[194] ALICE Collaboration, J. Adam *et al.*, "Centrality dependence of inclusive J/Ψ production in p-Pb collisions at $\sqrt{s_{\rm NN}} = 5.02$ TeV," *JHEP* 11 (2015) 127, arXiv:1506.08808 [nucl-ex].

[195] H. Paukkunen and C. A. Salgado, "Constraints for the nuclear parton distributions from Z and W production at the LHC," *JHEP* 03 (2011) 071, arXiv:1010.5392 [hep-ph].

[196] L. Apechetche. https://twiki.cern.ch/twiki/bin/view/ALICE/MuonIntegratedLuminosity#LHC12h_2292_w_SPD_583_w_o_SPD_nb.

[197] C. Hadjidakis and D. Stocco. https://twiki.cern.ch/twiki/bin/viewauth/ALICE/QAForTheSelectionOfGoodPhysicsRunsForMuonPhysics.

[198] J. Alwall *et al.*, "A Standard format for Les Houches event files," *Comput. Phys. Commun.* 176 (2007) 300–304, arXiv:hep-ph/0609017 [hep-ph].

UNIVERSITE BRETAGNE LOIRE

IMT Atlantique
Bretagne-Pays de la Loire
École Mines-Télécom

Thèse de Doctorat

Jianhui ZHU

Mesure de la production du boson W dans le canal muonique à rapidité à l'avant avec ALICE

W boson measurement in the muonic decay channel at forward rapidity with ALICE

Résumé

La haute densité d'énergie atteinte au Large Hadron Collider (LHC) au CERN permet une production abondante de sondes dures, telles que quarkonia, jets à haute impulsion transverse (p_T) et bosons vecteurs (W, Z), qui sont produits lors de la collision partonique initiale. Les bosons vecteur se désintègrent avant la formation du Plasma de Quark et de Gluons (PQG), une phase déconfinée de la matière, qui peut être produite lors de collisions d'ions lourds ultra-relativistes. Les leptons issus de la désintégration des bosons électrofaibles ne sont pas sensibles à l'interaction forte avec le PQG. Pour ces raisons les bosons électrofaibles fournissent une référence pour l'étude des modifications induites par le milieu sur les sondes colorées.
La production de bosons W en collisions pp à $\sqrt{s}$=8 TeV et en collisions p-Pb à $\sqrt{s_{NN}}$=5.02 TeV est mesurée dans le canal de désintégration muonique au LHC avec le détecteur ALICE. En collision pp, la gamme de rapidité couverte par la mesure est $-4<y_{cms}<-2.5$. En collision p-Pb, la différence d'énergie entre le proton et l' ion plomb donne lieu à un décalage en rapidité. En inversant la direction des faisceaux, il est possible de couvrir les régions de rapidité $-4.46<y_{cms}<-2.96$ et $2.03<y_{cms}<3.53$. Les résultats présentés dans cette thèse consistent dans la mesure de la section efficace de la production de muons avec p_T>10 GeV/c issus de la désintégration des bosons W+ et W-. La mesure de l'asymétrie de charge, définie comme la différence des taux de production des muons positifs et négatifs divisée par leur somme, est également effectuée. Les résultats sont comparés avec des calculs théoriques obtenus avec ou sans tenir compte des modifications des fonctions de distribution partonique dans les noyaux. La production du boson W est aussi étudiée en fonction de la centralité des collisions: nous observons que, dans les erreurs expérimentales, la section efficace des muons issus de la désintégration du boson W est proportionnelle aux nombre de collisions binaires entre les nucléons.

Mots clés

Collisions d'ions lourds, collisions hadroniques, Plasma de Quarks et de Gluons, LHC, ALICE, CERN, boson électrofaible, muon, fonction de distribution partonique, fonction de distribution partonique nucléaire, collisions p-Pb, collisions pp, 5 TeV, 8 TeV

Abstract

The high collision energies available at the LHC allow for an abundant production of hard probes, such as quarkonia, high-p_T jets and vector bosons (W, Z), which are produced in initial hard parton scattering processes. The latter decay before the formation of the Quark-Gluon Plasma (QGP), which is a deconfined phase of QCD matter produced in high-energy heavy-ion collisions. Their leptonic decay products do not interact strongly with the QGP. Thus electroweak bosons introduce a way for benchmarking in-medium modifications to coloured probes.
The production of W-boson in pp collisions at $\sqrt{s}$=8 TeV and p-Pb collisions at $\sqrt{s_{NN}}$=5.02 TeV are measured via the muonic decay channel at the LHC with the ALICE detector. In pp collisions the rapidity covered by the measurement is $-4<y_{cms}<-2.5$. In p-Pb collisions, on the other hand, the different energies of the proton and lead ion give rise to a rapidity shift. By exchanging the direction of the beams, it is possible to cover the rapidity ranges $-4.46<y_{cms}<-2.96$ and $2.03<y_{cms}<3.53$. The production cross section and charge asymmetry of muons from W-boson decays with p^{μ}_{T}>10 GeV/c are determined. The results are compared to theoretical calculations both with and without including the nPDFs. The W-boson production is also studied as a function of the collision centrality: the cross section of muons from W-boson decays is found to scale with the average number of binary nucleon-nucleon collisions with uncertainties.

Key Words

Heavy Ion Collisions, HIC, Hadronic Collisions, Quark Gluon Plasma, QGP, LHC, ALICE, CERN, Electroweak Boson, muon, Parton distribution functions, PDF, Nuclear parton distribution functions, nPDF, p-Pb collisions, pp collisions, 5 TeV, 8 TeV